ISSN 1300-3615 / e-ISSN 2667-7725 - https://dergipark.org.tr/tr/pub/isibted

ISI Bilimi ve Tekniği Dergisi

Journal of Thermal Science and Technology

TIBTD
TÜRK ISI BİLİMİ VE TEKNİĞİ DERNEĞİ
TURKISH SOCIETY FOR THERMAL SCIENCE AND TECHNOLOGY

ISI Bilimi ve Tekniği Dergisi

Journal of Thermal Science and Technology

(2025) Vol. 45, No. 1

https://dergipark.org.tr/tr/pub/isibted

Türk Isı Bilimi ve Tekniği Derneği tarafından yılda iki kez Nisan ve Ekim aylarında yayınlanır.

A publication of the Turkish Society for Thermal Sciences and Technology, published twice a year, in April and October.

TIBTD Adına Yayın Sahibi Sorumlu Yayımcı / *Publisher:*
Prof. Dr. Nuri YÜCEL, Gazi Üniversitesi

Sorumlu Yazı İşleri Müdürü - Editör / *Editor-in-Chief:*
Prof. Dr. M. Zeki YILMAZOĞLU, Gazi Üniversitesi
zekiyilmazoglu@gazi.edu.tr

Yayın Türü: Yaygın, süreli

Türk Isı Bilimi ve Tekniği Derneği (TIBTD)

Dernek ve bu dergi, Türkiye'de ısı bilimi ve tekniğini geliştirmek amacıyla 1976 yılında Prof. Dr. Yalçın A. GÖĞÜŞ tarafından kurulmuştur.

Turkish Society of Thermal Sciences and Technology

The association and the journal was founded by Prof. Dr. Yalçın A. GÖĞÜŞ in 1976 to improve thermal sciences and technology in Turkey.

Adresi / *Address:*
TIBTD, Mühendislik Fakültesi, Zemin Kat No.22,
Gazi Üniversitesi, 06570 ANKARA
www.tibtd.org.tr
ibtd@tibtd.org.tr

Üyelik aidatları için:
İş Bankası Maltepe Şubesi
Hesap No: 42120867567
IBAN: TR08 0006 4000 0014 2120 8675 67

ISSN: 1300-3615 / **e-ISSN:** 2667-7725

İçindekiler / *Contents*

Amaç / *Objective*
Isı bilimi ve tekniğinin geliştirilmesini teşvik etmek, ısı bilimi ve tekniği alanında özgün, teorik, sayısal ve deneysel çalışmaların yayınlanmasına olanak sağlamaktır.
To contribute to the improvement of thermal sciences and technology and publication of original, theoretical, numerical, and experimental studies in thermal sciences and technology.

İçerik / *Content*
Isı bilimi ve tekniği alanındaki özgün ve derleme makaleler.
Original and review articles in thermal sciences and technology.

Değerlendirme / *Evaluation*
Dergi hakemli bir dergi olup, her bir makale konusunda uzman en az iki hakem tarafından değerlendirilir.
Each article published in this journal is evaluated by at least two referees.

Science Citation Index Expanded (SCIE), Engineering Index (EI), EBSCO ve Mühendislik ve Temel Bilimler Veri Tabanı (TÜBİTAK-ULAKBİM) tarafından taranmaktadır.

Indexed by Science Citation Index Expanded (SCIE), Engineering Index (EI), EBSCO and Engineering and Natural Sciences Data Base (TÜBİTAK-ULAKBİM).

Journal Homepage: https://dergipark.org.tr/tr/pub/isibted

Isı Bilimi ve Tekniği Dergisi

Archive: https://tibtd.org.tr/dergi

Thermal Analysis of a Fluid Inside a Cubicle Surrounded by Peltier Modules

Lakshmanan S [1], Raghunath T [1], Karthik K [1], Bhuvaneswari S [2,*], Venkatesan M [1,*]

[1] *School of Mechanical Engineering, SASTRA Deemed University, Tirumalaisamudram, Thanjavur 613 401, Tamilnadu, India.*
[2] *Department of Computer Science and Engineering, Srinivasa Ramanujan Centre, SASTRA Deemed University, Kumbakonam 612 001, Tamilnadu, India.*

A R T I C L E I N F O

2025, vol. 45, no.1, pp. 1-9

doi: 10.47480/isibted.1485008

Research Article
Received: 17 May 2024
Accepted: 22 October 2024

* *Corresponding Authors*
e-mail: mvenkat@mech.sastra.edu
s.bhuvana@src.sastra.edu

Keywords:
Thermoelectric effect
Peltier module
Machine learning

ORCID Numbers in author order:
0009-0005-2227-2343
0009-0005-5770-5161
0009-0008-3774-9222
0000-0002-3182-7823
0000-0002-6513-7556

A B S T R A C T

Peltier modules are thermoelectric devices that convert electric energy to thermal energy. The cost of the cooling process by the module depends on the size of the module. The number of modules is vital in deciding the system's performance. A Peltier module has a high value of the coefficient of performance (COP) for the applied electrical power. The module finds many applications because of its compact size, eco-friendly nature, high durability, noise and vibration-free operation, and low maintenance. Despite these advantages, the Peltier module faces constraints for large-scale applications. This work presents a computational analysis of the temperature distribution of a fluid volume surrounded by four Peltier modules using COMSOL Multiphysics software. Nine different cuboids with multiple Peltier modules are analyzed. The temperature distribution as a function of time is presented. A Machine learning algorithm is developed to predict the temperature of the fluid for varying cuboid sizes surrounded by Peltier modules. The developed machine learning model can predict the average temperature of the fluid domain with an accuracy of 97% for any given Peltier size, fluid volume, applied current, and time.

Peltier Modülleriyle Çevreli Bir Küpün İçindeki Akışkanın Termal Analizi

M A K A L E B İ L G İ S İ

Anahtar Kelimeler:
Termoelektrik etki
Peltier modülü
Makine öğrenimi

Ö Z E T

Peltier modülleri, elektrik enerjisini termal enerjiye dönüştüren termoelektrik cihazlardır. Modül tarafından gerçekleştirilen soğutma işleminin maliyeti, modülün boyutuna bağlıdır. Modül sayısı, sistemin performansına karar vermede hayati bir rol oynar. Bir Peltier modülü, uygulanan elektrik gücü için yüksek bir performans katsayısı (COP) değerine sahiptir. Modül, kompakt boyutu, çevre dostu yapısı, yüksek dayanıklılığı, gürültüsüz ve titreşimsiz çalışması ve daha az bakım gerektirmesi nedeniyle birçok uygulama bulmaktadır. Bu avantajlara rağmen, Peltier modülü büyük ölçekli uygulamalar için kısıtlamalarla karşı karşıyadır. Bu çalışma, COMSOL Multiphysics yazılımını kullanarak dört Peltier modülüyle çevrili bir sıvı hacminin sıcaklık dağılımının hesaplamalı analizini sunmaktadır. Birden fazla Peltier modülüne sahip dokuz farklı küboid analiz edilmiştir. Sıcaklık dağılımı zamana bağlı olarak sunulmuştur. Peltier modülleriyle çevrili çeşitli küboid boyutları için sıvının sıcaklığını tahmin etmek üzere bir Makine Öğrenmesi algoritması geliştirilmiştir. Geliştirilen makine öğrenmesi modeli, herhangi bir Peltier boyutu, sıvı hacmi, uygulanan akım ve zaman için sıvı alanının ortalama sıcaklığını %97 doğrulukla tahmin edebilmektedir.

NOMENCLATURE

a	Coefficient of Absorption
C	Calorific capacity $(J/kg.K)$
c	Coefficient of Diffusion
D	Density vector of the electrical flux
d_a	Damping term
E	Electric field
E_a	Mass matrix (or mass coefficient)
f	Source term
g	Boundary source term
h	Field variable coefficient in Neumann Boundary condition
h^T	Transpose of h
J	Electric current density vector
n	Outward unit normal vector on $\partial\Omega$
q	Heat flow vector
r	Coefficient in Neumann Boundary condition
T	Absolute temperature (K)
u	Vector-valued field variable
V	Voltage / Tension (V)
$\emptyset$	The specific flow of heat sources (W/m^3)
Ω	Computational domain
$\partial\Omega$	Computational domain boundary
α	Seebeck Coefficient matrix Conservative flux convection coefficient
β	Convection coefficient
γ	Conservative flux source term
ε	Matrix of relative permittivity
λ	Thermal conductivity $(W/m.K)$
μ	Lagrange Multiplier
π	Matrix of Peltier coefficient
ρ	Density (kg/m^3)
σ	Electrical conductivity (S/m)
φ	Rate of heat production
$\nabla, \vec{\nabla}$	Gradient, Vectoral Gradient operator

INTRODUCTION

The Peltier effect, discovered by Jean Charles Athanase Peltier in 1834, is a phenomenon in which an electric current flowing through a junction of two different conductive materials causes a temperature difference across the junction. Peltier modules, known as thermoelectric coolers or TECs, utilize this effect to achieve precise and efficient temperature control. The module finds applications including green buildings, air coolers, Light emitting diode (LED) cooling, polymerase chain reaction (PNA), small-scale refrigerators, and mini/micro heat exchangers. Various works have been reported in the literature related to the analysis of thermal characteristics of Peltier Modules.

Zaferani et al., (2021) discussed the various applications of Peltier cells in aviation and the military using advanced materials like polymers and fibers. The applications include preparing flexible compounds and stretchable electronic devices such as nanogenerators, solar cells, supercapacitors, and carbon nanotube field effect transistors. Antonova and Aparicio et al., (2012) discussed the usage of thermoelectric coolers and calculated the Coefficient of performance. Convective and radiative modes of heat transfer were considered. The temperature sensitivity of the materials was discussed to understand the underlying physics. A tradeoff was found between selecting materials that have suitable electrical conductivity (γ), Seebeck coefficient (α), and thermal conductivity (κ). Seebeck coefficient must be high to have a pronounced Peltier effect. Electrical conductivity must be high to reduce Joule heating, and thermal conductivity must be low to reduce the heat transfer rate. Nasri et al., (2017) discussed the diverse designs of the thermoelectric generators that were flexible and dependent on parameters such as current Intensity and temperature difference. The module performed better with an increase in temperature. The module's energy consumption by cooling the hotter side was also determined. The application of thermoelectric generators in a condensing combi boiler was detailed by Zeki Yilmazoglu et al., (2013). It was concluded that the TEG installation of the combi boiler reduced the electricity consumption. Thermo-electric heating and cooling units were proposed as an alternative for HVAC applications by Zeki Yilmazoglu (2016).

Teffah et al., (2018) discussed using thermoelectric generators as a partial heat sink for the thermoelectric cooler by converting the lost heat into useful energy via the Seebeck effect. The performance of thermoelectric coolers at different input voltages was investigated via simulation and experiments. The results concluded that the electrical potential generation of the thermoelectric generator (TEG) was directly proportional to the input voltage to the thermoelectric cooler (TEC). The thermoelectric module was proposed as a cooling system and an electric power generator. Lyu et al., (2019) studied the thermal behavior of a single-cell battery subjected to different cooling methods, including forced convection using air and liquid cooling. A new design for a cooling system was proposed: a combination of liquid cooling, forced air cooling, and a thermoelectric module. A study was carried out using a hybrid TEC-liquid–air cooling system. The hybrid system showed an improved cooling effect compared to the individual cooling methods in an electric vehicle's battery thermal management system.

Villasevil et al., (2013) modeled a thermoelectric structure with pellets of non-standard geometry and materials. A correlation was proposed based on experiments and a numerical model. Material properties had a direct effect on the thermoelectric devices. For different current values, there was a corresponding shift in the temperature distribution, either above or below, depending upon the polarity of the current, i.e., heating or cooling. Looman (2005) proposed a finite element method to study thermoelectric devices using ANSYS Software. Steady-state and transient-state analyses were conducted in detail for TEGs and TECs. Jaegle (2008) proposed the adoption of thermoelectric multiphysics in the COMSOL Multiphysics library and detailed the governing equations. The temperature is fixed on one side and was commonly adopted in numerical models to quickly visualize the heating/cooling on a side. AB (2008) is a modeling guide used to study the modeling patterns and methods in the COMSOL Multiphysics software. It is used to understand the physical processes in the thermoelectric domain. Venkatesan and Venkataramanan (2020) proposed fixing the hot side temperature for Peltier modules. A fixed incremental value of 5K temperature was used in the study. The temperature difference increased with an increase in current. There was an increased cooling effect with a small

temperature difference and decreased cooling with a very intense hot side for a particular temperature difference.

Recent works report on using soft computing techniques for various thermal applications, including Peltier modules. Zhan et al., (2017) predicted the thermal boundary resistance for thermal management in high-power micro and optoelectronic devices. The concepts of phonon transport of heat transfer and the acoustic and diffuse mismatch models were proposed to calculate the resistance. The Gaussian process regression and Support Vector Regression models (SVRM) gave better results when calculating the regression coefficient. Machine learning models (ML) were suggested as an alternative to the computationally expensive molecular dynamics technique. It was found that the film thickness was one of the critical parameters that affect the thermal film resistance.

Song et al., (2019) proposed using ultrasound to enhance the heat transfer in industrial evaporators. The universal heat transfer coefficient increased by 20%. The most critical controlling variable was the temperature difference between heating steam and evaporation. The prediction used machine learning models. Lower root mean square error was reported by using SVM and NNet algorithms. Qian et al., (2019) predicted the performance of oscillating heat pipes during machining processes. A machine learning model was developed to predict the parameters to dissipate the heat generated during the machining process. Different machine learning algorithms were tested, and the extreme gradient boosting algorithms (XGBoost) performed well. Bassi et al., (2021) developed machine learning models to predict the energy utility of a building accurately. XGBoost, LightGBM, and CatBoost techniques were used to predict the power consumption. The performance characteristics of these algorithms with gradient-boosting regression trees were summarized. It was found that XGBoost was the best algorithm for the considered dataset.

The above literature details the works reported on the Peltier module and the application of soft computing for various related applications. Though Peltier modules have higher COP for lower power supply, their performance for larger-scale applications is limited. The present work attempts to understand the effects of the Peltier module on fluid cooling and heating in varying volumes. A machine learning model is developed to predict the temperature accurately. The specific contribution of parameters (cooling, current, time, Peltier size, and fluid volume for predicting the output temperature is done with SHAP values. The use of SHAP values by Lundberg & Lee (2017) was derived from Shapley's values based on Shapley's game theory (1953). The application of the machine learning model holds promise in predicting the average temperature of fluid bodies surrounded by large-sized Peltier modules, circumventing the need for computationally intensive simulations. By offering a rapid and reliable means of temperature prediction, the model stands to significantly expedite the design and optimization processes for systems incorporating large Peltier modules. The predicted technique can optimize cooling processes in applications such as electronic device cooling, automotive climate control, medical refrigeration, and industrial equipment thermal management.

PROBLEM DESCRIPTION

In the present work, a fluid is filled in a cubical volume surrounded by four Peltier modules, as shown in Fig. 1(a). Water is considered as the working fluid. The fluid can be heated or cooled by changing the polarity of the Peltier module. A transient analysis is done using the COMSOL Multiphysics package. The variation of the average temperature of the fluid with respect to time is analyzed for different Peltier dimensions, fluid volume, and input current. The current is supplied to one of the highlighted terminals, as shown in Fig. 1(b), while the other terminal is grounded. If the polarity of the supply is reversed, the heating or cooling effect can be changed. One side of the Peltier module is kept constant at 293K, as shown in Figure 1(a). It is assumed that the effect of rising and falling temperature on one side of the module is compensated by providing sufficient external resources, as mentioned in Teffah et al., (2018). It is done to keep the value of temperature difference (ΔT) minimal to obtain the maximum rate of cooling and to maintain adiabatic conditions, as mentioned in (Venkatesan & Venkataramanan (2020), Jaegle (2008) and Nasri et al., (2017)). A detailed parametric study is carried out on the fluid body to find the effect of Peltier dimensions, fluid volume, and input current on the average fluid temperature. Figure 1(b) shows the model setup for Peltier dimension 27x37(mm). A machine learning model is trained with six different Peltier modules of dimensions (in mm) 18x18, 18x27, 27x18, 27x27, 27x37 and 37x27. The model is tested with three datasets, each representing a unique Peltier module data. The testing dataset comprises Peltier modules of dimensions (in mm) 46x46, 56x46, and 46x56.

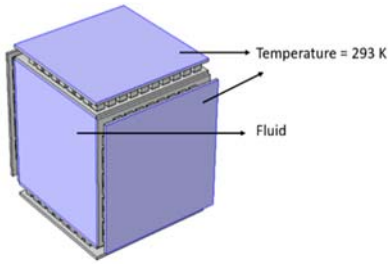

Fig. 1(a). Peltier module of dimension 46x46

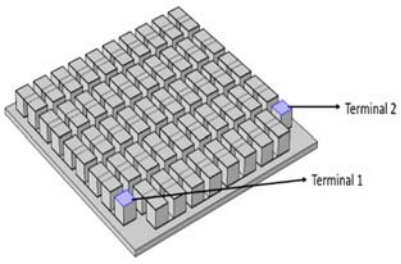

Fig. 1(b). Individual Peltier modules

MESHING AND GRID INDEPENDENCE STUDY

The results shown in Fig. 2 are for a mesh generated for the Peltier module setup of dimension 27 x 27(mm). Studies are carried out starting from extra course mesh to fine mesh elements. A grid independence test is performed to determine the optimal mesh size. The temperature values are supposed to be independent of the mesh size. The model is given a uniform normal meshing. When the number of domain elements exceeds 106841, as shown in Fig. 2, the temperature recorded does not change much. The optimal mesh quality is found to be 0.03556.

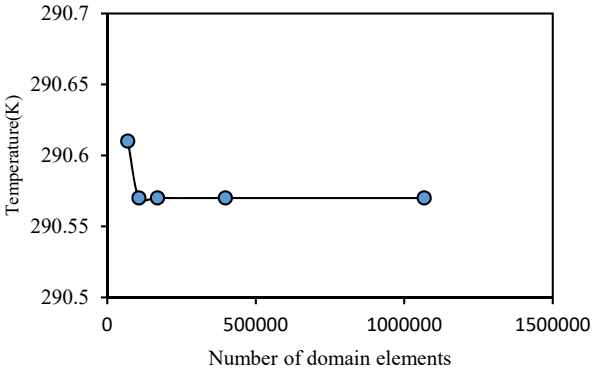

Fig. 2. Grid independence test

GOVERNING EQUATIONS AND BOUNDARY CONDITIONS

These governing equations considering thermoelectric effects and heat transfer for thermoelectric systems are given by Nasri et al., (2017). The Joule effect must be considered for effective modeling of the system. The equations are

$$\rho C \frac{\partial T}{\partial t} + \nabla_q = \emptyset \tag{1}$$

The equation of continuity of electric charge:

$$\nabla \left[J + \frac{\partial D}{\partial t} \right] = 0 \tag{2}$$

The electric field E can be obtained from an electric scalar potential as detailed in Antonova and Looman (2005) and is as follows:

$$E = -\nabla \varphi \tag{3}$$

The thermoelectric constitutive equations from Antonova and Looman (2005) are:

$$q = [\pi] J - [\lambda] \nabla T \tag{4}$$

$$J = [\sigma](E - [\alpha] \nabla T) \tag{5}$$

The constitutive equation for a dielectric medium from Antonova and Looman (2005):

$$D = [\varepsilon] E \tag{6}$$

The coupled heat equation and Poisson's equation are extended by the thermoelectric effects and solved simultaneously to obtain the temperature and Voltage values from Jaegle (2008):

$$-\vec{\nabla} \cdot \left((\sigma \alpha^2 T + \lambda) \vec{\nabla} T + \sigma \alpha T \vec{\nabla} V \right) = \sigma \left(\left(\vec{\nabla} V \right)^2 + \alpha \vec{\nabla} T \vec{\nabla} V \right) \tag{7}$$

$$\vec{\nabla} \cdot \left(\sigma \alpha \vec{\nabla} T \right) + \vec{\nabla} \cdot \left(\alpha \vec{\nabla} V \right) = 0 \tag{8}$$

While implemented in the COMSOL Multiphysics interface, the equations can be written as partial differential equations of the variable u (dependent on T and V) in one to three dimensions. The general form of the equation, as detailed in Jaegle (2008) and AB (2008), are

$$e_a \frac{\partial^2 u}{\partial t^2} + d_a \frac{\partial u}{\partial t} + \nabla \cdot (-c \nabla u - \alpha u + \gamma) + \beta \cdot \nabla u + a u = f \ in \ \Omega \tag{9}$$

$$n \cdot (-c \nabla u - \alpha u + \gamma) + q u = g - h^T \mu \ in \ \partial \Omega \tag{10}$$

$$h u = r \ in \ \partial \Omega \tag{11}$$

The first equation in this list is the PDE, which must be solved for thermoelectric systems.

Equation 10 has a Neumann boundary condition that allows for a constant heat flux at the boundary. Equation 11 has a Dirichlet boundary condition in which a constant surface temperature is given.

NUMERICAL MODEL AND VALIDATION

The model has been validated using the data reported by Villasevil et al., (2013). A comparison between numerical values of surface temperature and the results of Villasevil et al., (2013) for different current values is shown in Fig. 3. It is observed that the simulation results follow the same pattern as reported by Villasevil et al., (2013). The temperatures of the present numerical model match well with those of Villasevil et al., (2013) for 1A, 1.5A, and 2A. Further analysis of other cubical volumes is done with the validated numerical model.

RESULTS AND DISCUSSION

Heat transfer characteristics of a single Peltier module

The temperature distribution for nine different Peltier geometries is simulated with varying volumes of fluid and five different current values (1 A, 1.5 A, 2 A, 2.5 A, 3 A). The heating and cooling effects are studied for all the Peltier geometries. The variation of temperature with respect to time follows a parabolic curve where the temperature increases or decreases based on the polarity and reaches a steady state after a specific time. A single Peltier module is modeled, and its temperature distribution is studied. As a further extension, the cubical volume surrounded by four Peltier modules is modeled with a validated numerical model, and further analysis is done.

Surface temperature (Single Peltier module): The variation of surface temperature for a single 46 x 46mm Peltier module at 100s at 2A current for both heating and cooling

are shown in Fig. 4. The surface temperature variation for all the nine single modules is carried out.

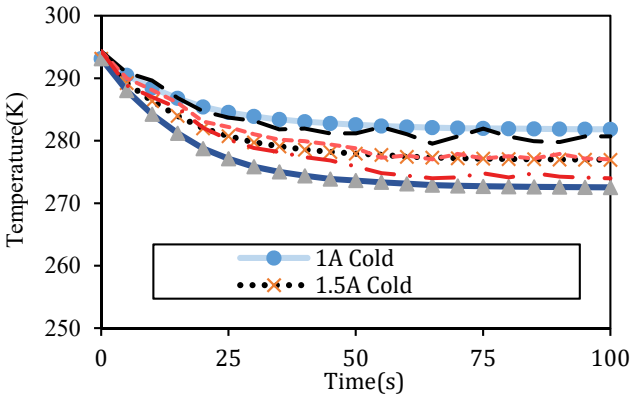

Fig. 3. Comparison of the temp. values with Villasevil et al., (2013)

It can be observed that there is a temperature rise or drop (based on the polarity) initially, and it settles down to a steady-state value depending upon the current and time. A steady temperature distribution is reached after the mentioned time. Different modules require different times to reach the steady temperature distribution, and they are noted for all nine single modules.

Bulk fluid surface temperature distribution: The fluid domain has been introduced, and Peltier modules of varying sizes surround it. The study carried out for the 27 x 27(mm) Peltier setup is shown in Fig. 5 (a), and its bulk surface temperature is also shown. The case is for the supply 1A, and the fluid surface temperature distribution in the 1800s is shown. Similar studies are done for other modules. Fig. 5(b) shows the transient temperature distribution for a 46 x 46 module at 100s

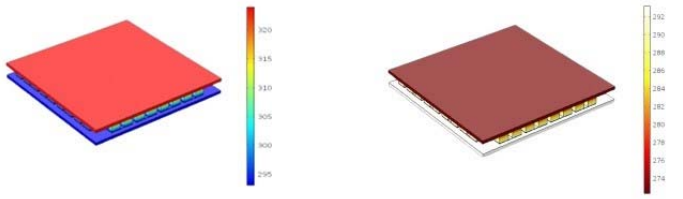

(a) Hot side (b) Cold side

Fig. 4. Surface temperature of module for current value 2 Amps (Time = 100s)

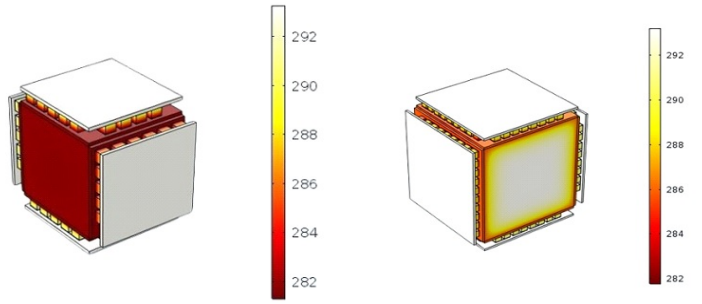

(a) Peltier module, size: 27x27mm, t = 1800s (b) Peltier module, size: 46x46mm, t = 100s

Fig. 5 Surface temperature distribution

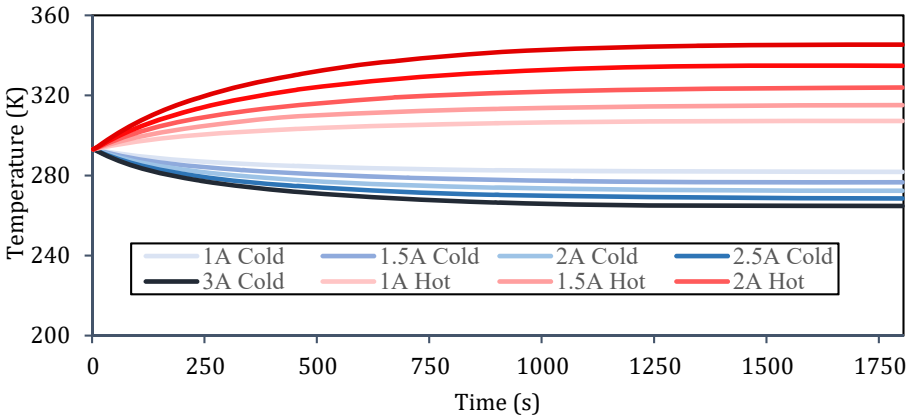

Fig. 6. Variation of Fluid Temperature for different current values (Peltier module, size: 27x27mm)

Bulk fluid surface temperature variation with respect to time at different current values for the Peltier module 27 x 27(mm) has been plotted. It is shown in Fig. 6. Here, the temperature of the fluid increases or decreases based on the polarity and reaches a steady state after some time, depending on the current value. It is to be noted that a steady state has been achieved in all the conditions around 1250s.

Training dataset

The temperature distribution is collected as a function of time for varying Peltier volume and current. The machine learning model is trained with six different Peltier geometries. The remaining three modules are used as test cases. The size of the model varies from 18mm to 46mm. The analysis is done for varying dimensions of length and breadth. The fluid volume depends upon the size of the module. The input current ranges from 1A to 3A, increasing in steps of 0.5A. Fig. 7 shows the six Peltier modules used to train the model. The parameters used as the input for the machine-learning model are

(i) length of the Peltier module (in mm),
(ii) breadth of the Peltier module (in mm),
(iii) volume of the fluid (in cubic mm),
(iv) polarity (1 for cooling and 0 for heating),
(v) input current (in A) and
(vi) time (in seconds).

Testing dataset

The testing dataset comprises Peltier modules of dimensions 46mm x 46mm, 46mm x 56mm, and 56mm x 46mm, varying from the training dataset's sizes. Input current ranges from 1A to 3A in 0.5A increments, akin to the training dataset. These dimensions ensure diversity, while fluid volume adjusts accordingly. Fig. 8 depicts the three

Peltier modules utilized for testing to evaluate the model's generalization to new dimensions. This dataset aims to assess the generalization capability of the machine learning model trained on the six Peltier geometries, extending its applicability to previously unseen dimensions.

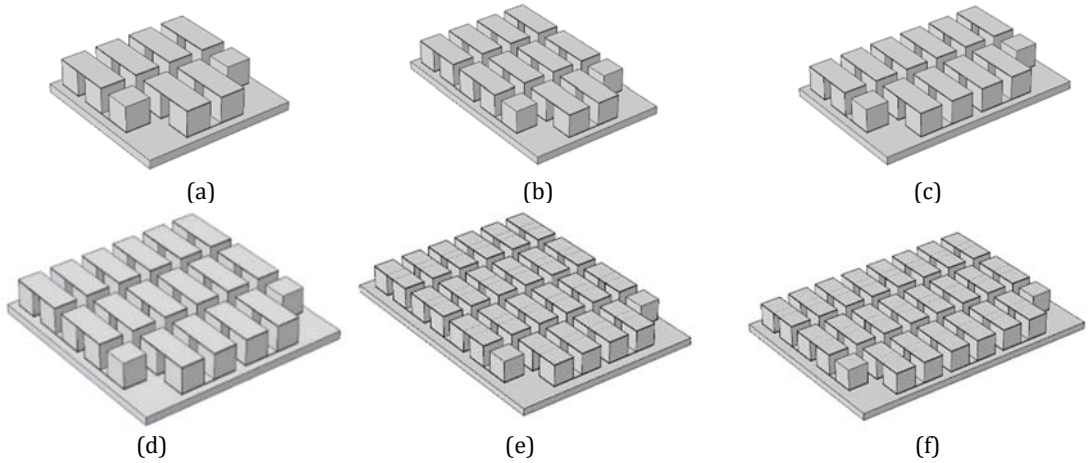

(a) (b) (c)

(d) (e) (f)

Fig. 7 Peltier module, size: (a) 18x18mm, (b) 18x27mm, (c) 27x18mm, (d) 27x27mm, (e) 27x37mm, (f) 37x27mm

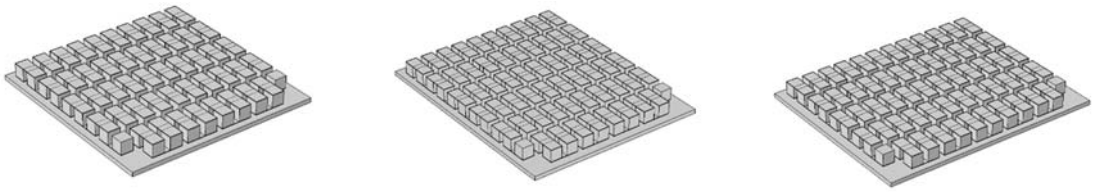

(a) (b) (c)

Fig. 8 Peltier module, size: (a) 46x46mm, (b) 46x56mm, (c) 56x46mm

Machine Learning Models

Machine learning algorithms are essential for temperature prediction of varying Peltier modules (Vipin et al., 2024). These algorithms enable prediction and thermal management with nonlinear mapping functions with a fair amount of data. This study examines four popularly demonstrated machine learning models to predict the average temperature of fluid domains at varying Peltier modules. Based on the diverse working nature of the models, Decision Tree, Gradient Boosting, Random Forest, and XGBoost are considered for comparison. Using open-source Python libraries like Scikit-Learn and Keras, the implementation for all four models has been done. The investigation of utilized learning algorithms is given below.

Decision Tree

A decision tree is a visual representation of the cognitive strategies employed in various decision-making processes (Dang et al., 2022). The decision tree has three types of nodes: the root, internal, and leaf nodes. The root nodes initiate the decision-making process, whereas the internal nodes segment the input space into subspaces guided by the discriminant function f(x), which begins at the root.

$$f(x) = W_g(x) + \theta$$

In the neural network, g(x) is the activation function of each neuron, and f(x) is its output function. The decision tree can be categorized into nonlinear and linear based on the form of g(x). Sometimes, an internal node within a decision tree may not necessitate branching to a leaf node. Therefore, these internal nodes are designated leaf nodes if conditions are met. The method employs a local search approach to train decision trees. Nevertheless, this approach may result in local optima and not guarantee global optimization.

Random Forest

In machine learning, Random Forest is an algorithm derived from baseline decision trees. It is designed to overcome the drawbacks using a single decision tree, namely overfitting and instability. Random forest algorithm aims to generate more reliable outcomes by aggregating predictions from multiple decision trees (Carvalho et al.,2019). Additionally, it does not require assumptions regarding the statistical distribution of the data, so it can be utilized even in scenarios where the relationships between variables are non-linear. Each decision tree in the forest has its unique training set generated from the original training dataset using bootstrap sampling in the RF formulation. The final output is constructed by the determining average over predictions of all decision trees:

$$Avg_{RF}(x) = \frac{\sum_{i=1}^{N} pred(x)}{N}$$

Gradient Boosting

A boosting algorithm is a type of learning algorithm that combines multiple sampler models to fit models. Models used in sampling are usually base models that have been trained using weak or base learners (Park et al., 2023). When a boosting technique is applied, the accuracy of these models is significantly enhanced compared to random guessing. With Gradient Boosting (GB), retrieving importance scores for each feature (attribute) is relatively straightforward. Based on these scores, assessing the significance of boosted decision trees in constructing a model is possible. In order to facilitate the ranking and comparison of attribute values, each feature in the dataset is ranked and compared based on its importance. The importance of a split point in a decision tree is determined based on how many observations are associated with that node. The performance measure can be the purity score or another error function for selecting split points.

XGBoost

A prominent implementation of boosting algorithms is Extreme Gradient Boosting (XGBoost). It is a free and open-source toolkit developed by the Distributed Machine Learning Community (DMLC) and distributed by the DMLC (Gao et al., 2024). It enhances transparency and facilitates straightforward tree visualization, thus fostering a vibrant and engaged community. There are several notable differences between XGBoost and other boosting solutions, including the proportionally shrinking of leaf nodes, the penalization of trees, and adding randomization parameters. As part of an ensemble machine learning framework based on decision trees, the XGBoost uses gradient to construct regression and classification models. This algorithm was developed by Chen et al., (2016) as an efficient implementation of the gradient-boosting methodology. It should be noted that XGBoost offers several advantages over gradient boosting, including more intelligent tree partitioning, shorter leaf nodes, random hidden node generation, and the ability to make predictions outside of the core. As a result of its seamless integration with the Python programming language and its widespread use in Kaggle competitions, the regression method has become increasingly popular in recent years. XGBoost outperformed four prominent machine learning models for predicting fluid domain temperatures across various Peltier modules. The next step may be to conduct sensitivity analyses, tune the parameters, and optimize XGBoost's predictive capabilities. With continuous optimization possibilities, the dynamic nature of machine learning algorithms is highlighted, and the potential of XGBoost in temperature prediction and thermal management for Peltier modules is encouraged. The XGBoost model is used to predict the temperature distribution curves for various combinations of the parameters.

The graph in Fig 9 shows a 56 x 46 module for a 1A current. Similar graphs are obtained for all combinations, and the prediction accuracy is 97%.

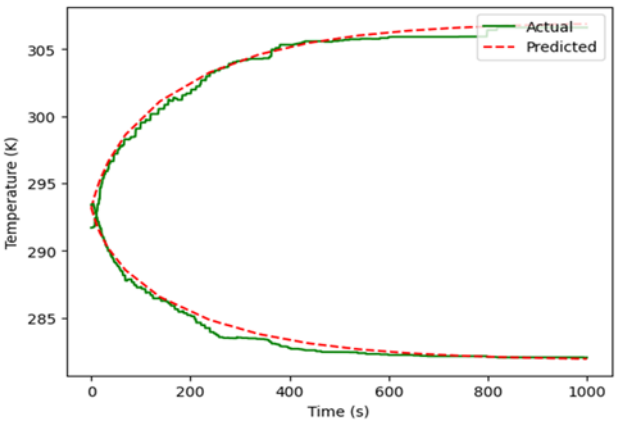

Fig. 9. Comparison between the numerical model and XGBoost model

Model Optimization

This section explains comprehensive insight into the intricacies of the hyperparameter tuning process for machine learning models, namely, XGBoost, Gradient Boosting, Random Forest, and Decision Tree (Cotorogea et al., 2022). These models are implemented to predict the fluid domain's average temperature with varying Peltier module sizes. Bayesian optimization efficiently identifies optimal hyperparameter values by iteratively selecting the most promising parameter configuration. This optimization technique effectively explores the set of hyperparameter spaces to search for optimal values. In selecting hyperparameters, objective functions of Bayesian optimization techniques such as Expected Improvement (EI) and Upper Confidence Bound (UCB) play a significant role in balancing exploration and exploitation of the hyperparameter space. The objective oversees estimating the potential improvement at any given point while evaluating the objective function given its existing state. As the proposed work is evaluated on three datasets, the table below consists of hyperparameters for each machine-learning model with its corresponding optimal values.

Table 1. List of optimal hyperparameter values using Bayesian Optimisation

Datasets	Models with their optimal hyperparameter values
1st dataset	XGBRegressor (gamma = 1, learning_rate = 0.05, max_depth = 5, min_child_weight = 9, n_estimators=38, reg_alpha=180)
	GradientBoostingRegressor (learning_rate=0.08, max_depth=4,max_features='sqrt', min_samples_leaf=50, min_samples_split=50,n_estimators=84)
	RandomForestRegressor (max_depth=6, max_features=0.72, min_samples_leaf=1, min_samples_split=10)
	DecisionTreeRegressor(max_depth=12,min_samples_split=12,max_leaf_nodes=19, max_features='auto')
2nd dataset	XGBRegressor (gamma = 8, learning_rate =0.08, max_depth = 5, min_child_weight =5, n_estimators=53, reg_alpha=28)
	GradientBoostingRegressor (learning_rate= 0.15, max_depth=4, max_features='sqrt', min_samples_leaf=34, min_samples_split=2,n_estimators=75)
	RandomForestRegressor (max_depth=6, max_features=0.7097968171311817, min_samples_leaf=6, min_samples_split=5)
	DecisionTreeRegressor (max_depth=5,max_leaf_nodes=20,min_samples_split=20)
3rd dataset	XGBRegressor(gamma = 8, learning_rate =0.08, max_depth = 5, min_child_weight =5, n_estimators=53, reg_alpha=28)
	GradientBoostingRegressor (learning_rate= 0.108, max_depth=6, max_features = 'sqrt', min_samples_leaf=8, min_samples_split=2,n_estimators=75)
	RandomForestRegressor(max_depth=6, max_features=0.721, min_samples_leaf=5, min_samples_split=4)
	DecisionTreeRegressor(max_depth=5,max_leaf_nodes=20,min_samples_split=6)

RESULTS AND DISCUSSIONS

The proposed machine learning models are implemented in hardware comprising a Windows 11 operating system and an Intel Core i5 processor with 8 GB RAM. The experimentations are performed using Jupyter Notebook, and the models are evaluated in terms of performance metrics, including accuracy (Acc), Mean Squared Error (MSE), and Mean Absolute Error (MAE). The following sections examine the evaluation of proposed machine learning models for temperature prediction. The experimental findings indicate the performance of each machine learning model with respect to three different datasets.

Performance comparison

Four diverse machine learning models have been chosen to compare the effectiveness of prediction tasks: XGBoost, gradient boosting, random forest, and decision tree.

Table 2 consists of an error metrics comparison over three considered datasets. It is observed that XGboost outperforms all other prediction models with the highest accuracy of 97% when trained on the first dataset, with the lowest average absolute error of 2.04. As XGboost exhibits superior performance, it can be concluded that it is the most suitable temperature prediction model for varying Peltier sizes.

Table 2. Performance comparison of four machine learning models using error metrics

ML models /Error metrics	1st Dataset			2nd Dataset			3rd Dataset		
	Acc	MSE	MAE	Acc	MSE	MAE	Acc	MSE	MAE
XGBoost	0.97	7.65	2.04	0.97	6.5	1.97	0.97	5.60	1.78
Gradient Boosting	0.96	8.01	2.16	0.96	6.9	2.05	0.96	977	2.20
Random Forest	0.94	13.07	2.83	0.95	12.52	2.65	0.95	2.57	12.01
Decision Tree	0.90	22.58	3.64	0.94	13.52	2.58	0.95	2.61	12.15

SHAP analysis

The SHAP (SHapley Additive exPlanations) analysis graphs are concerned with the feature's importance for model prediction. It consists of horizontal bars representing typical feature importance scores; notably, longer bars indicate more significant importance. By observing the direction of the bars, it can be stated that the positive SHAP values contribute towards increasing the model's prediction.

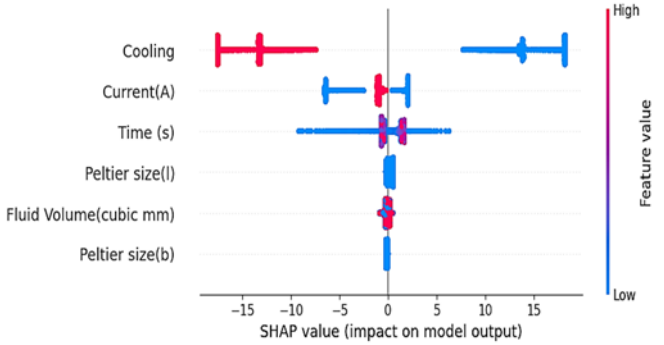

Fig. 10 (a) Illustration of SHAP values for XGBoost model using Peltier size of 46 × 46

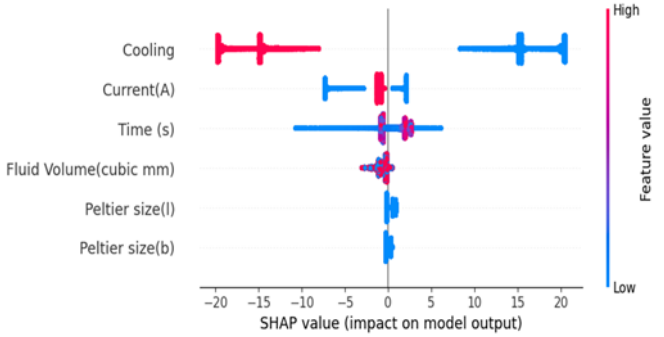

Fig. 10 (b) Illustration of SHAP values for XGBoost model using Peltier size of 56 × 56

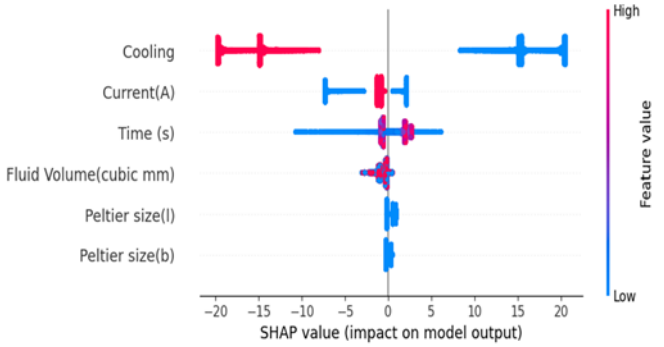

Fig. 10 (c) Illustration of SHAP values for XGBoost model using Peltier size of 46 × 56

Figure 10 shows the feature-based SHAP analysis of the best-proposed prediction model, XGBoost, for varying Peltier sizes. It is inferred from the graph that the "cooling" feature has longer bars, which is identified as the most influential feature that contributed to accurate predictions.

CONCLUSION

The effect of Peltier modules of varying sizes on cooling and heating fluid is detailed in the study. Peltier parameters such as width, height, input current, polarity, and the volume of the fluid body are varied. A machine learning model has been developed based on the collected data to predict the average temperature of the fluid body. The results show that the XGBoost algorithm predicted the fluid temperature well with an average accuracy of 97% across the three different testing datasets. The present study emphasizes the computational analysis of temperature distribution using COMSOL Multiphysics software. The approach addresses the computational expense of varying module sizes, ensuring accurate and efficient modeling. By developing a machine learning algorithm to predict fluid temperatures, the study highlights significant time savings and enhances the ability to evaluate different configurations quickly. This predictive mechanism reduces the need for extensive computational resources and allows rapid optimization. This ML model serves as a memory map, providing a valuable resource for expanding into other applications involving Peltier modules. The study will help to reduce the overall cost, time, and simulation efforts required to select the appropriate setup for Peltier-based devices. The research contributes to more economically viable and time-efficient solutions in thermoelectric systems by streamlining the evaluation process.

REFERENCES

AB, C., (2008). COMSOL Multiphysics Modeling Guide.

Antonova, E. E. & Looman, D. C., (2005). Finite Elements for Thermoelectric Device Analysis in ANSYS. *Canonsburg, USA*. https://doi.org/10.1109/ICT.2005.1519922

Aparicio, J. L. P., Palma, R. & Taylor, R. L., 2012. Finite element analysis and material sensitivity of Peltier thermoelectric cells coolers. International Journal of Heat and Mass Transfer, pp. 1363-1374. https://doi.org/10.1016/j.ijheatmasstransfer.2011.08.031

Bassi, A., Anika S., Arjun S., Hanna S., Connor G., and Jonathan H. Chan. (2021). Building Energy Consumption Forecasting:

A Comparison of Gradient Boosting Models. Bangkok, Thailand, 12th International Conference on Advances in Information Technology.
https://doi.org/10.1145/3468784.3470656

Carvalho, T. P., Soares, F. A., Vita, R., Francisco, R. D. P., Basto, J. P., & Alcalá, S. G. (2019). A systematic literature review of machine learning methods applied to predictive maintenance. Computers & Industrial Engineering, 137, 106024.
https://doi.org/10.1016/j.cie.2019.106024

Chen, T., Guestrin, C. (2016). Xgboost: A scalable tree boosting system. In Proceedings of the 22nd acm sigkdd international conference on knowledge discovery and data mining (pp. 785-794).
https://doi.org/10.1145/2939672.293978

Cotorogea, B. P. F., Marino, G., & Vogl, S. (2022). Data driven health monitoring of Peltier modules using machine-learning-methods. SLAS technology, 27(5), 319-326.
https://doi.org/10.1016/j.slast.2022.07.002

Dang, W., Guo, J., Liu, M., Liu, S., Yang, B., Yin, L., & Zheng, W. (2022). A semi-supervised extreme learning machine algorithm based on the new weighted kernel for machine smell. Applied Sciences, 12(18), 9213.
https://doi.org/10.3390/app12189213

Gao, X., Zhang, K., Zhang, Z., Wang, M., Zan, T., & Gao, P. (2024). XGBoost-based thermal error prediction and compensation of ball screws. Proceedings of the Institution of Mechanical Engineers, Part B: Journal of Engineering Manufacture, 238(1-2), 151-163.
https://doi.org/10.1177/095440542311571

Jaegle, M., 2008. Multiphysics Simulation of Thermoelectric Systems - Modeling of PeltierCooling and Thermoelectric Generation. Hannover, s.n.

Lundberg, S. M. & Lee, S. I., 2017. A unified approach to interpreting model predictions. Advances in neural information processing systems, p. 30.
https://doi.org/10.48550/arXiv.1705.07874

Lyu Y, Siddique A.R.M, Majid S.H., Biglarbegian M, Gadsden S.A., Mahmud S., (2019). Electric vehicle battery thermal management system with thermoelectric cooling. Energy Reports, 5, 822-827.
https://doi.org/10.1016/j.egyr.2019.06.016

Nasri W, Djebali R, Dhaoui S, Abboudi S, Kharroubi H, (2017). Finite Elements Multiphysics Investigation of Thermoelectric Systems for Electricity and Cooling Generation. International Journal of Modern Studies in Mechanical Engineering, 3(4), pp. 1-13.
http://dx.doi.org/10.20431/2454-9711.0304001

Park, H. I., Cho, T. J., Choi, I. G., Rhee, M. S., & Cha, Y. (2023). Object classification system using temperature variation of smart finger device via machine learning. Sensors and Actuators A: Physical, 356, 114338.
https://doi.org/10.1016/j.sna.2023.114338

Qian N , Wang X, Fu Y, Zhao Z, Xu J, Chen J, (2019). Predicting heat transfer of oscillating heat pipes for machining processes based on extreme gradient boosting algorithm. Applied Thermal Engineering, 164, 114521.
https://doi.org/10.1016/j.applthermaleng.2019.114521

Shapley, L. (1953) A Value for n-Person Games. In: Kuhn, H. and Tucker, A., Eds., Contributions to the Theory of Games II, Princeton University Press, Princeton, 307-317.
https://doi.org/10.1515/9781400881970-018

Song J, Tian W, Xu X, Wang Y, Li Z, (2019). Thermal performance of a novel ultrasonic evaporator based on machine learning algorithms. Applied Thermal Engineering, 148, pp. 438-446.
https://doi.org/10.1016/j.applthermaleng.2018.11.083

Teffah, K., Zhang, Y. & Mou, X., (2018). Modeling and Experimentation of New Thermoelectric Cooler–Thermoelectric Generator Module, Energies, 11(3), 576.
https://doi.org/10.3390/en11030576

Venkatesan, K. & Venkataramanan, M., (2020). Experimental and Simulation Studies on Thermoelectric Cooler: A Performance Study Approach. International Journal of Thermophysics, 41, Article number 38.
https://doi.org/10.1007/s10765-020-2613-2

Villasevil, F., López, A. & Fisac, M., (2013). Modeling and Simulation of a Thermoelectric Structure with Pellets of Non-Standard Geometry and Materials. International Journal of Refrigeration, 36 (5), 1570-1575.
https://doi.org/10.1016/j.ijrefrig.2013.02.014

Vipin, K. E., & Padhan, P. (2024). Machine-Learning Guided Prediction of Thermoelectric Properties of Topological Insulator Bi2Te3-xSex. Journal of Materials Chemistry C, 12, 7415-7425.
https://doi.org/10.1039/D4TC01058B

Zaferani, S., Sams, M., Ghomashchi, R. & Chen, Z.-G., (2021). Thermoelectric Coolers as Thermal Management Systems for Medical Applications: Design, Optimization, and Advancement. Nano Energy, Volume 90, Part A, 106572
https://doi.org/10.1016/j.nanoen.2021.106572

Zhan, T., Fang, L. & Xu, Y., (2017). Prediction of thermal boundary resistance by the machine learning method. Scientific Reports, 7(7109).
https://doi.org/10.1038/s41598-017-07150-7

Zeki Yilmazoglu, M., (2016). Experimental and numerical investigation of a prototype thermoelectric heating and cooling unit, Energy and Buildings, 113, 51–60.
https://doi.org/10.1016/j.enbuild.2015.12.046

Zeki Yilmazoglu, M., Salih K., Tamer C., Turgut O. Y., and Senol B., (2013). Experimental Study on Thermoelectric Generator Performance Applied to a Combi Boiler, 13th UK Heat Transfer Conference, UKHTC2013/143, 2 - 3 September 2013, Imperial College London, 143-1-8.

Journal Homepage: https://dergipark.org.tr/tr/pub/isibted

Isı Bilimi ve Tekniği Dergisi

Archive: https://tibtd.org.tr/dergi

Comparison of Reacting DDES and LES CFD Simulation Methodologies for a Dual Inlet Ramjet Engine Combustor

Mehmet Burak SOLMAZ [1, *], Sıtkı USLU [2]

[1] *Propulsion Systems Division, TUBITAK SAGE, Mamak, 06484, Ankara, Türkiye*
[2] *Department of Mechanical Engineering, TED University, Çankaya, 06420, Ankara, Türkiye*

A R T I C L E I N F O

2025, vol. 45, no.1, pp. 10-21

doi: 10.47480/isibted.1490666

Research Article
Received: 01 June 2024
Accepted: 18 February 2025

* *Corresponding Author*
e-mail: burak.solmaz@tubitak.gov.tr

Keywords:
Large eddy simulation
Delayed detached eddy simulation
Steady laminar flamelet
Richardson extrapolation

ORCID Numbers in author order:
0000-0003-3571-177X
0000-0003-4734-2625

A B S T R A C T

The design of a dual-inlet dump ramjet combustor is critical to the development of a ramjet propulsion system. Parameters such as pressure drop, pressure fluctuations, and combustion efficiency must be evaluated across different flight regimes. In this study, Large Eddy Simulation (LES) and Delayed Detached Eddy Simulation (DDES) techniques, coupled with the Steady Laminar Flamelet combustion model, are used to model a generic ramjet combustor. Grid convergence was ensured through the Richardson extrapolation method, and the grid quality was evaluated using the M-index. Close agreement between both LES and DDES approaches and experimental data confirms their accuracy in simulating the complex flow behaviour of the combustor. The present research demonstrates that the Steady Laminar Flamelet model is capable of predicting flow structures in a ramjet combustor under reacting conditions. In LES simulations, turbulent kinetic energy prediction in the near-wall region was enhanced, leading to faster mixing and an overestimation of combustion efficiency. DDES predictions achieved even closer agreement with experimental data, highlighting the effectiveness of eddy simulation with near-wall modelling when wall resolution is not feasible. This approach demonstrates improved agreement between DDES predictions and experimental data and highlights its efficiency in reducing the need for excessively refined meshes in studying dump-type low subsonic combustors.

Çift Girişli Ramjet Motor Yanma Odası İçin Reaktif DDES ve LES Benzetim Yöntemlerinin Karşılaştırılması

M A K A L E B İ L G İ S İ

Anahtar Kelimeler:
Büyük Burgaç Benzetimi
Gecikmeli Ayrılmış Burgaç Benzetimi
Kararlı Laminar Alevcikler
Richardson ekstrapolasyonu

Ö Z E T

Çift girişli bir ramjet motoru yanma odasının tasarımı, ramjet itki sistemi geliştirilmesinde kritik öneme sahiptir. Basınç düşüşü, basınç dalgalanmaları ve yanma verimliliği gibi parametreler, çeşitli uçuş rejimleri için ayrı ayrı değerlendirilmelidir. Bu çalışmada, bir ramjet yanma odasını modellemek için Kararlı Laminer Alevcik yanma modeli ile birlikte Büyük Burgaç Benzetimi (LES) ve Gecikmeli Ayrılmış Burgaç Benzetimi (DDES) teknikleri kullanılmıştır. Ağ yapısı yakınsaması, Richardson ekstrapolasyon yöntemi ile sağlanmış ve ağ kalitesi M-indisi kullanılarak değerlendirilmiştir. LES ve DDES yaklaşımları ile deneysel veriler arasında yakın bir uyum gözlemlenmiş ve yanma odasının karmaşık akış davranışı benzetiminde bu tekniklere başvurulabileceği doğrulamıştır. Mevcut araştırma, Kararlı Laminer Alevcik modelinin bir ramjet yanma odasındaki akış yapısını tahmin etme yeteneğini göstermektedir. LES benzetimlerinde, duvar yakınındaki bölgede türbülanslı kinetik enerji daha yüksek hesaplanmakta ve daha hızlı karışmaya ve yanma verimliliğinin fazla hesaplanmasına yol açmaktadır. Duvara yakın bölgede DDES hesaplamalarının büyük burgaç benzetimine kıyasla deneysel sonuçlara daha yakın değerler bulduğu gözlemlenmiştir. Ağ yapısında duvar kenarı çözünürlüğü sağlanamadığında modellemenin daha doğru sonuçlar doğurduğu anlaşılmaktadır. Bu çalışma, DDES çözümlemelerinin deneysel sonuçlar ile arasında iyi bir uyum olduğunu göstermesinin yanı sıra düşük sesaltı hızlara sahip yanma odası benzetimlerinde yüksek yoğunluklu ağ yapısı uygulamak mümkün olmadığında bu yöntemin elverişliliğini de vurgulamaktadır.

NOMENCLATURE

a_s	characteristic flamelet strain rate $[s^{-1}]$	Y	mass fraction of a specie
C	model constant	Z	mixture fraction
d	distance to wall $[m]$	γ	ratio of specific heats
D	diffusion rate $[m^2/s]$	Δ	largest grid space of the computational cell $[m]$
f	function	ε	eddy dissipation
f_{DDES}	DDES model multiplier	$\in_f$	error of f
G_d	dissipation term of k equation $[kg/ms^3]$	η	combustion efficiency
g_{ij}	velocity gradient tensor $[s^{-1}]$	κ	Karman constant
h_t	total enthalpy $[J/kg]$	λ	thermal conductivity $[W/mK]$
k	turbulent kinetic energy $[m^2/s^2]$	μ	dynamic viscosity $[Pa \cdot s]$
l	integral length scale $[m]$	ν	kinematic viscosity $[m^2/s]$
P	Probability Density Function	Π	pressure drop
Pr	Prandtl number	ρ	density $[kg/m^3]$
Q	Q criterion $[s^{-2}]$	σ	shear stress $[Pa]$
r_d	a parameter for DDES model	τ_{ij}	subgrid stress tensor $[kg/ms^2]$
Sc	Schmidt number	ϕ	a variable
S_{ij}	strain rate tensor $[s^{-1}]$	φ	equivalence ratio
S_{ij}^d	traceless symmetric part of the square of the velocity gradient tensor $[s^{-2}]$	χ	scalar dissipation rate $[s^{-1}]$
V	computational cell volume $[m^3]$	Ω	vorticity tensor $[s^{-1}]$
u_i	velocity component $[m/s]$		

INTRODUCTION

The concept of the integrated rocket ramjet was introduced in the 1960s, sparking decades of research into dump combustor design (Fry 2011; Le Pichon and Laverdant 2016; Timnat 1990). Fig. 1 illustrates the primary components of a dual-inlet dump-type integrated rocket ramjet combustor, comprising the primary reactor, secondary reactor, and mixing regions (Kim and Natan 2015; Roux 2009). Incoming air jets generate four corner vortices, while the dump section induces suction, collectively shaping the reactors. Key factors affecting overall ramjet engine performance include reactor size and efficiency, dump effects, air intake dimensions, intake angle and curvature, flow separators in the intake stream, Reynolds number, and combustor dimensions (Chuang et al. 1989; Kim and Natan 2015; Stowe et al. 2004; Stull et al. 1985). The inherent inability to scale ramjet engine combustion chambers (Blevins and Coleman 1999) poses a challenge when evaluating various geometrical configurations and operating conditions through experimentation. As a result, Computational Fluid Dynamics (CFD) becomes a crucial tool for advancing the development of ramjet propulsion engines.

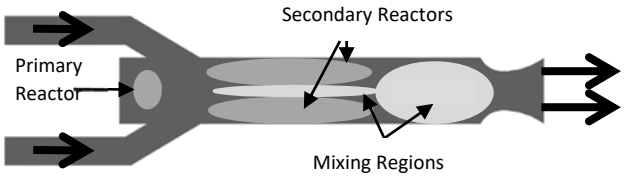

Fig. 1 Reactor zones definition of a dual inlet dump-type ramjet combustor.

A well-defined combustor configuration for understanding the internal dynamics of dual-inlet ramjets is the square cross-section ramjet engine introduced in 1995 by Ristori et al. (1999) and Gicquel et al. (2002). Optically accessible combustor walls made diagnostics possible for Laser Doppler Velocimetry, Particle Image Velocimetry, Planar Laser-Induced Fluorescence and Chemiluminescence. Researchers have used the data from these measurements to enhance the validity of their CFD predictions (Gicquel et al. 2006; Le Pichon and Laverdant 2016; Reichstadt et al. 2007; Roux et al. 2010).

While addressing the limitations of Reynolds-Averaged Navier-Stokes (RANS) approaches in predicting time-dependent changes within the combustor, an alternative method known as the Unsteady-RANS approach has gained recognition for simulating reactive flows (Nemati, Ong, and Walther 2022; Solmaz, Uslu, and Uzol 2014). However, the Unsteady-RANS computations have constraints in capturing fluctuating components and their associated frequencies, which are crucial performance parameters for ramjet engines (Stull et al. 1985).

In response to these limitations, Large Eddy Simulation (LES) studies have been conducted (Reichstadt et al. 2007) using grids composed of up to 3.4 million hexahedral elements (Roux et al. 2009). While the near-wall flow structures were not resolved with these grids having y+ values of approximately around 50 but the general flow field was properly predicted.

Researchers have employed various strategies to enhance the quality of LES results, including the application of different combustion models. Additionally, specific modifications were made to one of the global reaction mechanisms, and a more CPU-intensive Eddy Dissipation Concept combustion closure was employed to achieve successful solutions (Roux 2009).

Simulating eddy structures is crucial for accurately assessing the thermoacoustic instability performance of the combustor, a key parameter for ramjet engines. While consistent results have been achieved by researchers (Roux et al. 2010) using Large Eddy Simulation (LES), there is a limitation in simulating near-wall structures due to high y+ values, which extend beyond the viscous sublayer range. Therefore, a more reliable approach might involve modelling these near-wall structures. The Detached Eddy Simulation (DES), initially proposed by Spalart et al. (1997), offers a hybrid RANS/LES approach that effectively models turbulent structures near the walls, especially those that are computationally expensive to simulate. This method has been further enhanced by

Spalart et al. (2006) with the introduction of a delaying mechanism, which aims to postpone the transition from RANS to LES in scenarios with thick boundary layers.

Numerous successful combustor simulations have been reported in the literature, with several studies demonstrating the capabilities of the DES model such as the work of Sun et al. (2008). However, only a limited number of works, such as Ashoke et al. (2015), have specifically addressed the simulation of dump combustors, a relevant scenario for integrated rocket ramjet technology. In this study, we aim to showcase the potential of the hybrid RANS/LES model for side dump combustors, where low subsonic corner vortices generated after jet-on-jet impingement which play a significant role in the combustion process.

For the present simulations, the Steady Laminar Flamelet (SLF) combustion model is employed which encapsulates the outcomes of detailed chemistry schemes in a tabulated format, thereby accounting for finite-rate chemistry effects. One well-known drawback of this model is its inability to capture slow reactions. In order to see the predictability of the SLF, the results are compared with the predictions of the Flamelet Generated Manifold (FGM) combustion model which has proven its suitability in the case of slow reaction combustion problems (Yang et al., 2020; Cagdas, 2021). The comparison shows that similar results are observed for the given high-temperature air inlet condition with a global equivalence ratio close to stoichiometry. Similar results are obtained as the test case features a high-temperature air inlet with a global equivalence ratio near stoichiometry (Solmaz and Uslu, 2023).

NUMERICAL TOOLS

In this study, we conducted CFD simulations employing two distinct approaches. Firstly, Large Eddy Simulation (LES) was utilized in conjunction with Wall Adapting Local Eddy Viscosity (WALE) subgrid-scale (SGS) modelling. Then Detached Eddy Simulation (DES) is employed with Realizable k-ε turbulence model. For the present computations, the commercially available solver ANSYS Fluent R21 was used.

Favre-averaged filtered governing equations, detailed from Eq. (1) to Eq. (3), were employed (Garnier, Adams, and Sagaut 2009). Notably, when comparing the effects of various terms in the equations, the subgrid-scale pressure dilatation term, subgrid-scale viscous dissipation term, and other non-linear terms were found to have minimal impact compared to the convective and diffusive terms (Martín, Piomelli, and Candler 2000). Furthermore, Eq. (4) provides the resolved shear stress, while Eq. (5) to Eq. (9) outline the modelling of subgrid stresses.

$$\frac{\partial \bar{\rho}}{\partial t} + \frac{\partial \bar{\rho}\tilde{u}_i}{\partial x_i} = 0 \tag{1}$$

$$\frac{\partial \bar{\rho}\tilde{u}_i}{\partial t} + \frac{\partial \bar{\rho}\tilde{u}_i\tilde{u}_j}{\partial x_j} + \frac{\partial \bar{p}}{\partial x_i} - \frac{\partial \tilde{\sigma}_{ij}}{\partial x_j} = -\frac{\partial \tau_{ij}}{\partial x_j} \tag{2}$$

$$\frac{\partial \bar{\rho}\tilde{h}_t}{\partial t} + \frac{\partial \bar{\rho}\tilde{u}_i\tilde{h}_t}{\partial x_i} - \frac{\partial \bar{p}}{\partial t} - \tilde{u}_i\frac{\partial \bar{p}}{\partial x_i} - \frac{\partial}{\partial x_i}\left(\lambda\frac{\partial \tilde{T}}{\partial x_i}\right) = -\left[\frac{\partial \bar{\rho}(\widetilde{u_i h_t} - \tilde{h}_t\tilde{u}_i)}{\partial x_i}\right] \tag{3}$$

$$\tilde{\sigma}_{ij} = 2\mu\left(\tilde{S}_{ij} - \frac{1}{3}\delta_{ij}\tilde{S}_{kk}\right) \tag{4}$$

$$\tau_{ij} - \frac{1}{3}\tau_{kk}\delta_{ij} = -2\mu_t\left(\tilde{S}_{ij} - \frac{1}{3}\delta_{ij}\tilde{S}_{kk}\right) \tag{5}$$

$$\tilde{S}_{ij} \equiv \frac{1}{2}\left(\frac{\partial \tilde{u}_i}{\partial x_j} + \frac{\partial \tilde{u}_j}{\partial x_i}\right) \tag{6}$$

$$\mu_t = \rho l_{wale}^2 \frac{\left(S_{ij}^d S_{ij}^d\right)^{3/2}}{\left(\tilde{S}_{ij}\tilde{S}_{ij}\right)^{5/2} + \left(S_{ij}^d S_{ij}^d\right)^{5/4}} \tag{7}$$

$$l_{wale} = \min\left(\kappa d, C_w V^{1/3}\right) \tag{8}$$

$$S_{ij}^d = \frac{1}{2}\left(\tilde{g}_{ij}^{\,2} + \tilde{g}_{ji}^{\,2}\right) - \frac{1}{3}\delta_{ij}\tilde{g}_{kk}^{\,2}, \qquad \tilde{g}_{ij} = \frac{\partial \tilde{u}_i}{\partial x_j} \tag{9}$$

Here, λ, $\tilde{h}_t$, τ_{ij}, μ_t, δ_{ij}, $\tilde{S}_{ij}$, l_{wale}, κ, and d stand for thermal conductivity, filtered total enthalpy, subgrid stress tensor, subgrid turbulent viscosity, Kronecker delta, filtered rate of the strain tensor, turbulence length scale, Karman constant and normal distance to the wall respectively. The WALE constant is $C_w = 0.325$. Additionally, a homogenous mesh assumption is adopted for subgrid length calculation. The isotropic part of the subgrid stress tensor is neglected, as the subgrid-scale Mach number effect is negligible for most supersonic flows (Erlebacher et al. 1992). The subgrid enthalpy flux is modelled using a constant turbulent Prandtl number assumption, as given by Eq. (10).

$$\bar{\rho}\left(\widetilde{u_i h_t} - \tilde{u}_i\tilde{h}_t\right) = -\frac{\mu_t c_p}{Pr_t}\frac{\partial \tilde{T}}{\partial x_j} \tag{10}$$

In Eq. (3), it is important to note that there is no source term. Heat generation from reactions is incorporated into the total enthalpy formulation. Total enthalpy is the sum of chemical enthalpy (enthalpy of formation), sensible enthalpy, and kinetic enthalpy. Pre-tabulated chemistry is used for calculations, which is described below. The application of the ideal gas law is justified by the assumption that combustion occurs within the combustion chamber, where the flow remains in the low subsonic range.

The combustor under investigation has two jet inlets, resulting in jet-on-jet impingement that naturally oscillates and creates four circulating vortices in each corner of the combustor. Based on the work of Peters (1984), the steady laminar flamelet model, SLF, was used to account for the finite-rate effects in turbulent reacting flows. It is assumed that a turbulent flame brush consists of flamelets (Williams 1975), which are laminar, one-dimensional having small flame structures. The laminar flame structures are assumed to be dissipated under a certain strain rate which is a function of cross velocity for one-dimensional flame assumption. Figure 2 presents a schematic depiction of a strained laminar flame.

Species transport was modelled using the mixture fraction theory originally developed for diffusion flames (Bilger 1976, Burke and Schumann 1928). Eq. (11) outlines the transport equations for the filtered mean mixture fraction, denoted as $\tilde{Z}$. Here, μ_{eff} represents turbulent viscosity divided by the turbulent Prandtl number. The variance of the mixture fraction is calculated using the scaling relation method proposed by Pierce and Moin (1998). The definition of the mixture fraction variance is provided in Eq. (12). Mean scalar dissipation is defined based on work of Pierce and Moin (2004) in Eq. (13). In the present simulation, C_{LES} is a scaling constant set to 0.5, Sc_t is turbulent Schimdt number, taken as 0.85, and C_χ is a constant with a value of 2.

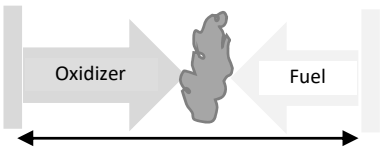

Fig. 2 Strained 1-D flame schematic.

$$\frac{\partial \bar{\rho}\tilde{Z}}{\partial t} + \frac{\partial \bar{\rho}\tilde{u}_i\tilde{Z}}{\partial x_i} = \frac{\partial}{\partial x_i}\left(\mu_{eff}\frac{\partial \tilde{Z}}{\partial x_i}\right) \quad (11)$$

$$\widetilde{Z''^2} = C_{LES} l_{les}{}^2 \left|\frac{\partial \tilde{Z}}{\partial x_i}\right|^2 \quad (12)$$

$$\tilde{\chi}_{st} = C_{\chi}\frac{(\mu_t+\mu)}{\rho Sc_t}\left|\nabla \tilde{Z}\right|^2 \quad (13)$$

Species mass fractions are derived from the Steady Laminar Flamelet (SLF) library based on the mean and variance of mixture fraction and scalar dissipation. To prepare for the CFD computations, an opposed-flame chemistry solver is employed to obtain species mass fractions, temperature, density, and enthalpy. These parameters are expressed as functions of mixture fraction, scalar dissipation, and enthalpy. Peters (1984) introduced the transformation of local coordinates to mixture fraction coordinates through the Crocco transformation methodology (Crocco 1940). Further details about this transformation can be found in Peters' original work (1984) or in textbooks such as Poinsot and Veynante (2012).

The scalar dissipation rate, denoted as χ, is defined by Eq. (14), where D represents the diffusion coefficient. The scalar dissipation rate at the stoichiometric mixture fraction is referred to as χ_{st}. When applying the laminar flamelet model to the opposed-jet burner, the strain between the flows can be calculated as the velocity difference divided by the distance between the feeding sources. Consequently, the calculation of stoichiometric scalar dissipation can be conducted after solving for the instantaneous mixture fraction within a one-dimensional laminar mixing layer.

Assuming constant density and diffusion coefficient and setting the boundary conditions to 1 and 0 for the fuel and oxidizer zones, respectively, the mixture fraction can be expressed as a function of the diffusion coefficient, strain rate a_s, and location (Peters 1984; Poinsot and Veynante 2012). With these boundary conditions for the stoichiometric mixture fraction, the stoichiometric scalar dissipation rate is defined as given in Eq. (15) (Claramunt 2006; Peters 1984; Poinsot and Veynante 2012).

$$\chi = 2D\left(\frac{\partial Z}{\partial x_i}\right)^2 \quad (14)$$

$$\chi_{st} = \frac{a_s}{\pi} exp\{-2[erfc^{-1}(2Z_{st})]^2\} \quad (15)$$

Where $erfc^{-1}$ is inverse complementary error function. This function is solved using an opposed-flow flame chemistry solver and extinction limits of stoichiometric scalar dissipation rates are calculated. The extension of the equation for variable density and mixture fraction is approximated by Eq. (16) (Claramunt 2006). Here Φ is the variable density effect factor (Kim and Williams, 1997) and is defined by Eq. (17) where ρ_O represents the density of the oxidiser stream. The combustion pressure is determined from prior CFD calculations, and this value is used to generate tables. Density is corrected for each computation cell using the predefined table pressure, cell pressure, and the ideal gas law during every CFD iteration.

$$\chi = \chi_{st}\frac{\Phi}{\Phi_{st}}\frac{exp\left\{-2[erfc^{-1}(2Z)]^2\right\}}{exp\{-2[erfc^{-1}(2Z_{st})]^2\}} \quad (16)$$

$$\Phi = \frac{3}{4}\frac{\left(\sqrt{\frac{\rho_O}{\rho}}+1\right)^2}{2\sqrt{\frac{\rho_O}{\rho}}+1} \quad (17)$$

A look-up table is generated for mixture fraction, its variance, scalar dissipation, and enthalpy. To account for turbulence-chemistry interactions, a Probability Density Function (PDF) is employed. This 4D table includes the compressibility effect by considering enthalpy change. Differences in enthalpy input lead to variations in the output variables of temperature and density. Notably, species mass fraction calculations exclude the effects of enthalpy change due to compressibility, as described by Müller, Breitbach, and Peters in 1994. Species concentrations are assumed to be the same as under adiabatic conditions. The flow chart of the solution methodology is given in Fig. 3.

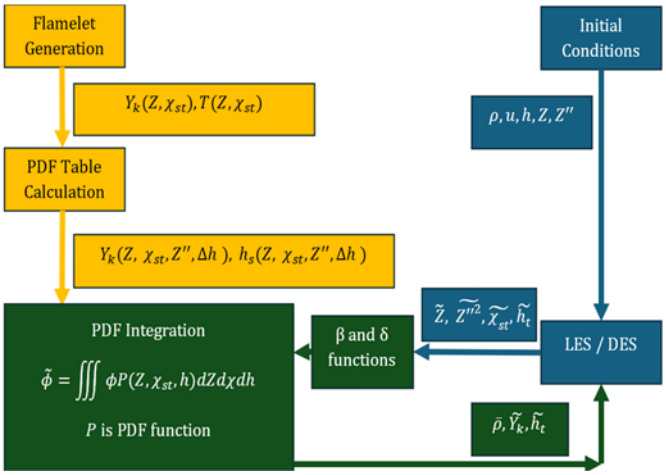

Fig. 3 Solution methodology of numerical framework.

In many applications, resolving near-wall scales is not the primary focus of the problem. Instead of utilizing a subgrid model, Detached Eddy Simulation (DES) employs Reynolds-Averaged Navier-Stokes (RANS) equations within the boundary layer when turbulent length scales become very small, making it impractical to resolve with Large Eddy Simulation (LES). Research conducted by Benim et al. (2008) demonstrated that when the near-wall mesh resolution is insufficient to capture near-wall eddies, DES predictions may yield more accurate results compared to the LES approach.

For problems characterised by thick boundary layers, DES transitions from RANS to LES within the boundary layer. This early switch leads to an incorrect prediction of the viscous sublayer, referred to as Modelled Stress Depletion (Spalart et al. 2006). To address this issue, Delayed DES (DDES) was introduced, specifically designed for situations where the cell edge length is smaller than the boundary layer thickness (Spalart et al. 2006).

In this study, the Realizable k-ε model with two equations is utilized for DDES formulation. This model is based on the eddy viscosity similarity concept applied to k-equation models, as proposed by Travin et al. (2002). Turbulent length selection is given in Eq. (18) where C_{DES} is a model constant (0.61), Δ is the largest edge of the computational cell and f_{DDES} serves as the multiplier of the turbulent length scale. The second term on the right-hand side of the equation becomes zero if l_{RANS} is smaller then l_{LES} which is the switch mechanism used by DDES. f_{DDES} and l_{RANS} are defined by Equations (19) to (21).

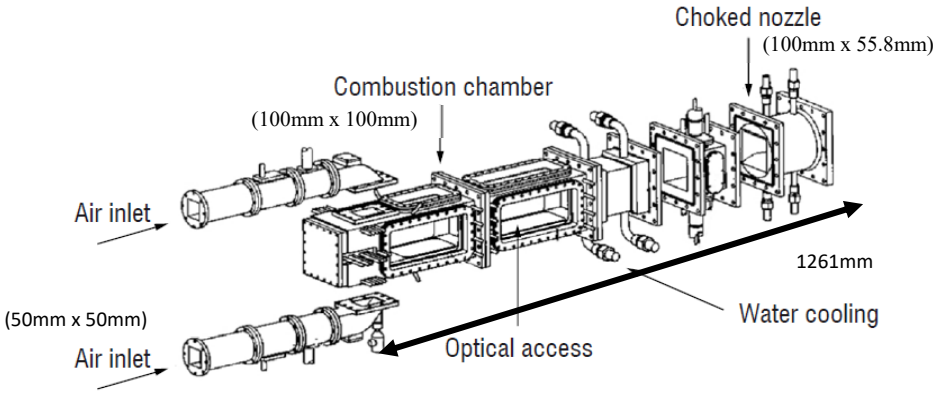

Fig. 4 Sketch of the modular experimental ramjet setup (Le Pichon and Laverdant 2016).

$$l_{DDES} = l_{RANS} - f_{DDES}\max(0, l_{RANS} - C_{DES}\Delta) \quad (18)$$

$$f_{DDES} = 1 - \tanh((20r_d)^3) \quad (19)$$

$$r_d = \frac{\nu_t + \nu}{\kappa^2 d^2 \sqrt{\frac{\partial u_i}{\partial x_j}\frac{\partial u_i}{\partial x_j}}} \quad (20)$$

$$l_{RANS} = \frac{k^{3/2}}{\varepsilon} \quad (21)$$

Here, ν_t represents the modelled kinematic viscosity, ν is the molecular kinematic viscosity, and k and ε are calculated using the realizable $k-\varepsilon$ model formulations (Shih et al. 1995). The dissipation term in the k equation, $G_d = \rho\varepsilon$, is reorganized by introducing the DES length scale to connect the kinetic energy production with DES formulation. The new dissipation term is defined by Eq. (22).

$$G_d = \frac{\rho k^{3/2}}{l_{DDES}} \quad (22)$$

Second and fourth-order temperature dependent polynomials are defined for thermal conductivity and viscosity respectively which are calculated by ANSYS Chemkin diffusion opposed-flow flame solver and curve-fitted with MATLAB R2021b. The GRI-Mech 3.0 (Smith et al. 1999) reaction mechanism and its thermal and transport data are used in all chemistry calculations.

EXPERIMENTAL WORK

The results of the experimental work performed by Ristori et al. (1999) were used for the validation of the simulation results. The research ramjet experimental combustor test setup has dual side air intakes with 50 mm x 50 mm cross-section areas connected to the main combustion chamber that has a square in shape of 100 mm x 100 mm as seen in Fig. 4. Electrically heated air is fed into the air inlets through choked nozzles. The combustor is 1261 millimetres long. A choked nozzle with a 55.8 mm x 100 mm throat size is located at the end of the combustor. Gaseous propane fuel is delivered via two tubes from a pre-injection chamber to the combustor. The chamber's metal walls are water-cooled.

Velocity measurements are carried out using Particle Doppler Anemometry, Laser Doppler Velocimetry, and Particle Image Velocimetry, with data collected through quartz-glass side windows. Flame diagnostics are conducted using OH* and CH* Chemiluminescence, as well as Plane Laser-Induced Fluorescence to measure OH and CH emissions (Le Pichon and Laverdant 2016; Roux 2009; Ristori 1999; Gicquel et al. 2002). This study focused on one of the published flight regimes, characterised by an inlet total temperature of 750 K and a mass flow rate of 0.9 kg/s. The fuel equivalence ratio for the operating condition designated as the "high altitude regime" is 0.75. total temperature of the fuel is 350 K.

COMPUTATIONAL DOMAIN and METHODOLOGY

Multiblock unstructured hexahedral meshing is used throughout the entire computational domain, except for the pre-injection region where polyhedral meshing was utilized. For the discretisation of momentum fluxes, a second-order bounded central differencing discretisation method is implemented.

The hexahedral-polyhedral meshing approach offers the distinct advantage of reducing the total number of grid elements compared to tetrahedral meshing. An axial plane section of the mesh is presented in Fig. 5. The analysis utilised two million cells. To ensure mesh quality, the expansion ratio of the computational mesh was maintained below 1.2, with values primarily around 1.1.

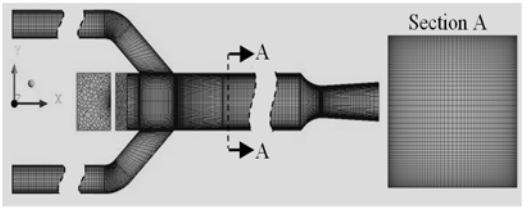

Fig. 5 Cross-section of studied mesh for LES and DDES analysis.

With 20 inner iterations and a bounded second-order implicit differencing scheme, the DDES analyses were initiated using an initial guess derived from an Unsteady RANS result. The results of the DDES analyses were used as the initial state for LES computations. Pressure monitors were strategically placed at various locations to track the convergence of flow dynamics. The cases were run for a minimum of 50 milliseconds before data collection for statistical analysis of the unsteady flow.

Verification Study

To assess the accuracy and spatial convergence of the employed mathematical models, a series of tests were conducted using three sets of meshes containing 0.6, 2.0, and 7.5 million cells, respectively. Only LES simulations were performed for the coarse and fine mesh cases. Combustion efficiency, pressure drop across the engine and the M-index were selected as observables which are defined by Eqs. (23)-(26). The M-index, a theoretical parameter proposed by Pope (2004) as an indicator of mesh quality, was evaluated for LES solutions. M-index is the ratio of modelled subgrid kinetic energy to total kinetic energy (resolved plus modelled).

$$\eta_{comb.eff.} = \frac{T_{t4} - T_{t2}}{T_a - T_{t2}} \quad (23)$$

$$\Pi_{2-4} = 1 - \frac{P_{t2} - P_{t4}}{P_{t2}} \quad (24)$$

$$k_{sgs}(x,t) = \left(\frac{\mu_t}{\rho l_{wale}}\right)^2 \quad (25)$$

$$M\_index = \frac{k_{sgs}}{k_{sgs} + k_{resolved}} \leq 0.2 \quad (26)$$

Where T_a is adiabatic flame temperature and it is calculated by ANSYS Chemkin Perfectly Stirred Reactor Solver with a sufficiently long time definition. The subscript t in Eqs. (23) and (24) indicates the total value. The station four in these equations is accepted as the cross-sectional plane close to the start of the converging duct, and the second station of the engine is accepted as inlets. The M-index comparison was performed for volume-averaged values.

For the exact value estimation of any function f, and its error $\in$ following Eqs. (27) and (28) were used (Roy 2010). The cell size is derived from volumetric average of whole domain, and it is found as 4.7 mm, 3.2 mm and 2.3 mm for $coarse, medium$ and $fine\ meshes$ respectively. Since second-order discretisation schemes were used for transport equations, $order$ is taken as 2. The *coarse* to *medium* cell size ratio and the *medium* to *fine* cell size ratio are very similar. Therefore, no modifications were applied to Eq. (27). Decay of error was observed for all parameters given in Fig. 6.

$$f = f_{fine} + \left\{ \frac{(f_{fine} - f_{medium})}{\left[\left(\frac{V_{medium}^{1/3}}{V_{fine}^{1/3}}\right)^{order} - 1\right]} \right\} \quad (27)$$

$$\in_f = f - f_{mesh} \quad (28)$$

To demonstrate that the mesh employed is sufficiently fine to capture large eddy structures, the M-index value was examined across the entire domain. An acceptable computational mesh for Large Eddy Simulation (LES) calculations is characterised by an M-index value of less than 20%, indicating that 80% of the turbulent kinetic energy is resolved (Pope, 2004). The M-Index, illustrated in Fig. 7 reveals that only approximately 5% of the Turbulent Kinetic Energy within the combustor is modelled.

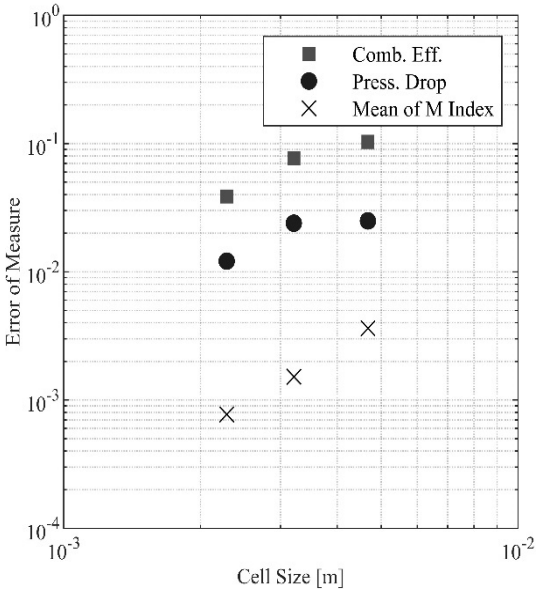

Fig. 6 Error decay due to mesh size in log-log scale of parameters; combustion efficiency, pressure drop and mean of M-index.

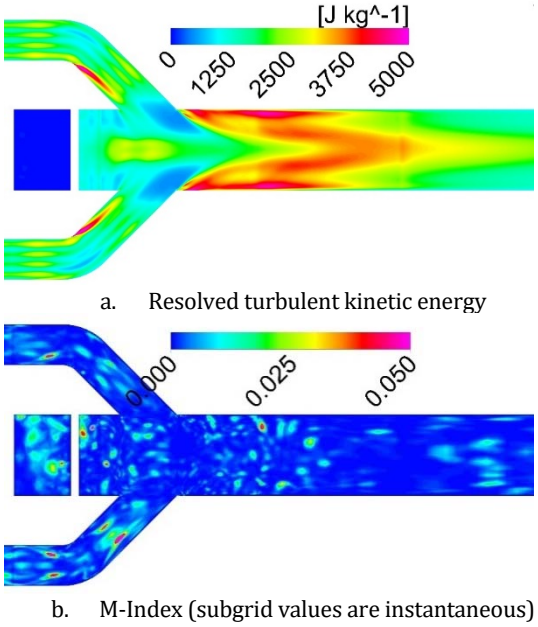

a. Resolved turbulent kinetic energy

b. M-Index (subgrid values are instantaneous)

Fig. 7 Resolved turbulent kinetic energy and M-Index distribution (LES).

For the Delayed Detached Eddy Simulation (DDES) simulations, the y+ value, which serves as a reliable indicator of near-wall resolution, assumes significant importance. y+ values above 30 were predominantly utilized across most of the domain, as depicted in Fig. 8.

Validation Study

This section presents a comparison of the mean normalised axial velocity results for three computational grids along the axial line starting from the combustion chamber's dome, compared with experimental data (Roux et al., 2009), as illustrated in Fig. 9. The simulations demonstrate a strong ability to predict outcomes, particularly in the region after the air inlet jets. Although the difference is not more than 10%, medium and fine meshes have better consistency, which is an indicator of mesh convergence The findings of verification and validation studies confirm that an acceptable mesh is used for LES and DDES simulations.

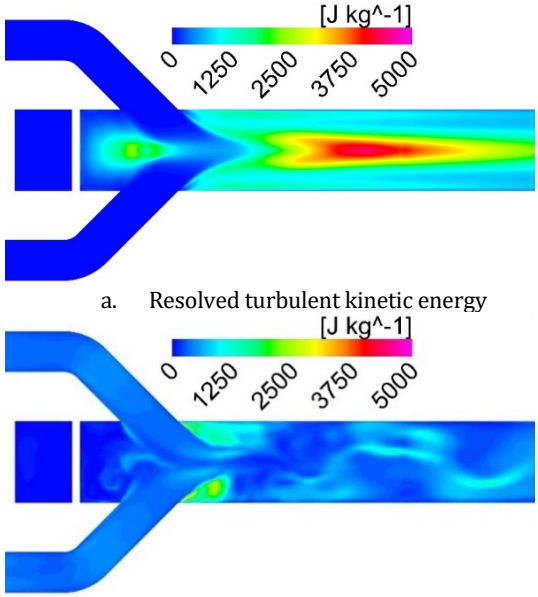

a. Resolved turbulent kinetic energy

b. Modeled instantaneous turbulent kinetic energy

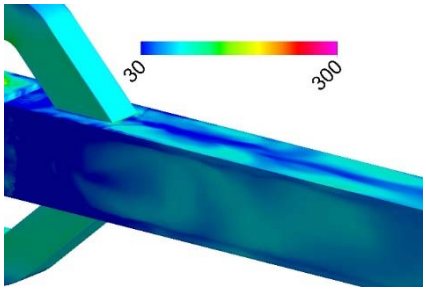

c. Instantaneous y+ distribution over walls

Fig. 8 Turbulent kinetic energy and y+ distribution (DDES).

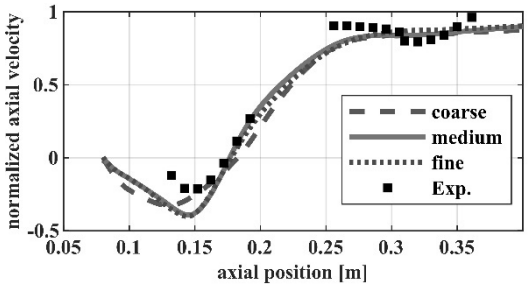

Fig. 9 Mesh study: Normalized axial velocity along the centre line of combustor.

RESULTS

Turbulent kinetic energy contours are displayed in Fig. 7(a) and Fig. 8(a) for LES and DDES computations respectively. When compared to the LES solution, the DDES approach yields lower levels of resolved turbulent kinetic energy, particularly in the air intakes and secondary combustion zones. The prediction of reduced Turbulent Kinetic Energy in the secondary combustion zone is attributed to differences in wall modelling. Lower Turbulent Kinetic Energy leads to a decrease in the mixing rate, thereby delaying the temperature increase. The implications of these results are discussed in this section.

Mean static pressure contours for DDES and LES computations are displayed in Fig. 10. LES computations predict a slightly lower pressure spot near the combustor dome, while the pressure distribution inside the combustor differs only marginally between DDES and LES computations.

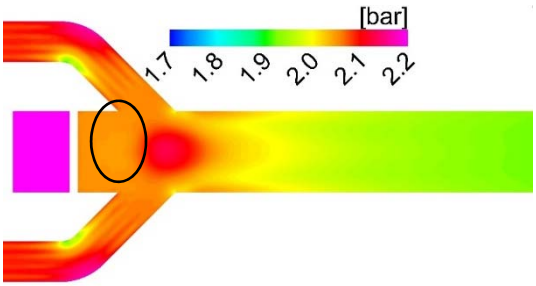

a. LES mean static pressure

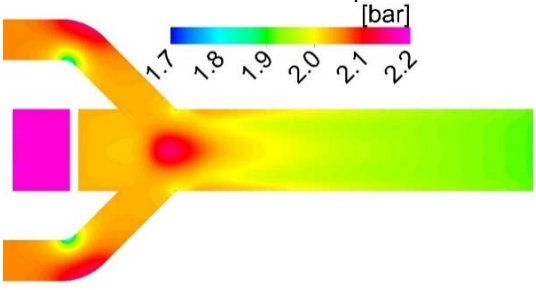

b. DDES mean static pressure

Fig. 10 Time-averaged static pressure contours on mid-plane.

Fig. 11(a) and (b) depict the time-averaged normalized mean axial velocity distribution within the computational domain for LES and DDES computations, respectively. A minor discrepancy is observed in the axial velocity between the two computations. In the case of LES, early flow expansion is noted, attributed to enhanced mixing and consequently higher reaction rates in the early stages of the combustor.

Mean static temperature contours on two planes for LES and DDES are shown in Fig. 12. Both approaches predict a temperature of approximately 1500K in the vicinity of the crossing jets. Due to enhanced fuel-air mixing predicted by the LES approach, it yields a more uniform and higher temperature in each cross-section along the combustor.

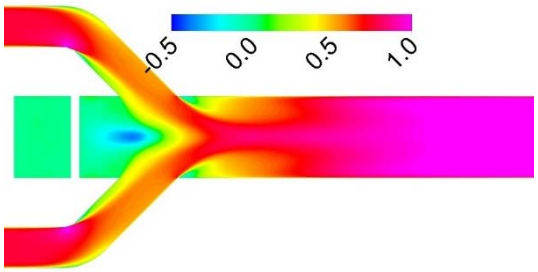

a. LES

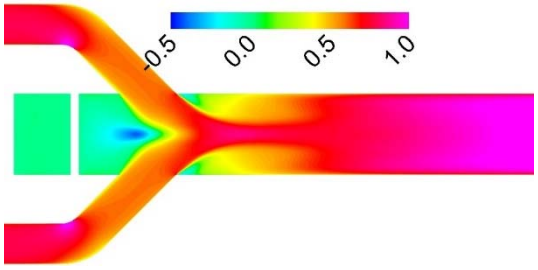

b. DDES

Fig. 11 Time-averaged normalized mean axial velocity contours on mid-plane.

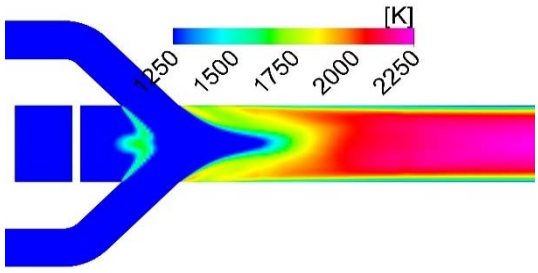

a. LES (X-Y)

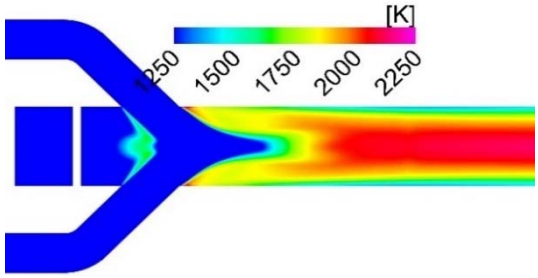

b. DDES (X-Y)

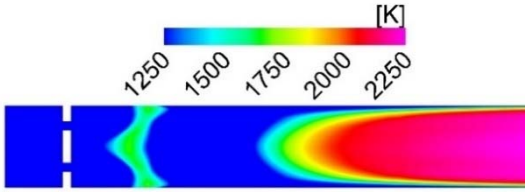

c. LES (X-Z)

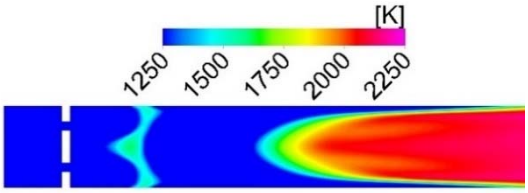

d. DDES (X-Z)

Fig. 12 Time-averaged static temperature contours on mid-plane.

Fig. 13 displays the mass flow-averaged total temperature distribution obtained from planes positioned every 50 mm along the combustor axis. The positions of the planes are indicated in the bottom right corner of the figure. LES computations indicate a temperature 44 K higher at the dump section (x=200 mm). A maximum temperature difference of 196 K between the two simulations is observed around the middle of the combustor. The temperature discrepancy diminishes to a value of 28 K at the end of the combustor, corresponding to a 2% lower combustion efficiency. Fig. 14 presents mean equivalence ratio (φ) contours calculated from the mean of the mixture fraction. The figure reveals that LES predicts a 50% higher fuel/air ratio at the beginning of the secondary reactor. The higher temperatures computed by LES simulations result in early flow expansion, as seen in Fig. 11.

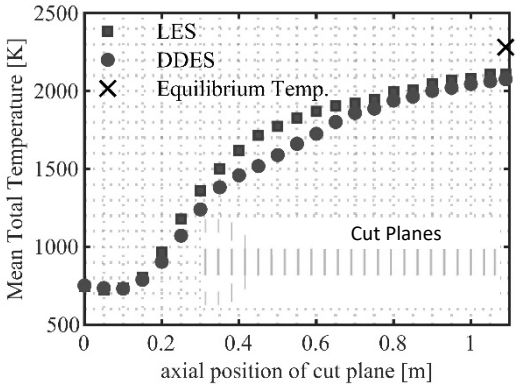

Fig. 13 Mass flow-averaged mean total temperature variation on the planes along the combustor axis.

Instantaneous velocity vectors at x=200 mm and x=300 mm planes are presented in Fig. 15, with vectors color-coded by OH mass fraction. Four secondary flow vortices are formed in the corners. It's worth noting that the location and shape of these corner vortices calculated at x=200 mm exhibit slight differences between the DDES and LES approaches. DDES, by virtue of its use of the RANS formulation, mitigates near-wall eddy generation in the boundary layer. Notably, elevated of OH mass fractions are observed at the edges of these vortices. As indicated in the x=200 mm vector plot, a hot gas flow emanating from the dome follows these vortices into the secondary reaction zone, effectively acting as a preheater to enhance reactions. This phenomenon is also observed in Fig. 16.

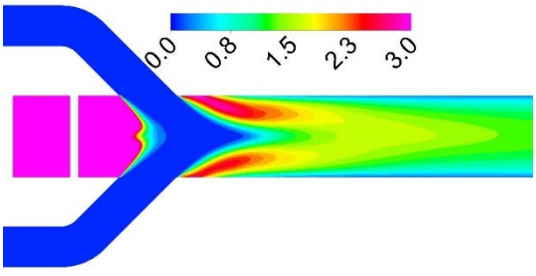

a. LES

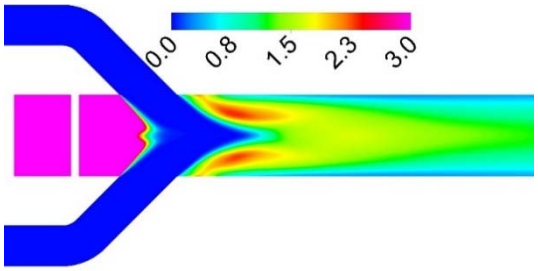

b. DDES

Fig. 14 Mean equivalence ratio contours at mid-plane.

Figure 15 depicts the Q criterion (Hunt, Wray, and Moin 1998), which stands for vorticity tensor. Four main swirling motions (colour-coded by temperature) are generated just downstream of the opposing jets in the combustor. The LES approach predicts a longer main swirling core and numerous small cores around the corners of the combustor. These smaller structures near the corners are induced by near-wall effects. However, it's important to note that the computational cell structure in the boundary layer may not have sufficient resolution for appropriate x+ and z+ values. Consequently, due to the poor near-wall resolution, small structures on the wall may produce incorrect Turbulent Kinetic Energy. DDES, on the other hand, applies Realizable $k-\varepsilon$ formulation in the near-wall region with Boussinesq's hypothesis and is expected to generate more accurate results with boundary cell elements having a high aspect ratio.

Contour plots with a positive Q criterion clearly illustrate the presence of four vortical structures in the corners, as depicted in Fig. 16. This phenomenon underscores the importance of adequately modelling the near-wall region, especially when LES may not effectively resolve it due to non-uniform mesh structures. In this research, the focus is on understanding the success of wall modelling rather than attempting to simulate it using a filter that assumes a uniform cell sizes.

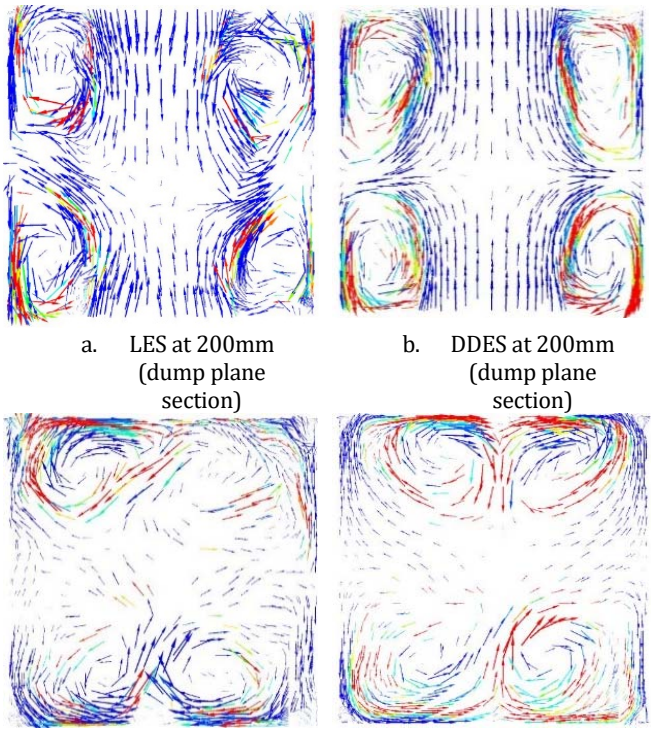

a. LES at 200mm (dump plane section)

b. DDES at 200mm (dump plane section)

c. LES at 300mm

d. DDES at 300mm

Fig. 15 Instantaneous tangential velocity vectors at x=200 mm (dump plane) and x=300 mm. Coloured by instantaneous OH mass fraction.

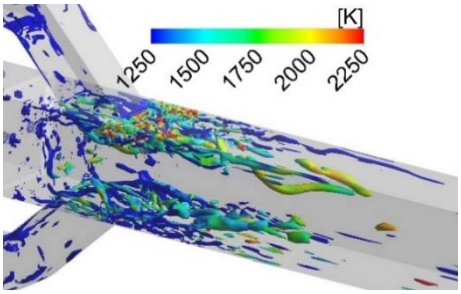

a. LES

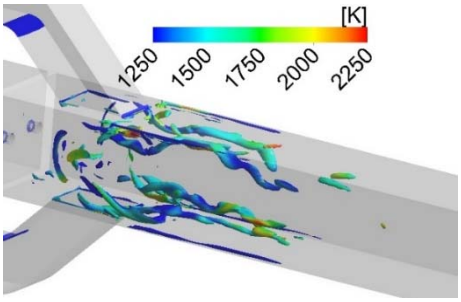

b. DDES

Fig. 16 Q criterion surfaces (positive) coloured with temperature.

The comparison of axial and vertical velocity profiles with measurements along one axial and five vertical lines (as shown in Fig. 17) is presented. Axial velocity profiles along the y-axis are compared with experimental data in Fig. 18. Both the DDES and LES approaches yield very similar results and demonstrate strong agreement with the measured data, particularly in the intersection zone of the jets where the flow field exhibits high complexity due to its inherently three-dimensional structure.

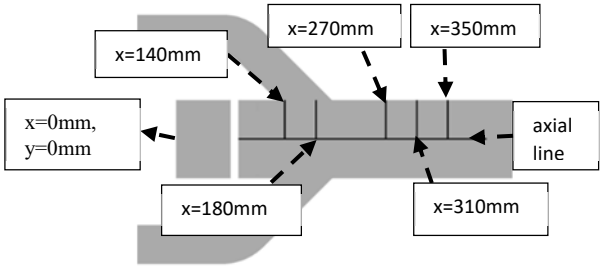

Fig. 17 Experimental measurement lines.

The DDES approach predicted slower flow expansion at the beginning of the secondary zone due to lower temperatures resulting from the previously mentioned slower reactions. This phenomenon is readily visible in the axial velocity profile at x=270 mm, where DDES results closely match the measured velocity profile. With a more uniform temperature distribution in the vertical direction, the LES approach predicts a smoother velocity profile at x=350 mm, aligning well with the measurements. A comparison between the current results and the predictions of Roux et al. (2009) reveals a notably improved agreement with the measured data in the current study, particularly at x=350 mm. This improvement can be partly attributed to the utilization of a hexahedral mesh in the current study, as opposed to the tetrahedral mesh used in Roux et al. (2009). However, the primary reason for the discrepancies between the current results and the predictions in Roux et al. (2009) is believed to be related to the combustion modelling approach. Specifically, the Steady Laminar Flamelet (SLF) combustion modelling employed in the current study was compared to the Dynamically Thickened Flame modelling used in the referenced work. Roux et al. (2009) used a single-step chemistry model with five chemical species, resulting in higher adiabatic flame temperatures under rich mixture conditions. These elevated temperatures, as predicted by the Dynamically Thickened Flame model, led to increased flow expansion, with axial velocity being approximately 30% higher than the measurements at x=350 mm within the combustor. The axial velocity profiles, particularly at x=270 mm, demonstrate a closer agreement when using the Delayed Detached Eddy Simulation (DDES) approach. This can be attributed to the application of a log-law in the near-wall treatment, as opposed to the less conclusive subgrid-scale (SGS) modelling utilized in Large Eddy Simulation.

Fig. 19 presents a comparison of vertical velocity profiles with experimental data. The use of the LES approach results in a more uniform temperature profile within the combustor, leading to greater flow expansion in the axial direction and consequently lower vertical velocity magnitudes. This behaviour agrees well with the experimental data.

Fig. 20 illustrates a comparison of CFD predictions of axial velocity with experimental data along the axis of the combustion chamber. Despite the CFD predictions indicating recirculation that is approximately twice as strong as the experimental data, the velocity field along the axis is well captured. The experimental data exhibit a sharp decrease around x=310 mm, marking the end of the secondary reactor zone. Beyond this point, the 3D vortex structures within the secondary reactor zone gradually dissipate, giving way to a strong axial jet. However, CFD simulations fail to predict the steep change in axial velocity observed at x=310 mm.

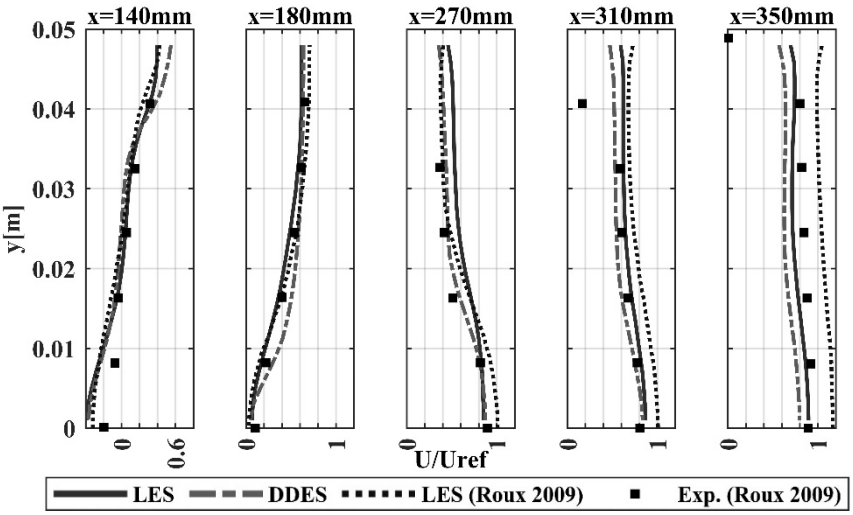

Fig. 18 Normalized axial velocity component along the y-axis (x-axis is the axial velocity normalized by the bulk velocity).

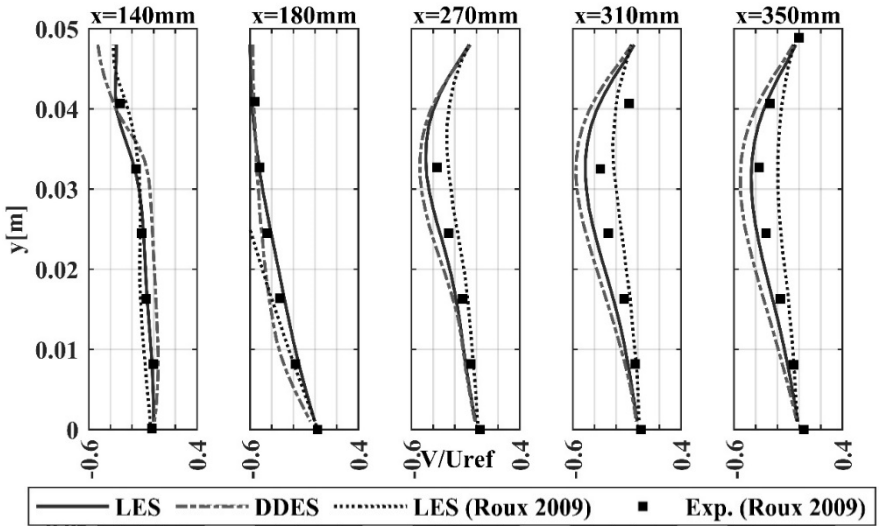

Fig. 19 Normalized vertical velocity component along the y-axis (x-axis is vertical velocity normalized by bulk velocity).

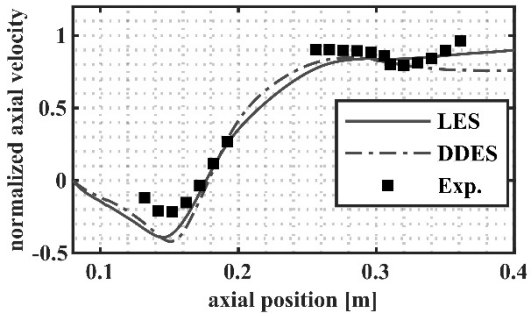

Fig. 20 Axial velocity distribution along the mid-axis.

In terms of integral parameters such as combustion efficiency and pressure drop, there are minor differences between the DDES and LES computations. The LES approach predicts a combustion efficiency of 89%, which is 2% higher than the DDES approach. LES predicts a 5% higher averaged streamline time, which corresponds directly to the combustion "residence time." The near-wall structures in LES enhance mixing, both through residence time and higher turbulent kinetic energy levels, resulting in higher combustion efficiency. Similar findings have been reported in other studies (Le Pichon and Laverdant, 2016) as well. According to Le Pichon and Laverdant (2016), LES predicts a combustion efficiency of 95%, whereas RANS simulations predict an efficiency of 83%. In the same study, however, the measured combustion efficiency was reported as 81%. The authors reported that the reasons for the large disparity between measurements and LES predictions remain unaddressed.

Both approaches accurately predict the pressure drop across the combustor compared to experimental data. The difference between CFD predictions and experimental data lies within the measurement error band reported by Le Pichon and Laverdant (2016). The total pressure loss was measured as 12%, while the simulation result is 11.7%. The total pressure loss is predicted to differ by only 0.5% between DDES and LES computations. The LES prediction of pressure loss is slightly lower.

CONCLUSION

In this study, a wall-modelled LES formulation known as Delayed Detached Eddy Simulation (DDES) is used and the results are compared with those obtained from the LES computations using the Wall-Adapting Local Eddy-Viscosity (WALE) subgrid-scale model in a dual-inlet ramjet combustor. The findings reveal that both approaches provide good agreement with experimental data on velocity profiles, with only minor discrepancies. However, a noteworthy distinction between DDES and LES lies in the behaviour and distribution of Turbulent Kinetic Energy.

LES with WALE subgrid-scale model tends to predict higher levels of Turbulent Kinetic Energy in the near-wall region compared to DDES, resulting in improved mixing and the formation of an early heated zone. This early combustion phase leads to a greater flow expansion and hence an increase in axial velocity, causing LES with WALE to overestimate axial velocity at x=270 mm, whereas DDES predictions align slightly better with the experimental data.

Both DDES and LES simulations overestimate combustion efficiency compared with measurements. However, the total pressure loss is well predicted by both approaches with only a discrepancy of lower than 0.3% compared to measured data that is well within the measurement error range. It's important to note that the overprediction of combustion efficiency remains an open issue, as discussed by other researchers (Le Pichon and Laverdant 2016) also. Future simulations could be extended to calculate heat loss to the walls, which might explain the overprediction of combustion efficiency.

This study demonstrates the promising accuracy of DDES, particularly for simulating a dual-inlet dump-type combustor with a low-subsonic reacting flow field and colliding air jets. DDES, when coupled with the Steady Laminar Flamelet combustion model, exhibited good performance in simulating the flow field and combustion behavior. Although wall-resolving Large Eddy Simulation was not conducted, the results of wall-modelled LES are promising and can serve as a valuable tool for scenarios where a wall-resolving grid is not feasible for industrial applications. Moving forward, our research will focus on using DDES to predict pressure fluctuations, an essential aspect of ramjet combustion. This is identified as a key area for future investigation and improvement.

ACKNOWLEDGMENTS

The authors acknowledge Defence Industries Research and Development Institute of The Scientific and Technological Research Council of Türkiye (TÜBİTAK SAGE) for providing computational resources.

REFERENCES

Benim, A. C., M. P Escudier, A. Nahavandi, K. Nickson, and K. J. Syed. 2008. DES Analysis of Confined Turbulent Swirling Flows in the Sub-critical Regime. In *Advances in Hybrid RANS-LES Modelling. Notes on Numerical Fluid Mechanics and Multidisciplinary Design,* ed. S.H. Peng and W. Haase. 97:172-181. Springer-Verlag Berlin Heidelberg. https://doi.org/10.1007/978-3-540-77815-8

Bilger, R. W. 1976. The Structure of Diffusion Flames. *Combustion Science and Technology*. 13:155-70. https://doi.org/10.1080/00102207608946733

Blevins, J. A., and H. W. Coleman. 1999. Apparent Failure of Scaling Methods in Ramjet Connected-Pipe Testing. *Journal of Propulsion and Power.* 15(5):689-98. https://doi.org/10.2514/2.5480

Burke, S. P., and T. E. W. Schumann. 1928. Diffusion Flames. *Industrial & Engineering Chemistry*. 20(10):998-1004. https://doi.org/10.1021/ie50226a005

Cagdas, C.E. 2021. Investigation Of The Relight Characteristics Of A Turbojet Engine Combustion Chamber Under High-Altitude Conditions Using Computational Flui D Dynamics Large Eddy Simulation. M.Sc. Thesis, TOBB University of Economics and Technology Institute of Natural and Applied Sciences Mechanical Engineering Science Programme, Ankara. http://www.theses.fr/2009INPT025H/document

Chuang, C. L., D.L. Cherng, W.H. Hsieh, G.S. Settles, and K.K. Kuo. 1989. Study of Flowfield Structure in a Simulated Solid-Propellant Ducted Rocket Motor. *27th Aerospace Sciences Meeting*. https://doi.org/10.2514/6.1989-11

Claramunt, K., R. Cònsul, D. Carbonell, and C.D. Pérez-Segarra. 2006. Analysis Of The Laminar Flamelet Concept For Nonpremixed Laminar Flames. *Combustion and Flame*. 145(4):845-62. https://doi.org/10.1016/j.combustflame.2005.11.005

Crocco, L. 1940. Sullo strato limite laminare nei gas lungo una parete piana. *Rendiconti del Circolo Matematico di Palermo*. 63:121-75. https://doi.org/10.1007/BF03015720
Erlebacher, G. Y., M. Hussaini, C.G. Speziale, and T.A. Zang. 1992. Toward the large-eddy simulation of compressible turbulent flows. *Journal of Fluid Mechanics*. 238:155-85. https://doi.org/10.1017/S0022112092001678

Fry, R. S. 2011. The U.S. Navy's Contribution to Airbreathing Missile Propulsion Technology. *AIAA Centennial of Naval Aviation Forum "100 Years of Achievement and Progress"*. AIAA Paper 2011-6942. https://doi.org/10.2514/6.2011-6942

Garnier, E., N. Adams, and P. Sagaut. 2009. LES Governing Equations. *Large Eddy Simulation for Compressible Flows*. 1st ed., Springer Netherlands, Dordrecht.

Gicquel, P., C. Brossard, M. Barat, and A. Ristori. 2002. Experimental Study of a High Speed Flow Inside a Dual Research Ducted Rocket Combustor Using Laser Doppler Velocimetry. *ASME 2002 Fluids Engineering Division Summer Meeting*. ASME Paper FEDSM2002-31432. https://doi.org/10.1115/FEDSM2002-31432

Gicquel, L. Y. M., Y. Sommerer, B. Cuenot, and T. Poinsot. 2006. LES and Acoustic Analysis of Turbulent Reacting Flows: Application to a 3D Oscillatory Ramjet Combustor. *44th AIAA Aerospace Sciences Meeting and Exhibit*. AIAA Paper 2006-151. https://doi.org/10.2514/6.2006-151

Hunt, J. C. R., A. A. Wray, and P. Moin. 1988. Eddies, Streams and Convergence Zones in Turbulent Flows. *Proceedings of the Summer Program 1988*. Center for Turbulence Research, Stanford University, Stanford, CA, 1988, pp. 193-208. https://web.stanford.edu/group/ctr/Summer/201306111537.pdf

Kim, S., and B. Natan. 2015. Inlet Geometry and Equivalence Ratio Effects on Combustion in a Ducted Rocket. *Journal of Propulsion and Power.* 31(2):619-31. https://doi.org/10.2514/1.B35369

Kim, J. S., and F. A. Williams. 1997. Extinction of diffusion flames with nonunity Lewis numbers. *Journal of Engineering Mathematics*. 31(2):101-18. https://doi.org/10.1023/A:1004282110474

Le Pichon, T., and A. Laverdant. 2016. Numerical Simulation of Reactive Flows in Ramjet Type Combustors and Associated Validation Experiments. *Journal of Aerospace Lab.* Paper AL11-03. https://doi.org/10.12762/2016.al11-03

Martín, P., M. Piomelli, and G. Candler. 2000. Subgrid-Scale Models for Compressible Large-Eddy Simulations. *Theoretical and Computational Fluid Dynamics*. 13(5):361-76. https://doi.org/10.1007/PL00020896

Müller, C.M., H. Breitbach, and N. Peters. 1994. Partially Premixed Turbulent Flame Propagation in Jet Flames. *Twenty-Fifth Symposium (International) on Combustion*. pp. 1099-1106. https://doi.org/10.1016/S0082-0784(06)80747-2

Nemati, A., J. Ong, and J. H. Walther. 2022. CFD Analysis of Combustion and Emission Formation Using URANS and LES Under Large Two-Stroke Marine Engine-Like Conditions. *Applied Thermal Engineering*, Vol. 216. https://doi.org/10.1016/j.applthermaleng.2022.119037

Peters, N. 1984. Laminar Diffusion Flamelet Models in Non-Premixed Turbulent Combustion. *Progress in Energy and Combustion Science.* 10(3):319-39. https://doi.org/10.1016/0360-1285(84)90114-X

Pierce, C. D., and P. Moin. 2004. Progress-Variable Approach for Large-Eddy Simulation of Non-Premixed Turbulent Combustion. *Journal of Fluid Mechanics*. 504:73-97. https://doi.org/10.1017/S0022112004008213

Pierce, C. D., and P. Moin. 1998. A Dynamic Model for Subgrid-Scale Variance and Dissipation Rate of a Conserved Scalar. *Physics of Fluids.* 10(12):3041-44. https://doi.org/10.1063/1.869832

Poinsot, T., and D. Veynante. 2012. *Theoritical and Numerical Combustion*. 3rd ed., T. Poinsot, Toulouse.

Pope, S. B. 2004. Ten Questions Concerning the Large Eddy Simulation of Turbulent Flows. *New Journal of Physics.* Vol. 6. https://doi.org/10.1088/1367-2630/6/1/035

Reichstadt, S., N. Bertier, A. Ristori, and P. Bruel. 2007. Towards LES of Mixing Processes Inside a Research Ramjet Combustor. *XVIII International Symposium on Air Breathing Engines*. ISABE Paper 2007-1188.

Ristori, A., G. Heid, A. Cochet, and G. Lavergne. 1999. Experimental and Numerical Study of Turbulent Flow inside a Research SDR Combustor. *35th AIAA/ASME/SAE/ASEE Joint Propulsion Conference and Exhibit*. AIAA Paper 99-2814. https://doi.org/10.2514/6.1999-2814

Roux, A. 2009. Simulation aux Grandes Echelles d'un statoréacteur. Ph.D. Dissertation, Dynamique des Fluides, Institut National Polytechnique de Toulouse. http://www.theses.fr/2009INPT025H/document

Roux, A., S. Reichstadt, N. Bertier, L. Gicquel, F. Vuillot, and T. Poinsot. 2009. Comparison of Numerical Methods and Combustion Models for LES of a Ramjet. *Comptes Rendus Mécanique.* 337(6-7):352-361. https://doi.org/10.1016/j.crme.2009.06.008

Roux, A., L. Y. M. Gicquel, S. Reichstadt, N. Bertier, , G. Staffelbach, , F. Vuillot, and T. J. Poinsot. 2010. Analysis of Unsteady Reacting Flows and Impact of Chemistry Description in Large Eddy Simulations of Side-Dump Ramjet Combustors. *Combustion and Flame.* 157(1):176-191. https://doi.org/10.1016/j.combustflame.2009.09.020

Roy, C. J., 2010. Review of Discretization Error Estimators in Scientific Computing. *48th AIAA Aerospace Sciences Meeting Including the New Horizons Forum and Aerospace Exposition*. AIAA Paper 2010-126. https://doi.org/10.2514/6.2010-126

Shih, T. H., W.W. Liou, A. Shabbir, Z. Yang, and J. Zhu. 1995. A New k-ϵ Eddy Viscosity Model for High Reynolds Number Turbulent Flows. *Computers & Fluids*. 24(3):227-238. https://doi.org/10.1016/0045-7930(94)00032-T

Smith, G. P., D.M. Golden, M. Frenklach, N.W. Moriarty, B. Eiteneer, M. Goldenberg, C. T. Bowman, R.K. Hanson, S. Song, Jr.W.C. Gardiner, V.V. Lissianski, and Z. Qin. 1999. http://combustion.berkeley.edu/gri-mech/version30/text30.html

Solmaz, M. B., and S. Uslu. 2023. Effects of turbukence and flamelet combustion modelling on the CFD simulation of a dual inlet ramjet combustor. *International Journal of Turbo & Jet Engines.* https://doi.org/10.1515/tjj-2023-0039

Solmaz, M. B., S. Uslu, and O. Uzol. 2014. Unsteady RANS for Simulation of High Swirling Non-Premixed Methane-Air Flame. *50th AIAA/ASME/SAE/ASEE Joint Propulsion Conference*. AIAA Paper 2014-3473. https://doi.org/10.2514/6.2014-3473

Spalart, P. R., S. Deck, M.L. Shur, K.D. Squires, M.K. Strelets, and A. Travin. 2006. A New Version of Detached-Eddy Simulation, Resistant to Ambiguous Grid Densities. *Theoretical and Computational Fluid Dynamics.* 20(3):181-195. https://doi.org/10.1007/s00162-006-0015-0

Spalart, P. R., W-H. Jou, M.K. Strelets, and S. R. Allmaras. 1997. Comments on the feasibility of LES for wings, and on a hybrid RANS/LES approach. 1st AFOSR Int. Conf. on DNS/LES, Aug. 4-8, 1997, Ruston, LA. In Advances in DNS/LES, C. Liu & Z. Liu Eds., Greyden Press, Columbus, OH

Stowe, R.A., C. Dubois, P.G. Harris, A.E.H.J. Mayer, A. deChamplain, and S. Ringuette. 2004. Performance Prediction of a Ducted Rocket Combustor Using a Simulated Solid Fuel. *Journal of Propulsion and Power.* 20(5):936-944. https://doi.org/10.2514/1.2799

Stull, F.D., R.R. Craig, G.D. Streby, and S. P. Vanka. 1985. Investigation of a Dual Inlet Side Dump Combustor Using Liquid Fuel Injection. *Journal of Propulsion and Power.* 1(1):83-88. https://doi.org/10.2514/3.22763

Sun, M.-B., Z.-G. Wang, J.-H. Liang, and H. Geng. 2008. Flame Characteristics in Supersonic Combustor with Hydrogen Injection Upstream of Cavity Flameholder. *Journal of Propulsion and Power.* 24(4):688-95. https://doi.org/10.2514/1.34970

Timnat, Y.M. 1990. Recent Developments In Ramjets, Ducted Rockets And Scramjets. *Progress in Aerospace Sciences.* 27(3):201-235. https://doi.org/10.1016/0376-0421(90)90007-7

Travin, A., M. Shur, M. Strelets, and P.R. Spalart. 2002. Physical and Numerical Upgrades in the Detached-Eddy Simulation of Complex Turbulent Flows. In *Advances in LES of Complex Flows*. ed. R. Friedrich, W. Rodi. Springer Netherlands, Dordrecht. https://doi.org/10.1007/0-306-48383-1_16

Williams, F.A. 1975. Recent Advances in Theoretical Descriptions of Turbulent Diffusion Flames. In *Turbulent Mixing in Nonreactive and Reactive Flows*, ed. S.N.B. Murthy. Springer New York. https://doi.org/10.1007/978-1-4615-8738-5_5

Yang, S., X. Wang, W. Sun, and V. Yang. 2020. Comparison of Finite Rate Chemistry and Flamelet/Progress-Variable Models: Sandia Flames and the Effect of Differential Diffusion. *Combustion Science and Technology.* 192(7):1137-1159. https://doi.org/10.1080/00102202.2020.1754809

Journal Homepage: https://dergipark.org.tr/tr/pub/isibted

Isı Bilimi ve Tekniği Dergisi

Archive: https://tibtd.org.tr/dergi

Effect of Infrarenal Flow Waveform on Hemodynamics of Abdominal Aortic Aneurysms and Selection of Rheology Models

Burcu RAMAZANLI [1, *], Cüneyt SERT [2], Mehmet Metin Yavuz [2]

[1] *ADA University, School of IT and Engineering, Baku, AZ1008, Azerbaijan*
[2] *Middle East Technical University, Mechanical Engineering Department, Çankaya, 06800, Ankara, Türkiye*

A R T I C L E I N F O

2025, vol. 45, no.1, pp. 22-35

doi: 10.47480/isibted.1499633

Research Article
Received: 14 June 2024
Accepted: 08 December 2024

* *Corresponding Author*
e-mail: bramazanli@ada.edu.az

Keywords:
Abdominal aortic aneurysm
hemodynamics
Wall shear stress (WSS) descriptors
Vortex transport
Blood rheology
Oldroyd-B model

ORCID Numbers in author order:
0000-0002-8864-7225
0000-0001-7510-9367
0000-0002-9491-4115

A B S T R A C T

The infrarenal flow waveform (IFW) demonstrates distinct patterns in response to varying cardiac conditions, raising questions regarding the applicability of the Newtonian model due to variations of the shear rate ($|\dot{\gamma}|$) distribution across different IFW patterns. This study aims to investigate the hemodynamic conditions generated by different IFW patterns within an Abdominal Aortic Aneurysm (AAA) model, and the impact of various rheological models on their predictions. Three IFW patterns are applied to the Newtonian, several shear-thinning and viscoelastic (Oldroyd-B) models. The results of numerical simulations demonstrate the transportation time of the vortices from proximal to distal regions within the bulge decreases by up to 50% with an increase in the mean flow rate. These alterations in the vortex transport mechanism (VTM) affect $|\dot{\gamma}|$ distribution, causing significant variations in the predictions of the rheological models. Even at high mean flow rates, the Newtonian predicts an OSI_{max} twice as large as that predicted by the Carreau and Power models, along with an $ECAP_{max}$ that is 5 times greater. Therefore, the Newtonian model is not appropriate for the AAA simulations. Together with $|\dot{\gamma}|$, a comprehensive assessment of IFW pattern and resulting VTM prior to the rheological model selection is critical and recommended.

İnfrarenal Akış Dalga Formunun Abdominal Aort Anevrizmalarının Hemodinamiği ve Reoloji Modellerinin Seçimi Üzerindeki Etkisi

M A K A L E B İ L G İ S İ

Anahtar Kelimeler:
Abdominal aort anevrizması
hemodinamiği
Duvar kayma gerilimi (WSS)
tanımlayıcıları
Girdap taşınması
Kan reolojisi
Oldroyd-B modeli

Ö Z E T

İnfrarenal akış dalga formu (IFW), farklı kardiyak koşullara yanıt olarak belirgin paternler sergilemektedir. Newtonyen modelin Abdominal Aort Anevrizması (AAA) hemodinamiği simülasyonlarında kullanılabilirliği, farklı IFW paternleri arasında kayma hızı ($|\dot{\gamma}|$) dağılımındaki değişiklikler nedeniyle soru işaretleri doğurmaktadır. Bu çalışma, bir AAA modeli içinde farklı IFW paternleri tarafından oluşturulan hemodinamik koşulları ve bu paternlerin çeşitli reolojik modellerin tahminlerine olan etkilerini araştırmayı amaçlamaktadır. Newtonyen, çeşitli kayma inceltici ve viskoelastik (Oldroyd-B) modellerine üç farklı IFW deseni uygulanmıştır. Sayısal simülasyonların sonuçları, anevrizma içinde proksimalden distal bölgelere doğru girdapların taşıma süresinin ortalama akış hızındaki artışla birlikte %50'ye kadar azaldığını göstermektedir. Girdap taşınma mekanizmasındaki (VTM) bu değişiklikler, $|\dot{\gamma}|$ dağılımını etkileyerek reolojik modellerin tahminlerinde önemli varyasyonlara yol açmaktadır. Yüksek ortalama akış hızlarında bile, Newtonyen model, Carreau ve Power modelleri tarafından tahmin edilenden iki kat daha büyük bir OSI_{max} ve beş kat daha büyük bir $ECAP_{max}$ öngörmektedir. Bu nedenle, Newtonyen model, AAA simülasyonları için uygun değildir denilebilir. Sonuç olarak, $|\dot{\gamma}|$'nin yanı sıra, reolojik model seçimi öncesinde IFW paternlerinin ve buna bağlı VTM'nin kapsamlı bir şekilde değerlendirilmesi kritik ve önerilmektedir.

SEMBOLLER / NOMENCLATURE

AAA	abdominal aortic aneurysm
IFW	infrarenal flow waveform
WSS	wall shear stress (Pa)
TAWSS	time-averaged wall shear stress (Pa)
ECAP	endothelial cell activation potential (1/Pa)
OSI	oscillatory shear index
Re_m	mean Reynolds number
λ_{ci}	λ_{ci}-criterion, swirling strength [1/s]
$\overline{\lambda_{ci}}$	time – averaged λ_{ci}-criterion [1/s]
$\dot{\gamma}$	shear rate (1/s)
$\bar{\dot{\gamma}}$	time-averaged shear rate (1/s)
α	Womersley number
ν	kinematic viscosity (m²/s)
μ	dynamic viscosity (Pa.s)

INTRODUCTION

Abdominal aortic aneurysm (AAA) is the dilatation of the abdominal aorta beyond 50% of the normal vessel diameter, due to degeneration of the arterial wall (McGloughlin and Doyle, 2010). The physiological flow waveform at the infrarenal section of the aorta, which is just upstream part of AAA, shows different patterns in different patients. Figure 1 shows measured infrarenal flow waveforms (IFW) for the resting condition of two different patients (Les et al., 2010). There is a significant variation between the peak systolic flow rate values, while the diastolic flow rate is nearly zero for both. However, for exercise conditions, the diastolic flow rate might be higher than zero. According to Les et al. (2010), the diastolic flow rate might reach up to 100 ml/sec during exercise. The variations in the IFW pattern might lead to differences in the hemodynamic conditions such as $|\dot{\gamma}|$ distributions and evolution of the vortex structures through AAAs during systolic and diastolic phases (Fuchs et al., 2021).

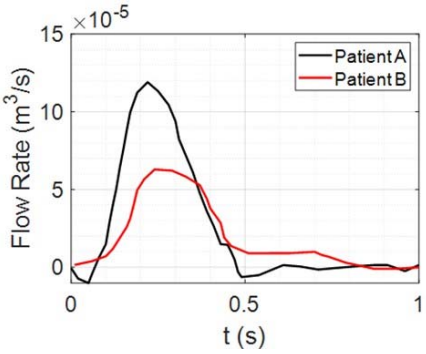

Figure 1. A comparison of measured physiological infrarenal flow rate during rest for two different patients (Les et al., 2010).

Blood is a concentrated suspension of various cellular elements, which are red blood cells, white blood cells and thrombocytes, within the plasma. Plasma, containing 93% water and 3% particles composed of organic molecules, electrolytes, proteins, and waste materials collected from the organism, behaves as a Newtonian fluid with a constant viscosity (Bessonov et al., 2016). However, at low $|\dot{\gamma}|$, especially $|\dot{\gamma}| < 100\ s^{-1}$, the non-Newtonian behavior of blood becomes more apparent. Red blood cells aggregate and form rouleaux, which are rod shaped stacks of individual cells (Bessonov et al., 2016). The aggregation and disaggregation of rouleaux results in a shear-thinning and elastic behavior of blood (Bessonov et al., 2016; Bilgi and Atalik, 2020; Bodnár et al., 2011). The abdominal aorta is a large artery with a high shear rate ($|\dot{\gamma}|$) distribution because the mean flow rate is also larger compared to other arteries (Salman et al., 2019). In literature, it is a common approach to assume the blood as a Newtonian fluid for the hemodynamic simulations of AAAs (Salman et al., 2019; Arzani and Shadden, 2016; Qiu et al., 2018; Soudah et al., 2013) because a vast number of studies agree that non-Newtonian effects diminish with increasing flow rate (Shibeshi and Collins, 2005; Soulis et al., 2008; Skiadopoulos et al., 2017), which leads to a high $|\dot{\gamma}|$ distribution. Indeed, inside the aneurysm sac, there are stagnant low-velocity recirculation regions due to the separation of bulk flow at the diastolic phase (Salman et al., 2019; Arzani, 2018), causing low $|\dot{\gamma}|$ at those zones. Non-Newtonian properties of blood might be more influential during diastole due to lower flow and shear rates (Fisher and Rossmann, 2009), compared to the peak systole. Moreover, aforementioned variations in the IFW pattern might lead different $|\dot{\gamma}|$ distributions through AAAs during the systolic and diastolic phases. Therefore, applicability of the Newtonian model to AAA hemodynamics under various physiological flow conditions remains uncertain.

In numerical studies, shear-thinning behavior of the blood is generally modeled by using various viscosity models, such as Carreau, Carreau-Yasuda, Cross, Casson, Quemada and Power-law. To evaluate differences between the shear-thinning and Newtonian viscosity models, studies have compared hemodynamic descriptors obtained by different shear-thinning models in the cerebral (Fisher and Rossmann, 2009), carotid (Razavi et al., 2011; Morbiducci et al., 2011; Lee and Steinman, 2007; Mendieta et al., 2020) and thoracic (Karimi et al., 2014; Faraji et al., 2022) arteries. For AAAs, several studies (Arzani, 2018; Biasetti et al., 2011; Bilgi and Atalik, 2019) have compared the hemodynamic predictions obtained by the Carreau-Yasuda and Newtonian models, while (Skiadopoulos et al., 2017) compared the results of the Casson, Quemada and Newtonian models. Most of these studies have reported variations between the results obtained with the Newtonian and shear-thinning models. The elastic nature of the blood is commonly modeled by using the Oldroyd-B model (Bodnár et al., 2011). Elhanafy et al. (2019) compared the results obtained by the Newtonian model with the results of viscoelastic Oldroyd-B for AAA, while Bilgi and Atalik (2020) compared the Newtonian, Carreau-Yasuda and modified Oldroyd-B models. However, to the authors' best knowledge, none of the available literature has parametrized the behavior of shear-thinning and viscoelastic rheology models under different hemodynamic conditions which are generated due to varying IFW patterns.

The objective of this study is to investigate the hemodynamic conditions generated by different IFW patterns and their impact on the predictions of a broad range of rheological models including the Newtonian, Carreau, Carreau-Yasuda, Casson, Power, Quemada, Cross, Modified and Simplified Cross, and Oldroyd-B models. For that purpose, three IFW patterns with different peak systolic and diastolic flow rates, which are the Base, Case 1 and 2, are utilized. In literature (Mutlu et al., 2023; Stergiou et al., 2019), hemodynamics of AAA is generally quantified by using WSS descriptors such as time-averaged wall shear stress (TAWSS), oscillatory shear index (OSI), endothelial cell activation potential (ECAP) and

relative residence time (RRT). However, WSS descriptors solely are not enough to bridge hemodynamics and aneurysm pathology because vortex patterns are also observed in AAAs (Saqr et al., 2020; Saha et al., 2024). Fuchs et al. (2021) observed the effect of IFW pattern on aorta hemodynamics, and their results highlighted a substantial impact of the IFW pattern on WSS descriptors. Moreover, they also revealed strong variations in vortex structures, but this aspect is not fully explored in the scope of their study. Hence, they recommend further investigation to understand the impact of IFW pattern on vortex evolution (Fuchs et al., 2021). Moreover, in a meta literature analysis study, Saqr et al. (2020) have reported that WSS is a scalar-tensor field, which loses its directionality. Visualizing vortex patterns rather than WSS descriptors is more meaningful owing to their directional nature. Therefore, together with WSS descriptors, quantifying the vortical structures and their evolution may lead to better understanding the effect of IFW both on AAA hemodynamics and predictions of various rheology models (Saqr et al., 2020; Saha et al., 2024).

METHODS

In their patient-specific aorta study, Fuchs et al. (2021) emphasized that variations in the IFW pattern considerably affect the vortex structures. However, they also highlighted that in the context of patient-specific geometries, the flow field becomes extremely complex, making it impractical to accurately parametrize the effect of IFW pattern on vortex structures (Fuchs et al., 2021). In this study, an idealized model of AAA is employed, chosen for its suitability for a comparative parametric study. Owing to its independence from geometric details, the use of an idealized geometry is advantageous for characterizing and comparing predictions of a broad range of rheology models according to different hemodynamic conditions under various IFW patterns. The AAA model used in this study is given in Fig. 2a. The geometry is two-dimensional, axisymmetric, and created based on Stamatopoulos et. al's study (2010). The entrance and exit parts are straight and cylindrical, while the aneurysm bulge is elliptical with a major radius of 0.034 m. The lengths of the entrance part, bulge and exit parts are $L_{ent} =$ 935 mm, $L_B = 62$ mm and $L_{ex} = 206$ mm, respectively. The artery and bulge radii are, $R = 9$ mm and $R_B = 22$ mm, respectively. The vessel and bulge dimensions are consistent with those of realistic abdominal arteries and aneurysms (Brewster et al., 2003; Les et al., 2010).

Figure 2b shows the IFW patterns used at the inlet, which are the Base, Case 1, and Case 2. In the Base case, the IFW pattern suggested by Finol and Amon is implemented, by preserving the overall waveform characteristics. However, the peak flow rate suggested by Finol and Amon (2001) is lower than the physiologically measured values (Suh et al., 2011). To align with the physiological range, the peak flow rate in the Base case is adjusted upward to reach a peak systolic flow rate of 42 ml/sec, starting from a diastolic flow rate of zero. It is important to note that, while IFW pattern is derived from the Finol and Amon's study (2001), there is no direct comparison between their results and the results of this study. Consequently, the results are not affected by the difference in the peak flow rates between the two studies. In Case 1, the diastolic flow rate remains consistent with that of the Base case, while the peak systolic flow rate is increased. On the other hand, in Case 2 the amplitude of peak systole is kept identical to that of the Base pattern, albeit with increased diastolic flow rate. Therefore, Cases 1 and 2 serve to investigate the impact of increased peak systolic and diastolic flow rates, respectively. The period of all waveforms is the same and equal to $T = 1$ s, yielding a Womersley number of $\alpha = 0.5D\sqrt{\omega/\nu} = 12.14$, where D is the artery diameter, $\omega = 2\pi/T$ is the frequency, and $\nu = 3.45 \times 10^{-6}$ m^2/s is the kinematic viscosity of the Newtonian model. The mean Reynolds numbers for the waveforms are $Re_m = U_m D/\nu = 120, 250$ and 1160, where $U_{\mathrm{m}} = 0.023, 0.048$ and 0.223 m/s are the time averaged velocities over one period for the Base, Case 1 and 2, respectively.

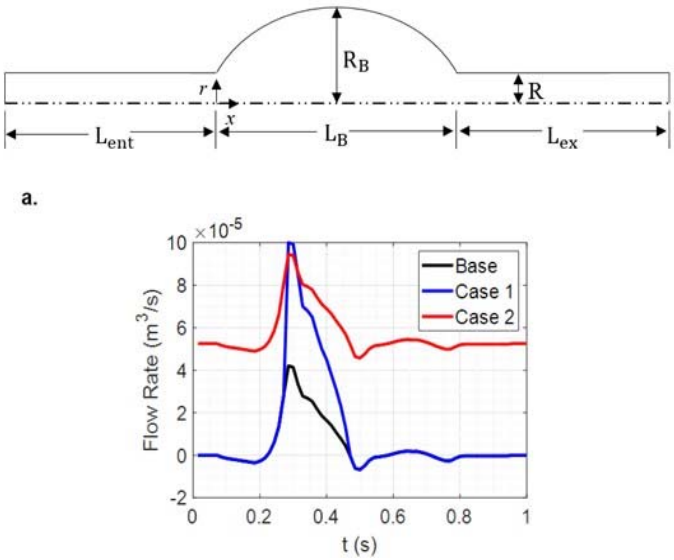

Figure 2. a. 2D axisymmetric flow domain (out of scale). Flow is from left to right, **b.** Physiological IFW patterns, Base (Finol and Amon, 2001), Case 1 and 2.

Unsteady plug flow is specified at the inlet. To capture the transient effects of physiological flow, a Womersley profile at the inlet is generally recommended (Madhavan and Kemmerling, 2018; Moyle et al., 2006; Ramazanli et al., 2023, Wei et al., 2019; Womersley, 1955). The preliminary analysis (Ramazanli et al., 2023) found that while a minimum entrance length of 10D is sufficient for fully developing Womersley flow, a longer entrance length (50D) was applied in this study to achieve consistency across different IFW cases and to ensure a fully developed profile at the bulge inlet. A constant reference pressure of 0 Pa is specified at the outlet, which is a frequently utilized approach in the literature for hemodynamic studies (Reza and Arzani, 2019; Soulis et al., 2008). Through the preliminary runs, it is ensured that the length of the exit part is long enough that the disturbance created by the bulge dies out before the flow reaches the outlet, enabling the use of constant pressure outlet.

The wall boundaries are taken as rigid with no-slip boundary conditions applied. Excluding the compliance effect by using rigid walls is quite common in literature (Arzani and Shadden, 2016; Finol and Amon, 2001; Reza and Arzani, 2019). Eight non-Newtonian models, Carreau, Carreau-Yasuda, Casson, Quemada, Power, Cross, Simplified and Modified Cross, with the details given in Table 1, are used. For the Power model, different constants are available in literature for the same hematocrit.

Table 1. Selected shear-thinning rheology models, which are frequently used to model blood (Bessonov et al., 2016; Shibeshi and Collins, 2005; Cho and Kensey, 1991; Quemada, 1978; Stergiou et al., 2019).

Carreau	$\frac{\mu(\dot{\gamma})-\mu_\infty}{\mu_0-\mu_\infty}=(1+(\lambda\dot{\gamma})^2)^{(n-1)/2}$	$\mu_0 = 0.056$ Pa · s $\mu_\infty = 0.00345$ Pa · s $\lambda = 3.313$ s $n = 0.3568$
Carreau-Yasuda	$\frac{\mu(\dot{\gamma})-\mu_\infty}{\mu_0-\mu_\infty}=(1+(\lambda\dot{\gamma})^a)^{(n-1)/a}$	$\mu_0 = 0.056$ Pa · s $\mu_\infty = 0.00345$ Pa · s $\lambda = 1.902$ s $n = 0.22$ $a = 1.25$
Quemada	$\mu=\mu_f\left[1-\frac{1}{2}\frac{K_0+K_\infty\sqrt{\frac{\lvert\dot{\gamma}\rvert}{\gamma_c}}}{1+\sqrt{\frac{\lvert\dot{\gamma}\rvert}{\gamma_c}}}\phi\right]$	$\mu_f = 0.0012$ Pa · s $K_0 = 4.65$ $K_\infty = 1.84$ $\gamma_c = 2.23$ s^{-1} $\phi = 0.4$
Casson	$\sqrt{\tau}=\sqrt{k_0}+\sqrt{k_1\dot{\gamma}}$	$k_0 = 0.05$ dyne/cm^2 $k_1 = 0.04$ dyne/cm^2
Cross	$\frac{\mu(\dot{\gamma})-\mu_\infty}{\mu_0-\mu_\infty}=\frac{1}{1+(m\dot{\gamma})^n}$	$\mu_0 = 0.056$ Pa · s $\mu_\infty = 0.00345$ Pa · s $m = 1.007$ s $n = 1.028$
Simplified Cross	$\frac{\mu(\dot{\gamma})-\mu_\infty}{\mu_0-\mu_\infty}=\frac{1}{1+m\dot{\gamma}}$	$\mu_0 = 0.103$ Pa · s $\mu_\infty = 0.005$ Pa · s $m = 8$ s
Modified Cross	$\frac{\mu(\dot{\gamma})-\mu_\infty}{\mu_0-\mu_\infty}=\frac{1}{(1+(m\dot{\gamma})^n)^a}$	$\mu_0 = 0.056$ Pa · s $\mu_\infty = 0.00345$ Pa · s $m = 3.736$ s $n = 2.406$ $a = 0.254$
Power	$\mu(\dot{\gamma})=K\dot{\gamma}^{n-1}$	$K = 0.017$ Pa · s^n $n = 0.708$ (Shibeshi and Collins, 2005) and $K = 0.035$ Pa · s^n $n = 0.6$ (Cho and Kensey, 1991)

In the present study, Power-1 (Shibeshi and Collins, 2005), and Power-2 (Cho and Kensey, 1991) are tested by using two frequently used constants. In Table 1, μ is the viscosity, μ_0 and μ_∞ are the asymptotic viscosity values at zero and infinite shear rates, λ is the relaxation time constant, K is the flow consistency index and n is the power law index (Bessonov et al., 2016; Shibeshi and Collins, 2005; Cho and Kensey, 1991). The kinematic viscosity is 3.45×10^{-6} m^2/s for the Newtonian approach, and the density is 1000 kg/m^3 for all models (Bessonov et al., 2016)To account for the elastic nature of blood, the stress tensor in the linear momentum equation can be decomposed into viscous and elastic parts as $\tau = \tau_s + \tau_e$. The viscous part of the Oldroyd-B model is Newtonian, $\tau_s = 2\mu_s(\nabla u + \nabla u^T)$ (Bodnár et al., 2011). The elastic part satisfies the following constitutive equation.

$$\tau_e + \lambda_1\left(\frac{\partial\tau_e}{\partial t}+u\cdot\nabla\tau_e-\tau_e\cdot\nabla u-\nabla u^T\cdot\tau_e\right) = \mu_e(\nabla u+\nabla u^T) \quad (1)$$

where μ_e is the elastic viscosity coefficient, and λ_1 is the relaxation time (Leuprecht and Perktold, 2001). For blood, $\mu_e = 0.0004$ Pa · s and $\lambda_1 = 0.06$ s (Leuprecht and Perktold, 2001). The Oldroyd-B model available in OpenFOAM is tested previosly (Habla et al., 2014; Guranov et al., 2013; Javidi et al. 2015).

The maximum number of iterations performed at each time step is taken as 10, and the solutions are considered to be converged when residuals for axial velocity component and pressure are less than 10^{-4}. Time step for all simulations is selected as 10^{-5} sec, and to ensure that the time periodic state is reached, calculations are repeated for 6 cardiac cycles for shear-thinning and Newtonian models. However, 12 cardiac cycles are used to reach the time periodic state for Oldroyd-B model. To select a suitable mesh, a mesh independence study is performed using four structured meshes given in Fig. 3.

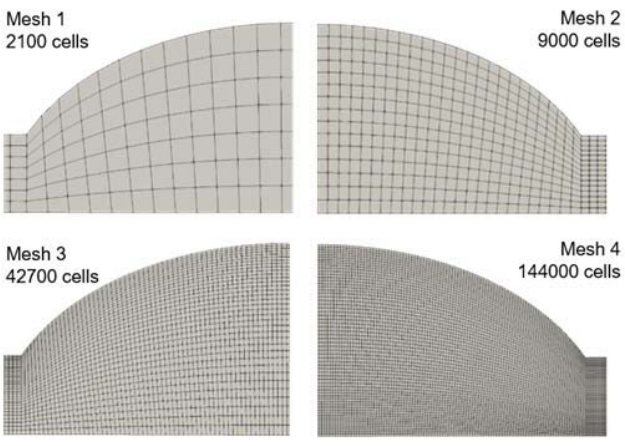

Figure 3. Four meshes used for the mesh independence check.

Figure 4a shows axial velocity profiles at the mid-plane of the aneurysm and swirling strength, λ_{ci} contours obtained at the peak systole and early diastole. In Figure 4b, OSI and ECAP distributions obtained are provided. The axial velocity profiles are identical and swirling strength contours are very similar for meshes 3 and 4. Albeit OSI and ECAP distributions are very sensitive to the mesh selection, Mesh 3 and 4 provided very similar OSI and ECAP distributions. Therefore, Mesh 3 is evaluated to be suitable and used to perform the simulations in the present study.

Stamatopoulos et al. (2010) have performed an experimental and numerical study in axisymmetric bulges similar to the those used in the present study with a steady inlet flow. As a general verification of the currently used simulation setup, axial velocity profiles obtained by Stamatopoulos et al. (2010) are compared with those obtained in the present study with a steady inlet flow in Fig. 5a. The match in the profiles is considered to be satisfactory. Ohtaroglu (2020) performed experiments with physiological, unsteady inlets using Stamatopoulos et al.'s geometry. Figure 5c compares the streamlines obtained in those experiments with the current simulation results at four different time instants of the physiological cycle. Progression of focus points in streamlines, which are the indication of vortex core movement, shows good agreement. Considering both the spatial and the temporal evolution during the cycle, the model predictions are considered to be satisfactory. In addition, simulations are performed to ensure the validity of 2D axisymmetric simplification by comparing results with those of 3D simulations. Considering the velocity profiles plotted at the mid plane of the bulge in Fig. 5c, 2D axisymmetric and 3D results turn out to be almost identical.

WSS descriptors and swirling strength

Generally, wall shear stress (WSS) distribution and different WSS descriptors are used in the literature to predict aneurysm development, thrombosis formation and rupture (Salman et al., 2019; Mutlu et al., 2023). TAWSS descriptor evaluates the total shear stress exerted on the wall throughout a cardiac cycle and OSI highlights zones where WSS shows directional changes over the cardiac cycle (Pinto and Campos, 2016). ECAP and RRT combine TAWSS and OSI in different ways. Mathematical definitions of these descriptors are given below

$$TAWSS = \frac{1}{T}\int_0^T |\tau_w| dt \tag{2}$$

$$OSI = 0.5\left(1 - \frac{\left|\frac{1}{T}\int_0^T \tau_w dt\right|}{\frac{1}{T}\int_0^T |\tau_w| dt}\right) \tag{3}$$

$$ECAP = \frac{OSI}{TAWSS} \tag{4}$$

$$RRT = \frac{1}{(1-2OSI)TAWSS} \tag{5}$$

where T and τ_w are the cardiac cycle period and the wall shear stress, respectively.

Vortex structures are studied extensively in fluid mechanics (Epps, 2017; Chen et al., 2015) because in many cases they provide important insights into the flow field. Inside the aneurysm sac, there is a vortex ring that evolves throughout the cardiac cycle (Bilgi and Atalik, 2019; Deplano et al., 2016). Therefore, together with WSS descriptors, vortex patterns also provide valuable information regarding AAA hemodynamics. Saqr et al. (2020) suggested investigating flow field within aneurysms via vector fields such as vorticity, rather than scalar-tensor fields. However, the vorticity field is not able to discriminate shear layers and vortices (Chen et al., 2015). Swirling strength, λ_{ci}, is a velocity gradient-based vortex identification criteria, which uses discriminant of characteristic equation to define a vortex without shear layers and takes the following form for a 2D axisymmetric flow (Chen et al., 2015)

$$\lambda_{ci} = \frac{1}{2}\sqrt{-4\frac{\partial u_r}{\partial x}\frac{\partial u_x}{\partial r} - \left(\frac{\partial u_x}{\partial x} - \frac{\partial u_r}{\partial r}\right)^2} \tag{6}$$

where u_r and u_x are radial and axial velocity components, respectively. λ_{ci} is larger than zero around a vortex region (Chen et al., 2015).

RESULTS

Effect of IFW pattern on AAA hemodynamics

To understand the hemodynamics of the three IFW patterns inside the AAA model, the temporal evolution of vortex structures, obtained by using the Carreau model, is presented in Supplementary Video 1. For all IFW patterns which are presented as the Base, Case 1 and 2, a primary vortex is generated due to acceleration of the bulk flow during early systole. It is separated from the inlet of the bulge at the peak systole, t = 0.3 sec, and transported downstream by means of advection. The primary phenomena differing from those of the Base, Case 1 and 2 are the acceleration and advection of the bulk flow. For the Base waveform, the acceleration is relatively minor compared to that in Case 1, resulting in only a weaker primary vortex with a small $|\lambda_{ci}|$. Advective effects are also not dominant due to low mean flow rate. Therefore, the primary vortex dissipates due to viscous diffusive effects before it reaches the central region. The largest acceleration is obtained by Case 1. During early systole, the larger acceleration generates a stronger vortex with a large $|\lambda_{ci}|$ compared to the Base case and Case 2. The vortex maintains itself as a strong identity and remains transported to the distal region until the end of the cardiac cycle at $t = T$. On the other hand, increased advective effects due to the larger mean flow rate in Case 2 resulted in the transport of the vortex to the distal site being completed by the end of the systolic phase at $t = 0.5T$. During the diastolic phase, the vortex in Case 2 is located at the distal zone and dissipates due to viscous effects by the end of the cycle, whereas the primary vortex of Case 1 maintains its strong identity even during late diastole.

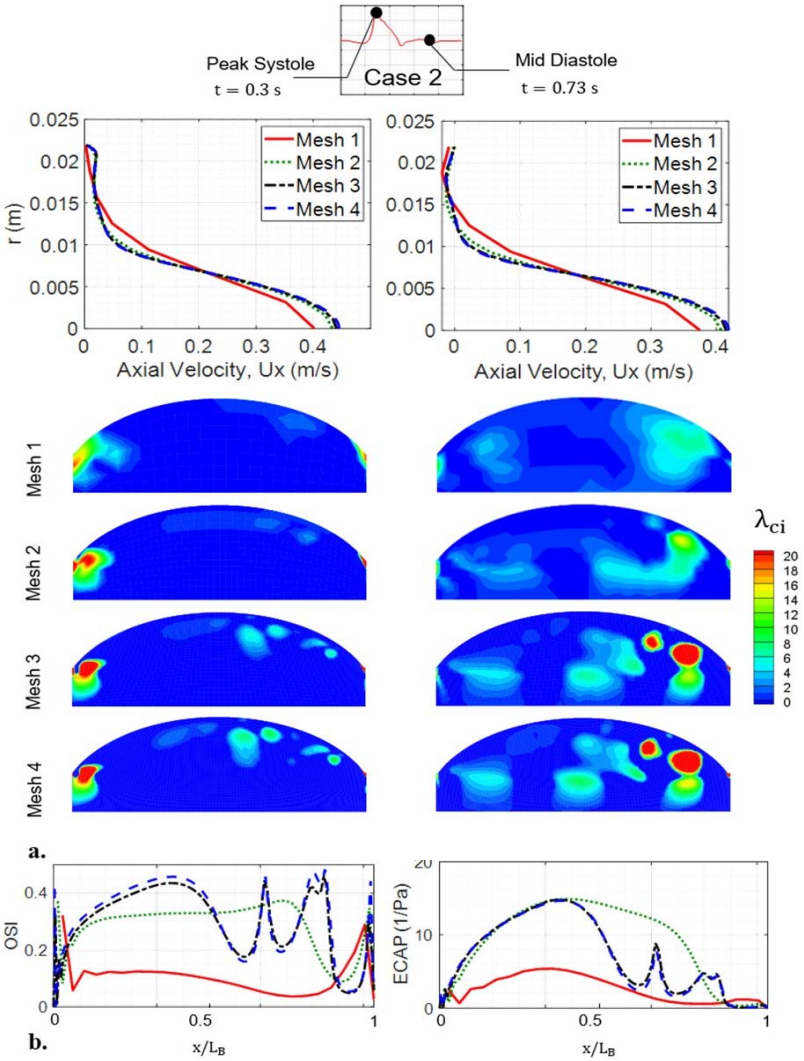

Figure 4. a. Axial velocity profiles obtained with four different meshes at the mid-plane of the aneurysm, $x/L_B = 0.5$, and swirling strength contours through the bulge at the peak systole and mid diastole, b. OSI and ECAP distributions of four meshes for Case 2.

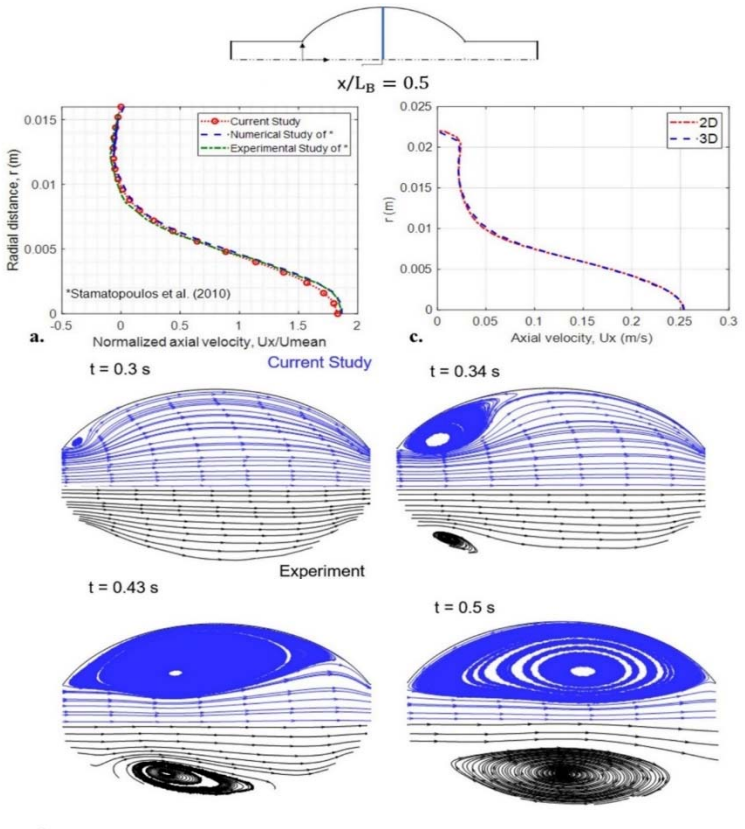

Figure 5. a. Comparison of the normalized axial velocity profile of the current study at x/L_B=0.5 with results of Stamatopoulos et al. (2010) for a steady inlet velocity, **b.** Comparison of the streamline patterns of different time instants for a cardiac cycle; upper halves show the current results and lower halves are from Ohtaroglu (2020), c. Comparison of the axial velocity profiles of 2D axisymmetric and 3D geometries at x/L_B=0.5 at t=0.3 sec of Base case.

Figure 6 presents the contours of the time-averaged swirling strength, $\overline{\lambda_{ci}}$, streamlines and variations in WSS descriptors for three IFW patterns. The Base pattern generates a single primary vortex pattern, in the proximal region of the bulge. However, for Cases 1 and 2, a second primary and a secondary vortex are also generated, and the primary vortex is located in the distal region with a larger magnitude of $\overline{\lambda_{ci}}$ than in the Base case. For Case 1, the second primary and secondary vortices are in the proximal and central regions, respectively. However, for Case 2, they are both located in the distal zone, in contrast to the Base case. As illustrated in Fig. 6, there is a strong correlation between WSS descriptors and vortex patterns. TAWSS obtains high values around the vortices, particularly in large $|\overline{\lambda_{ci}}|$ zones in proximity to the wall, where the OSI, ECAP and RRT are low. For all the cases magnitudes of the ECAP and RRT become zero with high $|\overline{\lambda_{ci}}|$ in the regions where the primary vortex is located. However, the ECAP and RRT values increase significantly in regions with high stagnation. $ECAP_{max}$ and RRT_{max} for the Base case are three times larger than those of Case 1, which has low stagnancy.

Effect of the IFW pattern on predictions of the rheology models

To investigate the effect of the IFW pattern on the behavior of rheology models, instantaneous WSS distributions, contours of swirling strength, λ_{ci}, and shear rate, $\dot{\gamma}$, are plotted in Fig. 7. In the literature, the most significant deviations between the Newtonian and shear-thinning models are observed at the diastolic phase due to the low flow rate (Shibeshi and Collins, 2005), which is consistent with the results of the present study. The mid-diastolic phase (Egelhoff et al., 1999) was selected as it corresponds to the lowest shear rates, where non-Newtonian blood behavior becomes more significant. To provide a comprehensive investigation of hemodynamics, Supplementary Material includes figures and videos showing the evolution of swirling strength throughout the entire cardiac cycle, covering all diastolic phases for each IFW case. Therefore, the results of mid diastolic phase, t = 0.73 sec, are presented in Fig. 7. In Case 1, $|\dot{\gamma}|$ remains low for most of the bulge, while $|\dot{\gamma}| > 50\ s^{-1}$ around the primary vortex. Compared to shear-thinning models, the Newtonian model overestimates the WSS peak, intensity of swirling strength contours and $|\dot{\gamma}|$, which is consistent with literature (Biasetti et al., 2011). The WSS distributions, patterns of λ_{ci} contours and their locations are very similar for the Casson and Quemada models, consistent with the results of (Skiadopoulos et al., 2017). The Carreau and Power models predict comparable λ_{ci} patterns and WSS distributions, as reported by (Shibeshi and Collins, 2005). Although not presented here, the Carreau-Yasuda, Cross, Modified and Simplified Cross models are also tested. The results obtained by the Carreau-Yasuda, Cross and Modified Cross are the same with Carreau and Power-1, while the Simplified Cross model provided very similar hemodynamic descriptors with the Casson and Quemada for all cases. For Case 2, $|\dot{\gamma}| > 50\ s^{-1}$ is obtained near the distal region and at the centerline of the aneurysm, while it remains close to zero in proximity to the wall for proximal and central regions. At regions with high $|\dot{\gamma}|$, contours of λ_{ci} and WSS distribution obtained by the Carreau, Carreau-Yasuda, Cross, Modified and Simplified Cross, Casson, Quemada and Newtonian models are very similar to each other. Therefore, the Newtonian model might be sufficient for the zones with $|\dot{\gamma}| > 50\ s^{-1}$, while the shear-thinning models are necessary for the stagnant regions with significantly lower shear rates.

In Supplementary Figure, the WSS distributions, λ_{ci} and $|\dot{\gamma}|$ contours of peak systolic phase, t = 0.3 sec, are presented at the post-bulge, straight artery segment for Case 1 and 2. In this specific region, near-wall $|\dot{\gamma}|$ values exhibit a significant increase compared to the values in proximity to the bulge. The results demonstrate that, the Casson and Quemada models demonstrate a diverging behavior from the Newtonian model as $|\dot{\gamma}|$ values are increasing, whereas the Carreau and Power models exhibit a more consistent behavior. It is the fact that for large $|\dot{\gamma}|$ values ($|\dot{\gamma}| > 100\ s^{-1}$), blood demonstrates Newtonian characteristics (Bessonov et al., 2016), the suitability of Casson and Quemada models in modeling the rheological behavior of blood might be questionable, particularly in scenarios characterized by elevated $|\dot{\gamma}|$ values.

Figure 8 shows contours of time-averaged swirling strength, $\overline{\lambda_{ci}}$, shear rate, $\bar{\dot{\gamma}}$, and streamlines obtained by the Carreau, Power, Casson, Quemada and Newtonian models for Base, Case 1 and 2. For the Base case, $|\bar{\dot{\gamma}}| < 10\ s^{-1}$ throughout the bulge, and the Newtonian model overestimates the magnitude and intensity of $\overline{\lambda_{ci}}$ contours of vortices. From the $\overline{\lambda_{ci}}$ contours, non-Newtonian behavior in low shear zones minimizes the size of the primary vortex pattern for all of the shear-thinning models (Soulis et al., 2008), and a second primary vortex is only obtained by the Newtonian model.

For Case 1, $|\bar{\dot{\gamma}}|$ is larger than $50\ s^{-1}$ only around the primary vortex, but it is nearly zero at other regions. $\overline{\lambda_{ci}}$ contours and streamline patterns of the Newtonian model are significantly different than the other rheology models. On the other hand, except the proximal and central regions, $|\bar{\dot{\gamma}}| > 50\ s^{-1}$ inside the bulge for Case 2. Therefore, $\overline{\lambda_{ci}}$ and streamline predictions of all shear-thinning models become very similar to the Newtonian model. With increasing shear rate, except the Power-2, all rheology models can predict the primary, second primary and secondary vortices. Biasetti et al. (2011) have reported that the Newtonian model predicted vortex structures at the core region, away from the near wall, which were not observed with the more accurate Carreau–Yasuda model. Moreover, Arzani (2016) has hypothesized that shear-thinning models predict different vortex patterns than the Newtonian model. The present study further supports those hypotheses quantitatively, revealing that the Newtonian model especially tends to overestimate the magnitude and intensity of $\overline{\lambda_{ci}}$ contours of secondary and second primary vortices.

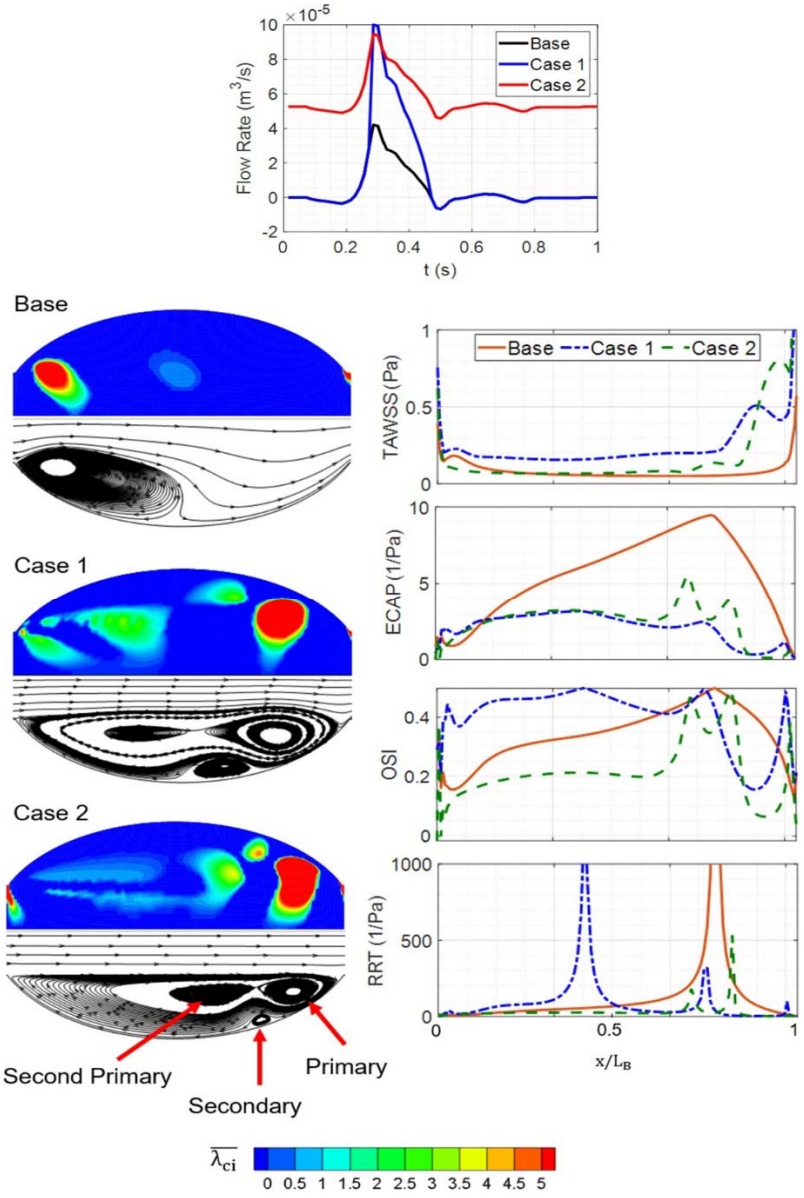

Figure 6. Comparison of time-averaged swirl strength contours, streamlines and variations in WSS measures on the aneurysm wall for the Carreau model for three IFW patterns

In Figure 9, OSI and ECAP distributions obtained by selected rheology models are presented. As observed in Fig. 6, OSI and ECAP values are near to zero around high $|\overline{\lambda_{ci}}|$ region, while they tend to increase for decreasing $|\overline{\lambda_{ci}}|$ for each waveform and rheology model. OSI and ECAP distributions obtained by the Casson and Quemada models are nearly the same, and closer to the Newtonian pattern at each waveform, consistent with the results of Fig. 8. OSI and ECAP estimations of the Carreau and Power-1 models are very similar and more dissipative than the Casson and Quemada, which is an expected behavior for a shear-thinning model (Biasetti et al., 2011). Power-2 is significantly dissipative and its OSI and ECAP patterns are very different than other shear-thinning models. Even for Case 1 and 2, with comparatively higher $|\bar{\dot{\gamma}}|$ values inside the bulge, the Newtonian model overestimates the OSI and ECAP values. Especially for Case 2 with the highest mean flow rate, OSI and ECAP values obtained by the Newtonian model are significantly larger for the proximal and central regions of the bulge ($0 < x/L_B < 0.65$) than the shear-thinning models, although they obtain quite similar $\overline{\lambda_{ci}}$ patterns as seen in Fig. 8.

OSI and ECAP estimations of the Carreau and Power-1 models are very similar and more dissipative than the Casson and Quemada, which is an expected behavior for a shear-thinning model (Biasetti et al., 2011). Power-2 is significantly dissipative and its OSI and ECAP patterns are very different than other shear-thinning models. Even for Case 1 and 2, with comparatively higher $|\bar{\dot{\gamma}}|$ values inside the bulge, the Newtonian model overestimates the OSI and ECAP values. Especially for Case 2 with the highest mean flow rate, OSI and ECAP values obtained by the Newtonian model are significantly larger for the proximal and central regions of the bulge ($0 < x/L_B < 0.65$) than the shear-thinning models, although they obtain quite similar $\overline{\lambda_{ci}}$ patterns as seen in Fig. 8. OSI_{max} value obtained by the Newtonian model at that segment is 2 times larger than the Carreau and Power, while 1.5 times larger than Casson and Quemada models. $ECAP_{max}$ value of the Newtonian at that zone is 5 and 2.5 times larger than Carreau-Power and Casson-Quemada pairs, respectively.

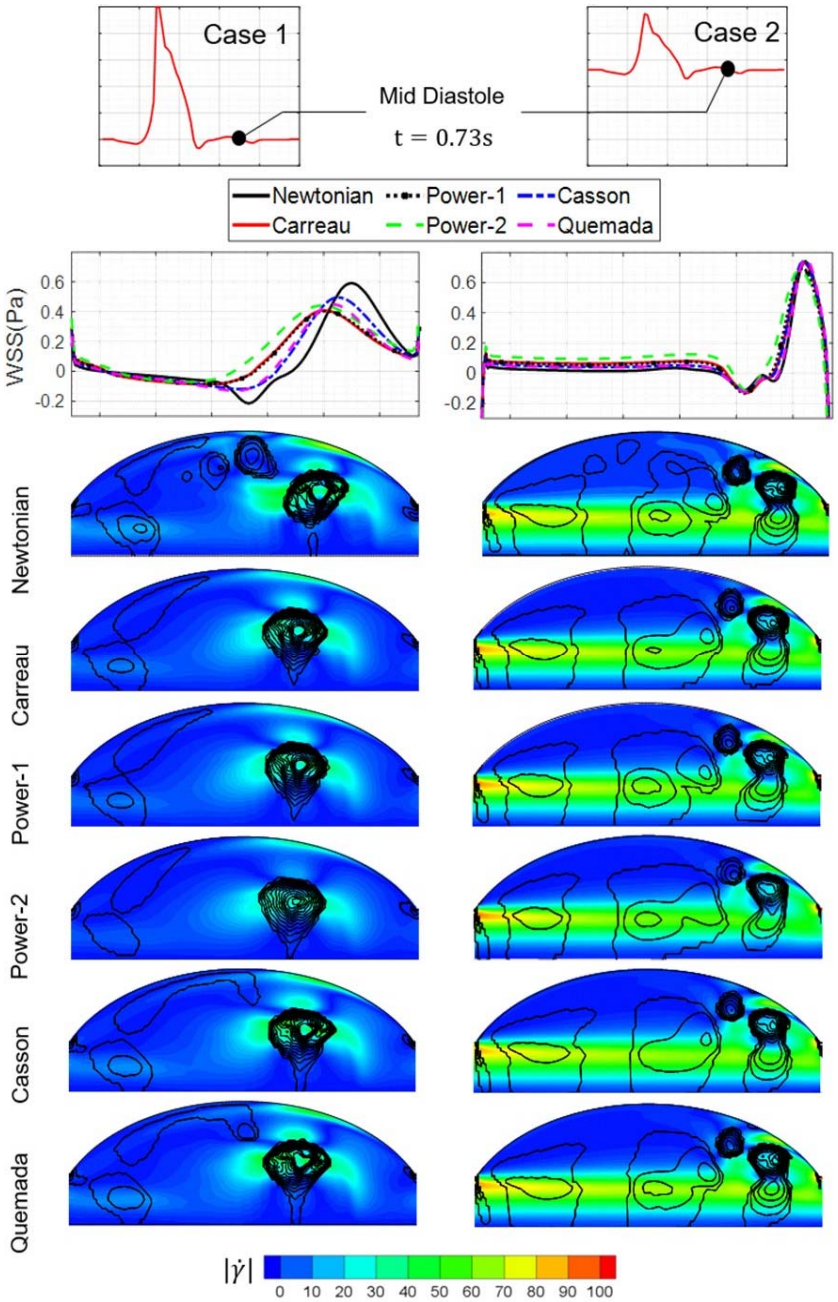

Figure 7. Comparison of WSS distributions, λ_{ci} and $|\dot{\gamma}|$ contours of Newtonian and selected shear-thinning rheology models at t = 0.73 sec, for cases 1 and 2.

Differences of the hemodynamic predictions of the Newtonian, shear-thinning and Viscoelastic models

To the author's best knowledge, this is the first study which utilizes Oldroyd-B model of OpenFOAM to simulate hemodynamics of an AAA model. Base case is selected here because the Oldroyd-B model available in OpenFOAM fails to provide a stable solution for high mean Reynolds numbers, such as Case 1 and 2. This observation is consistent with literature, where multiple studies have documented the inadequacies of the Oldroyd-B model in accurately capturing flow dynamics of high Reynolds numbers (Elhanafy et al., 2019; Leuprecht and Perktold, 2001). Indeed, the elasticity of blood is dominant for low shear rates, demonstrating a diminishing pattern with increasing shear rate ($|\dot{\gamma}| > 100\ s^{-1}$) (Bodnár et al., 2011). Therefore, comparing the results of the Newtonian, Viscoelastic, Quemada and Carreau models for the Base case with lower shear provides insights into the differences introduced by blood elasticity.

In Figure 10a, λ_{ci} contours and streamline patterns for the Base case are presented for the Newtonian, Viscoelastic, Quemada and Carreau models at the mid-diastolic phase (t = 0.73 sec). The selection of the Base case is motivated by its characteristic low shear rates. The viscous part of the Viscoelastic Oldroyd-B model is Newtonian, not shear-thinning. On the other hand, the Carreau and Quemada models are shear-thinning models and could only provide viscous behavior. Therefore, the difference between the Newtonian and Viscoelastic results is caused by the elastic effects, while the shear-thinning models and Newtonian case present variations caused only by viscous effects.

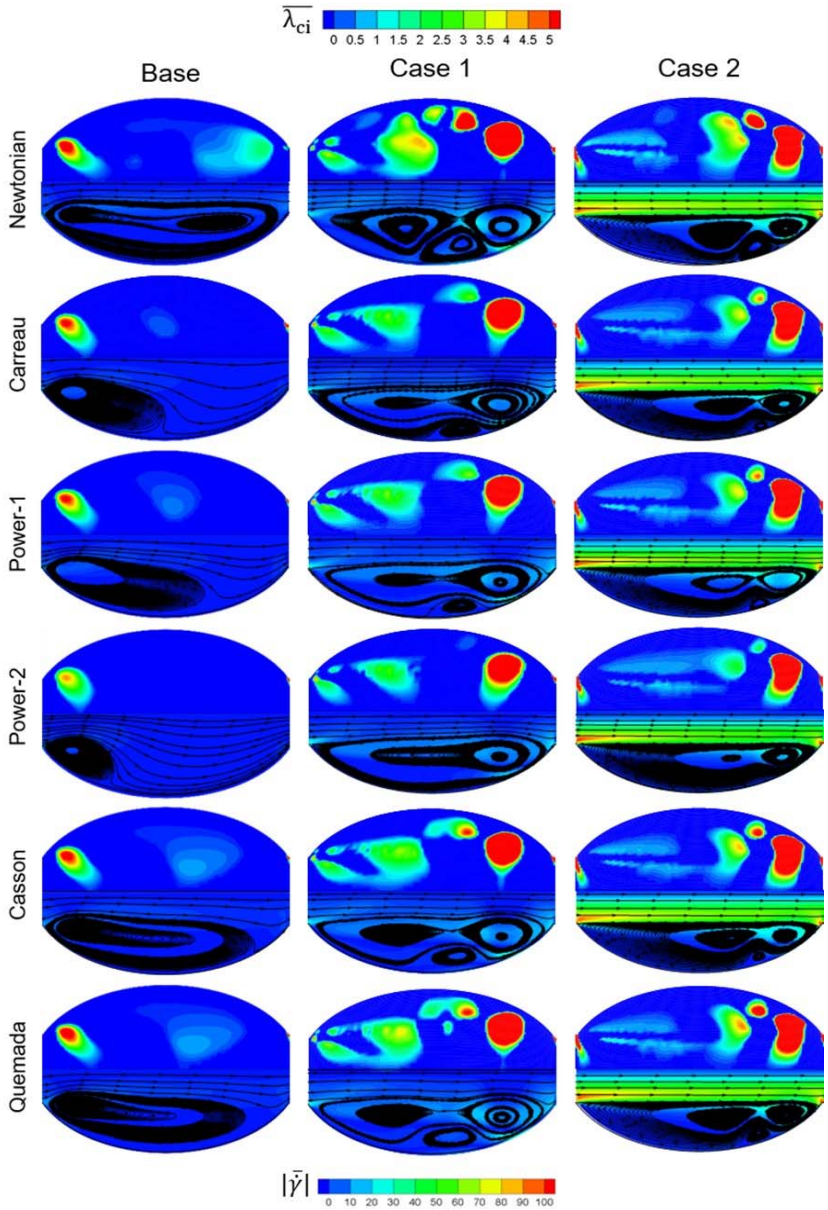

Figure 8. Comparison of time-averaged streamline patterns, $\overline{\lambda_{ci}}$ (upper parts) and $|\bar{\dot{\gamma}}|$ contours (bottom parts) of selected rheology models

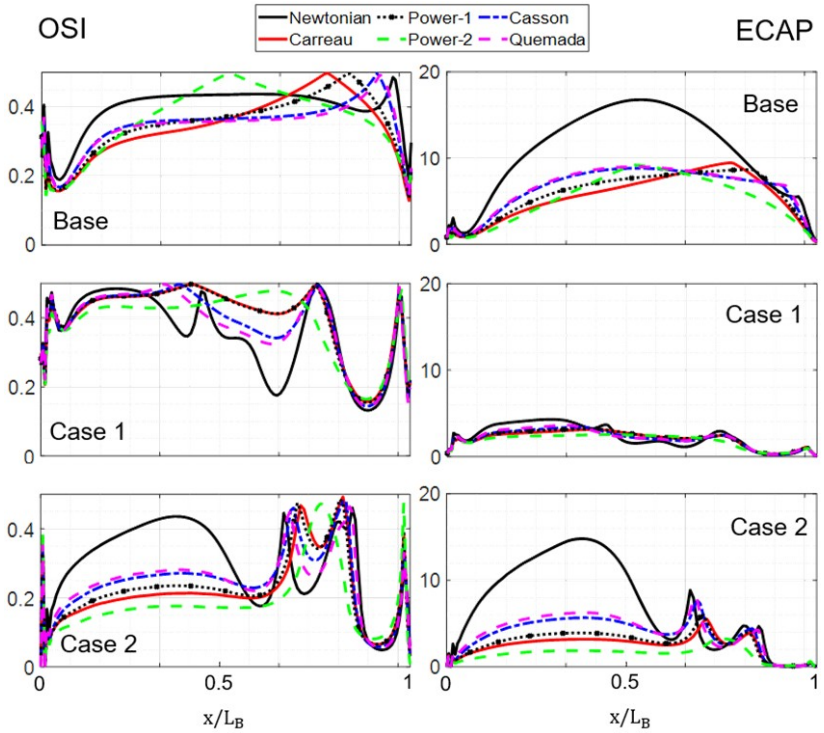

Figure 9. Comparison of OSI and ECAP distribution on the aneurysm wall of selected rheology models.

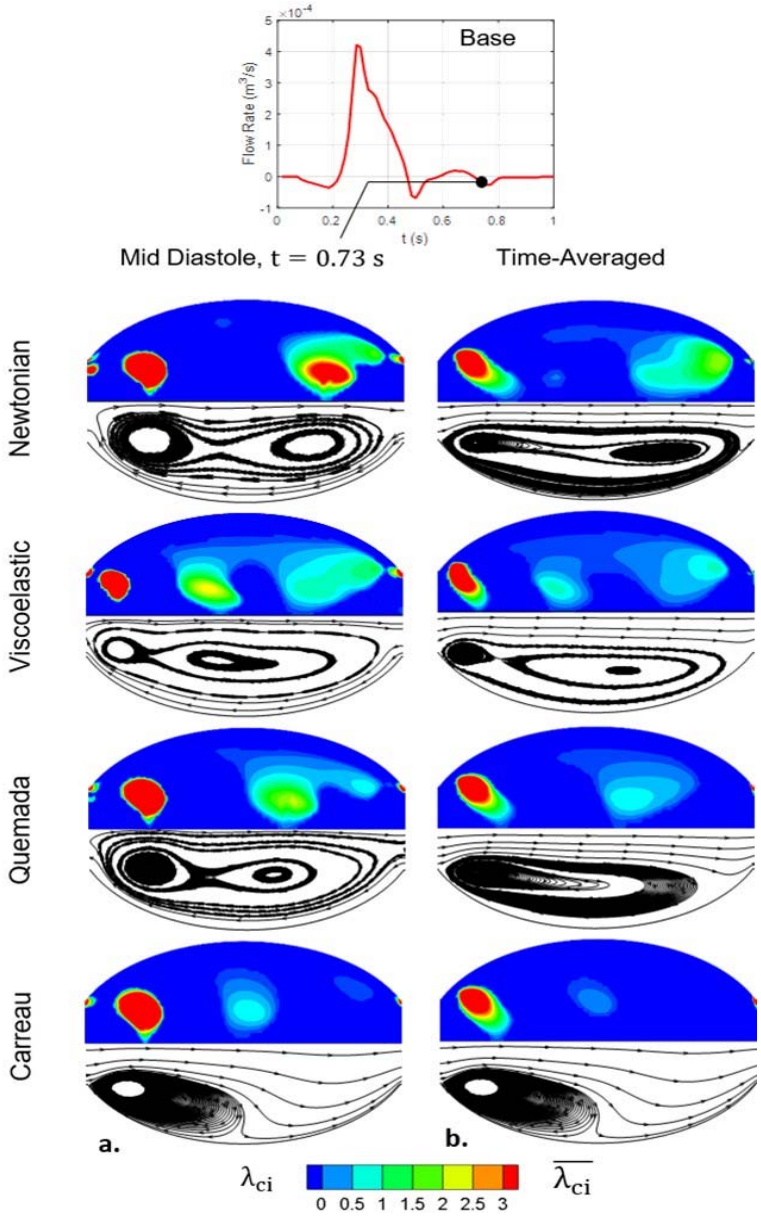

Figure 10. Comparison of a. λ_{ci} contours and instantaneous streamline patterns at t = 0.73 sec, b. $\overline{\lambda_{ci}}$ contours and time-averaged streamline patterns of selected models for the Base case.

Compared to other models, the size of primary vortex obtained by the Viscoelastic model is smaller and it is located in closer proximity to the inlet of the bulge. From the streamlines and contours of λ_{ci}, a second primary vortex is observed for the Newtonian, Viscoelastic and Quemada models, but the core locations are different. The core of the second primary vortex of the Newtonian model is located near to the distal region, while it is located at the central zone for the Viscoelastic and Quemada models. In Fig. 10b, the time-averaged streamline patterns are presented. Location of the time-averaged primary and second primary vortex cores and $\overline{\lambda_{ci}}$ contours obtained by the Viscoelastic model are more similar to the Newtonian model, compared to the Carreau and Quemada models. Aforementioned shear-thinning models do not predict a time-averaged second primary vortex.

DISCUSSION

The current study investigates the impact of infrarenal flow waveform (IFW) patterns on AAA hemodynamics and the behavior of the Newtonian, viscous shear-thinning and viscoelastic rheology models. For that purpose, three IFW patterns, Base, Case 1 and 2, are implemented in a simplified AAA model as the inlet boundary conditions. In comparison to the baseline represented by the Base case, Cases 1 and 2 are specifically designed to assess the impact of increased peak systolic and diastolic flow rates, respectively. Fig. 6 and Supplementary Video-1 clearly demonstrate that the IFW pattern exerts a significant influence on both the vortex structure and WSS descriptors. The primary vortex of the Base case cannot reach the distal region, while its transportation to the distal site is completed by the end of the systolic phase at $t = 0.5T$. On the other hand, the vortex transport for Case 1 persists until the end of one full cardiac cycle, $t = T$, with no fixed settling zone for an extended period. This prolongs the oscillatory nature of the flow pattern, resulting in elevated OSI values. Throughout the bulge, the magnitude of OSI for Case 1 is greater than that for the other waveforms, which might be related to vortex transport. Moreover, regions with large $|\overline{\lambda_{ci}}|$ values exhibit nearly zero OSI, ECAP and RRT values. Hence, both the strength of the vortex and its transportation mechanism (VTM) influence the distribution and magnitude of WSS descriptors.

Fig. 7 reveals that the shear-thinning rheology model is as effective for determining AAA hemodynamics as is the case for IFW patterns. The Newtonian model tends to overestimate the WSS peak, intensity, and magnitude of swirling strength of the

vortex patterns, compared to those of all shear-thinning models. Although instantaneous WSS distributions, and λ_{ci} and $\overline{\lambda_{ci}}$ contours agree that the Newtonian model is applicable for the regions with $|\dot{\gamma}| > 50\ s^{-1}$, in Fig. 9, there are significant differences in OSI and ECAP distributions between the Newtonian and shear-thinning models, especially for Case 2, which has the highest mean flow rate. Supplementary Video-2 presents the temporal evolution of $|\dot{\gamma}|$ distribution inside the bulge for all three waveforms. Together with the vortex structure, a larger $|\dot{\gamma}|$ region is also transported through the bulge. Although Case 1 could not obtain a large $|\dot{\gamma}|$ through the aneurysm, the transport of vortex pattern is slow, eliminating the long stagnation at specified sections inside the bulge. However, for Case 2, the transport of vortex pattern is accomplished within a very short time, leading to a highly stagnant flow structure at the proximal and central regions. In those highly stagnant regions, the Newtonian predicts an OSI_{max} twice as large as that predicted by the Carreau and Power models, along with an $ECAP_{max}$ that is 5 times greater. Therefore, within the aneurysm bulge, in addition to $|\dot{\gamma}|$ distribution, the vortex transport mechanism (VTM) is also an important factor to consider when selecting a rheology model.

For the shear-thinning models, the Casson and Quemada models are closer to the Newtonian model than the Carreau and Power models for $|\dot{\gamma}| < 100\ s^{-1}$, and they exhibit diverging behavior from the Newtonian model at high $|\dot{\gamma}|$, which is not expected. However, according to Fig. 10, the difference between the viscoelastic and Newtonian models is relatively small compared to that between the shear-thinning models even at low $|\bar{\dot{\gamma}}|$, which is consistent with the findings of (Bodnár et al., 2011).

CONCLUSIONS

The study yields the following conclusions:

- The IFW pattern has a significant impact on VTM,
- The strength of the vortices and their transportation mechanism (VTM) both influence the distribution and magnitude of the TAWSS, OSI, ECAP, and RRT,
- The vortex transport mechanism (VTM) is also an important factor to consider when selecting a rheology model because high $|\dot{\gamma}|$ region is also transported with VTM,
- The effect of elastic behavior is relatively minor compared to the effect of viscous shear-thinning behavior,
- Even at high flow rates, the Newtonian model is not appropriate for modeling AAA hemodynamics. Rather than the Newtonian model, the Carreau and Power models, together with proper patient-specific constants, are more stable than Casson and Quemada, and recommended (Saqr et al., 2020).

This study, as a comparative parametric analysis, is subject to several limitations that could influence the obtained results. The idealization of aneurysm bulge rather than utilizing patient-specific geometry may lead to inadequate simulation of the exact aneurysm hemodynamics, together with omitting the wall compliance and Windkessel boundary conditions. Therefore, future studies will aim to incorporate patient-specific geometries with elastic walls, Windkessel boundary conditions, along with implementing the Oldroyd-B model for high Reynolds number. Finally, VTM can be observed by applying a turbulence model such as LES.

REFERENCES

Arzani, A. (2016). Hemodynamics and transport in patient-specific abdominal aortic aneurysms (Doctoral dissertation, University of California, Berkeley).

Arzani, A. (2018). Accounting for residence-time in blood rheology models: Do we really need non-Newtonian blood flow modelling in large arteries? Journal of the Royal Society Interface, 15(146). https://doi.org/10.1098/rsif.2018.0486

Arzani, A., & Shadden, S. C. (2016). Characterizations and correlations of wall shear stress in aneurysmal flow. Journal of Biomechanical Engineering, 138(1). https://doi.org/10.1115/1.4032056

Bessonov, N., Simakov, A. S. S., Vassilevskii, Y., & Volpert, V. (2016). Methods of blood flow modelling. Mathematical Modelling of Natural Phenomena, 11(1), 1–25. https://doi.org/10.1051/mmnp/201611101

Biasetti, J., Hussain, F., & Gasser, T. C. (2011). Blood flow and coherent vortices in the normal and aneurysmatic aortas: A fluid dynamical approach to intraluminal thrombus formation. Journal of the Royal Society Interface, 8(63), 1449–1461. https://doi.org/10.1098/rsif.2011.0041

Bilgi, C., & Atalik, K. (2019). Numerical investigation of the effects of blood rheology and wall elasticity in abdominal aortic aneurysm under pulsatile flow conditions. Biorheology, 56(1), 51–71. https://doi.org/10.3233/BIR-180202

Bilgi, C., & Atalık, K. (2020). Effects of blood viscoelasticity on pulsatile hemodynamics in arterial aneurysms. Journal of Non-Newtonian Fluid Mechanics, 279, Article 104263. https://doi.org/10.1016/j.jnnfm.2020.104263

Bodnár, T., Sequeira, A., & Prosi, M. (2011). On the shear-thinning and viscoelastic effects of blood flow under various flow rates. Applied Mathematics and Computation, 217(11), 5055–5067. https://doi.org/10.1016/j.amc.2010.07.054

Brewster, D. C., Cronenwett, J. L., Hallett, J. W., Johnston, K. W., Krupski, W. C., & Matsumura, J. S. (2003). Guidelines for the treatment of abdominal aortic aneurysms: Report of a subcommittee of the Joint Council of the American Association for Vascular Surgery and Society for Vascular Surgery. Journal of Vascular Surgery, 37(5), 1106–1117. https://doi.org/10.1067/mva.2003.363

Chen, Q., Zhong, Q., Qi, M., & Wang, X. (2015). Comparison of vortex identification criteria for planar velocity fields in wall turbulence. Physics of Fluids, 27(8). https://doi.org/10.1063/1.4927647

Cho, Y. I., & Kensey, K. R. (1991). Effects of the non-Newtonian viscosity of blood on flows in a diseased arterial vessel. Part 1: Steady flows. Biorheology, 28(3–4), 241–262. https://doi.org/10.3233/BIR-1991-283-415

Deplano, V., Guivier-Curien, C., & Bertrand, E. (2016). 3D analysis of vortical structures in an abdominal aortic aneurysm by stereoscopic PIV. Experiments in Fluids, 57(11), 167. https://doi.org/10.1007/s00348-016-2263-0

Egelhoff, C. J., Budwig, R. S., Elger, D. F., Khraishi, T. A., & Johansen, K. H. (1999). Model studies of the flow in abdominal aortic aneurysms during resting and exercise conditions. Journal of Biomechanics, 32(12), 1319–1329. https://doi.org/10.1016/S0021-9290(99)00134-7

Elhanafy, A., Guaily, A., & Elsaid, A. (2019). Numerical simulation of Oldroyd-B fluid with application to hemodynamics. Advances in Mechanical Engineering, 11(5), 1–7. https://doi.org/10.1177/1687814019852844

Epps, B. P. (2017). Review of vortex identification methods. AIAA SciTech Forum - 55th AIAA Aerospace Sciences Meeting, 1–22. https://doi.org/10.2514/6.2017-0989

Faraji, A., Sahebi, M., & Salavati Dezfouli, S. (2022). Numerical investigation of different viscosity models on pulsatile blood flow of thoracic aortic aneurysm (TAA) in a patient-specific model. Computer Methods in Biomechanics and Biomedical Engineering, 0(0), 1–13. https://doi.org/10.1080/10255842.2022.2102423

Favero, J. L., Secchi, A. R., Cardozo, N. S. M., & Jasak, H. (2010). Viscoelastic flow analysis using the software OpenFOAM and differential constitutive equations. Journal of Non-Newtonian Fluid Mechanics, 165(23–24), 1625–1636. https://doi.org/10.1016/j.jnnfm.2010.08.010

Finol, E. A., & Amon, C. H. (2001). Blood flow in abdominal aortic aneurysms: Pulsatile flow hemodynamics. Journal of Biomechanical Engineering, 123(5), 474–484. https://doi.org/10.1115/1.1395573

Fisher, C., & Rossmann, J. S. (2009). Effect of non-Newtonian behavior on hemodynamics of cerebral aneurysms. Journal of Biomechanical Engineering, 131(9), 1–9. https://doi.org/10.1115/1.3148470

Fuchs, A., Berg, N., & Prahl Wittberg, L. (2021). Pulsatile aortic blood flow—A critical assessment of boundary conditions. ASME Journal of Medical Diagnostics, 4(1), 011002. https://doi.org/10.1115/1.4048978

Guranov, I., Ćoćić, A., & Lečić, M. (2013). Numerical studies of viscoelastic flow using the software OpenFOAM. Proceedings in Applied Mathematics and Mechanics, 13(1), 591–592. https://doi.org/10.1002/pamm.201310276

Habla, F., Tan, M. W., Haßlberger, J., & Hinrichsen, O. (2014). Numerical simulation of the viscoelastic flow in a three-dimensional lid-driven cavity using the log-conformation reformulation in OpenFOAM. Journal of Non-Newtonian Fluid Mechanics, 212, 47–62. https://doi.org/10.1016/j.jnnfm.2014.08.005

Javidi, M., & Hrymak, A. N. (2015). Numerical simulation of the dip-coating process with wall effects on the coating film thickness. Journal of Coatings Technology and Research, 12(5), 843–853. https://doi.org/10.1007/s11998-015-9699-7

Juster, H. R., Distlbacher, T., & Steinbichler, G. (2014). Viscosity analysis of a polymer-based drug delivery system using open-source CFD methods and high-pressure capillary rheometry. International Polymer Processing, 29(5), 570–578. https://doi.org/10.3139/217.2892

Karimi, S., Dabagh, M., Vasava, P., Dadvar, M., Dabir, B., & Jalali, P. (2014). Effect of rheological models on the hemodynamics within human aorta: CFD study on CT image-based geometry. Journal of Non-Newtonian Fluid Mechanics, 207, 42–52. https://doi.org/10.1016/j.jnnfm.2014.03.007

Lee, S. W., & Steinman, D. A. (2007). On the relative importance of rheology for image-based CFD models of the carotid bifurcation. Journal of Biomechanical Engineering, 129(2), 273–278. https://doi.org/10.1115/1.2540836

Les, A. S., Shadden, S. C., Figueroa, C. A., Park, J. M., Tedesco, M. M., Herfkens, R. J., Dalman, R. L., & Taylor, C. A. (2010). Quantification of hemodynamics in abdominal aortic aneurysms during rest and exercise using magnetic resonance imaging and computational fluid dynamics. Annals of Biomedical Engineering, 38(4), 1288–1313. https://doi.org/10.1007/s10439-010-9949-x

Leuprecht, A., & Perktold, K. (2001). Computer simulation of non-Newtonian effects on blood flow in large arteries. Computer Methods in Biomechanics and Biomedical Engineering, 4(2), 149–163. https://doi.org/10.1080/10255840008908002

Maazioui, S., Kissami, I., Benkhaldoun, F., Maazouz, A., & Ouazar, D. (2021). Concentrated phosphate slurry flow simulations using OpenFOAM. Proceedings of the International Conference on Industrial Engineering and Operations Management, 1843–1852.

Madhavan, S., & Kemmerling, E. M. C. (2018). The effect of inlet and outlet boundary conditions in image-based CFD modeling of aortic flow. Biomedical Engineering Online, 17(1), 1–21. https://doi.org/10.1186/s12938-018-0497-1

McGloughlin, T. M., & Doyle, B. J. (2010). New approaches to abdominal aortic aneurysm rupture risk assessment. Arteriosclerosis, Thrombosis, and Vascular Biology, 30(9), 1687–1694. https://doi.org/10.1161/ATVBAHA.110.204529

Mendieta, J. B., Fontanarosa, D., Wang, J., Paritala, P. K., McGahan, T., Lloyd, T., & Li, Z. (2020). The importance of blood rheology in patient-specific computational fluid dynamics simulation of stenotic carotid arteries. Biomechanics and Modeling in Mechanobiology, 19(5), 1477–1490. https://doi.org/10.1007/s10237-019-01282-7

Morbiducci, U., Gallo, D., Massai, D., Ponzini, R., Deriu, M. A., Antiga, L., Redaelli, A., & Montevecchi, F. M. (2011). On the importance of blood rheology for bulk flow in hemodynamic models of the carotid bifurcation. Journal of Biomechanics, 44(13), 2427–2438. https://doi.org/10.1016/j.jbiomech.2011.06.028

Moyle, K. R., Antaki, J. F., Greenwald, L., Hariharan, P., & Reddy, V. M. (2006). Comparison of inflow boundary conditions for hemodynamic simulations in idealized and anatomically realistic models of the aorta. Journal of Biomechanical Engineering, 128(5), 745–749. https://doi.org/10.1115/1.2187035

Mutlu, O., Salman, H. E., Al-Thani, H., El-Menyar, A., Qidwai, U. A., & Yalcin, H. C. (2023). How does hemodynamics affect rupture tissue mechanics in abdominal aortic aneurysm: Focus on wall shear stress derived parameters, time-averaged wall shear stress, oscillatory shear index, endothelial cell activation potential, and relative residence time. Computers in Biology and Medicine, 154. https://doi.org/10.1016/j.compbiomed.2023.106609

Ohtaroglu, O. (2020). Experimental investigation of physiological flow in abdominal aortic aneurysm (Master's thesis, Middle East Technical University, Ankara, Turkey).

Pinto, S. I. S., & Campos, J. B. L. M. (2016). Numerical study of wall shear stress-based descriptors in the human left coronary artery. Computer Methods in Biomechanics and Biomedical Engineering, 19(13), 1443–1455. https://doi.org/10.1080/10255842.2016.1149575

Qiu, Y., Yuan, D., Wen, J., Fan, Y., & Zheng, T. (2018). Numerical identification of the rupture locations in patient-specific abdominal aortic aneurysms using hemodynamic parameters. Computer Methods in Biomechanics and Biomedical Engineering, 21(1), 1–12. https://doi.org/10.1080/10255842.2017.1410796

Quemada, D. (1978). Rheology of concentrated disperse systems. Rheologica Acta, 653, 643–653.

Ramazanli, B., Yavuz, M. M., & Sert, C. (2023). Effect of inlet velocity profile and entrance length on abdominal aortic aneurysm hemodynamics simulations. Journal of Thermal Science and Technology, 43(2), 159–174. https://doi.org/10.47480/isibted.1391391

Razavi, A., Shirani, E., & Sadeghi, M. R. (2011). Numerical simulation of blood pulsatile flow in a stenosed carotid artery using different rheological models. Journal of Biomechanics, 44(11), 2021–2030. https://doi.org/10.1016/j.jbiomech.2011.04.023

Reza, M. M. S., & Arzani, A. (2019). A critical comparison of different residence time measures in aneurysms. Journal of Biomechanics, 88, 122–129. https://doi.org/10.1016/j.jbiomech.2019.03.028

Saha, S. C., Francis, I., Saha, G., Huang, X., & Molla, M. M. (2024). Hemodynamic Insights into Abdominal Aortic Aneurysms: Bridging the Knowledge Gap for Improved Patient Care. Fluids, 9(2), 50. https://doi.org/10.3390/fluids9020050

Salman, H. E., Ramazanli, B., Yavuz, M. M., & Yalcin, H. C. (2019). Biomechanical investigation of disturbed hemodynamics-induced tissue degeneration in abdominal aortic aneurysms using computational and experimental techniques. Frontiers in Bioengineering and Biotechnology, 7, Article 111. https://doi.org/10.3389/fbioe.2019.00111

Saqr, K. M., Rashad, S., Tupin, S., Niizuma, K., Hassan, T., Tominaga, T., & Ohta, M. (2020). What does computational fluid dynamics tell us about intracranial aneurysms? A meta-analysis and critical review. Journal of Cerebral Blood Flow & Metabolism, 40(5), 1021–1039. https://doi.org/10.1177/0271678X19854640

Scotti, C. M., Jimenez, J., Muluk, S. C., & Finol, E. A. (2008). Wall stress and flow dynamics in abdominal aortic aneurysms: Finite element analysis vs. fluid-structure interaction. Computer Methods in Biomechanics and Biomedical Engineering, 11(3), 301–322. https://doi.org/10.1080/10255840701827412

Soudah, E., Loong, E. Y. K., Bordone, T. H., Pua, M., & Narayanan, S. (2013). CFD modelling of abdominal aortic aneurysm on hemodynamic loads using a realistic geometry with CT. Computational and Mathematical Methods in Medicine, 2013, Article 472564. https://doi.org/10.1155/2013/472564

Soulis, J. V., Giannoglou, G. D., Chatzizisis, Y. S., Seralidou, K. V., Parcharidis, G. E., & Louridas, G. E. (2008). Non-Newtonian models for molecular viscosity and wall shear stress in a 3D reconstructed human left coronary artery. Medical Engineering & Physics, 30(1), 9–19. https://doi.org/10.1016/j.medengphy.2007.02.001

Stamatopoulos, C., Papaharilaou, Y., Mathioulakis, D. S., & Katsamouris, A. (2010). Steady and unsteady flow within an axisymmetric tube dilatation. Experimental Thermal and Fluid Science, 34(7), 915–927. https://doi.org/10.1016/j.expthermflusci.2010.02.008

Stergiou, Y. G., Athanasios, G. K., Aikaterini, A. M., & Spiros, V. P. (2019). Fluid-Structure Interaction in Abdominal Aortic Aneurysms: Effect of Haematocrit. Fluids, 4(1), 11. https://doi.org/10.3390/fluids4010011

Suh, G.-Y., Les, A. S., Tenforde, A. S., Shadden, S. C., Spilker, R. L., Yeung, J. J., Cheng, C. P., Herfkens, R. J., Dalman, R. L., & Taylor, C. A. (2011). Hemodynamic Changes Quantified in Abdominal Aortic Aneurysms with Increasing Exercise Intensity Using MR Exercise Imaging and Image-Based Computational Fluid Dynamics. Annals of Biomedical Engineering, 39(2), 864–883. https://doi.org/10.1007/s10439-011-0313-6

Wei, Z. A., Huddleston, C., Trusty, P. M., Singh-Gryzbon, S., Fogel, M. A., Veneziani, A., & Yoganathan, A. P. (2019). Analysis of inlet velocity profiles in numerical assessment of Fontan hemodynamics. Annals of Biomedical Engineering, 47(11), 2258–2270. https://doi.org/10.1007/s10439-019-02307-z

Weller, H. G., Tabor, G., Jasak, H., & Fureby, C. (1998). A tensorial approach to computational continuum mechanics using object-oriented techniques. Computers in Physics, 12(6), 620. https://doi.org/10.1063/1.168744

Womersley, J. R. (1955). Method for the calculation of velocity, rate of flow, and viscous drag in arteries when the pressure gradient is known. The Journal of Physiology, 127(3), 553–563. https://doi.org/10.1113/jphysiol.1955.sp005276

Zheng, E. Z., Rudman, M., Singh, J., & Kuang, S. B. (2019). Direct numerical simulation of turbulent non-Newtonian flow using OpenFOAM. Applied Mathematical Modelling, 72, 50–67. https://doi.org/10.1016/j.apm.2019.03.003

Journal Homepage: https://dergipark.org.tr/tr/pub/isibted

Isı Bilimi ve Tekniği Dergisi

Archive: https://tibtd.org.tr/dergi

A systematic approach to numerical analysis and validation for industrial oven design and optimization

Serdar ŞAHİN [1]

[1] *Çukurova University, Mechanical Engineering Department, Adana, Türkiye*

A R T I C L E I N F O

2025, vol. 45, no.1, pp. 36-46

doi: 10.47480/isibted.1505298

Research Article
Received: 27 June 2024
Accepted: 26 October 2024

* *Corresponding Author*
e-mail: serdarsa@gmail.com

Keywords:
Taguchi DOE
Design of experiments
Orthogonal arrays
Computational fluid dynamics (CFD)
Optimization

ORCID Numbers in author order:
0000-0002-6451-3329

A B S T R A C T

The findings of this research not only provide valuable insights into industrial oven design but also demonstrate the broader importance of adopting systematic approaches and incorporating numerical analysis techniques to achieve clean energy goals. By leveraging such approaches across various industrial sectors, we can pave the way for a greener future, where energy efficiency, environmental sustainability, and economic growth can harmoniously coexist. In today's rapidly evolving world, where the need for sustainable practices and clean energy solutions is more critical than ever, research plays a pivotal role in driving innovation and addressing environmental challenges. The study presented in this article aligns with this overarching goal by focusing on the optimization of industrial oven design, aiming to achieve energy efficiency and high-quality product outcomes. Efficient oven design and optimization hold significant implications for energy conservation, reducing greenhouse gas emissions, and minimizing environmental footprints. By precisely controlling heat distribution and velocity within industrial ovens, such as the one investigated in this study, resource consumption can be minimized, resulting in reduced energy usage and improved operational efficiency. Moreover, the enhanced uniformity in temperature and airflow distribution ensures optimal product quality, reducing waste and promoting sustainable production practices. A systematic approach to numerical analysis and validation for industrial oven design and optimization is developed. Computational fluid dynamics (CFD) and the Taguchi design of experiment methods were employed to determine the influential design variables. The 3D CFD model was then compared with experimental results to validate its accuracy. An experimental oven design was developed based on optimal signal-to-noise (S/N) ratios, and the numerical findings were corroborated through experimental measurements, demonstrating a strong agreement. The proposed approach, encompassing the design, manufacturing, and analysis stages, can be applied to diverse industrial oven designs. Using the Taguchi method, the optimal configuration for the industrial oven was determined with the following parameters: four fans (A), spaced 240 mm apart (B), and positioned at a height of 250 mm (C). This configuration was found to provide the best balance of airflow distribution and heat transfer, ensuring uniform cooking throughout the chamber.

Endüstriyel fırın tasarımı ve optimizasyonuna yönelik sayısal analiz ve doğrulamaya sistematik bir yaklaşım

M A K A L E B İ L G İ S İ

Anahtar Kelimeler:
Taguchi DOE
Deney tasarımı
Ortogonal diziler
Hesaplamalı akışkanlar dinamiği (HAD)
Optimizasyon

Ö Z E T

Bu araştırmanın bulguları yalnızca endüstriyel fırın tasarımına dair değerli bilgiler sağlamakla kalmıyor, aynı zamanda temiz enerji hedeflerine ulaşmak için sistematik yaklaşımları benimsemenin ve sayısal analiz tekniklerini birleştirmenin büyük önemini de gösteriyor. Çeşitli endüstriyel sektörlerde bu tür yaklaşımlardan yararlanarak enerji verimliliğinin, çevresel sürdürülebilirliğin ve ekonomik büyümenin uyumlu bir şekilde bir arada var olabileceği daha yeşil bir geleceğin yolu açılabilir. Verimli fırın tasarımı ve en iyileştirilmesi, enerji tasarrufu, sera gazı emisyonlarının azaltılması ve çevresel ayak izlerinin en aza indirilmesi gibi önemli etkilere sahiptir. Bu çalışmada endüstriyel fırın tasarımı ve en iyileştirilmesine yönelik sayısal analiz ve doğrulamaya yönelik sistematik bir yaklaşım geliştirilmiştir. Etkili tasarım değişkenlerini belirlemek için hesaplamalı akışkanlar dinamiği (HAD) ve Taguchi deney tasarım yöntemleri kullanılmıştır. 3 boyutlu HAD modellerinden çıkan sonuçlara bağlı olarak, sinyal-gürültü (S/N) oranları belirlenmiş, en yüksek verimlilik için, tasarım değişkenlerinin değerleri tespit edilmiş ve bu değerlere bağlı olarak deneysel bir fırın tasarımı geliştirilmiştir. HAD analizlerinden elde edilen sayısal değerler ile deneysel ölçümlerden elde edilen değerler arasında güçlü bir uyum görülmüştür. Tasarım, üretim ve analiz aşamalarını kapsayan önerilen yaklaşım, çeşitli endüstriyel fırın tasarımlarına uygulanabilir. Taguchi yöntemi kullanılarak, endüstriyel fırın için optimum yapılandırma aşağıdaki parametrelerle belirlendi: dört fan (A), 240 mm aralıklı (B) ve 250 mm yükseklikte konumlandırılmış (C). Bu yapılandırmanın, hava akışı dağılımı ve ısı transferi arasında en iyi dengeyi sağlayarak, hazne boyunca düzgün pişirme sağladığı bulundu.

INTRODUCTION

The aim of the design process is to address future customer demands. To achieve this, design offices should follow five key steps: identifying needs, defining requirements, conducting background research, developing solutions, and continuously improving solutions based on testing. In a world of rising energy costs and increased competition, there is a growing demand for multifunctional and modular designs that offer lower energy consumption. Furthermore, intense competition and rapidly changing market conditions require design offices and manufacturers to restructure their processes to deliver products to end-users faster and more reliably. This shift is also essential for industrial ovens operating at high capacities. Companies that align their design processes with this approach will gain a competitive advantage. In recent years, numerical simulations have been increasingly utilized to streamline the preliminary design, development, and testing processes of products. By reducing the number of required tests and prototypes, these simulations help to minimize costs. Numerous researchers have conducted studies on similar topics, highlighting the significance of this approach.

Norton and Sun reviewed the studies of using CFD as an effective design and analysis tool in the food industry (Norton & Da-WenSun, 2006). Boulet et al. modeled the transient heat transfer in a baking oven using Fluent (Boulet et al., 2010). Their model showed good agreement with the experiments and revealed the contribution of wall temperatures of the chamber. They did not take moisture into account. They used the reliable k-epsilon turbulence model. Kokolj et.al. studied different fan covers for a forced convection oven and presented a validation of numerical methodology. Uniformity between browning and temperature distribution is chosen as the assessment point. Their simulations were 3D time-dependent with both convective and radiative heat transfer mechanisms and also include an evaporation model for the baking process. They developed and validated a CFD model to predict the baking performance and grade of browning of a forced convection oven (Kokolj et al., 2017). Rek et.al. used CFD as a design tool for a new-generation cooking appliance. They created different discrete models and analyzed the influence of geometry boundary condition changes (Rek et al., 2012). They validated the result with measurements taken from an oven prototype. Fahey et.al. studied the flow through the door of a pyrolytic oven. They made a steady-state 2D numeric analysis using ANSYS CFX and compared the velocity and temperature results on specific points. They used hot-wire anemometry for velocity measurements and thermocouples attached with aluminum tapes and found all CFD results agree within %3 of the experimental results (Fahey et al., 2008). Smolka et.al. present CFD analysis and experimental analysis of the flow and heat transfer mechanism in a natural convection oven. They used extensive thermocouple arrays and PIV for verifying the temperature distribution and the velocity distribution (Smolka et al., 2013). Morales et.al. defined a linear programming problem and modeled the brick oven's combustion process to determine the burner's optimal location (Vizguerra-Morales et al., 2016). Tank et.al. developed a CFD model to study temperature profiles during the baking process for partially and fully loaded ovens (Tank et al., 2014). Yi et al developed a CFD model for simulating the thermal transfer efficiency of an existing hot air continuous convection oven. To increase the line speed, they investigated the effect of the velocity of airflow and temperature (Yia et al., 2017). Stojanovic and his colleagues examined the tribological behavior of an aluminum-based hybrid composite material using the Taguchi method and determined the factor that most affects the wear rate by examining it with the ANOVA method (Stojanović et al., 2015). Ünver and Küçük made an efficiency comparison for plate heat exchangers using the Taguchi method and CFD, and found that the most effective variables were duct height and air flow rate (Ünverdi & Küçük, 2019). Biçer and his colleagues proposed a new and innovative baffle design in shell-tube heat exchangers, using the CFD and Taguchi methods, to significantly reduce the shell-side pressure loss without losing thermal efficiency, and achieved a 49% reduction in the shell-side pressure drop compared to the traditional structure (Biçer et al., 2020). Tambolkar and his colleagues performed filter design optimization using CFD-Separated Phase Modeling and Taguchi approach to maximize filtration efficiency and increase the reusability of the liquid by changing the input parameters (Tambolkar et al., 2020). Obidowski et al. used the response surface method combined with genetic algorithm to develop an effective approach to the problem of geometry optimization of a non-axisymmetric flow channel (Obidowski et al., 2021). Amadene and his colleagues used a 3-level, 3-variable Taguchi approach and CFD simulations to optimize the variables affecting fuel cell efficiency (Amadane et al.). Chandra and his colleagues used CFD simulation and Taguchi experimental design method to optimize the natural ventilation of indoor spaces (Chandra et al., 2022). Aydin et al. designed and optimized a multi-compartment heat exchanger on the basis of lowest cost, using an optimization method he developed (Aydın et al., 2022). Yüce and his colleagues used Taguchi, ANOVA and GRA experimental methods and CFD simulations to optimize ventilation efficiency in buildings (Yuce et al., 2022). İç and Yıldırım used the Taguchi approach to determine the levels of factors that optimize the product quality of a washing machine (İç & Yıldırım, 2012). Özer et al. carried out CFD analysis of the squeezing phase of a washing machine and showed its compatibility with experimental results (Özer et al., 2016). Demir and Aküner determined the variables affecting the in-wheel asynchronous motor efficiency with the Taguchi approach and designed the experiment, and then determined the variable levels according to the experimental results using the ANSYS RMXprt program (Demir & Aküner, 2018). Türkan, on the other hand, carried out the experiments he designed using the Taguchi experimental design method for vehicle cooler optimization with CFD simulations and determined the levels of the variables that gave the best efficiency value (Türkan, 2024). Kahraman and Sugozu used Taguchi method to optimize the design parameters of brake pad (Kahraman & Sugözü, 2019). Shimpy et al. used Response Surface Methodology and CFD to design a domestic solar dryer. They defined design variables and created a design of experiment array. They used COMSOL software for experiment runs (Shimpy et al., 2024).

This study focuses on optimizing the internal velocity and heat distribution in an industrial belt oven with forced convection, utilizing the Taguchi design method developed by Dr. Genichi Taguchi. The objective is to meet the demands for low operating costs and low product prices by enhancing the homogeneity of internal air and heat distribution in the oven. By achieving improved product quality and reducing operating

and manufacturing costs, the study aims to optimize the oven's performance. The modeling of in-oven airflow is conducted using a three-dimensional cooking volume, employing computational fluid dynamics (CFD) with the Ansys CFX commercial software. The conservation equations for mass, momentum, and energy are solved using the finite volume method for incompressible flow. The design variables considered are the number of fans, the distance between fans, and distance from fans to the belt surface. Evaluation criteria include belt surface temperature, heat gradient deviation, and belt surface velocity deviation, each with three different levels. To validate the accuracy of the CFD analysis, an experimental oven design is created based on optimal signal-to-noise (S/N) ratios. The study parameterizes different geometries and determines their impact on air distribution. The findings of the numerical model are corroborated through experimental measurements, demonstrating a strong agreement. This comprehensive study fills a gap in the literature by providing a detailed experimental investigation of forced convection in a continuous-feed belt oven. The combination of CFD simulations and the Taguchi design method offers a systematic approach to optimizing industrial oven performance. The proposed approach, encompassing design, manufacturing, and analysis stages, can be applied to a wide range of industrial oven designs.

METHOD

In this research, a comprehensive design methodology comprising several steps has been developed to address the project's objectives. The initial stage involves formulating a preliminary design based on specific customer requirements, followed by the identification of potential variables and their respective levels. To efficiently manage the experimentation and analyses, orthogonal variable level strings are constructed using an experimental design approach, effectively reducing the number of required tests. These identified variable level strings are then utilized to create the necessary geometry through CAD software, which is subsequently imported into mesh software for mesh generation.

The next crucial step entails performing numerical modeling within a specialized CFD software. This involves establishing a robust mathematical model, defining material properties, and setting boundary conditions to accurately simulate the system under investigation. The CFD results are meticulously evaluated using the experimental design approach, leading to the determination of optimal parameter values.

Furthermore, a physical prototype is manufactured based on the identified optimal variable values, and its performance is compared to the results obtained from the CFD analysis conducted with the same optimal variable values. Should the observed differences between the physical prototype and the CFD analysis be justifiable and fall within acceptable levels, the design and its corresponding variable levels are accepted, paving the way for the commencement of the detailed design process. Conversely, if the differences prove unacceptable or unexplainable, the project undergoes a thorough reevaluation, necessitating a return to the preliminary design phase to rectify any discrepancies.

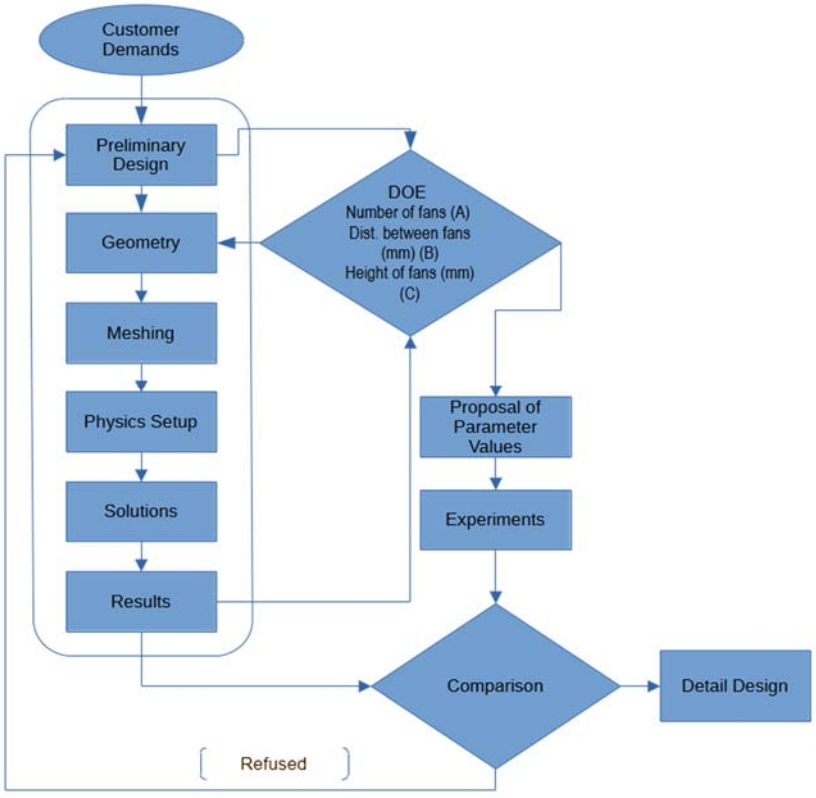

Fig.1 Methodology

The Intended Oven Geometry and Operation of the Device

When the forced convection industrial ovens are examined, it is seen that the fans with radial geometry are mostly aligned along the direction of travel. Fans can be blown directly over the belt or air can be sucked and redirected through a channel. In such a discrete channel structure, the position of the suction holes and the location of the blow holes in which the air is directed to different regions of the belt is of high importance for the air distribution in the oven and therefore for the optimization of the heat distribution. The heaters can be placed in parallel with the flow direction. The amount of heat needed will be reduced as a result of the optimization of the indoor air distribution.

In the general design stages of the belt oven, the systematic steps of conformity were followed. The design has been realized by taking into consideration the ease of installation and manufacturing, based on the use of modular, common parts. In the detail design phase, the assembly and manufacturing difficulties encountered during the prototype production were eliminated and visual improvements were made. The dimensions of the main cooking chamber are 1128mm in length, 295mm in width, and 337 mm in height with a porous belt surface located at the height of 100 mm. Fans sucked the air inside the chamber to a discrete channel structure and the air is blown back to the main cooking chamber with blowing holes located at a height of 63mm.

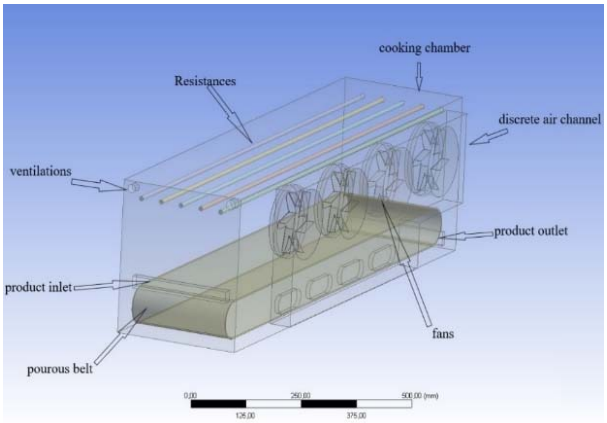

Fig.1 General layout

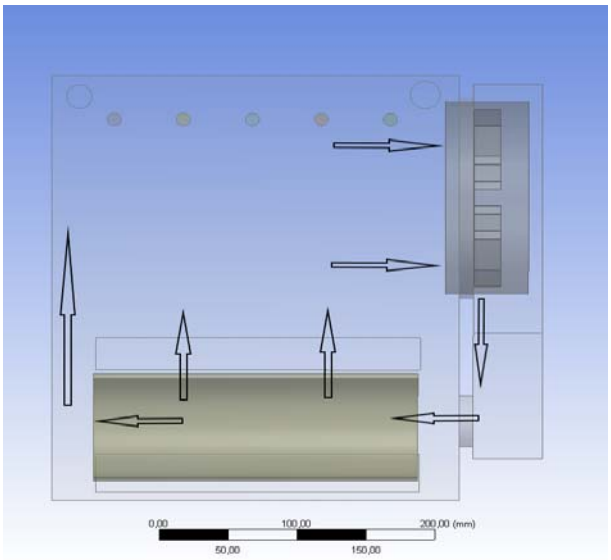

Fig.2 Air circulation

The distance between the suction fans (L_f) is parameterized, which changes between 170 mm to 240 mm with 35mm increments. Also, the vertical location of fans is parameterized, which is changed between 200mm to 250mm with 25 mm increments. The number of fans changed between 2 to 4. Fans are positioned symmetrically on both sides of the oven centerline. Product inlet and product outlet details are excluded from the design because of the complexity. Air circulating hole dimensions and locations were kept constant due to construction issues. A stainless-steel chain belt with a porosity of 0.5 volume fraction is used. Resistances are located under the top side of the oven. Each resistance has a power of 900W. Although the total power of the heaters used in the oven is 4.5kw, only a certain amount of this power will be used to maintain the temperature inside the oven after the set temperature is reached. In Fig.1, the schematic drawing of the proposed oven is given. In Fig.2, a schematic of the proposed air circulation is given.

All sides of the heating chamber were covered with 20 mm glass wool isolation material except the product inlet, the product outlet, and the ventilation openings. The heating chamber was isolated from the main chassis to prevent critical areas such as maintenance doors and electronics from overheating.

Design of Experiments

The most important factor on product quality is minimizing the changes in the conditions on the belt surface where the products start to bake. Therefore, the temperature and velocity standard deviation over the belt surface was determined as the oven's performance criterion. First of all, all the factors affecting the oven performance were revealed by using the fishbone diagram. Based on the fishbone diagram, the factors to be taken as constant and variable during the experiments were decided (Fig. 3). The type and humidity of the grains to be processed are not controllable parameters due to the multifunctionality of the oven. Depending on the user's needs, the operating temperature and fan speed can be changed by the user, so these two parameters are considered fixed. Ambient temperature and ambient humidity are also not controllable variables. For economic reasons, the material variables are assumed to be constant. equipment parameters have been chosen as variables. The Taguchi experimental design method used to define orthogonal arrays containing variables and the different levels of variables to investigate how different variables affect process performance. Instead of testing all variable combinations as in the classical factorial design, combination pairs are tested in the Taguchi method, reducing the number of tests necessary to collect the necessary data to determine the variables that affect the process the most, thus saving time and resources.

Three different factors and three different levels for each factor are given in Table 1. After the experimental parameters and levels were determined, the three-variable, three-level Taguchi orthogonal array, L9(3^3), is created and given in Table 2. While 27 experiments will be conducted with factorial design, only 9 experiments were conducted using Taguchi experimental design.

Table 1 Parameters and levels

Parameters	L1	L2	L3
Number of fans (A)	2	3	4
Dist. between fans (mm) (B)	170	205	240
Height of fans (mm)(C)	200	225	250

Table 2 Taguchi L9 Orthogonal Array

	Taguchi L9 (3^2), P3, L3		
Run	A	B	C
1	2	170	200
2	2	205	225
3	2	240	250
4	3	170	225
5	3	205	250
6	3	240	200
7	4	170	250
8	4	205	200
9	4	240	225

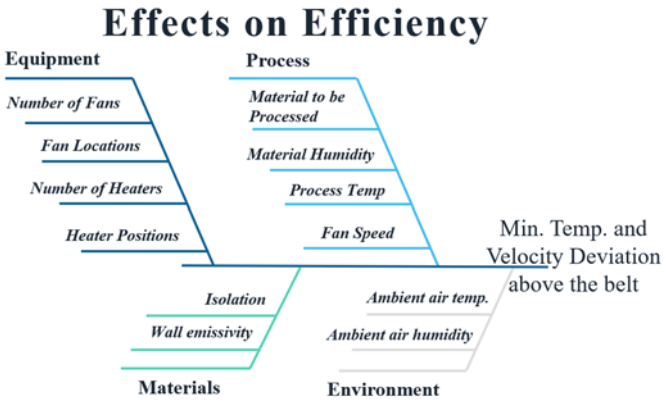

Fig. 3 Fishbone diagram

Numerical Solutions

To analyze a continuous and differential fluid flow, Navier-Stokes equations, which are derived from the laws of conservation of mass (continuity), conservation of energy (first law of thermodynamics), and conservation of momentum (Newton's second law of motion), are used. Conservation of mass is the general law that states that the amount of mass change in a given fixed control volume is equal to the difference between the amount of mass entering and leaving. The law can be formulated for compressible flows in differential form as:

$$\frac{\partial \rho}{\partial t} + \nabla.(\rho V) = 0 \quad (1)$$

And for incompressible flows $\left(\frac{\partial \rho}{\partial t} = 0\right)$, law of continuity will be:

$$\nabla.(V) = 0 \quad (2)$$

Conservation of energy or the first law of thermodynamics simply states that energy can neither be created nor destroyed, it can only be converted from one form to another. In other words, for a fixed control volume, the rate of energy change is equal to the heat addition and work done, total energy remains constant. For the steady state, incompressible flow conservation of energy law will be:

$$\rho c_v \frac{dT}{dt} = k\nabla^2 T + \theta \quad (3)$$

The Law of conservation of momentum or Newton's second law of motion states that the rate of momentum change in a control volume is equal to the sum of the external forces. For the steady state, incompressible flow conservation of momentum law will be:

$$\rho \frac{dV}{dt} = \rho g - \nabla p + \mu \nabla^2 V \quad (4)$$

For the above equations, V is the velocity field, p is the pressure, T is the temperature, k is the thermal conductivity, ρ is the density, g is the gravity, t is the time, μ is the viscosity, Θ is the viscous dissipation function.

The Navier-Stokes equations have no analytical solutions except for very simple flows under ideal conditions. To find solutions in real flows, numerical methods using algebraic approaches must be used. For numerical modeling and solving the conservation equations, ANSYS CFX, a computational fluid dynamics program that uses the finite volume method, was used. ANSYS CFX uses an element-based finite volume method, which first involves discretizing the spatial domain using a mesh. The mesh is used to construct finite volumes, which are used to conserve relevant quantities such as mass, momentum, and energy (Inc A. , 2011). The finite volume method is widely used in fluid dynamics and heat transfer problems (Norton & Da-WenSun, 2006).

All fans are modeled as rotating bodies that had transient rotor-stator interface model boundary conditions in a stationary fluid domain, based on the standard Φ150mm diameter oven fan (Fig.4).

Fig.4 Φ150mm oven fan

Angular velocities of all rotating fan bodies are equal to 2800rpm and constant. Possible rpm changes due to temperature are neglected. All walls have a thermal conductivity value of 0.04W/m.K.

The standard k-epsilon turbulence model is not recommended for flows impinging on surfaces because the turbulence energy may be over-predicted at the stagnation points (Durbin, 1996). SST (shear stress turbulence) method is validated by researchers (Kokolj et al., 2017) (Kokolj et al., 2017) and also used for this analysis. For the heat transfer mechanism Total Energy and for thermal radiation Monte Carlo approaches were used. For more accurate solutions, physical modeling errors and mesh quality must be considered. Ansys CFX uses scalable wall functions to solve the boundary layer profile near-wall regions in turbulent flow with an acceptable computational load. But there is a danger of overestimating the boundary layer so a non-dimensional parameter y+ (YPLUS) is used for quality check. y+ is a non-dimensional variable representing the distance from the wall to the first node away from the wall. As the y+ increase, the wall-type conditions will be imposed further from the wall by scalable wall functions. By definition, y+ is dependent on the size of the mesh near wall regions (Inc., 2011). The upper limit of y+ is a function of the Reynolds number and for large Reynolds numbers as $Re=10^9$, y+ can be around 1000 or more but for typical applications which have lower Reynolds numbers, entire boundary layers might only extend around y+=300 for not overestimations, and not to underestimate the boundary layer, lower bound for y+ will be y+=30. (Inc A. , 2011). As Ansys CFX uses scalable wall functions, no need to worry about the lower limit for y+. The growth rate of the elements was kept low to avoid poor quality cells but as a result of the low growth rate and complex oven geometry. Mesh size range changes due to geometric parameterization. In

Table **3** summary of the settings used in the simulation is given.

Table 3 Summary of settings used in simulations Governing equations

	Total Energy for conduction and convection
	Monte Carlo for thermal radiation
	SST (shear stress turbulence) method for turbulence modeling
Material properties	
	All air properties temperature-dependent
	Thermal conductivity of the wall insulation, 0.04 W/(mK)
	Constant solid material properties
Boundary conditions	
	Product inlet, product outlet, and ventilation holes defined as openings
	External walls, mixed convective and radiative heat flux

The mesh is a hybrid of tetrahedra and hexahedra elements. The maximum element skewness, aspect ratio, and orthogonal quality index values of the elements and their recommended values (Inc A. , 2009) are given in Table 4. Air is defined as an incompressible ideal gas. The thermal conductivity, viscosity, density, and specific heat of air were considered temperature-dependent. All solid material properties were considered fixed. Product inlet, product outlet, and ventilation holes are defined as openings to the atmospheric pressure and ambient room temperature (25 °C). The belt speed is not included in the simulations as it varies according to the product to be processed.

All analyses were performed as transient with a full buoyancy model due to the extreme complexity of the flow and heat transfer mechanisms. The first-time step is 1 s with an adaptive timestep setting and the max number of the time steps is 80. The target max loop number is 5 and the target min loop number is 2. The Total Energy heat transfer model and Monte Carlo thermal radiation model with isotropic scattering model were used. The inflation layer settings for meshing were defined with a transition ratio of 0.77, maximum layers of 5, and a growth rate of 1.2. The smooth transition option was used to ensure a gradual increase in layer thickness, optimizing the boundary layer resolution without a sharp size change in the mesh elements (Fig.5). Grid sensitivity analysis is done for Run1 with 2.5, 3, 3.5 and 4 million elements. And found that for above 3 million elements, belt surface temperatures deviations for intended point is below % 2. For timestep 80, temperature levels stabilized. From these results model concluded as grid independent.

Table 4 Mesh quality parameters

	Model	Recommended
Elm. size range	~3,500.000	
Max.Elm. skewness	0.9481	<0.95
Max. Aspect ratio	34.186	<35/1
Orthogonal quality	0.25	>0.14

A grid sensitivity analysis was conducted to ensure the accuracy and reliability of the CFD results for the industrial oven, specifically focusing on the belt surface temperature at three distinct points (x:0.24, y:0.15; x:0.502, y:0.15; x:0.753, y:0.15) (Table 5). The analysis was performed using four different grid sizes: 2.5, 3, 3.5, and 4 million cells. The belt surface temperatures at the selected points demonstrate that, as the grid resolution increases, the temperature values converge. For instance, at Point 1 (x:0.24, y:0.15), the temperature increases from 204.8°C with a 2.5M grid to 278.7°C with a 3.5M grid, before slightly stabilizing at 272.3°C with a 4M grid. Similar trends are observed at Points 2 and 3, where the temperature values fluctuate initially but show stabilization as the grid resolution increases. These results indicate that the solution becomes grid-independent between 3.5M and 4M cells, confirming that further refinement would not significantly alter the simulation outcomes. Therefore, a grid size of 3.5M cells was selected as a compromise between accuracy and computational efficiency.

Table 5 Grid Sensitivity

	Belt surface temp at point		
	x:0.24 y:0.15	x:0.502 y:0.15	x:0.753 y:0.15
Grid	p1	p2	p3
2.5	204.8	148.1	192.5
3	259.2	153.3	158.0
3.5	278.7	157.5	169.9
4	272.3	164.9	162.3

For each model, it took approximately 8 hours to calculate the mesh structure and numerical simulations. All calculations were made on a workstation with a quad-core 3.80GHz Xeon processor and 32GB of ram.

In the Taguchi method, the signal-to-noise ratio (S/N Ratio) is used to measure the variability between experimental data. Three types of S/N Ratios are defined in the Taguchi method: smaller is the best, nominal is the best, and larger is the best. In this study, the smaller is the best (Eq.(5)) approach was used since it is aimed to have the lowest deviations in the temperature and velocity distribution on the belt surface where the product is treated. CFD models were compared due to belt surface velocity and temperature deviations. Belt surface temperature and velocity deviations transformed into S/N ratios are given in Table 6 . The aim of this study is to minimize the deviations so the S/N ratio is defined as in equation (5).

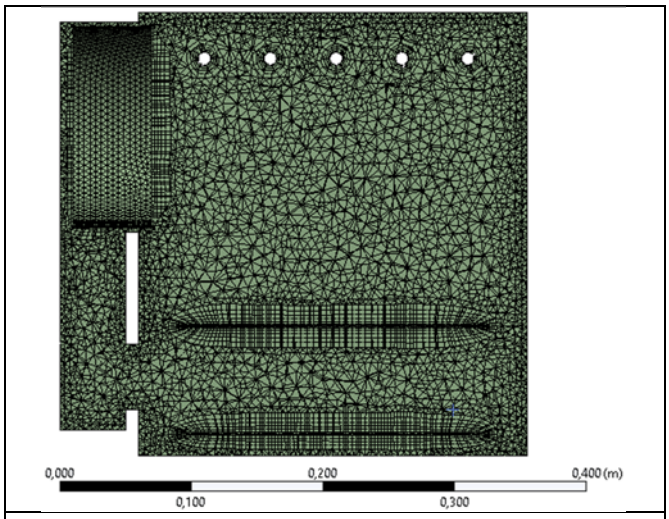

Fig.5 Mesh structure with inflation layers

$$SN_s = -10\log(\frac{1}{n}\sum_{i=1}^{n} y_i^2) \quad (5)$$

Table 6 S/N ratios for Taguchi DOE runs

Run	A	B	C	SNRA-Temp	SNRA-Vel
1	1	1	1	-32.856	-0.172
2	1	2	2	-34.762	0.468
3	1	3	3	-29.971	3.715
4	2	1	2	-33.174	-0.442
5	2	2	3	-32.690	0.250
6	2	3	1	-29.311	-0.649
7	3	1	3	-30.365	4.243
8	3	2	1	-32.826	-2.047
9	3	3	2	-31.716	0.543

Table 7 Response Table of means of SN Ratios for temperature deviations

Level	Mean A-Temp	Mean B-Temp	Mean C-Temp
1	-32.529	-96.395	-94.993
2	-31.725	-100.278	-99.651
3	-31.636	-90.998	-93.026
Delta	0.089	5.397	6.626
Rank	3	2	1

Table 8 Response Table of means of SN Ratios for velocity deviations

Level	Mean A-Vel	Mean B-Vel	Mean C-Vel
1	1.337	3.629	-2.868
2	-0.280	-1.329	0.569
3	0.913	3.608	8.207
Delta	0.424	-0.020	7.638
Rank	2	3	1

In Fig.6 and Fig.7 mean velocity change and mean temperature change are given in the X direction. To find the belt surface average temperature, 100 different point values were taken along the X-axis at the Y=0.05m, Y=0.15m, and Y=0.25m positions. All values were taken 0.01 m above the belt.

The purpose of this study is to provide the most appropriate heat and air speed distribution on the belt surface in order to ensure the continuity of the desired quality in the products to be cooked, in other words, to prevent product burning due to excessive heat formation in any area on the belt or insufficient cooking due to insufficient heat formation. For this, it is desired that the deviations in the belt temperature distributions given in Table 7 and the belt air speed distributions given in Table 8 are low. For the factors examined, the average of the signal-to-noise ratios was calculated and the factors that most affected the deviations in the temperature (Table **7**) and velocity distribution (Table 8) were determined. Regardless of which of the smaller is the best, nominal is the best, and larger is the best approaches are used to evaluate the experimental results, in calculating the S/N ratio, as the value of the calculated S/N ratio gets higher, its effect on the test result increases. For belt surface temperature deviation minimization, with the respect to the criteria smaller is the best, and the best combination of factors is A3B3C3. For belt surface velocity deviation minimization, with the respect to the criteria smaller is the best, and the best combination of factors is A1B1C3.

Variance analyzes of the parameters were performed using the S/N ratios obtained from the experimental results (Table 9, Table 10). In Table 9 and Table 10 Param. is for parameter, DOF is for degree of freedom, SS is for sum of squares, MS is for mean of squares and Cont. is for contribution.

The purpose of analysis of variance is to determine to what extent the examined variables affect the targeted values and how different levels cause variability, and at the same time to test the statistical reliability of the results obtained. The F values calculated in the analysis of variance were compared with the values taken from the F value table for $F_{0.05,2,6}$ and it was seen that 95% confidence level was provided. A3B3C3 variance is chosen for product verification.

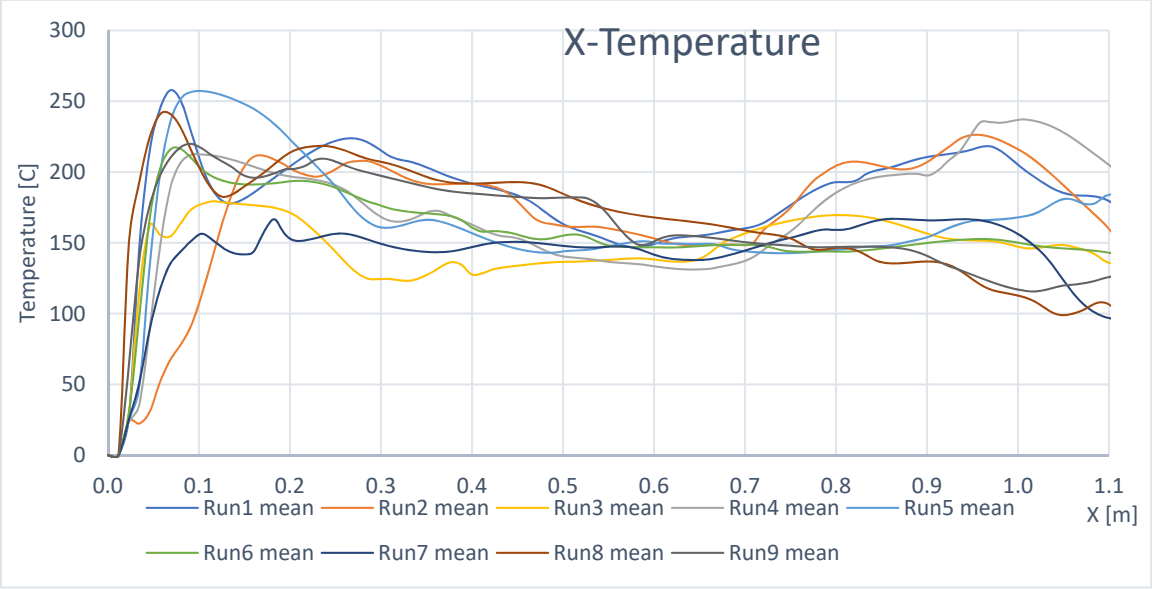

Fig.6 Velocity change in the X direction

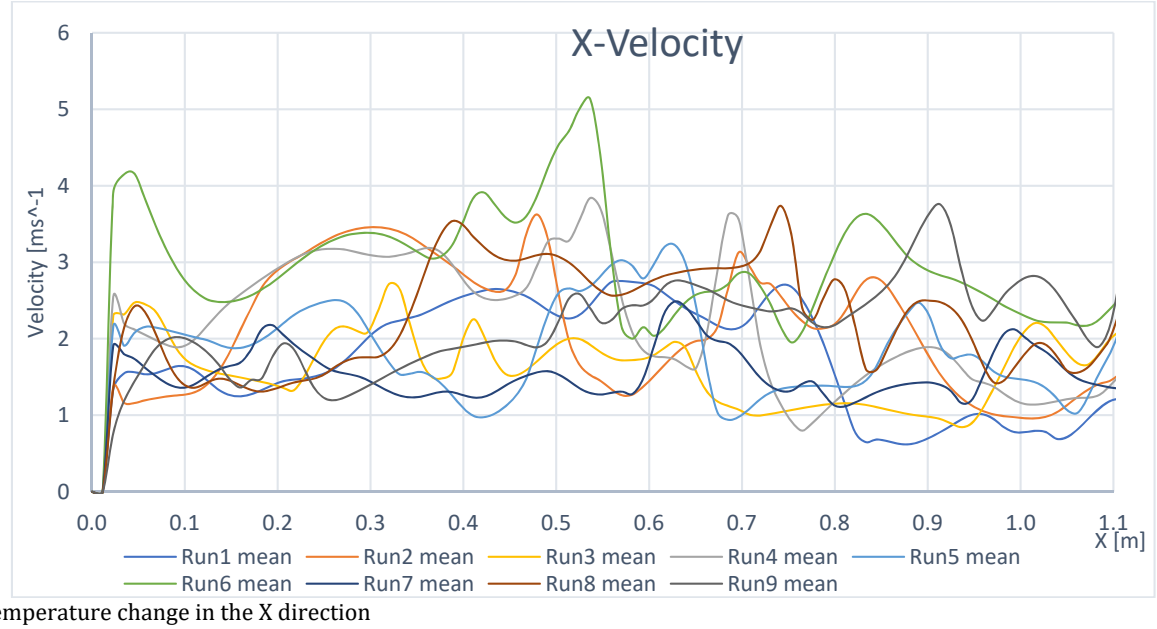

Fig.7 Temperature change in the X direction

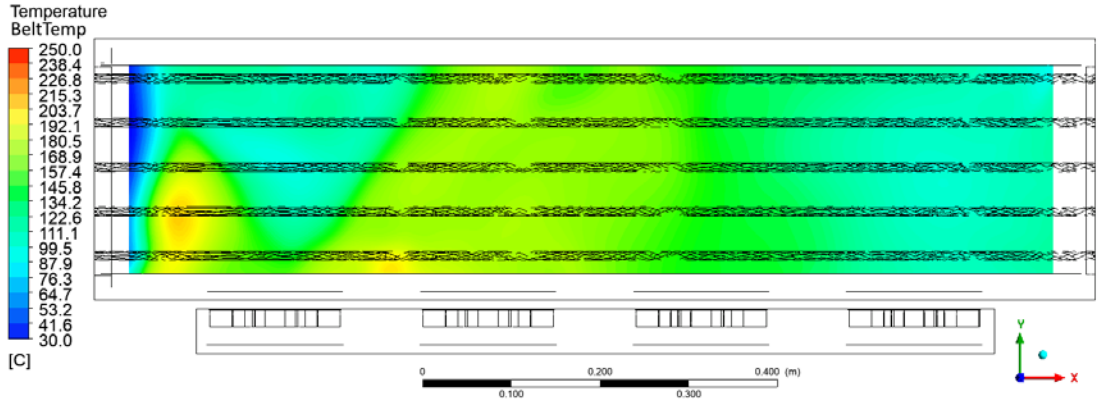

Figure 8 Belt Surface Temperature Distribution for A3B3C3 variant

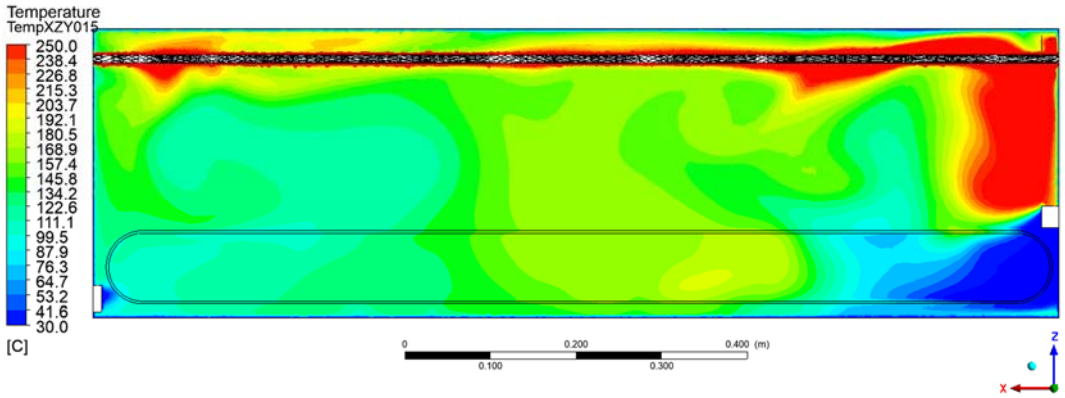

Figure 9 Mid-Section Surface Temperature Distribution for A3B3C3 variant

Table 9 Analysis of variance table for heat distribution

Param.	DOF	SS	MS	Cont. %	F
	2	16348	8174	66%	1528
B	2	4217	2108	17%	394
C	2	4156	2078	17%	388
Err.	2	11	5	0%	
Ttl.	8	24732		100%	

Table 10 Analysis of variance table for vel. distribution

Param.	DOF	SS	MS	Cont. %	F
A	2	11.1	5.6	4%	10.2
B	2	50.7	25.3	20%	46.5
C	2	194.5	97.3	76%	178.6
Err.	2	1.1	0.5	0%	
Ttl.	8	257,4		100%	

RESULTS AND DISCUSSIONS

Mathematical approaches, limited computational capacity, and insufficient understanding of the physical model cause uncertainties in computational fluid dynamics (CFD) simulations. As a result, the reliability of CFD in design processes depends on the experiments performed during the design verification process (Marvin, 1988). Due to this necessity, a prototype was manufactured and tested according to the dimensions specified in the A3B3C3 factors (Table 11) and CFD results compared with the temperature and velocity measurements, taken 1 cm above the porous band, which is thought to be the most important region in terms of product quality. Fahey et al (Fahey et al., 2008) indicated that the difference between the flow rates of heated and nonheated air passing around the cooling circuit can be neglected. Flow velocities are measured in ambient air in the unheated oven using hot-wire anemometry in specified locations. Typical accuracy for hot wire anemometers usually provides an accuracy within ±1% to ±5% of the measured velocity under optimal conditions and the manufacturer spec value for device is ±4% which is high but acceptable for highly turbulent flow.

Table 11 Prototype values

Parameters	Value
Number of fans (A)	4
Dist. between fans (mm) (B)	240
Height of fans (mm)(C)	250

To find the temperature distribution on the belt surface, standard J-type thermocouples consisting of iron and constantan which are operating in the range of 0-760 centigrade were attached 1 cm above the band surface. Thermocouples were placed along the lines Y=0.05 and Y=0.25, from the position X=0.15m to X=1.05m with 0.15m increments. For thermostat input, a thermocouple is located at x=0.4m at the midsection. When the thermostat was set to 160 °C, the oven reached a steady state at 20 minutes with 5 °C fluctuations. Iron–constantan thermocouples (Type J) offer a sensitivity of 55 μV/°C and are commonly used for general temperature measurements within the range of −40 °C to +750 °C, with an average measurement error of ±0.75% and is neglectable for a highly turbulent flow. Their functionality remains largely unaffected in both oxidizing and reducing environments (Morris & Langari, 2016).

A comparison of simulation results with experimental results is given in Fig. 10 and Fig. 11. In order to avoid human-induced errors, all experimental measurements were repeated 3 times and averaged To determine the accuracy of the simulation, the measurement values, and relative deviations are given in Table 12 and Table 13. The deviations were calculated according to the formulas below:

$$\Delta V = \frac{V_{calc} - V_{meas}}{Vmeas} x100\% \quad (6)$$

$$\Delta T = \frac{T_{calc} - T_{meas}}{Tmeas} x100\% \quad (7)$$

The model can simulate velocity and temperature profiles with acceptable accuracy for a turbulence convection heat transfer study. Deviations may be due to measurement techniques and limited access to the oven due to it being a closed volume. Specifically, the measured velocities were predicted with a relatively low deviation at most points. For measurement on the Y0.05 line, the line close to fans, most points are underpredicted with a maximum deviation of 25.28% at X=0.90m, which is near the product outlet. For measurements on the Y0.25 line, points are over or underpredicted with a maximum deviation of 19.12% at X=0.15 which is a more acceptable value for such a complex analysis. The error rate also shows a certain height because the velocity measurements are made when the oven is cold but the trend of experimental measurements is similar to the trend of CFD results.

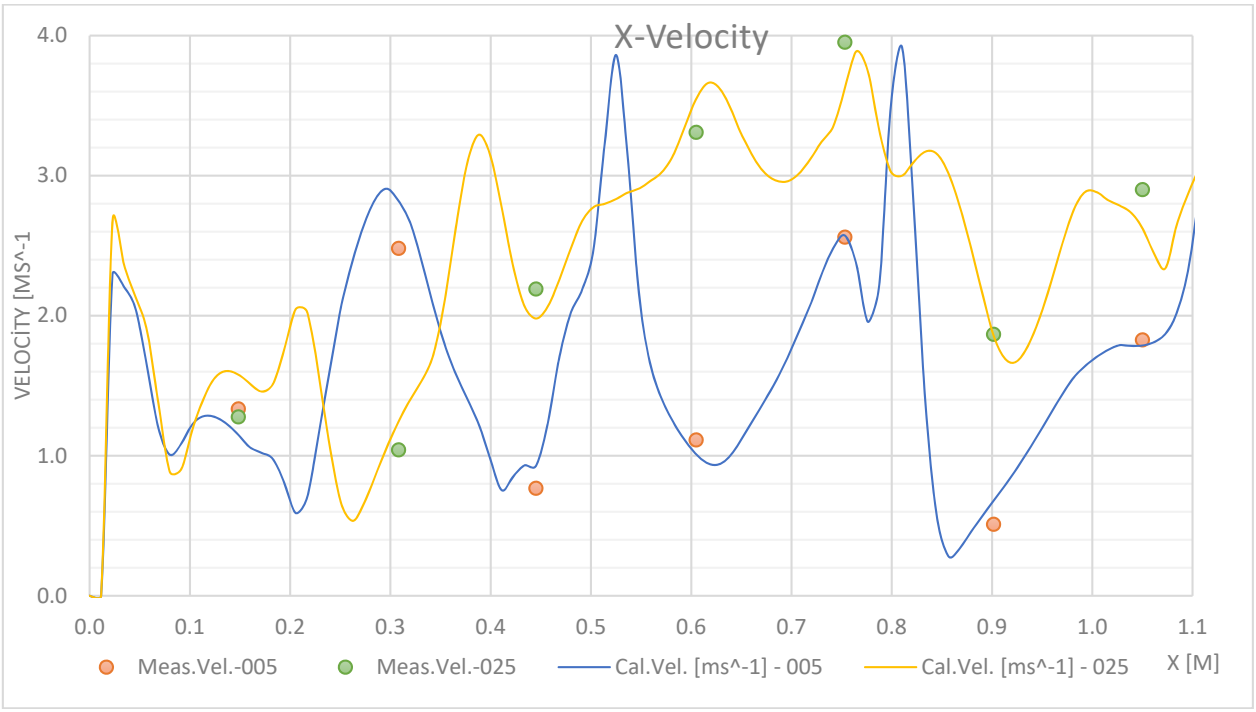

Fig. 10 Velocity distribution in the longitudinal direction

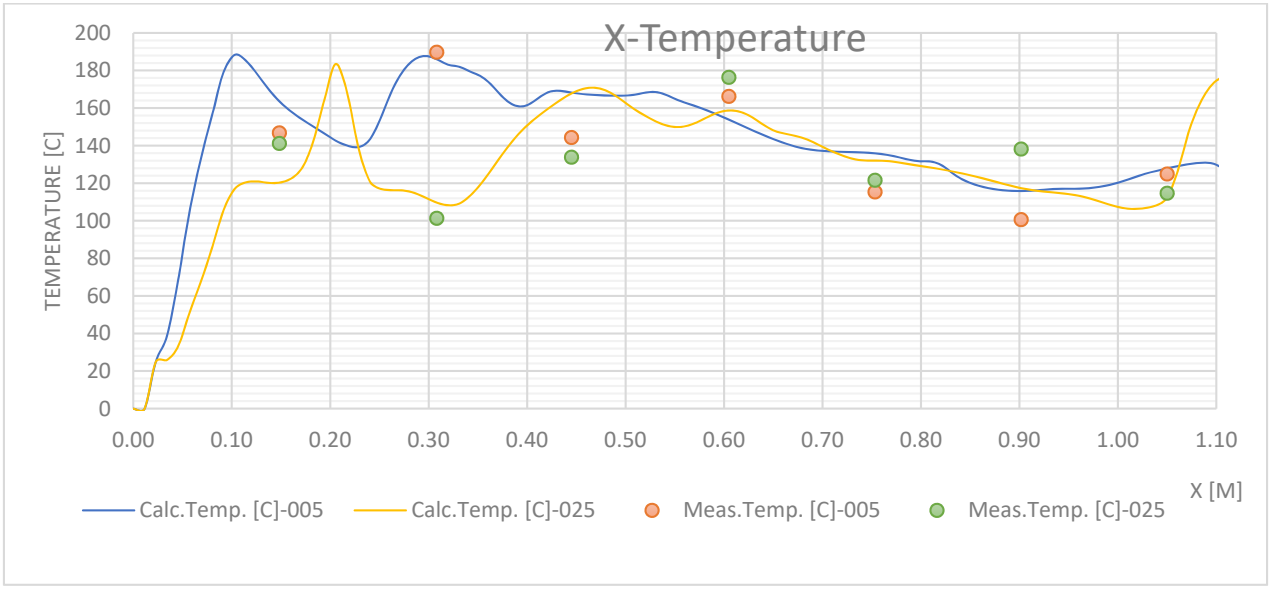

Fig. 11 Temperature distribution in the longitudinal direction

Table 12 Velocity Measurements

Vel.	Y 0.05			Y 0.25		
X [m]	Calc.(m/s)	Meas.(m/s)	Dev.%	Calc.(m/s)	Meas.(m/s)	Dev.%
0.15	1.15	1.33	16.13%	1.58	1.28	-19.12%
0.31	2.82	2.48	-11.95%	1.24	1.04	-16.39%
0.45	0.93	0.77	-17.41%	1.98	2.19	10.58%
0.60	1.01	1.11	10.12%	3.55	3.31	-6.76%
0.75	2.57	2.56	-0.47%	3.63	3.95	8.95%
0.90	0.68	0.51	-25.28%	1.85	1.87	0.67%
1.05	1.79	1.83	2.17%	2.62	2.90	10.47%

Table 13 Temperature Measurements

Temp. X [m]	Y 0.05 Calc (°C)	Meas. (°C)	Dev.%	Y 0.25 Calc (°C)	Meas. (°C)	Dev.%
0.15	163.54	146.77	-10.25%	120.30	141.09	17.28%
0.31	185.96	189.70	2.01%	109.71	101.31	-7.66%
0.45	168.25	144.23	-14.28%	167.86	133.76	-20.31%
0.60	153.76	166.18	8.08%	158.75	176.32	11.06%
0.75	135.94	115.26	-15.21%	132.06	121.54	-7.97%
0.90	115.86	100.58	-13.18%	117.40	138.15	17.67%
1.05	127.88	124.83	-2.38%	112.59	114.64	1.82%

Values read in temperature measurements show lower deviation rates compared to velocity measurements. While the maximum deviation in the measurements made on the Y0.05 line is -15.21% at X=0.75m, the maximum deviation in the measurements made on the Y0.25 line is 20.31%. at X=0.45m. The general distribution of the measurements made on both lines is compatible with the trend created based on the calculated values.

Although the deviation values are generally high, the experimentally measured values show a distribution by the trend drawn depending on the calculated values. Relatively high deviations can be accepted in such complex geometry problems where heat and fluid transfer in different environments are examined. Difficulties in reaching the closed oven volume and related measurement errors should not be ignored.

CONCLUSION

The performance of industrial ovens plays a critical role in achieving efficient and uniform drying and cooking processes. In this study, we focus on optimizing the internal velocity and heat distribution of an industrial belt oven utilizing Taguchi design principles. By employing computational fluid dynamics (CFD) simulations and experimental measurements, we aim to identify the key design variables and their impact on the oven's performance. This research provides valuable insights for designing and analyzing industrial ovens in various applications.

The continuous belt oven under investigation consists of a permeable stainless-steel belt and axial fans with stick-type heaters. The fans draw hot air from the main chamber and deliver it beneath the permeable belt through a back chamber. To improve the airflow distribution, the positioning of the fans and the geometry of the back chamber were carefully assessed. The internal flow patterns were analyzed to ensure optimal heat transfer and uniform drying/cooking throughout the oven.

The Taguchi design of experiments was employed to determine the most influential design variables affecting the oven's performance. The number of fans, the distance between fans, and the distance from fans to the belt surface were selected as the key design factors. The objective was to minimize belt surface temperature deviation and belt surface velocity deviation.

A 3D computational fluid dynamics model was developed to simulate the airflow and heat transfer within the oven. By systematically varying the design variables defined in the Taguchi experiment, the model allowed us to assess their impact on the internal velocity and heat distribution. This approach enabled efficient exploration of the design space and facilitated the identification of optimal settings. The proposed approach, encompassing the design, manufacturing, and analysis stages, can be applied to diverse industrial oven designs. Using the Taguchi method, the optimal configuration for the industrial oven was determined with the following parameters: four fans (A), spaced 240 mm apart (B), and positioned at a height of 250 mm (C). This configuration was found to provide the best balance of airflow distribution and heat transfer, ensuring uniform cooking throughout the chamber.

To validate the accuracy of the numerical findings, an experimental oven design was developed based on the optimal S/N ratios obtained from the Taguchi analysis. Experimental measurements were conducted to compare the actual oven performance with the CFD predictions. The results demonstrated a strong correlation between the two, confirming the reliability of the numerical model.

This study successfully optimized the internal velocity and heat distribution in an industrial belt oven using Taguchi design principles and computational fluid dynamics simulations. By determining the key design variables and their effects on performance, the study provides valuable insights for the design and analysis of industrial ovens in various applications. The experimental validation further reinforces the reliability of the proposed approach. Future work may involve applying this methodology to optimize other types of industrial ovens, thereby enhancing their efficiency and uniformity in heat distribution

ACKNOWLEDGEMENT

This study was supported by The Scientific and Technological Research Council of Turkey (TUBİTAK) project number 7160496.

Conflicts of interest

The authors declare no conflicts of interest.

REFERENCES

Amadane, Y., Mounir, H., Marjani, A., Ettouhami, M., & Atifi, A. (n.d.). Using CFD Simulation and Taguchi Approach to Optimize the Parameters Influencing the Performance of PEM Fuel Cell with the Serpentine Flow Field. *Ezziyyani, M. (eds) Advanced Intelligent Systems for Sustainable Development (AI2SD'2019). AI2SD 2019. Lecture Notes in Electrical Engineering*(624). https://doi.org/10.1007/978-3-030-36475-5_29

Aydın, A., Yaşar, H., Engin, T., & Büyükkaya, E. (2022). Optimization and CFD analysis of a shell-and-tube heat exchanger with a multi segmental baffle. *Thermal Science, 1*(26), pp. 1-12. https://doi.org/10.2298/TSCI200111293A

Biçer, N., Engin, T., Yasar, H., Büyükkaya, E., Aydın, A., & Topuz, A. (2020). Design optimization of a shell-and-tube heat exchanger with novel three-zonal baffle by using CFD and taguchi method. *International Journal of Thermal Sciences, 155*. https://doi.org/10.1016/j.ijthermalsci.2020.106417.

Boulet, M., Marcos, B., Dostie, M., & Moresoli, C. (2010). CFD modeling of heat transfer and flow field in a bakery pilot oven. *Journal of Food Engineering, 97*(3), pp. 393-402. https://doi.org/10.1016/j.jfoodeng.2009.10.034

Chandra, A. S., Reddy, P. N., & R, H. (2022). ArticleNatural ventilation in a lege space with heat source: CFD visualization and taguchi optimization. *Journal of Thermal Engineering*(8), pp. 642-655. https://doi.org/10.18186/thermal.1190545

Demir, U., & Aküner, M. C. (2018). Elektrikli bir araç için tekerlek içi asenkron motorun tasarım ve optimizasyonu. *Journal of the Faculty of Engineering and Architecture of Gazi University, 33*(4), pp. 1517-1530. https://doi.org/10.17341/gazimmfd.416448

Durbin, P. (1996). On the k-3 stagnation point anomaly. *International Journal of Heat and Fluid Flow, 17*(1), pp. 89-90. https://doi.org/10.1016/0142-727X(95)00073-Y

Fahey, M., Wakes, S. J., & Shaw, C. T. (2008). Use of computational fluid dynamics in domestic oven design. *Int. Jnl. of Multiphysics, 2*(1). https://doi.org/10.1260/175095408784300216

İç, Y. T., & Yıldırım, S. (2012). Çok kriterli karar verme yöntemleriyle birlikte taguchi yöntemini kullanarak bir ürünün tasariminin geliştirilmesi. *Journal of the Faculty of Engineering and Architecture of Gazi University, 27*(2), pp. 447-458.

Inc, A. (2009). *ANSYS Fluent User Guide Release 12.* Ansys Inc.

Inc, A. (2011). *ANSYS CFX-Solver Theory Guide, Release 14.* Canonsburg, PA: ANSYS Inc.

Inc., A. (2011). *ANSYS CFX-Solver Modeling Guide*, Rel. 14. 452-453.

Jegede, F., & Polley, G. (1992). Optimum Heat-Exchanger Design. *Chemical Engineering Research & Design*(70), pp. 133-141.

Kahraman, F., & Sugözü, B. (2019). An integrated approach based on the taguchi method and response surface methodology to optimize parameter design of asbestos-free brake pad material. *Turkish Journal of Engineering, 3*(3), pp. 127-132. https://doi.org/10.31127/tuje.479458

Kokolj, U., Škerget, L., & Ravnik, J. (2017). A numerical model of the shortbread baking process in a forced convection oven. *Applied Thermal Engineering, 111*, pp. 1304-1311. https://doi.org/10.1016/j.applthermaleng.2016.10.031.

Kokolj, U., Škerget, L., & Ravnik, J. (2017). The Validation of Numerical Methodology for Oven Design Optimization Using Numerical Simulations and Baking Experiments. *Strojniški vestnik - Journal of Mechanical Engineering, 63*(4), pp. 215-224. https://doi.org/10.5545/sv-jme.2016.4089

Marvin, J. G. (1988). *Accuracy Requirements and Benchmark Experiments for CFD Validation.* National Aeronautics and Space Administration.

Morris, A. S., & Langari, R. (2016). *Measurement and Instrumentation (Second Edition).* Elsevier Inc. https://doi.org/10.1016/C2013-0-15387-1

Norton, T., & Da-WenSun. (2006). Computational fluid dynamics (CFD) – an effective and efficient design and analysis tool for the food industry: A review. *Trends in Food Science & Technology, 17*(11), 600-620. https://doi.org/10.1016/j.tifs.2006.05.004

Obidowski, D., Stajuda, M., & Sobczak, K. (2021). Efficient Multi-Objective CFD-Based Optimization Method for a Scroll Distributor. *Energies, 14*(2-377). https://doi.org/10.3390/en14020377

Özer, M., Altınkaynak, A., Temiz, V., Mutlu, T., Dışpınar, T., Özgen, A. K., & Yücel, M. (2016). Önden yüklemeli bir çamaşır makinesinin sonlu elemanlar yöntemiyle dinamik olarak modellenmesi. *Journal of the Faculty of Engineering and Architecture of Gazi University, 31*(3), pp. 773-780. https://doi.org/10.17341/gummfd.78923

Rek, Z., Rudolf, M., & Zun, I. (2012). Application of CFD Simulation in the Development of a New Generation Heating Oven. *Strojniški vestnik - Journal of Mechanical Engineering*(58), pp. 134-144. https://doi.org/10.5545/sv-jme.2011.163

Shimpy, S., Kumar, M., & Kumar, A. (2024). Design and optimization of a domestic solar dryer: an analytical approach. *Engineering Computations, 41*(4), pp. 947-965. https://doi.org/10.1108/EC-12-2023-0916

Smolka, J., Bulinski, Z., & Nowak, A. J. (2013). The experimental validation of a CFD model for a heating oven with natural air circulation. *Applied Thermal Engineering*, pp. 387-398. http://dx.doi.org/10.1016/j.applthermaleng.2013.02.014

Stojanović, B., Babić, M., Veličković, S., & Blagojević, J. (2015). Optimization Of Wear Behaviour In Aluminium Hybrid Composites Using Taguchi Method. *14th International Conference on Tribology, SERBIATRIB '15.* Belgrade, Serbia.

Tambolkar, P., Ponkshe, A., Mulay, V., & Bewoor, A. (2020). Use of Taguchi DOE for CFD Simulation to maximize the Reusability of Working Fluids of Centrifugal Filter. *Procedia Manufacturing, 46*, pp. 608-614. https://doi.org/10.1016/j.promfg.2020.03.087

Tank, A., Chhanwal, N., Indrani, D., & Anandharamakrishnan, C. (2014). Computational fluid dynamics modeling of bun baking process under different oven load conditions. *J Food Sci Technol, 51*(9), pp. 2030-2037. https://doi.org/10.1007/s13197-012-0736-6

Türkan, B. (2024). Elektrikli araçlarda optimum soğutucu tasarımı için TRIZ algoritmasının uygulanması ve Taguchi analizi. *Journal of the Faculty of Engineering and Architecture of Gazi University, 39*(1), pp. 521-534. https://doi.org/10.17341/gazimmfd.1072512

Ünverdi, M., & Küçük, H. (2019). Taguchi yöntemi ve hesaplamalı akışkanlar dinamiği kullanılarak tasarlanan levhalı ısı değiştiricilerin performanslarının karşılaştırılması. *Pamukkale Univ Muh Bilim Derg, 25*(4), pp. 373-386. https://doi.org/10.5505/pajes.2018.35493

Vizguerra-Morales, P., Va´zquez-Castillo, J. A., Romero-Toledo, R., Aguilera-Alvarado, A. F., & Ponce-Ortega, J. M. (2016). Optimization and CFD modeling of an improved rustic oven for producing bricks. *Clean Techn Environ Policy*(18), pp. 1599-1609. https://doi.org/10.1007/s10098-016-1139-6

Yia, Y., Salonitisa, K., Tsoutsanisb, P., Litos, L., & Patsavelas, J. (2017). Improving the curing cycle time through the numerical modeling of air flow in industrial continuous convection ovens. *The 50th CIRP Conference on Manufacturing Systems. 63*, pp. 499-504. Procedia CIRP. https://doi.org/10.1016/j.procir.2017.03.167

Yuce, B. E., Nielsen, P. V., & Wargocki, P. (2022). The use of Taguchi, ANOVA, and GRA methods to optimize CFD analyses of ventilation performance in buildings. *Building and Environment*(225). https://doi.org/10.1016/j.buildenv.2022.109587

Journal Homepage: https://dergipark.org.tr/tr/pub/isibted

Isı Bilimi ve Tekniği Dergisi

Archive: https://tibtd.org.tr/dergi

Improving The Efficiency Of Waste Heat Recovery Systems By Means Of A Combined Turbine-Peltier System

Ozan TEKİN [1], Ramin BARZEGAR [2,*], Mehmet Sait SÖYLEMEZ [1]

[1] *Gaziantep University, Engineering Faculty, Mechanical Engineering, Şahinbey, 27310, Gaziantep, Türkiye*
[2] *Hacettepe University, Faculty of Engineering, Mechanical Engineering, Çankaya, 06800, Ankara, Türkiye*

A R T I C L E I N F O

2025, vol. 45, no.1, pp. 47-55

doi: 10.47480/isibted.1443975

Research Article
Received: 03 July 2024
Accepted: 06 November 2024

* *Corresponding Author*
e-mail:
raminbarzegar@hacettepe.edu.tr

Keywords:
Waste Heat Recovery,
Thermoelectric Generator,
Heat Exchanger,
Turbine Generator,
Internal Combustion Engine.

ORCID Numbers in author order:
0000-0001-9812-7752
0000-0003-2796-7126
0000-0001-8570-1321

A B S T R A C T

A novel Combined Turbine-Peltier System (CTPS) was designed and built to harness both the thermal and kinetic energies of an engine's exhaust gas and convert it to electrical power. The turbine generator was connected to the turbocharger shaft and the Thermoelectric Generators (TEG) were assembled between the heat exchangers mounted on the exhaust pipe. The Computational Fluid Dynamics (CFD) approach and Taguchi optimization technique were employed in order to analyze and optimize the flow field and heat transfer characteristics of the system. Based on the optimized numerical results, an experimental setup was designed and manufactured, and the experiments were conducted on an engine operating at different load and speed conditions. The harvested maximum power output for a single TEG was 5.5 W with the thermal efficiency of 3.6% and the net output power of the CTPS was 190 W obtained at the engine speed of 3000 rpm. The maximum increase in the power of the ICE combined with the CTPS method was calculated as 1.6%. The obtained numerical results were compared with the experiments and showed a good accordance with the maximum deviation of 6%.

Kombine Türbin-Peltıer Sistemi Aracılığıyla Atık Isı Geri Kazanım Sistemlerinin Verimliliğinin İyileştirilmesi

M A K A L E B İ L G İ S İ

Anahtar Kelimeler:
Atık Isı Kazanımı
Termoelektrik Jeneratör
Isı Değiştirgeci
Türbin Jeneratör
İçten Yanmalı Motorlar

Ö Z E T

Yeni bir Kombine Türbin-Peltier Sistemi (CTPS), bir motorun egzoz gazının hem termal hem de kinetik enerjilerini kullanmak ve bunu elektrik gücüne dönüştürmek için tasarlandı ve üretildi. Türbin jeneratörü turboşarj miline bağlandı ve Termoelektrik Jeneratörler (TEG) egzoz borusuna monte edilen ısı değiştiriciler arasına monte edildi. Sistemin akış alanı ve ısı transferi özelliklerini analiz etmek ve optimize etmek için Hesaplamalı Akışkanlar Dinamiği (CFD) yaklaşımı ve Taguchi optimizasyon tekniği kullanıldı. Optimize edilmiş sayısal sonuçlara dayanarak, deneysel bir kurulum tasarlandı ve üretildi ve deneyler farklı yük ve hız koşullarında çalışan bir motorda gerçekleştirildi. Tek bir TEG için hasat edilen maksimum güç çıkışı %3,6 termal verimlilikle 5,5 W oldu ve CTPS'nin net çıkış gücü 3000 rpm motor hızında elde edildi ve 190 W oldu. ICE'nin gücündeki maksimum artış CTPS yöntemi ile birleştirildiğinde %1,6 olarak hesaplandı. Elde edilen sayısal sonuçlar deneylerle karşılaştırıldığında maksimum %6 sapmaya rağmen iyi bir uyum gösterdiği görülmüştür.

NOMENCLATURE

CTPS	Combined Turbine-Peltier System
HX	Heat Exchanger
ICE	Internal Combustion Engine
TEG	Thermoelectric Generator
WHRS	Waste Heat Recovery System
ORC	Organic Rankine Cycle
ZT	Figure of Merit
S/N	Signal to Noise
T	Temperature Difference [K]
T_C	Cold Surface Temperature [K]
T_H	Hot Surface Temperature [K]
T_0	Dead State Temperature [K]
$\dot{W}$	Power [W]
α	Seebeck coefficient (V/K)
δ	Thermal Conductivity (W/m. K)
σ	Electrical Resistivity (S/m)
η	First Law Efficiency
μ	Second Law Efficiency
γ	Exergy or Availability [W]
s	Entropy of the State (kJ/kg. K)
h	Enthalpy of the State (kJ/kg. K)
$\dot{m}$	Mass Flow Rate (kg/sec)

INTRODUCTION

In Internal Combustion Engines (ICE), the stored chemical energy in the fuel is converted into thermal energy and then into mechanical energy. Due to thermodynamics laws and mechanical losses, this transformation can never be complete, and studies have shown that only about 38% of the chemical energy of the fuel is converted into mechanical energy (Orr et al., 2016). Figure 1 shows the total fuel energy distribution in a typical ICE in which the energy wasted through the exhaust system is about 33%. This energy is in the form of kinetic energy and enthalpy of exhaust gases. Waste heat recovery systems (WHRS) such as turbochargers, Organic Rankine Cycle (ORC), and Thermoelectric Generators (TEG) were introduced as an attempt to harness this energy (Stobart et al., 2017). Turbochargers only take advantage of the kinetic energy of the exhaust gases via a turbine-compressor combination to increase the intake air pressure of the ICE. On the other hand, ORC and TEG systems are driven by the enthalpy carried by the gases. Due to the fact that TEGs have fewer mechanical parts and maintenance needs, their implementation on the exhaust system of vehicles is more convenient and economical than ORC (Stobart et al., 2017).

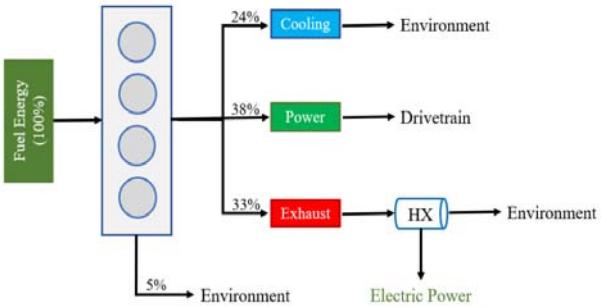

Figure 1. The distribution of the fuel energy in a typical ICE

TEGs are operating according to the Seebeck law in which electrical power is generated when there is a temperature difference between the semiconductor surfaces. The internal structure of TEGs includes p-type and n-type semiconductors for electricity generation, copper plates for electrical connection, and ceramic plates for insulation (Snyder & Ursell, 2003). The internal structure of TEGs can be seen in Figure 2.

The efficiency of the TEGs is calculated using Figure of Merit (ZT) which is defined as [6]:

$$ZT = \frac{\alpha^2 \cdot T}{\sigma \cdot \delta} \tag{1}$$

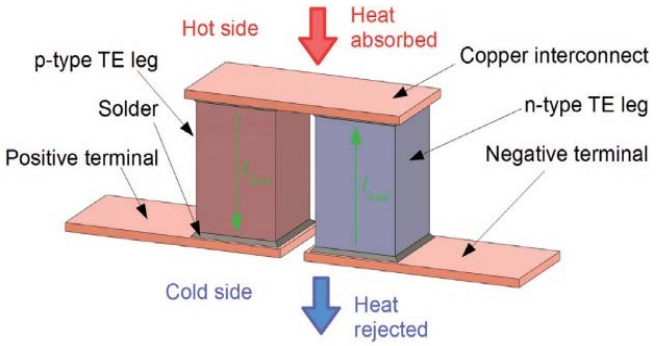

Figure 2. The internal structure of TEGs (Kempf & Zhang, 2016).

In which α is the Seebeck coefficient, T is the temperature difference between the TEG surfaces, σ is the electrical resistivity, and δ is the thermal conductivity. In order to calculate the efficiency of the TEG modules, the Carnot efficiency term was used considering the ZT value and the efficiency correlation is as follows:

$$\eta_{TEG} = \left(\frac{\sqrt{1 + ZT_{avg}} - 1}{\sqrt{1 + ZT_{avg}} + \frac{T_C}{T_H}} \right) \times \frac{(T_H - T_C)}{T_H} \tag{2}$$

Where, the ZTavg indicates that the average ZT value at the average T. Also, Tc and TH were the cold and hot surface temperatures of the TEG. Application of TEGs on the surfaces of the exhaust pipe is an effective method to produce electrical power from heat energy (Shen et al., 2019). Mastbergen et al. used both experimental and numerical methods to evaluate the efficiency of TEGs. The extended surfaces had been installed on TEG hot and cold surfaces to create a temperature difference. The working fluid for both heating and cooling purposes was air and the material of p-type and n-type semiconductors was Bi2Te3. The efficiency of TEG was calculated at around 1% during the test conditions. The deviation between the numerical results and experimental results has been reported at about 15% (Mastbergen et al., 2005).

Hsiao et al. have developed a mathematical model to evaluate the TEG application in automotive exhaust systems. The computer-aided evaluation method has been used to calculate the efficiency of TEGs. According to the results of this study, the maximum power density of TEGs has been measured as 51.13 mW/m3 (Hsiao et al., 2010).

The application of heat exchangers on the exhaust pipe of vehicles is a method used to enhance TEG performance. Karri et al. have manufactured a heat exchanger model that had finned surfaces assembled on the exhaust pipe. The effect of

TEG on the overall fuel economy of two different vehicles has been investigated. The obtained results have revealed that a fuel economy of about 4% could be achieved using the TEGs on the exhaust system (Karri et al., 2011a).

Evaluation of the heat exchanger performance has been conducted numerically by Wang and Liu in order to obtain a uniform temperature distribution on the surfaces of the heat exchangers. It has been suggested that the efficiency of the TEGs can be improved by the application of an alternative finned surface orientation in the heat exchangers mounted on the exhaust system (Wang & Liu, 2014a). Computational Fluid Dynamics (CFD) model was employed by Wang and Ma to study the increase in the efficiency of the heat exchanger with a spiral shape extended surface installed on the exhaust pipe. The efficiency of the heat exchangers had been increased by about 8.4% resulting in an increase in the efficiency of the TEGs by about 2% (Wang & Liu, 2014b).

In order to minimize the overall cost and complexities in the application of the TEG in vehicles, it has been suggested that the surface of the exhaust muffler of the automobiles be considered as heat exchanger (B. Huang & Shen, 2022). It has been shown that one of the immediate benefits of this method was that the increase in back pressure in the exhaust system of the vehicle has been canceled by applying the TEGs on the muffler surface (Hewawasam et al., 2020).

Enhancing the thermal efficiency of the TEGs directly relies on maintaining the uniform surface temperature on each side of the heat exchanger. To achieve this condition, Huang et al. have developed a new heat exchanger model that includes the phase change material (PCM) inside the hot and cold surfaces. Theoretical calculations resulted in a 15% increase in the thermal efficiency. However, in order to maintain a uniform temperature between the surfaces of the HX, a portion of the harvested heat energy from the exhaust was consumed by the PCM material. Consequently, the second law efficiency of the system decreased (K. Huang et al., 2021).

A comprehensive study of the literature showed that the commercialization of TEGs in automobiles could be possible by addressing issues such as non-uniform temperature distribution on the surfaces of heat exchangers, pressure drop effect, low thermal efficiency of TEGs, and the required cooling source. This study aims to tackle some of these issues by means of optimization techniques as well as numerical and experimental analysis. Additionally, due to the fact that the power produced by the turbine of the turbocharger is more than enough to just drive the compressor, a generator was mounted on the turbocharger shaft to harness the excess power. Therefore, a novel Combined Turbine-Peltier system (CTPS) was developed by combining a TEG system for waste heat recovery.

MATERIAL AND METHODS

Experimental Test Setup

The developed CTPS was a combination of two HXs, 20 pieces of Bi2Te3-based TEGs, a turbine-generator system, a water reservoir, and a cooling pump. The exhaust gas was passed through a heating channel acting as the hot reservoir and the water was circulated via a pump through the cooling channel and a water reservoir. The TEGs were sandwiched between the heating and cooling channels. In order to obtain a comparable temperature distribution for TEGs, the crossflow orientation for the hot and cold sides was used. The turbine-generator was mounted immediately after the engine exhaust manifold to generate the electrical power using the kinetic energy of exhaust gas. Figure 3 indicates the overall system configuration.

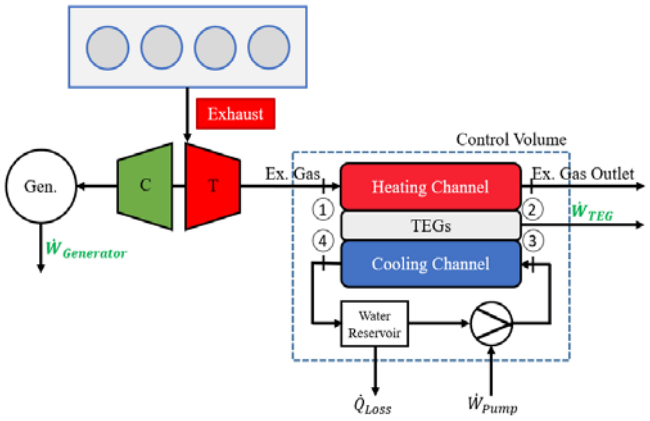

Figure 3. Configuration of the designed CTPS

The engine used was an 1150 cc Renault D4F spark ignition engine mounted on an AVL test bed shown in Figure 4. The engine speed and engine load were controlled with a dynamometer and the exhaust gas properties were measured by a set of thermocouples and mass flow controllers. The WHRS was connected immediately after the exhaust manifold to minimize the heat loss in the exhaust pipe. In the current study, the experimental data was collected after observing the steady temperature and mass flow rates of the exhaust gas at the test bench, and the delay time for the data gathering was measured at about 20 minutes. In order to check the validity of the experiments, more than ten measurements were recorded in the same environment and boundary conditions and the average value of the was presented in the Tables and Figures.

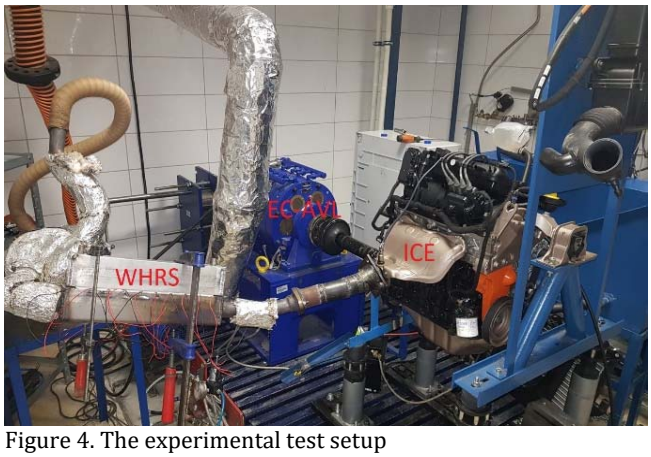

Figure 4. The experimental test setup

In the developed CTPS, the electrical power was produced by both WHRS and the turbine-generator system. The produced power from a turbine-generator was 3-phase due to the principles of the generators. Considering the regulation, all components located in the vehicle should operate with single-phase or DC. Thus, the produced 3-phase electrical power was converted to single-phase by means of an h-bridge constructed with six diodes. Figure 5 shows the turbine-generator circuit schematics and device in which the "K" signs the A2212 brushless DC motor, the "C" signs the multimeter, and the "L" signs the h-bridge.

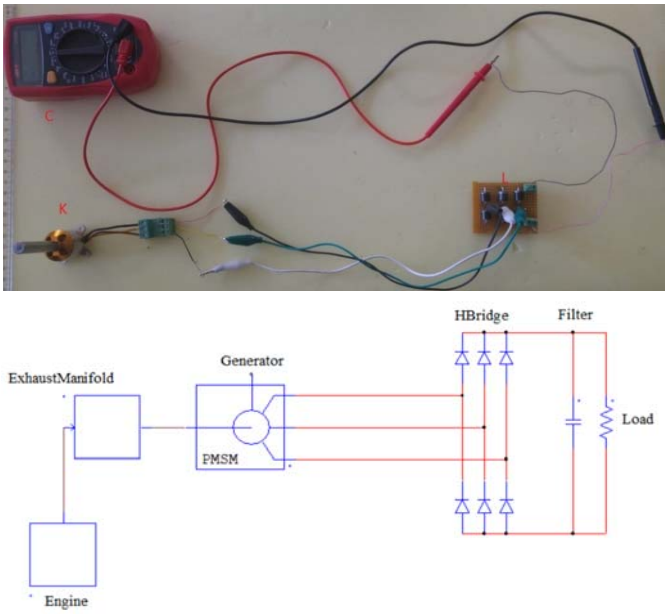

Figure 5. Turbine-Generator circuit schematic and device

In the analysis of thermal systems, whereas the general evaluation method calculates the thermal efficiency using the first law approaches, the exact performance indicator of the system is the second law efficiency since it gives a system whether effective or not. Therefore, to calculate the second law efficiency of the control volume that is presented in Figure 3, the availability energy of the exhaust gas and water was calculated using the Equation 3. Moreover, the overall second law efficiency of the CTPS was evaluated by employing the combined second law efficiencies of HX and TEGs as given in Equations 4 and 5, respectively. So, the overall second law efficiency of the system was calculated using the Equation 6 (Patowary & Baruah, 2018).

$$\gamma = \dot{m} \times [(h - h_0) - T_0 \times (s - s_0)] \quad (3)$$

$$\mu_{HX} = \frac{\dot{W}_{HX}}{\gamma_1 - \gamma_2} \quad (4)$$

$$\mu_{TEG} = \frac{\dot{W}_{TEG}}{(\gamma_2 - \gamma_1) - (\gamma_4 - \gamma_3)} \quad (5)$$

$$\mu_{II,overall} = \eta_{HX} \cdot \eta_{TEG} \quad (6)$$

Where W_HX is the power of the HX, W_TEG is the power of the TEG, η_HX and η_TEG are their efficiencies, respectively. In equation 6, the efficiency is based on the total produced power in the TEG system. Hence, to calculate the total power and net power values, Equation 7 was used as follows:

$$\dot{W}_{net} = \dot{W}_{TEG} + \dot{W}_{Generator} - \dot{W}_{Pump} \quad (7)$$

Numerical Study of CTPS

In the HX studies, the vane thickness, number of vanes, and gap size are directly related to the effectiveness of the HX, and these parameters should be selected considering the types of applied boundary conditions (Borcuch et al., 2017; Moon & Kim, 2014; Söylemez, 2003). In order to design an optimized HX model, the extended surface dimensions for the exhaust gas heating channel were selected using the Taguchi L9 (3 by 3) optimization method since the Taguchi model calculates the sensitivity of the design parameters on the output parameters by changing of the design points systematically. So, the required analysis points could be reduced from 27 to 9. The selected vane heights were 10, 20, and 40 mm considering the hydraulic diameter of the exhaust pipe, and the gap between the vanes was selected as 5 and 10 mm. A gap size larger than 10 mm was not considered due to limitations in the heat exchanger manufacturing process. During the optimization studies, the cooling channel dimensions were kept constant according to the previous studies (Kara et al., 2019; Tekin et al., 2019). The cooling water flow rates of 0.1, 0.25, and 0.5 kg/sec were preferred in order to obtain minimum power consumption by cooling pump. The selected control factors and levels for Taguchi L9 are given in Table 1. The output parameters in the optimization were the pressure drop and the temperature difference between TEG surfaces which was chosen to be around 120°C to obtain maximum efficiency based on studies in the literature (Patil et al., 2018; Patowary & Baruah, 2018). The designed Taguchi L9 optimization matrix can be seen in Table 2.

Table 1. The Taguchi design parameters

Control Factors	**Levels**
Exhaust Channel Vane Height [mm]	10, 20, 40
Vane Gap [mm]	5, 10
Water Flow Rate [kg/sec]	0.1, 0.25, 0.5
Output Parameters	
Temperature Difference between the Surfaces of TEGs [K]	The desired value is 120
Pressure Drop [Pa]	The desired value is 0.1

Table 2. The Taguchi L9 design matrix

Experiment Number	***Control Factors***		
	Vane Height [mm]	**Vane Gap [mm]**	**Water Flow Rate [kg/sec]**
Exp. 1	10	5	0.1
Exp. 2	10	10	0.25
Exp. 3	10	5	0.5
Exp. 4	20	5	0.5
Exp. 5	20	10	0.1
Exp. 6	20	10	0.25
Exp. 7	40	5	0.25
Exp. 8	40	10	0.5
Exp. 9	40	5	0.1

In order to obtain the optimal HX model, CAD models were created for each of the experiments according to the Taguchi design table which can be seen in Figure 6. The numerical analyses were conducted utilizing the Ansys Fluent software.

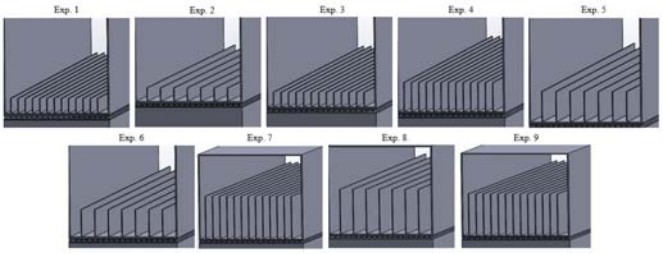

Figure 6. The heating channels of the HX for the numerical analysis

The obtained data from the performance test of the engine were applied as boundary conditions in the numerical analysis as shown in Table 3. In the numerical study, the air properties were used in the heating channel due to the fact that exhaust

gas properties are comparable to that of air and the working fluid in the cooling channel was water. In the computational fluid dynamics (CFD) analyses of the heat exchangers, the Reynold-Average Navier Stokes approach (RANS) was preferred by selecting the k-epsilon viscous model since this viscous model provides an appropriate near-wall modeling for the heat transfer solution in the conjugate heat and fluid problems. To estimate the actual heat flux and temperature distributions over the HX surfaces, the time-dependent analysis type was selected and the analysis duration was 3600 seconds based on the suggestions from the literature (Harun et al., 2018; Kutt & Lehtonen, 2015; Liu et al., 2014).

Table 3. Boundary conditions of the numerical study

Parameters	Cooling Channel	Heating Channel
Fluid Type	Liquid Water	Air
Inlet Temperature	303 [K]	753 [K]
Dynamic Viscosity	0.7978 [mPa.s]	3.48e-05 [kg/m.s]
Channel Material	Aluminum	Aluminum
Viscous Type	k-epsilon Realizable	k-epsilon Realizable
Y+ Value	30	30

RESULTS AND DISCUSSION

In order to estimate the system efficiency and optimization of the HX model that was designed for cooling and heating purposes, initially, the engine was tested without the CTPS. After benchmarking the engine in the test bed, the engine exhaust gas properties were measured considering the literature recommendations (Champier, 2017; Yang, 2005; Zhou et al., 2014). In order to obtain the engine exhaust gas flow rate and temperature values, the AVL test bed was operated using the speed/alpha mode. In this mode, to measure the exhaust gas and engine properties, the butterfly angle was increased continuously by about 5% until the torque value of 50 N-m was achieved. The preferred torque value was obtained in full throttle at 2000 rpm, and in 70% and 50% of butterfly angles at 2500 and 3000 rpm, respectively. Table 4 indicates the engine exhaust gas properties at different engine speeds.

Table 4. The engine output results at different speeds

Parameters	2000 [rpm]	2500 [rpm]	3000 [rpm]
Exhaust Gas Flow Rate [kg/sec]	0.0075	0.0088	0.0103
Exhaust Gas Temperature [K]	753	789	818
Engine Torque [N-m]	50	50	50
Brake Power [kW]	11.7	13.1	15.7

In the Taguchi analysis method, the effects of the control factors on the output parameters are assessed by changing the control factor levels. In this way, whether the selected control and output factors are suitable or not could be checked. The selected output control parameters were the temperature difference between the surfaces of the HX and the pressure drop in the exhaust channel. For the CFD analysis of the Taguchi L9 array, the 2000 rpm engine speed was chosen as a boundary condition because not only it was expected that the minimum temperature difference and exhaust gas mass flow rate would occur at this speed but also to optimize and increase the effectiveness of the CTPS system considering the minimum conditions.

The CFD analysis was carried out for all the experiments based on the control factors suggested by the Taguchi optimization method in order to obtain the temperature difference and pressure drop values for each of the models. Initially, the mesh independency tests were carried out with four different element numbers ranging from 0.8 up to 6.5 million cells. As can be seen in Figure 7a, the mesh size of about 5.3 million cells provided sufficient accuracy for the numerical model. The created mesh structure is also presented in Figure 7b.

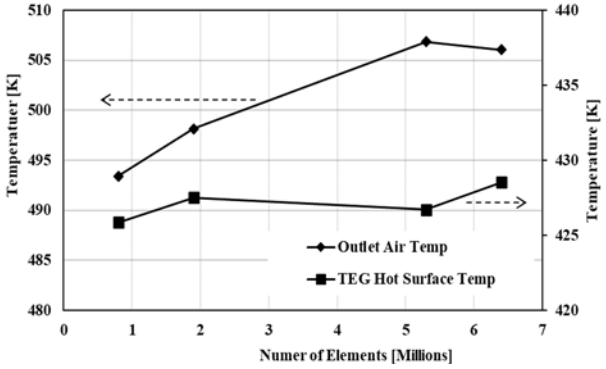

(a)

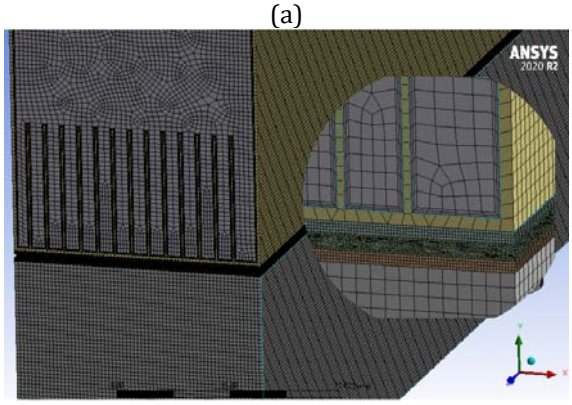

(b)

Figure 7. The mesh independence test results (a) and the constructed grid (b)

Figure 8 shows the temperature distribution on the hot and cold surfaces of TEGs. It was seen that while the temperature over the hot surface decreased from the inlet to the outlet, the cold surface temperature increased from the inlet to the outlet since the cross-flow method was selected. The surface temperature difference on the TEGs was in the range of about 85 to 190 K with an average value of around 113 K which is in the optimum range of TEG operational conditions (Patowary & Baruah, 2018). The results for the average temperature difference on the TEG surface as well as the pressure drop for the experiments are presented in Table 5. These results were used to assess the optimum dimensions and cooling flow rate in the Taguchi optimization method.

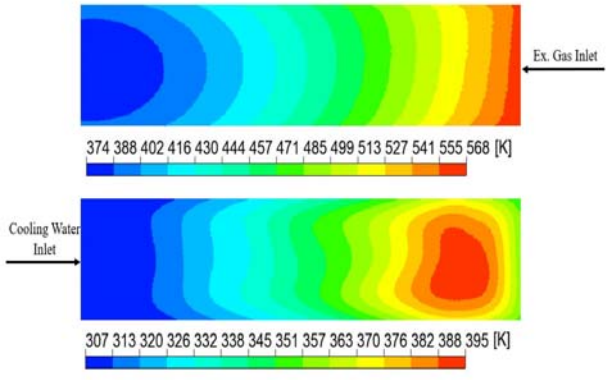

Figure 8. The temperature distribution on the hot and cold surfaces of TEGs

In order to assess the effect of control factors on temperature difference between TEG surfaces and pressure drop in the heating channel, the signal-to-noise (S/N) analysis was performed, and the results are presented in Figure 9. Considering the obtained data from S/N analysis for the temperature difference, it was seen that the effect of vane height was more significant than the other two factors. Increasing the vane height to 40 mm resulted in an increase in temperature difference by about 17% above the mean values. However, the effect of change in the vane distance and cooling flow rate was less than 5%. The same results were also noticed for pressure drop values as well. It can be concluded that the most important control factor on the HX was the vane height.

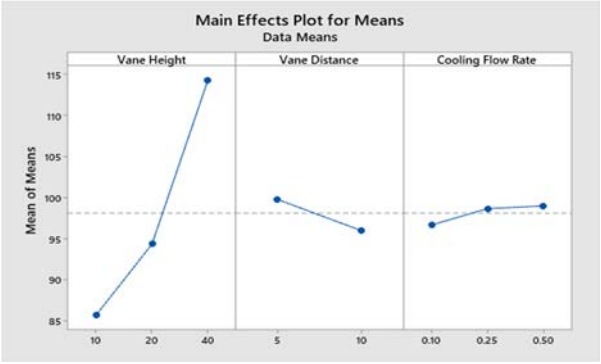

(a)

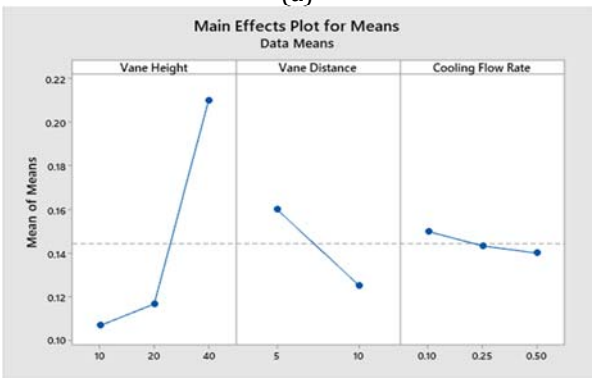

(b)

Figure 9. The S/N curves for (a) temperature difference and (b) pressure drop

Table 5 shows the temperature difference and pressure drop results for the different control factors. It was seen that the highest temperature difference was obtained at Exp. 7 at about 117 K and the lowest pressure drop was measured at Exp. 2 at about 0.10 Pa. Reducing the cooling flow rate from 0.25 kg/sec in Exp. 7 to 0.1 kg/sec in Exp. 9 resulted in a temperature difference decrease by about 4 K, however, the required pumping power for cooling water was also decreased significantly. When the obtained results from the numerical analysis were investigated together as given in Table 5 and Figure 8, to obtain the maximum temperature differences between the TEG surfaces, the hot channel vane height should be 40 mm. Moreover, the vane distance changes strongly affect the pressure drop more than the temperature differences, the vane distance was selected as 5 mm since the pressure drop in the channel was negligible considering the environmental pressure was about 101,3 kPa. When the sensitivity of the cooling flow rate on the temperature differences and pressure drop were examined, the results showed that the cooling flow rate was insensitive to the output parameters. So, to reduce the required power for the circulation of the cooling fluid in the cold channel, the cooling flow rate was selected as 0.1 kg/sec. Considering the results, Exp. 9 with a vane height of 40 mm, vane distance of 5 mm, and cooling flow rate of 0.1 kg/sec was preferred as optimal geometry for the experimental analysis and manufacturing. Moreover, when the vane height, hot surface temperature, and pressure drop results were investigated together, the increase rate of the vane height was directly proportional to the increase rate of the temperature and pressured drop due to the flow area being reduced and the high turbulence intensity being occurred.

After obtaining the optimum HX model from optimization studies, the CFD studies of the CTPS were carried out by defining the engine test results given in Table 4 as boundary conditions. During the analysis, three exhaust gas flow rates and temperatures obtained under three engine speeds measured at constant torque were used.

Considering the results, when the exhaust gas flow rate increased at higher engine speeds, the temperature difference and pressure drop increased by about 12% and 25%. The numerical analysis results of the CTPS are listed in Table 6.

Table 5. The obtained numerical results for the temperature difference and pressure drop

	Control Factors			***Result Factors***	
Experiment Number	**Fin Height [mm]**	**Fin Distance [mm]**	**Cold Flow Rate [kg/sec]**	**Temp. Diff. [K]**	**Pressure Drop [Pa]**
Exp. 1	10	5	0.1	85	0.11
Exp. 2	10	10	0.25	85	0.10
Exp. 3	10	5	0.5	87	0.11
Exp. 4	20	5	0.5	97	0.13
Exp. 5	20	10	0.1	92	0.11
Exp. 6	20	10	0.25	94	0.11
Exp. 7	40	5	0.25	117	0.22
Exp. 8	40	10	0.5	113	0.18
Exp. 9	**40**	**5**	**0.1**	**113**	**0.23**

Table 6. The numerical results of the optimum HX model

Parameters	**2000 [rpm]**	**2500 [rpm]**	**3000 [rpm]**
Temperature Difference [K]	108.8	123.3	147.5
Pressure Drop of Heating Channel [Pa]	0.18	0.24	0.35
Outlet Air Temperature [K]	528.3	561.6	584
Outlet Water Temperature [K]	305.3	305.7	305.9
Inlet Water Temperature [K]	303	303	303
Inlet Air Temperature [K]	753	798	818
Water Flow Rate [kg/sec]	0.1	0.1	0.1

The obtained results from the experimental study as given in Table 6 were used to calculate the first and second law efficiencies of the TEG system by using Equations 3 to 6 and the calculated results are presented in Table 7. The exergy (γ) was calculated considering the environmental condition and the produced energy was collected from the experiment. It was seen that the first and second-law efficiencies were increased with the engine speed due to the increase in the mass flow rate and converted energy from the exhaust gas. Moreover, the selected control volume for the exergy analysis is given in Figure 3.

The maximum thermal efficiency of the TEGs was 3.6% and the maximum second law efficiency was about 10% obtained at 3000 rpm. The calculated maximum theoretical efficiency of TEGs based on Equation 1 was 6.36% which was about 43% higher than the obtained thermal efficiency. This was because in theoretical calculations, the temperature distribution on the TEG surfaces was considered to be uniform, and the Seebeck coefficient and thermal conductivity of the materials were assumed to be identical.

Table 7. The first and second law efficiencies of the TEG system

Parameters	2000 [rpm]	2500 [rpm]	3000 [rpm]
Calculated Power Output of TEGs [W]	68.5	101.7	148.9
Exergy of Inlet Air [W]	1411.4	1866.9	2395.9
Exergy of Outlet Air [W]	468.9	680.9	911.5
Reversible Energy of Air [W]	942.5	1186.0	1484.4
Reversible Energy of Water [W]	61.0	102.3	113.2
Second Law Efficiency of TEGs [%]	7.27	8.57	10.03
Theoretical First Law Efficiency of TEGs [%]	4.86	5.41	6.36
Calculated First Law Efficiency of TEGs [%]	2.6	3.0	3.6

In order to reveal the performance increases with the CTPS in the WHRS, the already shared similar studies were compared with the current study as given in Table 8. The measured or calculated thermal efficiencies gradually increase in the thermoelectric generator studies by year because of the optimized utilization and obtaining the smooth temperature gradient over the HX surfaces. The comparison parameters for the WHRS studies that are related to TEGs were the produced power quantity from the single TEG and the thermal efficiency of the TEGs. Therefore, the singular TEG power quantity and thermal efficiency were used in Table 8. Considering the obtained results, the thermal efficiency was higher than the study conducted in 2022 by about 32.2%. Additionally, the produced power quantity from the single TEG was greater than the study conducted in 2011 at around 27.2%.

Table 8. Comparison of the results for the designed TEG with the results in the literature

Reference	Year Published	TEG Material	Method	Output Power per a TEG [W]	Thermal Efficiency [%]
(Ikoma et al., 1998)	1998	Si-Ge	Experimental	2.8	0.9
(Mastbergen et al., 2005)	2005	Bi_2Te_3	Experimental	2.1	1.0
(Espinosa et al., 2010)	2010	Mg_2Si/Zn_4Sb_3- Bi_2Te_3	Simulation	1.2	0.8
(Hsiao et al., 2010)	2010	Bi_2Te_3	Experimental	1.24	0.4
(Karri et al., 2011b)	2011	Bi_2Te_3	Experimental	4.0	1.26
(Liu et al., 2014)	2014	Bi_2Te_3	Simulation and Experimental	1.0	1.4
(B. Huang & Shen, 2022)	2022	PbSn	Simulation	0.4	2.44
Current Study	-	Bi_2Te_3	Simulation and Experimental	5.5	3.6

After conducting the numerical analysis, the HX was manufactured and assembled on the experimental test setup. During the experimental studies, the engine was operated at three different speeds and four different engine torques. All TEGs were connected in series and the total voltage and current were measured utilizing a rheostat as a load resistor. The same method was used for turbine-generator output power, as well. The consumed power of the cooling pump was at a constant value of 9.7W with a mass flow rate of 0.1 kg/sec. The obtained results showed that the power output value of the turbine generator and TEGs were directly proportional to the increment of the engine speed and torque values. Under the no-load condition, the power generated by TEGs was significantly higher than the turbine-generator system. However, by increasing the engine torque, the rate of increase in power generated by the turbine compressor was much higher than that of TEGs. The maximum net power output values measured at 2000, 2500, and 3000 rpm engine speeds were 90.6, 132.7, and 190.4 W, respectively.

The CTPS power ratio defined as the percentage of increase in the engine brake power was also calculated. Even though the highest power output of 190.4 W was measured under 75 N-m load at 3000 rpm, the maximum CTPS power ratio was evaluated as 1.6% under 25 N-m load at 3000 rpm. The reason for this condition can be clarified with the ZT value of the TEGs because the efficiency of the CTPS system is directly proportional to TEGs efficiency. The measured experimental results are presented in detail in Table 9.

In order to illustrate the relationship between the waste heat recovery systems and the engine speed, the net power output values of the CTPS are given in Figure 10. It can be seen that the net power output of the system had a linear correlation with the engine torque, especially at higher engine speeds. This linear trend was not followed at 2000 rpm due to the fact that at this speed the maximum torque of 50 N-m was achieved at fully open throttle conditions and the exhaust gas temperature was at its maximum.

In order to validate the numerical model, the deviation between the simulation results and experimental data was compared. The numerical results were conducted by applying the exhaust gas flow rate and temperature values which were obtained for engine speeds of 2000 to 3000 rpm at 50 N-m engine load. The maximum temperature deviation between the experimental data and numerical results was around 6%. Figure 11 shows the comparison between the experiments and the numerical results at different engine speeds.

Table 9. The experimental test results of the CTPS

Engine Speed [rpm]	Engine Torque [N-m]	Engine Brake Power [kW]	Temp. Difference [K]	TEGs Ratings [V-A]	TEGs Power Output [W]	Turbine-Generator Power [W]	Cooling System Power [W]	Net Power Output [W]	CTPS Power Ratio [%]
2000	0	1.9	62	47.7-0.3	14.3	6	9.7	10.6	0.6
2000	25	5.2	85	56.6-0.42	23.7	12	9.7	26.0	0.5
2000	38	10.5	103	68.2-0.55	37.5	25	9.7	52.8	0.5
2000	50	15.7	118	80.4-0.65	52.3	48	9.7	90.6	0.6
2500	0	3.1	95	62.8-0.53	33.2	12	9.7	35.5	1.1
2500	25	6.5	112	77.4-0.62	47.9	28	9.7	66.2	1.0
2500	50	13.1	128	92-0.7	64.4	50	9.7	104.7	0.8
2500	75	19.6	141	99.2-0.78	77.4	65	9.7	132.7	0.7
3000	0	4.7	115	78.5-0.63	49.5	30	9.7	69.8	1.5
3000	25	7.9	142	99.6-0.79	78.7	55	9.7	124.0	1.6
3000	50	15.7	152	112-0.82	91.8	73	9.7	155.1	1.0
3000	75	23.6	168	117-0.95	111.1	89	9.7	190.4	0.8

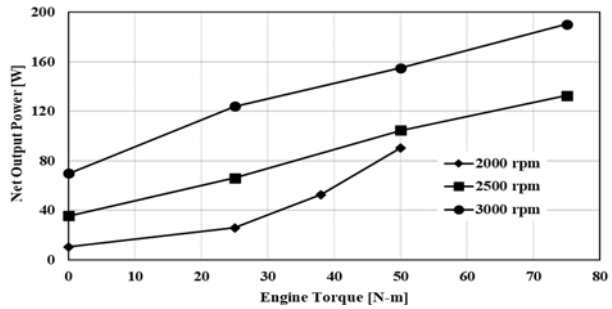

Figure 10. Illustration of the net power output of the CTPS

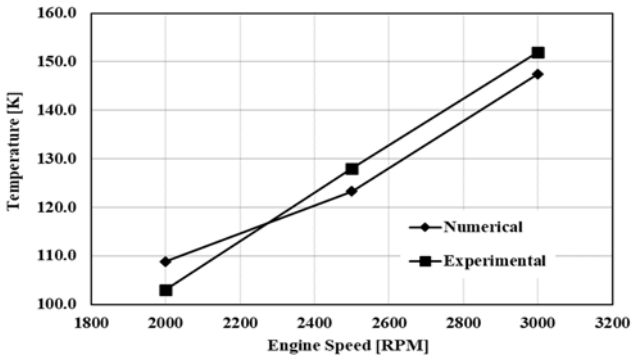

Figure 11. Comparison of the temperature between the experimental and numerical results

CONCLUSION

In this study, the optimization methods, analysis, and experimental approaches were employed to design and manufacture a novel Combined Turbine-Peltier System (CTPS) to harness the energy of the exhaust gases from an ICE operating under different conditions. The obtained results can be summarized as follows:

- In the design of HX, the effect of vane height was more significant than the vane distance and the cooling flow rate. Increasing the vane height to 40 mm resulted in an increase in temperature difference by about 17% above the mean values.
- By increasing the engine speed from 2000 rpm to 2500 rpm and then to 3000 rpm, the exhaust gas flow rate increased and resulted in a higher temperature difference between TEG surfaces by about 12% and 25%.
- The first and second law efficiencies were directly proportional to the engine speed and the maximum thermal efficiency of the TEGs was 3.6% and the maximum second law efficiency was about 10% obtained at 3000 rpm. Also, the maximum obtained power from a single TEG was 5.5W.
- Under the no-load condition, the power generated by TEGs was significantly higher than the turbine-generator system. However, by increasing the engine torque, the rate of increase in power generated by the turbine-compressor was much higher than that of TEGs. The maximum net power output values measured at 2000, 2500, and 3000 rpm engine speeds were 90.6, 132.7, and 190.4W, respectively.
- The highest CTPS power ratio was evaluated as 1.6% under 25 N-m load at 3000 rpm.
- The maximum temperature deviation between the experimental data and numerical results was around 6%.

ACKNOWLEDGMENTS

This study was supported by Gaziantep University Research Development Unit (Project No: MF.YLT.19.09) and Atilim University (Project No: ATU-LAP-1920-18). The authors also would like to extend their special thanks to Numesys Advanced Engineering Inc. for technical support.

REFERENCES

Borcuch, M., Musiał, M., Gumuła, S., Sztekler, K., & Wojciechowski, K. (2017). Analysis of the fins geometry of a hot-side heat exchanger on the performance parameters of a thermoelectric generation system. Applied Thermal Engineering, 127, 1355–1363. https://doi.org/10.1016/j.applthermaleng.2017.08.147

Champier, D. (2017). Thermoelectric generators: A review of applications. In Energy Conversion and Management (Vol. 140, pp. 167–181). https://doi.org/10.1016/j.enconman.2017.02.070

Espinosa, N., Lazard, M., Aixala, L., & Scherrer, H. (2010). Modeling a thermoelectric generator applied to diesel automotive heat recovery. Journal of Electronic Materials, 39(9), 1446–1455. https://doi.org/10.1007/s11664-010-1305-2

Harun, M. H., Azmi, M. W. N., Aras, M. S. M., Azlan, U. A. A., Azahar, A. H., Annuar, K. A. M., Halim, M. F. M. A., Yaakub, M. F., & Abidin, A. F. Z. (2018). A study on the potential of peltier in generating electricity using heat loss at engine and exhaust vehicle. Journal of Advanced Research in Fluid Mechanics and Thermal Sciences, 49(1), 77–84.

Hewawasam, L. S., Jayasena, A. S., Afnan, M. M. M., Ranasinghe, R. A. C. P., & Wijewardane, M. A. (2020). Waste heat recovery from thermo-electric generators (TEGs). Energy Reports, 6, 474–479. https://doi.org/10.1016/j.egyr.2019.11.105

Hsiao, Y. Y., Chang, W. C., & Chen, S. L. (2010). A mathematic model of thermoelectric module with applications on waste heat recovery from automobile engine. Energy, 35(3), 1447–1454. https://doi.org/10.1016/j.energy.2009.11.030

Huang, B., & Shen, Z. G. (2022). Performance assessment of annular thermoelectric generators for automobile exhaust waste heat recovery. Energy, 246. https://doi.org/10.1016/j.energy.2022.123375

Huang, K., Yan, Y., Wang, G., & Li, B. (2021). Improving transient performance of thermoelectric generator by integrating phase change material. Energy, 219. https://doi.org/10.1016/j.energy.2020.119648

Ikoma, K., Munekiyo, M., Furuya, K., Kobayashi, M., Izumi, T., & Shinohara, K. (1998). Thermoelectric module and generator for gasoline engine vehicles. In International Conference on Thermoelectrics, ICT, Proceedings. https://doi.org/10.1109/ict.1998.740419

Kara, E., Tekİn, O., & Söylemez, M. S. (2019). Experimental Analysis of the Automotive Waste Heat Recovery Using a Novel Turbine-Peltier Design YenİBİrTürbin -Peltİer Tasarimi KullanaraGerçekleştirilen. In Prof. Dr. İlhan Tekin ÖZTÜRK (Ed.), Experimental Analysis of the Automotive Waste Heat Recovery Using a Novel Turbine-Peltier Design (pp. 1–5). ULIBTK'19 22th Congress of Thermal Sciences and Technology. http://ctst2019.kocaeli.edu.tr/

Karri, M. A., Thacher, E. F., & Helenbrook, B. T. (2011a). Exhaust energy conversion by thermoelectric generator: Two case studies. Energy Conversion and Management, 52(3), 1596–1611. https://doi.org/10.1016/j.enconman.2010.10.013

Karri, M. A., Thacher, E. F., & Helenbrook, B. T. (2011b). Exhaust energy conversion by thermoelectric generator: Two case studies. Energy Conversion and Management, 52(3), 1596–1611. https://doi.org/10.1016/j.enconman.2010.10.013

Kempf, N., & Zhang, Y. (2016). Design and optimization of automotive thermoelectric generators for maximum fuel efficiency improvement. Energy Conversion and Management, 121, 224–231. https://doi.org/10.1016/j.enconman.2016.05.035

Kutt, L., & Lehtonen, M. (2015). Automotive waste heat harvesting for electricity generation using thermoelectric systems-An overview. International Conference on Power Engineering, Energy and Electrical Drives, 2015-Septe, 55–62. https://doi.org/10.1109/PowerEng.2015.7266296

Liu, X., Yu, C. G., Chen, S., Wang, Y. P., & Su, C. Q. (2014). Experiments and simulations on a heat exchanger of an automotive exhaust thermoelectric generation system under coupling conditions. Journal of Electronic Materials, 43(6), 2218–2223. https://doi.org/10.1007/s11664-014-3015-7

Mastbergen, D., Willson, B., & Joshi, S. (2005). Producing Light from Stoves using a Thermoelectric Generator. ETHOS International Stove Research Conference.

Moon, M. A., & Kim, K. Y. (2014). Analysis and optimization of fan-shaped pin-fin in a rectangular cooling channel. International Journal of Heat and Mass Transfer, 72, 148–162. https://doi.org/10.1016/j.ijheatmasstransfer.2013.12.085

Orr, B., Akbarzadeh, A., Mochizuki, M., & Singh, R. (2016). A review of car waste heat recovery systems utilising thermoelectric generators and heat pipes. Applied Thermal Engineering, 101, 490–495. https://doi.org/10.1016/j.applthermaleng.2015.10.081

Patil, D. S., Arakerimath, R. R., & Walke, P. V. (2018). Thermoelectric materials and heat exchangers for power generation – A review. In Renewable and Sustainable Energy Reviews (Vol. 95, pp. 1–22). https://doi.org/10.1016/j.rser.2018.07.003

Patowary, R., & Baruah, D. C. (2018). Thermoelectric conversion of waste heat from IC engine-driven vehicles: A review of its application, issues, and solutions. In International Journal of Energy Research (Vol. 42, Issue 8, pp. 2595–2614). John Wiley and Sons Ltd. https://doi.org/10.1002/er.4021

Shen, Z. G., Tian, L. L., & Liu, X. (2019). Automotive exhaust thermoelectric generators: Current status, challenges and future prospects. In Energy Conversion and Management (Vol. 195, pp. 1138–1173). Elsevier Ltd. https://doi.org/10.1016/j.enconman.2019.05.087

Snyder, G. J., & Ursell, T. S. (2003). Thermoelectric efficiency and compatibility. Physical Review Letters, 91(14), 148301/1-148301/4. https://doi.org/10.1103/PhysRevLett.91.148301

Söylemez, M. S. (2003). On the thermoeconomical optimization of fin sizing for waste heat recovery. Energy Conversion and Management, 44(6), 859–866. https://doi.org/10.1016/S0196-8904(02)00091-2

Stobart, R., Wijewardane, M. A., & Yang, Z. (2017). Comprehensive analysis of thermoelectric generation systems for automotive applications. Applied Thermal Engineering, 112, 1433–1444. https://doi.org/10.1016/j.applthermaleng.2016.09.121

Tekin, O., Kara, E., & Soylemez, M. S. (2019). CFD Analysis and Optimal Sizing of Finned Surface on a Novel Combined Turbine-Peltier System. In Prof. Dr. H. Serdar Yücesu (Ed.), CFD Analysis and Optimal Sizing of Finned Surface on a Novel Combined Turbine-Peltier System (Issue September, pp. 1–13). Internatıonal Symposıum on Automotıve Scıence and Technology. www.isastech.org

Wang, W. S., & Liu, X. (2014a). Experiments and analysis on thermoelectric generators of automotive exhaust under the multi-field coupling. Advanced Materials Research, 850–851, 217–220. https://doi.org/10.4028/www.scientific.net/AMR.850-851.217

Wang, W. S., & Liu, X. (2014b). Experiments and analysis on thermoelectric generators of automotive exhaust under the multi-field coupling. Advanced Materials Research, 850–851(1), 217–220. https://doi.org/10.4028/www.scientific.net/AMR.850-851.217

Yang, J. (2005). Potential applications of thermoelectric waste heat recovery in the automotive industry. International Conference on Thermoelectrics, ICT, Proceedings, 2005, 170–174. https://doi.org/10.1109/ICT.2005.1519911

Zhou, M., He, Y., & Chen, Y. (2014). A heat transfer numerical model for thermoelectric generator with cylindrical shell and straight fins under steady-state conditions. Applied Thermal Engineering, 68(1–2), 80–91. https://doi.org/10.1016/j.applthermaleng.2014.04.018

Journal Homepage: https://dergipark.org.tr/tr/pub/isibted

Isı Bilimi ve Tekniği Dergisi

Archive: https://tibtd.org.tr/dergi

Machine Learning-Based Reduced Order Modeling for Operational Analysis of Industrial Glass Melting Furnaces Using CFD Solutions

Engin Deniz CANBAZ [1,2] *, Mesut GÜR[1]

[1] *İstanbul Teknik Üniversitesi, Makina Fakültesi, Makina Mühendisliği Bölümü, Beyoğlu, 34437, İstanbul, Türkiye*
[2] *Şişecam Bilim, Teknoloji ve Tasarım Merkezi, Modelleme ve Simülasyon Teknolojileri Müdürlüğü, Gebze, 41400, Kocaeli, Türkiye*

A R T I C L E I N F O

2025, vol. 45, no.1, pp. 56-68

doi: 10.47480/isibted.1512812

Research Article
Received: 08 July 2024
Accepted: 04 December 2024

* *Corresponding Author*
e-mail: canbaze@itu.edu.tr
dcanbaz@sisecam.com

Keywords:
Glass Melting Furnaces
Computational Fluid Dynamics
Machine Learning
Reduced Order Model
Autoencoders

ORCID Numbers in author order:
0000-0002-6287-8770
0000-0002-0407-0298

A B S T R A C T

Computational fluid dynamics (CFD) models are essential for analyzing industrial glass melting furnaces, providing insights into energy consumption, temperature distribution, and glass quality. However, their computational expense limits practical application in daily operations. This study addresses this issue by developing a machine-learning-based reduced order model (ROM) using parametric solution data from a CFD model of a glass melting tank of a furnace. Key operational parameters, namely pull rate, heat flux from combustion space, and electrical potential difference to supply electrical power, are chosen to create a CFD solution dataset. The ROM utilizes an autoencoder with convolutional neural networks to predict temperature and velocity fields. Operational parameters are linked to its decoder through an auxiliary neural network. The performance of the ROM is assessed for both interpolation and extrapolation. Comparison between the data generated by the ROM and the ground-truth CFD solutions indicates less than 1% deviation and an R2 score of 0.99, demonstrating the ROM's capability. The ROM achieved a mean squared error (MSE) of 2.82E-06 for the interpolation and 2.79E-05 for the extrapolation tests, further supporting its accuracy. Additionally, the ROM offers significant advancements in solution time, achieving reduction by up to three orders of magnitude, which enhances its practical utility.

HAD Çözümlerini Kullanarak Endüstriyel Cam Ergitme Fırınlarının İşletme Analizi İçin Makine Öğrenimi Tabanlı İndirgenmiş Model Geliştirilmesi

M A K A L E B İ L G İ S İ

Anahtar Kelimeler:
Cam Ergitme Fırınları
Hesaplamalı Akışkanlar Dinamiği
Makine Öğrenimi
İndirgenmiş Model
Otokodlayıcı

Ö Z E T

Endüstriyel cam ergitme fırınlarında enerji tüketimi, cam kalitesi, sıcaklık dağılımının belirlenmesini sağlayan hesaplamalı akışkanlar dinamiği (HAD) modelleri, fırınların tasarım süreçlerinde de kritik öneme sahiptir. Ancak, cam ergitme prosesinin geniş zaman ve uzunluk boyutları nedeniyle, bu modellerin yüksek hesaplama maliyeti günlük fırın operasyonlarında kullanılmasını kısıtlamaktadır. Bu zorluğu aşabilmek için, bu çalışmada bir cam ergitme fırınının cam banyosu HAD modelinden elde edilen sonuçlar kullanılarak, makine öğrenimi tabanlı bir indirgenmiş model geliştirilmiştir. İndirgenmiş model, çekiş hızı, doğal gaz kaynaklı ısı akısı ve elektrik potansiyel farkı sınır koşullarının değişimini içeren parametrik HAD verileri ile oluşturulmuştur. Bu veri seti ile sıcaklık ve hız alanı tahminleri yapabilecek, konvolüsyonel nöral ağ tabanlı bir otokodlayıcı eğitilmiştir. Sonrasında, otokodlayıcının boyutsal yükseltme yapan bölümü, ek bir tam bağlantılı nöral ağ aracılığıyla, işletme parametreleri olan sınır koşullarıyla ilişkilendirilmiştir. Bu iki ağın birleşimiyle indirgenmiş model elde edilmiştir. İndirgenmiş modelin performansı, interpolasyon ve ekstrapolasyon testlerinde değerlendirilmiş; test sonuçlarında %1'den az sapma, 0.99 R^2 skoru elde edilmiştir. İnterpolasyon ve ekstrapolasyon testlerinde kaydedilen ortalama karesel hata ise, sırasıyla, 2.82E-06 ve 2.79E-05'tir. Ayrıca indirgenmiş model, yeni HAD çözümü tahmin süresini üç mertebeye kadar hızlandırmıştır. Bu çalışma, makine öğrenimi tabanlı indirgenmiş modellerin operasyonel analizler için etkili bir araç olduğunu kanıtlamakta ve cam ergitme fırınlarında uygulanabilirliğini başarıyla göstermektedir.

NOMENCLATURE

ARD%	Average Relative Difference Percentage
CFD	Computational Fluid Dynamics
CNN	Convolutional Neural Network
MAE	Mean Absolute Error
MSE	Mean Squared Error
ML	Machine Learning
R^2	Coefficient of Determination
ROM	Reduced Order Model
SELU	Scaled Exponential Linear Unit
c_p	Specific Heat (J/kg.K)
k_{eff}	Effective Thermal Conductivity (W/m.K)
n	Number of Computational Cells
p	Pressure (Pa)
S_{joule}	Joule Heating Source (W/m^3)
T	Temperature (K)
y_i	Ground-Truth Solution
$\bar{y}$	Mean of Ground-Truth Solution
$\hat{y}_i$	ROM Prediction
ρ	Density (kg/m^3)
μ	Dynamic Viscosity (Pa.s)
σ	Electrical Conductivity (1/ohm.m)
v	Velocity (m/s)
φ	Electric Potential (V)

INTRODUCTION

Modern continuous glass furnaces are quite complex thermal-fluid systems involving various physical phenomena, including batch-to-melt conversion, radiation transport in the molten glass, natural convection due to thermal expansion, joule heating with AC electrodes, turbulent combustion, and thermal coupling between the combustion atmosphere and glass bath (M. K. Choudhary et al., 2010; Cravero and Marsano, 2023; Faber et al., 2020; Pigeonneau and Flesselles, 2012; Pokorny et al., 2012, 2020; Viskanta, 1994). The glass furnaces have various types such as regenerative, recuperative, and all-electric furnaces (Atzori et al., 2023; Zier et al., 2021). Continuous regenerative furnaces, the most commonly used in the glass industry, are particularly efficient in conserving energy through heat recovery from exhaust gases. However, their high energy consumption contributes to CO_2 emissions, raising concerns about global warming and the need for sustainable energy solutions. Their design is critical, as it not only influences furnace efficiency but also impacts the greenhouse gas emissions by the furnace. By applying computational fluid dynamics (CFD), these furnaces can be analyzed in depth, allowing engineers to evaluate design and operational parameters and their environmental impact.

Numerous studies focus on different aspects of glass melting and related process. For example, CFD studies have examined the electric field and heat source generated by the immersed electrodes in the glass melt and the use of bubbling to enhance mixing by momentum transfer (Daurer et al., 2022; Matsuno et al., 2008; Simcik and Ruzicka, 2015; Soubeih et al., 2015). Radiative heat transfer in the glass melt, due to its high temperature nature, and the heat transfer mechanism between the combustion space and the melt are also key areas of interest (M. K. Choudhary et al., 2018; Raič et al., 2021). These CFD simulations support the furnace design process and operation (Abbassi and Khoshmanesh, 2008; Han et al., 2022; Jebava and Němec, 2018; Li et al., 2020; Pigeonneau et al., 2023). However, while CFD models provide a comprehensive understanding, multiphysics and multiscale features of glass melting process, the time-intensive nature of model preparation and solution poses challenges for real time decision-making during furnace operation (Gao et al., 2021).

Recently, the concept of creating digital twins for glass furnaces has gained traction to enhance operational efficiency. Digital twins dynamically replicate the physical furnace in a virtual environment, potentially bridging the gap between theoretical modeling and real-time operational insights. One of the approaches creating digital twins is through physics-based models, which defines the system based on the physical laws. However, the use of physics-based models, such as CFD, encounters hurdles in the form of requisite expertise and substantial solution times. Another approach is data-driven methods. Today, large volumes of data containing valuable information about processes and operations can be gathered from industrial equipment. Using this data, along with a bidirectional flow of information between the physical and digital systems, it is possible to replicate the operation and forecast the condition of the physical system (Cassar et al., 2018; Gao et al., 2021; Pazarlioglu et al., 2022; Taşkesen et al., 2023). However, digitally replicating every system using field data is challenging due to raw data being noisy, often incomplete, and requiring significant pre-processing before being effectively used to construct data-driven models (Molinaro et al., 2021).

Addressing these challenges, model order reduction emerges as a promising solution. By significantly reducing the dimensionality of data and the physical model while retaining essential information, models with reduced order offer a pathway to swiftly assess the effects of changing operational parameters on system properties. Techniques such as Galerkin projection of the Navier–Stokes equations onto an orthogonal basis of proper orthogonal decomposition (POD) modes provide a direct link to the governing equations. However, this approach is intrusive and relies on human expertise to develop models based on a working simulation (Brunton et al., 2020; Rowley and Dawson, 2017). Additionally, these models may perform poorly when dealing with advection-dominant problems or systems highly sensitive to minor state changes (Mücke et al., 2021).

To better capture, replicate, or predict the key dynamic physical features, machine learning (ML) algorithms can be utilized (Molinaro et al., 2021). This approach combines data-driven methods with physics-based methods. Obtaining a solution with the new inputs for the underlying governing equations is much faster compared to solving the system of equations. Specifically, this simulation-based digital twin method utilizes the simulation data, covering a broad range of operating conditions, to train a machine learning model, potentially eliminating the need for further simulations (Catsoulis et al., 2022). Meanwhile, with advancements in simulation capabilities and experimental techniques, fluid dynamics is evolving into a data-rich field, making it suitable for ML algorithms (Brunton et al., 2020). A significant part of the progress can also be attributed to the accessibility of open-

source software platforms like PyTorch (Paszke et al., 2017) and Tensorflow (Abadi et al., 2015). These platforms have simplified the process of implementation and training, eliminating the need for specialized knowledge. Furthermore, the advancement of computation-accelerating hardware, such as GPUs, has made it feasible to train extremely large models (Mücke et al., 2021). However, the black-box nature of machine learning methods, which often lack physical interpretability, is making it difficult to analyze results based on the underlying physics of the problem. Enhancing the physical interpretability of these models and incorporating the problem's physics into them are still challenging tasks (Masoumi-Verki et al., 2022).

The successful implementation of machine learning methods into physics-based models highlights the potential for integrating similar techniques in other engineering disciplines. Zhang et al. developed a surrogate model for structural seismic response prediction using a physics-guided convolutional neural network (Zhang et al., 2020). The developed deep neural network utilizes existing physics, such as the laws of dynamics, to mitigate overfitting and reduce the requirement for large training datasets. The effectiveness of the proposed method was demonstrated through both numerical and experimental data, with the authors suggesting that the proposed algorithm can be scaled to other structures and to other types of hazard events. Similarly, Cho et al. applied a comparable approach to predict lithium-ion battery lifetime (Cho et al., 2022). They developed a physics-informed neural network by incorporating the energy balance law into the loss function to predict battery temperature with limited data. They plan to expand the study to include actual electric-vehicle driving profiles. Pfaff et al. developed a mesh-based graph network to address physics simulations which takes the advantage of adaptive meshing (Pfaff et al., 2020). This technique overcomes the limitations of grid-based methods (such as convolutional neural networks) by learning predictions on existing computational meshes and it can be applied on a wide range of physical systems, from simulating cloth and structural mechanics to fluid dynamics. The predictions by the trained network showed that acceleration of 1-2 orders of magnitude, faster than the simulation it was trained on.

Meanwhile, machine learning methods in the development of reduced order models (ROM) using CFD solutions have also gained popularity in recent years. Erichson et al. studied shallow decoders to reconstruct flow field from limited sensor data (Erichson et al., 2019). They achieved superior performance with fully connected shallow networks compared to conventional model approximation methods, such as proper orthogonal decomposition, while utilizing fewer sensors. He et al. proposed a ROM for fast prediction of natural convection of nanofluids in annulus pipes (He et al., 2022). They utilized U-net structure of deep convolutional neural networks (CNNs). The Nearest Wall Signed Distance Function is combined with numerical data to train the network for better geometry adaptation. A two-dimensional annulus is utilized to investigate the feasibility, accuracy, and stability of the proposed method. They reported that predicting the velocity field is somewhat more challenging than predicting the temperature field. However, error analysis showed that the proposed network model still achieves satisfactory results, with an average error of less than 1%. Wiewel et al. studied the temporal progression of physical functions of fluid flow problems using deep learning (Wiewel et al., 2019). Their approach uses the combination of learned latent spaces with Long Short-Term Memory (LSTM) to predict the temporal changes in the field solutions. To show the capabilities of the method, they predicted the temporal solutions of a series of liquid simulations and a set of single-phase buoyancy simulations. Using the developed data-driven solver, they achieved 150 times faster simulation time than a standard pressure solver. Kim et al. utilized CNN networks to train on various transient CFD simulations enabling the generation of fluid simulations from the reduced parameters (Kim et al., 2019). They ensured the condition of divergence-free is strictly met using stream functions. The resulting ROM facilitated the interpolation of CFD solutions and time advancement of an existing simulation. Authors also stated up to 700 times faster computation time compared to a CFD simulation. Thuerey et al. extended the application of ROM models to Reynolds-Averaged Navier-Stokes solutions of airfoil flows (Thuerey et al., 2020). They utilized U-net deep learning architecture using physics informed feature normalization to learn from velocity and pressure distribution, and to predict the field solution for unknown airfoil shapes. The paper also explored the impact of training data size and the number of weights on the model accuracy. In the context of glass furnace solutions, a similar application of machine learning methods has been investigated to enhance furnace operation support (Castillo and Kornish, 2017). The authors reported 98% accuracy in generating flow field and post-processed outputs. This body of work collectively demonstrates the growing significance of leveraging machine learning techniques to advance the capabilities of CFD-based reduced order models across diverse engineering domains.

This study focuses on leveraging machine learning methodologies, particularly autoencoders integrated with CNNs, applied to parametric CFD solution data. The primary objective is to represent the complex dynamics of the glass furnace CFD solution, consisting of 2D velocity and temperature fields, in lower dimensions within a latent space, and to predict new CFD solutions by using this reduced domain and up sampling of the decoder network. This approach enables rapid and accurate decision support for daily furnace operations using ROM-generated CFD solutions. The ROM developed using 2D solutions can serve as a baseline for developing a ROM for a full-scale furnace. The novelty of this study lies in the fact that, although ML-based ROMs have been applied to other thermal flow problems, to the authors' knowledge, this is the first time such a model has been applied to a glass furnace with a fully detailed process explanation. Additionally, this study explains the operational benefits of the reduced order model with well-detailed examples.

CFD MODEL

A CFD model of an end-fired glass melting furnace was constructed to generate training and test dataset for the machine learning-based ROM development process. Ansys Fluent 2022R2 is used to prepare the CFD model and to obtain parametric solutions. The results from this CFD model are used to train the ROM and evaluate the accuracy of the ROM-generated CFD predictions by comparing them with the ground-truth CFD solutions. For the sake of simplicity and computation time, a 2D representation of glass melting tank is generated. The schematic view of the furnace and the plane, which is the solution geometry, is shown in Figure 1. This simplified model focuses on the essential features of an industrial glass melting furnace, specifically targeting the middle plane of the melting

tank. Industrial type glass furnaces are typically more elongated in length and width compared to their height. Therefore, primary flow patterns occurs in the longitudinal direction and it is assumed that the problem can be studied as a long 2D cavity (Pigeonneau and Flesselles, 2012). The 2D model in this study includes raw batch melting interface and outlet section, where the molten glass proceeds to undergo further conditioning processes.

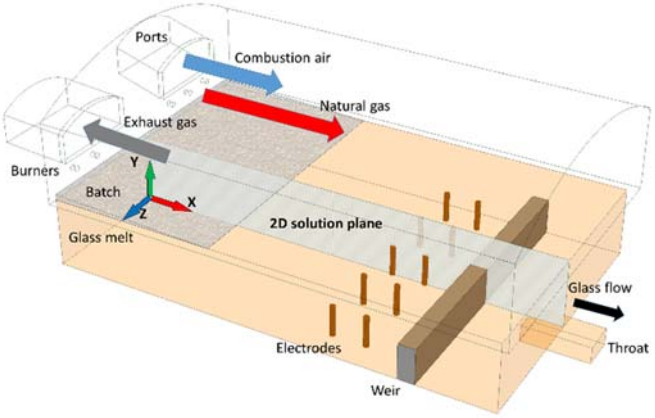

Figure 1. The schematic view of an end-fired glass melting furnace. The top part represents the combustion chamber, while the bottom part illustrates the glass melting tank. The 2D solution plane, which is the focus of the CFD study, is the middle plane of the melting tank along the flow direction.

In glass melting tanks, due to temperature differences within the domain, natural convection is dominant, and it creates characteristic flow currents, which enhances the homogenization process. In this 2D CFD demonstration, we aim to create the flow patterns with the presence of temperature differences; 1 - underneath the batch blanket and open melt surface and 2 - top and bottom sections of the glass domain. With the presence of the unique flow patterns, 2D CFD solutions can provide valuable insights into the operational dynamics of the glass melting furnace.

Governing Equations

The molten glass flow inside the furnace is mathematically described by the conservation Eq. 1-4 listed below (ANSYS Inc., 2022). Laminar flow is assumed due to the high viscosity of the melt under the operating conditions. Gravity source term must be added into the momentum equation to resolve buoyancy driven flow patterns (Schill and Chmelar, 2004).

Due to the high-temperature nature of the glass melt, radiative heat transfer is dominant within the domain. However, if complete absorption of radiation over the depth of the glass melt is assumed, the Rosseland approximation method can be used (Lankhorst et al., 2013). In this study, the glass melt is assumed to be optically thick, allowing the use of the Rosseland approximation (M. K. Choudhary and Potter, 2005). Effective thermal conductivity (k_{eff}) is used in the energy equation, which combines the effects of conductive and radiative heat transfer rates. Furthermore, the energy conservation equation introduces a source term (S_{joule}) to specifically address the joule heating effect resulting from electric current flow within the melt (Eq. 5) (ANSYS Inc., 2022; Matsuno et al., 2008).

To compute electric current, additional electric potential (φ) equation is solved, which describes potential field induced by electrodes immersed in the melt (M. Choudhary, 1985). The gradient of the electric potential yields the electrical current field. Natural Lorentz force is induced by the interaction between current density and magnetic flux in the vicinity of electrodes. This force acts only in the tiny area around the electrode tips and it is weaker compared to other forces such as gravitational and viscous forces. Therefore, it is ignored (Soubeih et al., 2015; Staněk, 1990). The product of the square of the electric current and electrical conductivity (σ) of the glass melt quantifies the joule heating output (Simons et al., 2008). High temperature thermophysical properties of the glass melt are given in Table 1.

$$\nabla.\vec{v} = 0 \quad (1)$$

$$\rho(\vec{v}.\nabla)\vec{v} = -\nabla p + \mu\nabla^2\vec{v} + \rho\vec{g} \quad (2)$$

$$\rho c_p(\vec{v}.\nabla)T = k_{eff}\nabla^2 T + S_{joule} \quad (3)$$

$$\nabla.(\sigma\nabla\varphi) = 0 \quad (4)$$

$$S_{joule} = \sigma|\nabla\varphi|^2 \quad (5)$$

Table 1. Thermophysical properties of the glass melt.

Density (kg/m³)	$\rho(T) = 2521 - 0.138T(K)$
Specific heat (J/kg.K)	1300
Effective thermal conductivity (W/m.K)	$k_{eff} = 556 - 0.87T(K) + 0.00036T(K)^2$
Viscosity (Pa.s) (M. K. Choudhary et al., 2018)	$\log(\mu) = -2.834 + \frac{4678.7}{T(K) - 504.6}$
Electrical conductivity (1/ohm.m)	$\sigma = -45.4 + 0.04T(K)$

Geometry and Mesh

A two-dimensional geometry is prepared to demonstrate change of velocity and temperature fields with the operational parameters (Figure 2). This is the middle plane of a typical glass packaging furnace including a batch blanket interface, a couple of electrode rods immersed from the bottom, a weir for flow separation between melting and refining sections, and an outlet. Batch partially covers the melt surface. That predetermined section serves as the inlet face. The rest of the top surface is open to combustion atmosphere. Therefore, constant heat flux boundary condition is applied on the open section. Usually, electrodes are inserted from the bottom into the furnaces. For simplicity, two electrodes are positioned before the weir to generate joule heating with the potential differences applied on their corresponding surfaces. Weirs are usually placed to adjust flow currents between the melting and refining zones. Following the weir is a throat which glass melt leaves through. There are additional structures such as working end and forehearth for further conditioning of the glass melt before molding. However, these structures are beyond the scope of this study. Essential dimensions of the glass melting tank are listed in Table 2. The dimensions are selected based on a packaging glass furnace with a specific pull rate of 2.5 t/day.m². This value corresponds to 100 t/day of molten glass for a furnace with 60 m² of melting area. Discretization uncertainty in the CFD model is evaluated following the method described by (Celik et al., 2008). The numerical uncertainty for the mesh in this study is calculated by comparing the converged temperature values at the outlet, resulting in an approximate relative error of 0.88% and an extrapolated relative error of 2.06%.

Table 2. Dimensions of the glass melting tank

Length	8000 mm
Glass depth (height)	1245 mm
Electrode diameter	100 mm
Electrode height	600 mm
Outlet depth	600 mm
Outlet opening	600 mm
Weir thickness	350 mm
Weir height	645 mm

Boundary Conditions and Parameters

Boundary conditions for CFD simulations are listed in Table 3. The inlet condition is constant velocity at the batch-melt interface derived from the furnace pull rate. It is assumed that batch is converted into glass melt at a constant temperature, and this constant temperature applied at the inlet boundary. A shear-free surface condition is applied at the rest of the top surface and heat flux boundary condition is applied to model the effect of the combustion atmosphere above. Heat loss at the walls of the tank is much smaller compared to the heat flux from the combustion space due to insulation layers installed on the furnace. Therefore, walls are assumed to be perfectly insulated in this CFD setup. The electric potential is kept at 0 V at the first electrode, while a positive potential value is applied on the second to create a potential difference within the domain, influencing the electric current distribution and, consequently, the joule heating effect. Electric current flux is assigned as zero on the other surfaces of the melting tank.

To generate a dataset for the training, validation and test of the ROM, three key parameters are selected. The first one is the inlet velocity, reflecting changes in the pull rate of the furnace. Second is the heat flux at the top surface. This parameter represents variations in fuel consumption within the combustion space. The third parameter is the potential difference between the electrodes capturing variations in the power output of the electrodes. The higher the electric potential between the electrodes, the more joule heating is generated. The values for these parameters are specified in Table 4.

Through systematic changes in these parameters, a total of 27 CFD solutions is obtained, constituting the training and validation dataset for the ROM development. Computation time of each case is approximately 30 minutes running on single central processing unit (CPU). The convergence of each solution is also determined based on whether the relative change in the temperature monitor at the outlet is below 1E-05, in addition to the convergence criteria of the residuals.

This dataset will serve as the foundation for training the ROM, enabling efficient exploration of the complex interactions within the glass furnace under diverse operational conditions. Test dataset is generated using the same model with the same operational parameters. Two sets of data are generated. The first one, namely interpolation cases, consists of solutions of parameters within the specified operational range. The second set, extrapolation cases, involves solutions that at least one parameter is out of the specified operational range. The details about the interpolation and extrapolation cases are given in the results section.

Table 3. Boundary conditions applied in the CFD model.

	Mass-Momentum	Energy
Inlet	3.01E-05 – 3.68E-05 m/s	1200 K
Outlet	0 Pa	1500 K for reverse flow
Top surface	Free surface	61.0-73.2 kW/m^2
Walls	No slip	0 W/m^2

Table 4. Operational parameters and their values. By interchanging the values, 27 CFD solutions are generated to train the ROM.

	Inlet velocity (m/s)	Heat flux (W/m^2)	Electric potential (V)
1	3.01E-05	61000	75
2	3.31E-05	67100	88
3	3.68E-05	73200	100

REDUCED ORDER MODEL

Convolutional Neural Networks (CNNs) have been selected as the foundation for developing the machine learning-based ROM due to their efficacy in reducing dimensionality with significantly fewer weights (network parameters) compared to fully-connected neural networks. This makes CNNs better suited for large-scale and high-dimensional problems (Gao et al., 2021). Another benefit of CNNs is their ability to leverage low-dimensional, high-level abstractions through convolution. The central concept of a CNN is to learn these representations and subsequently use a fully connected layer to map the relationship between the high-level representations and the output (Bhatnagar et al., 2019). The ROM leverages the inherent capabilities of CNNs to streamline the representation of complex field solutions. CFD solutions are sampled with a uniform grid over the solution domain, due to a major limitation of CNN. This limitation lies in the fact that traditional CNNs and their convolution operations were initially developed for processing images, which are sampled on a uniform grid (Chollet, 2021). However, problems with irregular domains are making the use of CNNs inapplicable and this constraint greatly restricts their use in general scientific problems. Rectangular shape of glass furnaces, especially the glass melting tanks, provides the opportunity to apply convolutional filters.

A deep convolutional autoencoder network is constructed to systematically reduce the dimensionality of the field solution of u and v velocity components and temperature, condensing it into a latent space, and subsequently predicting the u and v velocity, and the temperature fields from this reduced representation. This bow-tie structure of autoencoder is comprised of two integral components: the encoder and the decoder. The encoder's role is to efficiently compress the full-sized field data into a smaller, yet information-rich representation contained within the latent space. During the encoding phase, the size of the image is systematically reduced by half using strided convolutions. This process enables the network to capture information that is progressively more general and conceptual across an expanding set of feature channels (Thuerey et al., 2020). Conversely, the decoder is tasked with reconstructing a full-sized CFD-like data from the essential information stored in the latent space. The decoding phase of the network reverses the data reduction process, enhancing the image's spatial detail through up sampling layers while simultaneously decreasing the quantity of feature channels.

The latent space, essentially a low-dimensional representation of the CFD solution, captures the essential features required for accurate predictions. To establish the relationship between

changes in this low-dimensional representation and the corresponding alterations in boundary conditions (operational parameters), an auxiliary fully-connected neural network is introduced. This auxiliary network facilitates mapping of boundary conditions to the latent space, establishing the ROM's ability to predict the full flow field solution under varying operating conditions. Schematic representation of the described model is given in Figure 3.

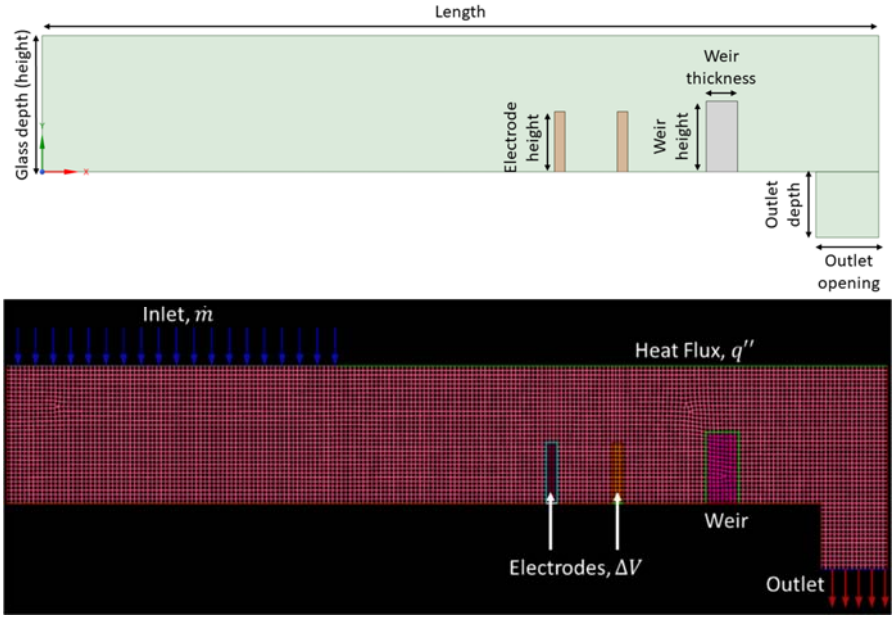

Figure 2. Geometry and mesh of the computational domain. The computational domain consists of glass melting tank including two electrodes, a weir, and a submerged outlet section.

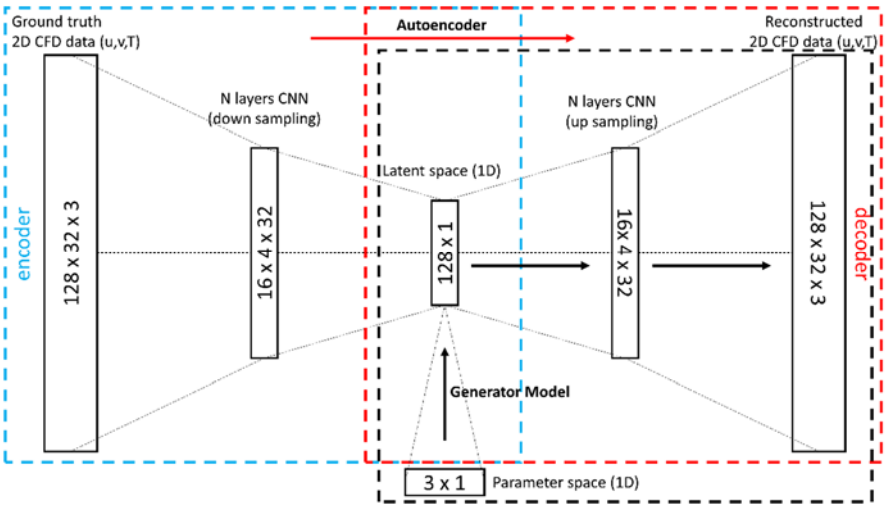

Figure 3. The schematic representation of the autoencoder and generator. The autoencoder takes the structured CFD solution data as input and aims to reconstruct the full CFD solution through its encoder and decoder sections. The generator model uses an auxiliary network, which establishes connection between parameter space (boundary conditions – operational parameters) and the latent space, and pre-trained decoder network to predict the CFD solution corresponding to the given boundary conditions.

Steps taken in this study to develop a successful machine learning-based ROM to predict CFD results using a parametric CFD solution dataset are given here:

1) A CFD model of the process is created.
2) Operational parameters and their range (boundary conditions for the CFD model) are defined. These parameters will be the inputs of the ROM.
3) Parametric CFD solutions are obtained based on the defined parameter range. Optionally, a design of experiments (DOE) method may be employed in this step for an efficient dataset generation.
4) From the parametric CFD solutions, a supervised training dataset is prepared. The CFD solutions are sampled to a 128×32 grid for CNN compatibility. The dataset is then split into training and validation dataset to prevent overfitting.
5) An autoencoder network is constructed using CNNs. This reconstructs CFD solutions by down sampling and up sampling the actual CFD data. This network is trained with the parametric CFD solution dataset.
6) A generator network is built by linking an auxiliary neural network, which connects the operational parameters to the latent space, with the pre-trained decoder from the autoencoder. This network takes operational parameters as inputs and predicts the corresponding CFD solution. During training, only the auxiliary network's weights are optimized. Once trained, this generator network acts as the ROM, predicting CFD solutions based on the input parameters.
7) Performance of the generator network (the ROM) is evaluated through interpolation and extrapolation tests. New set of parameters are defined for testing, and corresponding CFD solutions are obtained. The ROM's predictions for these new parameters are compared to the ground-truth CFD solutions.

Autoencoder

The input to the autoencoder consists of a 128x32 matrix with 3 channels representing u-velocity, v-velocity, and temperature. The CFD solutions are sampled with 128 nodes in X-direction and 32 nodes in Y-direction. Then each field solution concatenated to form the channels of input matrix. Prior to entering the autoencoder, each field is normalized to have values between 0 and 1. The normalization process involves using the minimum and maximum values from the training dataset for each field. This ensures consistent normalization for both training and test datasets.

A comprehensive study on latent space dimensions revealed that a latent space reduced to 128 dimensions is adequate for this specific problem. This dimensionality is found to be effective in extracting and retaining essential information about flow and temperature patterns from the CFD training data. The decoder, structured symmetrically to the encoder, takes an input of 128 variables and generates an output with the same dimensions (128x32 matrix with 3 channels). During the supervised training phase, the decoder is optimized to produce an output with minimal error compared to the input CFD data provided to the encoder. Mean squared error (MSE) loss function is used during training and mean absolute error (MAE) metric is also monitored. MSE and MAE is given by Eq. 6 and 7, respectively, where n is number of cells within the domain, y_i is the ground-thruth solution, and $\hat{y}_i$ is the solution predicted by the ROM (Abadi et al., 2015). Training dataset is split into training and validation sets to prevent overfitting during training, by selecting 5 CFD solutions out of 27 solutions for validation. MSE value of 6.55E-07 and MAE value of 5.85E-04 are obtained for the training data, while validation data resulted in an MSE of 2.10E-06 and MAE of 9.08E-04. After training, coefficient of determination (R^2) and average relative difference percentage (ARD%) scores are calculated using Eq. 8 and 9, respectively (Abooali and Khamehchi, 2019; Pedregosa et al., 2011). An R^2 score of 0.99 and ARD% of 0.20% are obtained for the validation cases. The supervised training runtime was 45 minutes completing 20k epochs using V100 graphics processing unit (GPU). The MSE changes over epochs for both training and validation data are given in Figure 4.

$$MSE = \frac{1}{n}\sum_{i=1}^{n}(y_i - \hat{y}_i)^2 \quad (6)$$

$$MAE = \frac{1}{n}\sum_{i=1}^{n}|y_i - \hat{y}_i| \quad (7)$$

$$R^2 = 1 - \frac{\sum_{i=1}^{n}(y_i - \hat{y}_i)^2}{\sum_{i=1}^{n}(y_i - \bar{y})^2} \quad (8)$$

$$ARD\% = \frac{100}{n}\sum_{i=1}^{n}\left|\frac{y_i - \hat{y}_i}{y_i}\right| \quad (9)$$

The layers of the autoencoder (encoder + decoder), with the input/output dimensions of each layer, are detailed in Table 5 and Table 6, respectively.

Hyperparameter optimization is a crucial step, involving the selection of appropriate activation functions, adjustment of the number of convolution filters, and tuning the kernel size of the filters. Additionally, strides are employed to downsize the input of the layers, with a stride of 2 halving the dimension in both x and y directions, ultimately reducing the size to 2. The ROM's training and test evaluation are completed using the best resulting hyperparameters, as listed in Table 5 and Table 6. The resulting network's encoder section has 7 CNN layers and a flattening layer to adjust the form of output matrix into a 128-dimensional vector. Symmetrically, the decoder section starts with a reshaping layer to transform the input into the correct form and then, 7 CNN layers follow to increase the dimensions to the sampled-CFD data size. The resulting autoencoder network has 123,663 weights (network parameters) to be optimized during training process.

Table 5. Encoder network parameters. There are 7 convolutional neural network layers and 1 reshaping layer to flatten the output tensor.

Input/Output				Kernel	Strides
x	y	Channel	Activation	x/y	x/y
128	32	3	SELU	4/4	1/1
128	32	64	SELU	4/4	2/2
64	16	32	SELU	3/3	2/2
32	8	32	SELU	2/2	2/2
16	4	32	SELU	2/2	2/1
8	4	32	SELU	2/2	2/1
4	4	32	SELU	2/2	2/2
2	2	32	SELU	2/2	-
-	-	128	-	-	-

Table 6. Decoder network parameters. The decoder network gradually increases the dimensions using transposed CNN networks, and finally reconstructs full-sized CFD data.

Input/Output				Kernel	Strides
x	y	Channel	Activation	x/y	x/y
-	-	128	-	-	-
2	2	32	SELU	2/2	2/2
4	4	32	SELU	2/2	2/1
8	4	32	SELU	2/2	2/1
16	4	32	SELU	2/2	2/2
32	8	32	SELU	3/3	2/2
64	16	32	SELU	4/4	2/2
128	32	64	Sigmoid	4/4	1/1
128	32	3	-	-	-

Generator Network: Auxiliary Neural Network + Decoder

Following the training phase of the autoencoder, an auxiliary dense neural network has been introduced before the decoder network. Fully-connected, dense neural network was utilized to express the nonlinear relationship between the boundary conditions and the latent space (Figure 3), consequently, the CFD solution. The auxiliary network consists of two layers with 2240 weights to be trained. The network takes a set of boundary conditions, structured as a 3x1 vector, as input and outputs a latent space vector sized 128x1, (Table 7). As mentioned previously, the primary objective of this auxiliary network is to establish a connection between the boundary conditions (parameters) and the latent space. To achieve this, an additional supervised training step is implemented to optimize the weights of the auxiliary network.

Table 7. Parameters of the auxiliary dense neural network placed before the pre-trained decoder. The auxiliary network establishes connection between operational parameters (boundary conditions) and latent space of the autoencoder network, which is also the input of the decoder network.

Layers	Input	Output	Weights
1	3	16	48
2	16	128	2048

It is important to note that, during this training process, the weights of the decoder network are kept constant. This decision is made because the decoder has already undergone training and optimization to generate accurate CFD solution data from the latent space. Keeping the decoder weights fixed ensures that the learned representation of the latent space is preserved and

consistently utilized during the training of the auxiliary network. Training dataset is again split into training and validation datasets to avoid overfitting. MSE loss function is used during training and MAE is also monitored. MSE value of 1.94E-06 and MAE value of 9.96E-04 are achieved for the training data. MSE value of 4.45E-06 and MAE value of 1.30E-03 are achieved for the validation data. R^2 and ARD% scores of 0.99 and 0.27% are obtained for the validation dataset, respectively. Runtime of the supervised training of the auxiliary + decoder network was 31 minutes, completing 30k epochs during that time, using V100 GPU. The change of MSE loss over epochs is given in Figure 5.

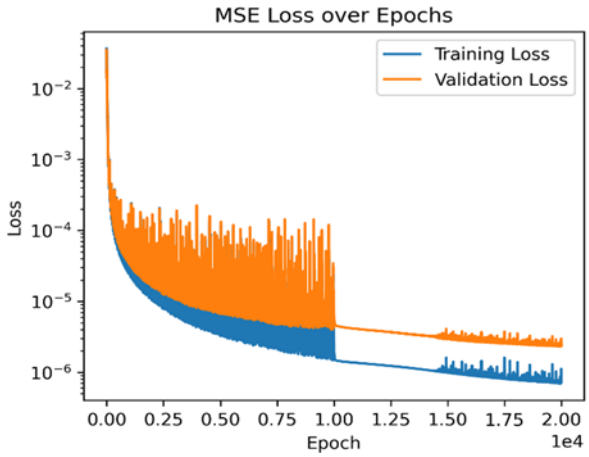

Figure 4. Change of Mean Squared Error (MSE) over epochs for training and validation dataset during supervised training of the autoencoder network. Y-axis in logarithmic scale.

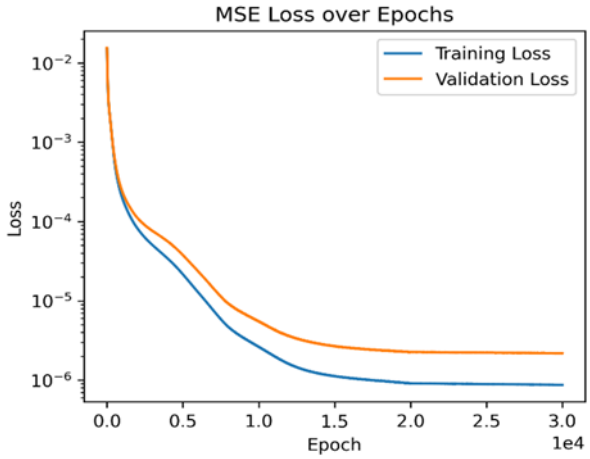

Figure 5. Change of Mean Squared Error (MSE) over epochs for training and validation dataset during supervised training of the generator: auxiliary neural network + decoder network. Y-axis in logarithmic scale.

RESULTS

The ROM's performance is rigorously assessed through both interpolation and extrapolation evaluations using an additional CFD dataset. Both interpolation and extrapolation cases are predicted less than a second using the generator (auxiliary + decoder) network, running on a V100 GPU. In the interpolation test phase, seven cases with randomly generated parameters are selected within the parameter range utilized during the training phase. These cases, detailed in Table 8, are aimed at showcasing the ROM's ability to consistently produce continuous and reliable results across various operational scenarios. This comprehensive demonstration illustrates the ROM's potential as a robust tool for supporting furnace operation, highlighting its capability to generate meaningful outputs within the specified parameter range.

For the extrapolation test, eight distinct cases, as listed in Table 9, are considered. The first two cases involve changes in potential difference beyond the training range, while keeping other parameters at the midpoint of their intervals. The subsequent two cases simulate variations in heat flux parameters, one below and one above the trained range. Case #5 and Case #6 represent changes in the inlet velocity outside of the training range. Finally, Case #7 and Case #8 examine scenarios where all parameters are set at their lowest and highest values, respectively. This selection of parameters for the extrapolation test simulates the ROM's performance when the furnace is operated outside the specified range – a scenario that may occur during actual operations due to various reasons.

Solution data predicted by the ROM for interpolation and extrapolation cases is compared with ground-truth CFD solutions. The error between the predicted and actual solutions is evaluated using several metrics and they are presented in Table 10. As expected, performance of the ROM in the extrapolation test, where the inputs are out of the specified operational range, is lower, than in the interpolation test. This is reflected in the increase in MSE and MAE values. While R^2 score change is negligible, the rise in ARD% score also indicates greater error in the extrapolation cases.

Table 8. Operational parameters of the interpolation cases to analyze interpolation performance of the ROM.

Case No.	Inlet velocity (m/s)	Heat flux (W/m^2)	Electric potential (V)
1	3.08E-05	62140	80
2	3.08E-05	72059	93
3	3.08E-05	72059	80
4	3.62E-05	62140	93
5	3.62E-05	62140	80
6	3.62E-05	72059	93
7	3.62E-05	72059	80

Table 9. Operational parameters of extrapolation cases to evaluate the performance of the ROM outside the defined operational range.

Case No.	Inlet velocity (m/s)	Heat flux (W/m^2)	Electric potential (V)
1	3.35E-05	67100	70
2	3.35E-05	67100	105
3	3.35E-05	59000	88
4	3.35E-05	75000	88
5	2.90E-05	67100	88
6	3.80E-05	67100	88
7	2.90E-05	59000	70
8	3.80E-05	75000	105

Table 10. Error metrics of the solutions predicted by the ROM for the interpolation and extrapolation test parameters.

Metrics	Interpolation Test	Extrapolation Test
MSE	2.82E-06	2.79E-05
MAE	1.24E-03	2.90E-03
R^2	0.99	0.99
ARD%	0.21%	3.59%

Interpolation Test Results

The results from the interpolation test dataset are summarized in Table 11. MAE and MSE metrics are computed for each test case. Notably, the average MAE value across all seven cases is consistently below 0.01 for all variables. Figure 6 shows the

histogram of the relative difference between the ROM's interpolation predictions and ground-truth CFD solutions. The error distribution approximates a normal distribution centered around 0.0, with the majority of errors falling below 0.005. The maximum error is observed in Case #2, where the heat flux is close to the highest value in the parameter range, and the potential difference above the midpoint value. Conversely, Case #7 exhibits the lowest prediction error among all test cases. Electric potential seems to influence this outcome; as higher values corresponds to larger prediction errors. The comparison between Case #4 and #5 confirms this conclusion. In general, a comparative analysis of prediction error of the cases indicates that cases with higher inlet velocity tend to have lower error. The MAE comparison between Case #2 and #6, and Case #3 and #7 supports this outcome.

Ground truth, generated field data, and error contours are presented in Figure 8 for u-velocity and temperature fields, focusing on Case #2 due to its larger error.

A detailed examination of the u-velocity field reveals distributed errors across the domain. However, high concentration of maximum and minimum errors occurs in regions associated with strong forward and backward flows – specifically, before the weir and beneath the inlet boundary condition, respectively. These types of errors are also reported by other studies, which link them to higher gradients in those regions (He et al., 2022; Thuerey et al., 2020). Despite these localized errors, the overall velocity patterns are accurately predicted, and contour lines exhibit a smooth profile. This suggests that the gradient of the predicted field can be effectively utilized for post-processing applications.

Similarly, a comparison is conducted for the temperature field, again focusing on Case #2. The generated temperature field closely resembles the ground-truth solution, albeit with more discontinuous behavior in the contour lines compared to the U-velocity field. However, peak error values for temperature are lower than those observed in the U-velocity field, and errors are more uniformly distributed across the domain.

Extrapolation Test Results

MAE and MSE values for all eight extrapolation test cases are compiled in Table 12. The error histogram for extrapolation cases is shown in Figure 7. While the error between the prediction and the ground-truth is still centered around 0.0, it is skewed and displays a wider range of both negative and positive errors. Case #8, characterized by the highest parameter values, exhibits the highest error for all field variables. In contrast, Case #7, with all parameters set to their minimum values, displays relatively lower error values. However, Case #2 stands out with the second-highest error in Mean Absolute Error (MAE), despite having only one extreme parameter value. When Case #7 and #8 are excluded, Case #1 and #2 exhibit the maximum error, with minimum and maximum electric potential as the input parameters, respectively. Changes in electric potential beyond the defined operational range notably increase the prediction error of the model. The ground truth field data, ROM-predicted field data, and error contours for Case #2 are presented in Figure 9 for u-velocity and temperature fields.

Comparing the generated u-velocity field with the ground-truth solution in Figure 9 reveals less similarity than observed in the interpolation test. False predictions are evident at the core of the forward and backward flows, yet the overall error for this case remains under 1% (MAE). The general flow patterns are generated without major issues, showcasing the model's ability to extrapolate beyond the trained parameter range. Stronger discontinuous behavior is observed in the contour lines for the generated temperature field compared to the results obtained in the interpolation test. Maximum error occurs at the bottom of the weir, where the temperature is over predicted, while temperature values in the vicinity of the outlet section are under predicted. Once again, the overall calculated error remains below 1% (MAE) for the extrapolation Case #2, indicating that the model maintains reasonable accuracy even in extrapolation scenarios.

Error distributions given in Figure 8 and Figure 9 show larger localized error for the velocity field than for the temperature field. However, MAE and MSE values for the velocity field are lower compared to those for the temperature field, as presented in Table 11 and Table 12. This finding also contradicts another result reported in the literature (He et al., 2022). As noted in the introduction section, machine learning methods, such as CNN, often function as black boxes, making it difficult to interpret results based on the underlying physics of the problem. Enhancing the physical interpretability of these models and incorporating the problem's physics into them remain a significant challenge (Masoumi-Verki et al., 2022).

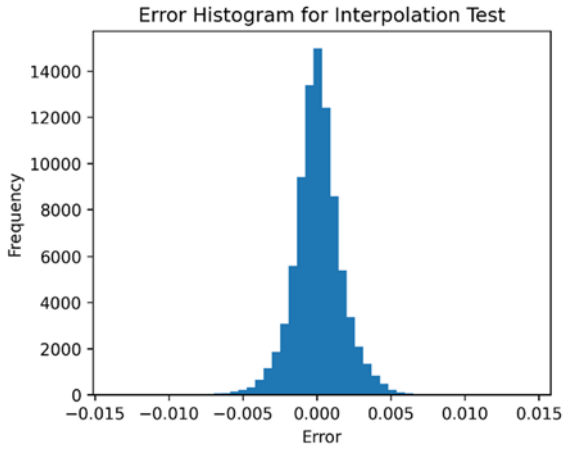

Figure 6. The histogram of differences between the normalized ground-truth interpolation CFD data and the predicted solution data displays a normal distribution.

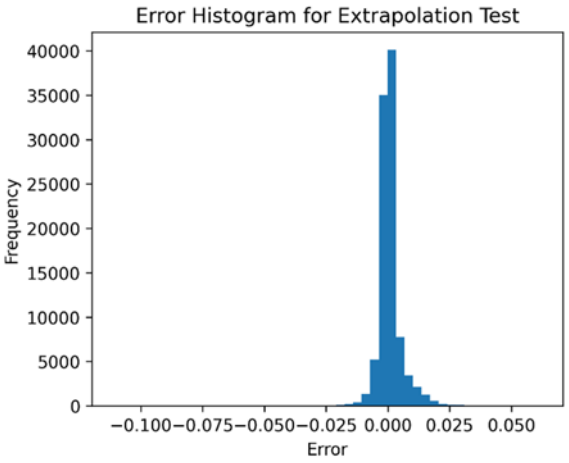

Figure 7. The histogram of differences between the normalized ground-truth extrapolation CFD data and the predicted solution data shows a skewed distribution. Larger negative and positive error values are present compared to those observed in interpolation test

Table 11. MAE and MSE obtained for each interpolation case and variable.

Interpolation Case No.	U-velocity		V-velocity		Temperature	
	MAE	MSE	MAE	MSE	MAE	MSE
1	1.21E-03	2.29E-06	7.63E-04	1.01E-06	1.94E-03	5.73E-06
2	1.96E-03	6.63E-06	9.84E-04	2.22E-06	1.93E-03	6.27E-06
3	1.12E-03	2.00E-06	7.90E-04	1.14E-06	1.49E-03	3.47E-06
4	1.33E-03	2.91E-06	8.55E-04	1.41E-06	1.35E-03	2.73E-06
5	1.19E-03	2.22E-06	7.25E-04	9.17E-07	1.82E-03	5.26E-06
6	1.32E-03	3.16E-06	8.20E-04	1.21E-06	1.58E-03	3.99E-06
7	9.83E-04	1.51E-06	6.75E-04	8.09E-07	1.22E-03	2.33E-06
Average	1.30E-03	2.96E-06	8.02E-04	1.25E-06	1.62E-03	4.25E-06
Deviation	2.02E-04	1.10E-06	7.25E-05	3.26E-07	2.37E-04	1.28E-06

Table 12. MAE and MSE obtained for each extrapolation case and variable.

Extrapolation Case No.	U-velocity		V-velocity		Temperature	
	MAE	MSE	MAE	MSE	MAE	MSE
1	1.70E-03	4.63E-06	9.58E-04	1.80E-06	3.99E-03	2.44E-05
2	7.17E-03	1.06E-04	2.76E-03	3.37E-05	5.55E-03	4.99E-05
3	1.45E-03	3.28E-06	9.83E-04	1.90E-06	2.46E-03	1.35E-05
4	1.42E-03	3.62E-06	8.93E-04	1.70E-06	1.56E-03	7.18E-06
5	1.08E-03	2.21E-06	7.91E-04	1.33E-06	1.41E-03	7.08E-06
6	1.16E-03	2.36E-06	8.19E-04	1.72E-06	1.90E-03	9.52E-06
7	3.51E-03	2.05E-05	1.79E-03	6.32E-06	4.68E-03	3.82E-05
8	8.93E-03	1.52E-04	3.60E-03	5.95E-05	9.07E-03	1.17E-04
Average	3.30E-03	3.69E-05	1.57E-03	1.35E-05	3.83E-03	3.34E-05
Deviation	2.43E-03	4.62E-05	8.57E-04	1.66E-05	1.99E-03	2.63E-05

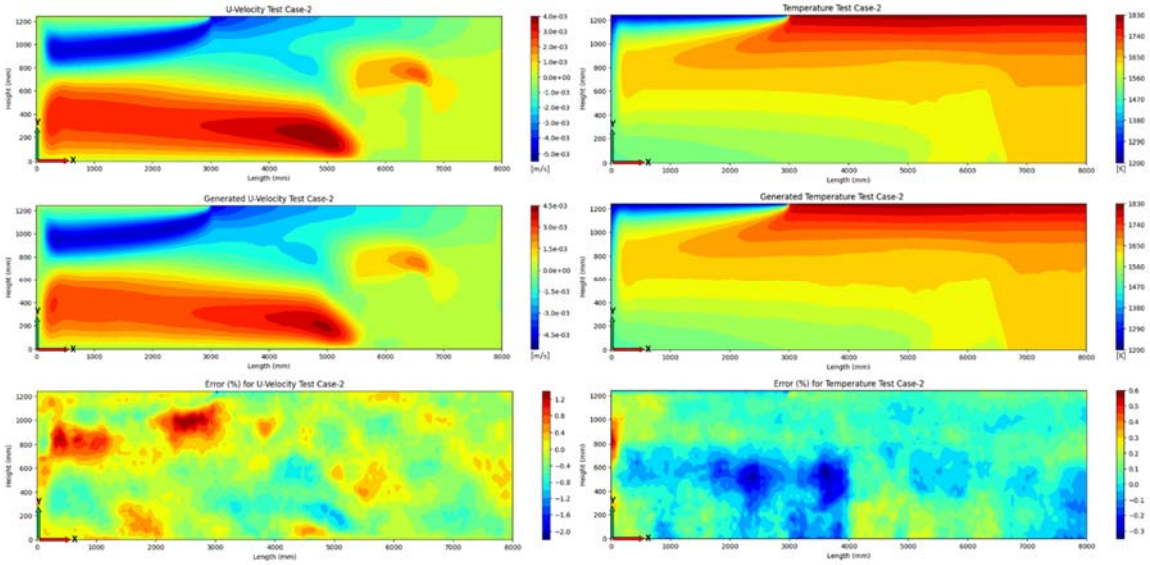

Figure 8. U-velocity and temperature contours for the interpolation Case #2 (top: CFD, middle: ROM, bottom: relative error)

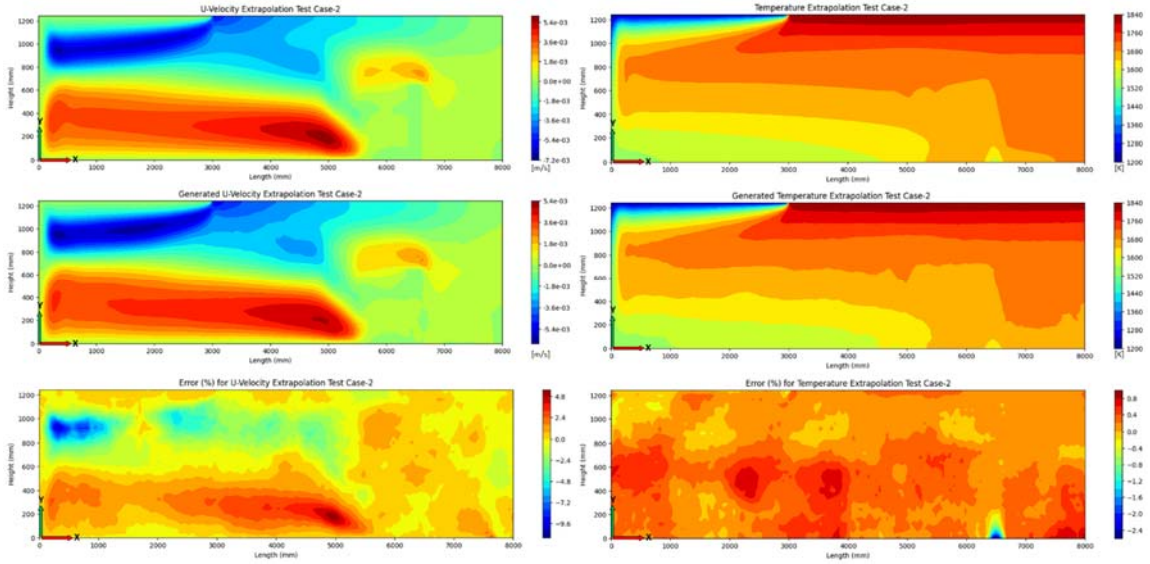

Figure 9. U-velocity and temperature contours for the extrapolation Case #2 (top: CFD, middle: ROM, bottom: relative error)

Using ROM for the Operational Analysis

The positive outcomes obtained from the interpolation and extrapolation test cases open the way for the effective use of the ROM in CFD-assisted operational analysis. Field solutions for velocity and temperature provide numerous opportunities to investigate the condition of the furnace and gain insights.

Similar to parametric CFD studies, a ROM, generated using parametric CFD solutions, can be utilized during furnace operations to address the physical phenomena encountered. The temperature predictions by the ROM, as shown in Figure 10, serve as an example to demonstrate this capability.

Thermocouples (T/C) positioned at the bottom of the tank are used to monitor temperature of the melt. In Figure 10, we see temperature predictions for a possible thermocouple location, which is at the bottom and where x equals to 7 m. The developed ROM can be used to predict temperature at that location and map the change of temperature within the specified operating range. Both an increase in the potential difference between the electrodes (x-axis) and an increase in the heat flux from the combustion space (y-axis) result in a higher temperature at the T/C location. However, the influence of the potential difference on the temperature is greater than that of the heat flux.

This kind of process requires several CFD solutions to obtain a result with satisfactory resolution. The developed ROM enables each CFD prediction to be made in under a second, thereby providing an opportunity for real-time support during furnace operation.

The results of another investigation conducted for the furnace operation using the developed ROM are presented in Figure 11 and Figure 12. In this scenario, the effects of an increase in power input from the combustion space and the electrodes on the depth-wise velocity and temperature profiles at the middle of the melting tank are examined.

Sequentially, the heat flux (denoted as heat flux+), the potential difference (denoted as potential+) and finally both of them are increased by 5%. The resulting profiles are plotted against the base-case to observe the influence of each power input and their combined effect. The resulting profiles are derived from the field solutions predicted by the ROM using the corresponding boundary conditions.

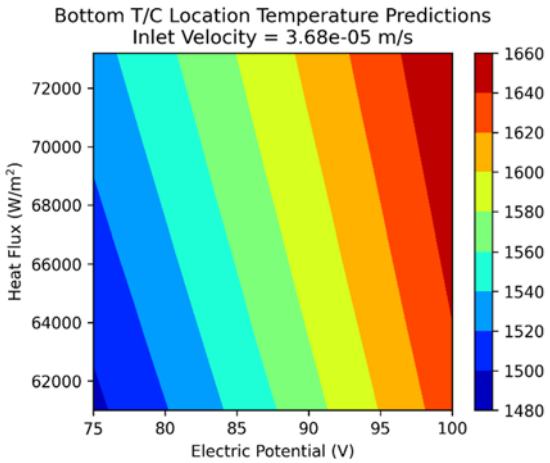

Figure 10. Continuous temperature predictions, generated by the ROM at the T/C location varying with changes in heat flux and potential difference. This demonstrates the on-demand information extraction capability within the operating range.

In Figure 11, a significant increase in the magnitude of backward and forward flow components is observed in the cases of increased potential difference, compared to a sole boost in heat flux.

Similar observation are made in Figure 12, which represents the depth-wise temperature profiles. The temperature difference is more apparent at the bottom section compared to the section near the glass surface. The overall increase in temperature leads to lower viscosity, which can be regarded as the root cause of the faster glass velocities.

These operational analysis examples demonstrate the post-processing capability of the machine learning-based ROMs. Thanks to the unprecedented interpolation feature of the ROMs, it is possible to extract more information than with conventional CFD post-processing.

CONCLUSION

This study presents a new method for integrating Computational Fluid Dynamics (CFD) models into the routine operations of industrial glass melting furnaces. The research achieves this through an autoencoder-based ROM with CNNs trained on parametric CFD data. A 2D CFD model is developed as a foundation for a machine-learning-based reduced-order model (ROM), demonstrating the potential of machine learning (ML) techniques to create efficient ROMs. Although glass melting in a furnace is inherently a 3D process, this study simplifies the analysis by using a 2D approach. Treating the 3D process as a series of 2D snapshots, this methodology can be extended to a 3D study using similar sampling techniques and convolutional neural networks, though a 3D study would involve a larger dataset and more network parameters to train. The developed generator network, i.e., the ROM, accurately predicts temperature and velocity fields, achieving MAE under 1% for validation, interpolation, and extrapolation tests compared to the ground-truth CFD solutions. Mean squared error is 1.94E-06 for training, 4.45E-06 for validation, 2.82E-06 for interpolation, and 2.79E-05 for extrapolation cases. In addition, R^2 score of 0.99 is achieved during training, validation and tests for the generator network. These results indicate ROM's potential as an accurate analysis tool for daily furnace operation, providing insights into key operational parameters. Furthermore, the ROM demonstrates significant improvements in solution time, enabling almost instantaneous solutions for temperature and velocity fields, which enhances its practical usefulness in real-time decision-making. Its robustness has been presented through interpolation and extrapolation tests, demonstrating consistent and reliable results across various operational scenarios.

This application of ML-based ROMs in glass furnace operations represents a substantial step forward in efficiency and optimization. However, a ROM based on CFD data is inherently constrained to the range of parameters it was trained on. Expanding the ROM to accommodate new parameters requires additional CFD data generation and model retraining. Additionally, while the ROM performs well within its trained parameter space, extrapolation beyond this range can lead to decreased accuracy, as demonstrated in this study. This limitation underscores the importance of careful ROM training to match the intended operational range. Overall, the integration of ML-based ROMs within industrial glass furnace operations showcases significant potential for broader applications in computational modeling and decision-support systems in various industrial contexts.

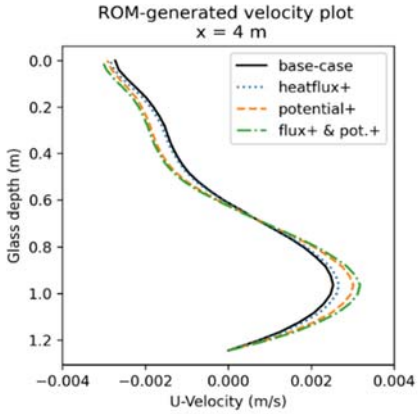

Figure 11. ROM-generated depth-wise u-velocity profiles at the middle of the melting tank. Velocity profiles change with the varying combustion space and electrical power input.

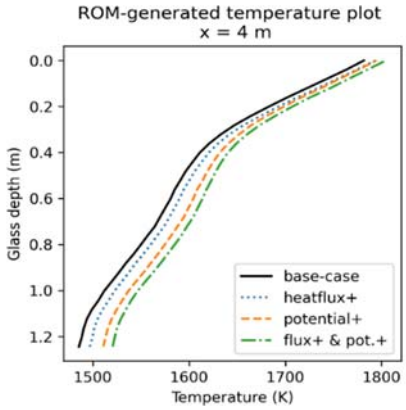

Figure 12. ROM-generated depth-wise temperature profiles at the middle of the melting tank, showing the effect of the varying energy input.

REFERENCES

Abadi, M., Agarwal, A., Barham, P., Brevdo, E., Chen, Z., Citro, C., Corrado, G. S., Davis, A., Dean, J., Devin, M., Ghemawat, S., Goodfellow, I., Harp, A., Irving, G., Isard, M., Jia, Y., Jozefowicz, R., Kaiser, L., Kudlur, M., … Zheng, X. (2015). *TensorFlow: Large-Scale Machine Learning on Heterogeneous Systems, Version 1.15*. https://www.tensorflow.org/

Abbassi, A., & Khoshmanesh, K. (2008). Numerical simulation and experimental analysis of an industrial glass melting furnace. *Applied Thermal Engineering*, 28(5–6), 450–459. https://doi.org/10.1016/j.applthermaleng.2007.05.011

Abooali, D., & Khamehchi, E. (2019). New predictive method for estimation of natural gas hydrate formation temperature using genetic programming. *Neural Computing and Applications*, 31(7), 2485–2494. https://doi.org/10.1007/s00521-017-3208-0

ANSYS Inc. (2022). *Ansys Fluent User's Guide*. https://www.ansys.com

Atzori, D., Tiozzo, S., Vellini, M., Gambini, M., & Mazzoni, S. (2023). Industrial Technologies for CO2 Reduction Applicable to Glass Furnaces. *Thermo*, 3(4), 682–710. https://doi.org/10.3390/thermo3040039

Bhatnagar, S., Afshar, Y., Pan, S., Duraisamy, K., & Kaushik, S. (2019). Prediction of aerodynamic flow fields using convolutional neural networks. *Computational Mechanics*, 64(2), 525–545. https://doi.org/10.1007/s00466-019-01740-0

Brunton, S. L., Noack, B. R., & Koumoutsakos, P. (2020). Machine learning for fluid mechanics. *Annual Review of Fluid Mechanics*, 52(1), 477–508. https://doi.org/10.48550/arXiv.1905.11075

Cassar, D. R., de Carvalho, A. C. P. L. F., & Zanotto, E. D. (2018). Predicting glass transition temperatures using neural networks. *Acta Materialia*, 159, 249–256. https://doi.org/10.1016/j.actamat.2018.08.022

Castillo, V., & Kornish, B. (2017). *Development of Reduced Glass Furnace Model to Optimize Process Operation*, Final Report CRADA No. TC02241.

Catsoulis, S., Singh, J.-S., Narayanan, C., & Lakehal, D. (2022). Integrating supervised learning and applied computational multi-fluid dynamics. *International Journal of Multiphase Flow*, 157, 104221. https://doi.org/10.1016/j.ijmultiphaseflow.2022.104221

Celik, I. B., Ghia, U., Roache, P. J., Freitas, C. J., Coleman, H., & Raad, P. E. (2008). Procedure for estimation and reporting of uncertainty due to discretization in CFD applications. *Journal of Fluids Engineering, Transactions of the ASME*, 130(7), 0780011–0780014. https://doi.org/10.1115/1.2960953

Cho, G., Wang, M., Kim, Y., Kwon, J., & Su, W. (2022). A physics-informed machine learning approach for estimating lithium-ion battery temperature. *IEEE Access*, 10, 88117–88126. https://doi.org/10.1109/ACCESS.2022.3199652

Chollet, F. (2021). *Deep learning with Python*. Simon and Schuster.

Choudhary, M. (1985). Three-dimensional Mathematical Model for Flow and Heat Transfer in Electric Glass Furnaces. *Heat Transfer Engineering*, 6(4), 55–65. https://doi.org/10.1080/01457638508939639

Choudhary, M. K., & Potter, R. M. (2005). Heat transfer in glass-forming melts. In L. D. Pye, A. Montenero, & I. Joseph (Eds.), *Properties of glass-forming melts* (pp. 249–294). Taylor & Francis Publications. https://doi.org/10.1201/9781420027310

Choudhary, M. K., Purnode, B., Lankhorst, A. M., & Habraken, A. F. J. A. (2018). Radiative heat transfer in processing of glass-forming melts. *International Journal of Applied Glass Science*, 9(2), 218–234. https://doi.org/10.1111/ijag.12286

Choudhary, M. K., Venuturumilli, R., & Hyre, M. R. (2010). Mathematical modeling of flow and heat transfer phenomena in glass melting, delivery, and forming processes. *International Journal of Applied Glass Science*, 1(2), 188–214. https://doi.org/10.1111/j.2041-1294.2010.00011.x

Cravero, C., & Marsano, D. (2023). Numerical Simulation of Melted Glass Flow Structures inside a Glass Furnace with Different Heat Release Profiles from Combustion. *Energies*, 16(10), 4187. https://doi.org/10.3390/en16104187

Daurer, G., Raič, J., Demuth, M., Gaber, C., & Hochenauer, C. (2022). Comprehensive and numerically efficient CFD model for bubbling in an industrial glass tank. *Chemical Engineering Research and Design*, 186, 82–96. https://doi.org/10.1016/j.cherd.2022.07.044

Erichson, N. B., Mathelin, L., Yao, Z., Brunton, S. L., Mahoney, M. W., & Kutz, J. N. (2019). Shallow learning for fluid flow reconstruction with limited sensors and limited data. *ArXiv Preprint* ArXiv:1902.07358. https://doi.org/10.1098/rspa.2020.0097

Faber, A.-J., Rongen, M., Lankhorst, A., & Meneses, D. D. S. (2020). Characterization of high temperature optical spectra of glass melts and modeling of thermal radiation conductivity. *International Journal of Applied Glass Science*, 11(3), 442–462. https://doi.org/10.1111/ijag.15116

Gao, H., Sun, L., & Wang, J.-X. (2021). PhyGeoNet: Physics-informed geometry-adaptive convolutional neural networks for solving parameterized steady-state PDEs on irregular domain. *Journal of Computational Physics*, 428, 110079. https://doi.org/10.1016/j.jcp.2020.110079

Han, J., Li, L., Wang, J., Chen, S., Liu, C., & Li, C. (2022). Simulation and evaluation of float glass furnace with different electrode positions. *Journal of the American Ceramic Society*, 105(12), 7097–7110. https://doi.org/10.1111/jace.18700

He, X.-J., Yu, C.-H., Zhao, Q., Peng, J.-Z., Chen, Z.-H., & Hua, Y. (2022). Reduced order modelling of natural convection of nanofluids in horizontal annular pipes based on deep learning. *International Communications in Heat and Mass Transfer*, 138, 106361. https://doi.org/10.1016/j.icheatmasstransfer.2022.106361

Jebava, M., & Němec, L. (2018). Role of glass melt flow in container furnace examined by mathematical modelling. *Ceram-Silik*, 62, 86–96. https://doi.org/10.13168/cs.2017.0049

Kim, B., Azevedo, V. C., Thuerey, N., Kim, T., Gross, M., & Solenthaler, B. (2019). Deep fluids: A generative network for parameterized fluid simulations. *Computer Graphics Forum*, 38(2), 59–70. https://doi.org/10.1111/cgf.13619

Lankhorst, A. M., Thielen, L., Simons, P. J. P. M., & Habraken, A. F. J. A. (2013). Proper modeling of radiative heat transfers in clear glass melts. *73rd Conference on Glass Problems*, 249–258. https://doi.org/10.1002/9781118710838.ch19

Li, L., Han, J., Lin, H.-J., Ruan, J., Wang, J., & Zhao, X. (2020). Simulation of glass furnace with increased production by increasing fuel supply and introducing electric boosting. *International Journal of Applied Glass Science*, 11(1), 170–184. https://doi.org/10.1111/ijag.13907

Masoumi-Verki, S., Haghighat, F., & Eicker, U. (2022). A review of advances towards efficient reduced-order models (ROM) for predicting urban airflow and pollutant dispersion. *Building and Environment*, 216, 108966. https://doi.org/10.1016/j.buildenv.2022.108966

Matsuno, S., Iso, Y., Uchida, H., Oono, I., Fukui, T., & Ooba, T. (2008). CFD modeling coupled with electric field analysis for joule-heated glass melters. *Journal of Power and Energy Systems*, 2(1), 447–455. https://doi.org/10.1299/jpes.2.447

Molinaro, R., Singh, J.-S., Catsoulis, S., Narayanan, C., & Lakehal, D. (2021). Embedding data analytics and CFD into the digital twin concept. *Computers & Fluids*, 214, 104759. https://doi.org/10.1016/j.compfluid.2020.104759

Mücke, N. T., Bohté, S. M., & Oosterlee, C. W. (2021). Reduced order modeling for parameterized time-dependent PDEs using spatially and memory aware deep learning. *Journal of Computational Science*, 53, 101408. https://doi.org/10.1016/j.jocs.2021.101408

Paszke, A., Gross, S., Chintala, S., Chanan, G., Yang, E., DeVito, Z., Lin, Z., Desmaison, A., Antiga, L., & Lerer, A. (2017). *Automatic differentiation in pytorch*.

Pazarlioglu, H. K., Tepe, A. Ü., & Arslan, K. (2022). Optimization of Parameters Affecting Anti-Icing Performance on Wing Leading Edge of Aircraft. *European Journal of Science and Technology*. https://doi.org/10.31590/ejosat.1062495

Pedregosa, F., Varoquaux, G., Gramfort, A., Michel, V., Thirion, B., Grisel, O., Blondel, M., Prettenhofer, P., Weiss, R., Dubourg, V., Vanderplas, J., Passos, A., Cournapeau, D., Brucher, M., Perrot, M., & Duchesnay, É. (2011). Scikit-learn: Machine Learning in Python. *Journal of Machine Learning Research*, 12(85), 2825–2830. http://jmlr.org/papers/v12/pedregosa11a.html

Pfaff, T., Fortunato, M., Sanchez-Gonzalez, A., & Battaglia, P. W. (2020). Learning mesh-based simulation with graph networks. *ArXiv Preprint* ArXiv:2010.03409.

Pigeonneau, F., & Flesselles, J.-M. (2012). Practical laws for natural convection of viscous fluids heated from above in a shallow cavity. *International Journal of Heat and Mass Transfer*, 55(1–3), 436–442. https://doi.org/10.1016/j.ijheatmasstransfer.2011.09.057

Pigeonneau, F., Pereira, L., & Laplace, A. (2023). Dynamics of rising bubble population undergoing mass transfer and coalescence in highly viscous liquid. *Chemical Engineering Journal*, 455, 140920.

Pokorny, R., Hrma, P., Lee, S., Klouzek, J., Choudhary, M. K., & Kruger, A. A. (2020). Modeling batch melting: Roles of heat transfer and reaction kinetics. *Journal of the American Ceramic Society*, 103(2), 701–718. https://doi.org/10.1111/jace.16820

Pokorny, R., Pierce, D. A., & Hrma, P. (2012). Melting of glass batch: model for multiple overlapping gas-evolving reactions. *Thermochimica Acta*, 541, 8–14. https://doi.org/10.1016/j.tca.2012.04.020

Raič, J., Gaber, C., Wachter, P., Demuth, M., Gerhardter, H., Knoll, M., Prieler, R., & Hochenauer, C. (2021). Validation of a coupled 3D CFD simulation model for an oxy-fuel cross-fired glass melting furnace with electric boosting. *Applied Thermal Engineering*, 195, 117166. https://doi.org/10.1016/j.applthermaleng.2021.117166

Rowley, C. W., & Dawson, S. T. M. (2017). Model reduction for flow analysis and control. *Annual Review of Fluid Mechanics*, 49(1), 387–417. https://doi.org/10.1146/annurev-fluid-010816-060042

Schill, P., & Chmelar, J. (2004). Use of computer flow dynamics in glass technology. *Journal of Non-Crystalline Solids*, 345, 771–776. https://doi.org/10.1016/j.jnoncrysol.2004.08.199

Simcik, M., & Ruzicka, M. C. (2015). CFD model for pneumatic mixing with bubble chains: Application to glass melts. *Chemical Engineering Science*, 127, 344–361. https://doi.org/10.1016/j.ces.2015.01.052

Simons, P., Jochem, K., & Aiuchi, K. (2008). A power consistent mathematical formulation for Joulean heat release. *Glass Technology-European Journal of Glass Science and Technology Part A*, 49(3), 109–118.

Soubeih, S., Luedtke, U., & Halbedel, B. (2015). Improving residence time distribution in glass melting tanks using additionally generated Lorentz forces. *J. Chem. Chem. Eng*, 9, 203–210. https://doi.org/10.17265/1934-7375/2015.03.006

Staněk, J. (1990). Problems in electric melting of glass. *Journal of Non-Crystalline Solids*, 123(1), 400–414. https://doi.org/10.1016/0022-3093(90)90812-Z

Taşkesen, E., Dirik, M., Tekir, M., & Pazarlioğlu, H. K. (2023). Predicting heat transfer performance of Fe3O4-Cu/water hybrid nanofluid under constant magnetic field using ANN. *Journal of Thermal Engineering*, 9(3), 811–822. https://doi.org/10.18186/thermal.000000

Thuerey, N., Weißenow, K., Prantl, L., & Hu, X. (2020). Deep learning methods for Reynolds-averaged Navier–Stokes simulations of airfoil flows. *AIAA Journal*, 58(1), 25–36. https://doi.org/10.2514/1.J058291

Viskanta, R. (1994). Review of three-dimensional mathematical modeling of glass melting. *Journal of Non-Crystalline Solids* (Vol. 177). https://doi.org/10.1016/0022-3093(94)90549-5

Wiewel, S., Becher, M., & Thuerey, N. (2019). Latent space physics: Towards learning the temporal evolution of fluid flow. *Computer Graphics Forum*, 38(2), 71–82. https://doi.org/10.48550/arXiv.1802.10123

Zhang, R., Liu, Y., & Sun, H. (2020). Physics-guided convolutional neural network (PhyCNN) for data-driven seismic response modeling. *Engineering Structures*, 215, 110704. https://doi.org/10.1016/j.engstruct.2020.110704

Zier, M., Stenzel, P., Kotzur, L., & Stolten, D. (2021). A review of decarbonization options for the glass industry. *Energy Conversion and Management: X*, 10(February), 100083. https://doi.org/10.1016/j.ecmx.2021.100083

Journal Homepage: https://dergipark.org.tr/tr/pub/isibted

Isı Bilimi ve Tekniği Dergisi

Archive: https://tibtd.org.tr/dergi

Extended Second Law Analysis for Turboramjet Engines

Sara FAWAL [1, *], Ali KODAL [2]

[1] *Department of Aeronautical Engineering, İstanbul Gelişim Üniversitesi, Cihangir Mah., Avcılar / İstanbul*
[2] *Department of Aeronautical Engineering, İstanbul Gelişim Üniversitesi, Cihangir Mah., Avcılar / İstanbul*

A R T I C L E I N F O

2025, vol. 45, no.1, pp. 69-83

doi: 10.47480/isibted.1516527

Research Article
Received: 15 July 2024
Accepted: 14 December 2024

* *Corresponding Author*
e-mail: sfawal@gelisim.edu.tr

Keywords:
Brayton Cycle
TBCC Propulsion Performance
Maximum Power
EPLOS and PLOS

ORCID Numbers in author order:
0000-0002-2700-1682
0000-0001-7867-9672

A B S T R A C T

Turbine based combined cycles (TBCC) monopolizes the benefits from the two different thermodynamic cycle configurations involved. The TBCC, which is based on an irreversible Brayton cycle, considered in this study is a wraparound configuration turboramjet engine. The turboramjet can be utilized in either turbojet (afterburner (AB) being ON or OFF), ramjet and even dual mode operation. However, for the dual mode operation the turbojet engine AB are considered to be ON. In addition, the ramjet thermodynamic assessment considers multi-oblique shock and single normal shock solution and Rayleigh flow calculation for the combustion chamber. The performance analysis and comparison for the turboramjet engine for dual mode operation is based on a maximum power approach under variations of Mach number and altitude. Moreover, the dual mode operation considered variations of inlet air mass flow; the split of air mass flow between the turbojet and ramjet. In addition, a brief comparison is provided of the turbojet while the afterburner is in ON or OFF mode utilizing the maximum power, EPLOS and PLOS optimization functions for variations of altitude and Mach number. Moreover, a component based evaluation under maximum power conditions for variation of Mach number is provided. The turbojet with an AB shows greater advantage at Mach number higher than unity as well as attaining maximum power outputs at minimum PLOS for lower compressor ratio parameters (θ_c). Whereas the turboramjet indicates that as the split of inlet air mass flow to the ramjet is increased beyond 50% the advantage in terms of η_{th}, η_o, f, TSFC, I_a, thrust and v_{NOZZLE} far supersede that of the turbojet with an AB.

Turboramjet Motorları için Genişletilmiş İkinci Yasa Analizi

M A K A L E B İ L G İ S İ

Anahtar Kelimeler:
Brayton Çevrm
TBCC İtki Performans
Maximum Güç
EPLOS ve PLOS

Ö Z E T

Türbin tabanlı birleştirilmiş çevrimler (TBCC), iki farklı termodinamik çevrim konfigürasyonundan faydalarını tekelleştirir. Bu çalışmada ele alınan TBCC bir turboramjet motoru, tersinmez bir Brayton çevrimi sahiptir ve sarmalayıcı konfigürasyonludur. Turboramjet, turbojette (art yakıcı (AB) AÇIK veya KAPALI), ramjette ve hatta çift modlu çalışmada kullanılabilir. Ancak, çift modlu çalışma için turbojet motoru AB'nin AÇIK olduğu kabul edilir. Ek olarak, ramjet termodinamik değerlendirmesi, çoklu eğik şok ve tek normal şok çözümünü ve yanma odası için Rayleigh akış hesaplamasını dikkate alır. Çift modlu çalışma için turboramjet motorunun performans analizi ve karşılaştırması, Mach sayısı ve irtifa değişiklikleri altında maksimum güç yaklaşımına dayanmaktadır. Dahası, çift modlu çalışma, giriş hava kütlesi akışındaki değişiklikleri; hava kütlesi akışının turbojet ve ramjet arasında bölünmesini dikkate alır. Ek olarak, turbojetin, irtifa ve Mach sayısının değişimleri için maksimum güç, EPLOS ve PLOS optimizasyon fonksiyonlarını kullanarak, art yakıcı AÇIK veya KAPALI modundayken kısa bir karşılaştırması sağlanır. Ayrıca, Mach sayısının değişimi için maksimum güç koşulları altında bileşen tabanlı bir değerlendirme sağlanır. AB'li turbojet, daha düşük kompresör oranı parametreleri (θ_c) için minimum PLOS'ta maksimum güç çıkışlarına ulaşmanın yanı sıra birlikten yüksek Mach sayısında daha büyük avantaj gösterir. Turboramjet ise, ramjet'e giden giriş hava kütlesi akışının bölünmesi %50'nin üzerine çıktıkça, η_{th}, η_o, f, TSFC, I_a, itki ve v_{NOZZLE} açısından avantajın AB'li turbojetin çok ötesine geçtiğini gösterir.

NOMENCLATURE

AB	AB Afterburner
ALT	Altitude (km)
EPLOS	Effective Power Loss Parameter
MP	Maximum power (kW)
F_s	Specific Thrust (N-s/kg)
I_a	Air Specific Impulse (s)
$\dot{m}_a$	Inlet Mass flow of air (kg/s)
$\dot{m}_{fb}$	Fuel Mass flow of Burner (kg/s)
$\dot{m}_{fAB}$	Fuel Mass flow of Afterburner (kg/s)
PLOS	Power Loss Parameter
Q_R	Fuel Heating Value (kJ/kg)
$\dot{Q}_{HT}$	Total Heat Transfer (kJ/s)
$\dot{Q}_{LT}$	Total Heat Rejection (kJ/s)
$\dot{Q}_{LK}$	Rate of Heat Leak (kJ/s)
ST	Specific Thrust (N-s/kg)
TBCC	Turbine Based Combined Cycle
TSFC	Thrust Specific Fuel Consumption (kg/N-s)
T_H	Temperature of Hot Reservoir (K)
T_L	Temperature of Cold Reservoir (K)
η_b	Burner Efficiency
η_c	Compressor Efficiency
η_i	Intake/Diffuser Efficiency
η_j	Jet/Nozzle Efficiency
η_m	Mechanical Efficiency
η_p	Propulsive Efficiency
η_t	Turbine Efficiency
η_{th}	Thermal Efficiency
f_b	Fuel to Air Ratio of Burner
f_{ab}	Fuel to Air Ratio of Afterburner
f_r	Fuel to Air Ratio of Ramjet
θ_c	Compression Ratio Parameter
M_∞	Flight Mach Number
v_{NOZZLE}	Specific Volume (m^3/kg)

INTRODUCTION

In terms of the ramjet, turbojet with afterburner and turbine based combined cycle (TBCC) engines, researchers have used the application of exergy exploration on various aspects in accordance to task requirements. (Şöhret et al. 2017) applied an exergy efficiency analysis for a ramjet engine using hydrogen fuel on a component (inlet, combustion zone and nozzle) and overall engine level. (Latypov 2009) conducted an exergy investigation based on various energy supplies to the air flow of the ramjet duct. (Latypov 2013) also assessed the specific impulse and thrust-economic characteristics of the ramjet using exergy analysis. (Ayaz and Altuntaş 2017) used exergy analysis on a generic ramjet engine under three different Mach regimes. (Moorhouse 2003) expanded the exergy method to the design of a complete aircraft vehicle based on mission requirements including component level evaluation. (Moorhouse and Suchomel C. F. 2001) further expands his study to the application of hypersonic vehicle design as an energy problem. (Moorhouse et al. 2002) also applied the exergy concept to the hypersonic inlet flow problem to determine the optimal shock-on-lip position for off-nominal flight condition. (Marley and Riggins D. W. 2011) also made use of exergy evaluation for a combined ramjet and turbojet engine during transient manoeuvres as well as the wake region of the turbojet engine. (Ispir et al. 2020) used an exergy simulation based platform for the thermodynamic cycle and performance optimization of the STRATOFLY MR3 aircraft vehicle in DMR mode, ATR combustor, regenerator, nozzle, turbomachinery components and air turbo rocket bypass line. (Ehtaei et al. 2013) utilized an exergy approach for a turbojet engine with an afterburner (J85-GE-21) on a component level where the highest exergy efficiency was observed for the compressor and nozzle. (Roth and Marvis 2000) considered the loss management method for the analysis and quantification of technology impact of the F-5E/J85-GE-21 engine/airframe combinations and its relation to vehicle mass properties (weight). (Camberos and Moorhouse 2011) have published a book specifically describing the advantage of exergy analysis in the field of astronautics and aeronautics for various types of propulsion systems and even applying the concepts of exergy to airfoil drag evaluation. (Hayes et al. 2017) showed that exergy can be adopted to various aspects in aerospace including design, performance and thermodynamic analysis of commercial aerospace systems, propulsion systems, aerodynamic and structural optimization, multi-disciplinary optimization based on the Breguet equation and mapping exergy over a variable flight envelope. (Riggins and Taylor 2006) also makes use of the laws of thermodynamics for the evaluation of a hyperspace vehicle applicable to both ramjets or scramjets using individual stream tubes as components within the overall fluid control volume. (Balli 2017) conducted a study of exergy destruction rates within engine components which were split into endogenous/exogenous and avoidable/unavoidable parts on a military turbojet engine with afterburner. (Balli 2017) then used the J85 turbojet engine with afterburner to assess the performance, exergetic, exergoeconomic, sustainability and environmental damage cost at Idle (ID), Intermediate (INT), Military (MIL) and Afterburner (AB) operation modes. (Balli 2014) further considered the afterburning effect on energetic and exergetic performance of an experimental Turbojet Engine (TJE) and to determine thermodynamic inefficiencies at military (MIL) and afterburner (AB) operation modes. (Akkaya et al. 2007) defined an exergetic performance coefficient (EPC) to assess a fuel cell power generation system (fuel cell stack, afterburner, fuel and air compressors, and heat exchangers) fed by hydrogen. (Yüksel et al. 2020) evaluated the exergetic analyses at Military (MIL) and Afterburner (AB) process modes of the (J85-GE-5H) military turbojet engine using kerosene (JP-8) and hydrogen (H2) fuels. (Balli and Güneş 2017) conducted a performance assessment for both MIL and AB operation modes; and while under afterburner operation, examined energetic and exergetic performances and the effects on the environmental, ecological and sustainability metrics of the engine. (Akkaya et al. 2008) utilize an exergetic performance coefficient (EPC) for a gas turbine to investigate design parameters including fuel utilization, current density, recuperator effectiveness, compressor pressure ratio and pinch point temperature, to achieving higher exergy output with lower exergy loss in the system. (Bastani et al. 2015) applied exergy analysis and showed that the greatest exergy loss is in the afterburner due to its high irreversibility; therefore, the optimization of afterburner has an important role in reducing the exergy loss of total turbojet engine cycle.

(Yüksel et al. 2020) conducted an exergy-based economic and sustainability analysis for a (J85-GE-5H) military turbojet engine (TJE) using kerosene and H2 fuel under MIL and AB regimes where higher exergy destruction occurred in the afterburner exhaust duct (ABED) and combustion chamber (CC) which led to higher exergy destruction costs. (Niknamian 2020) exergy analysis on J85-GE-21 turbojet engine and system optimization based on PSO (Particle Swarm Optimization) methods which showed that highest and lowest exergy efficiency of the engine components corresponded to the diffuser and compressor respectively. (Sürer and Arat 2018) performed a critical mini review exergy analyses of jet engines which concluded that if there is no afterburner, the combustion chamber has the greatest exergy destruction and thus minimum exergy efficiency due to its highly thermodynamically irreversible process; whereas the presence of an afterburner constitutes the biggest exergy destruction and smallest exergy efficiency. (Dong et al. 2018) revealed that the exergy analysis method can be used as a direct indication of the weaknesses of an entire energy system, reveal the interactions among system components and estimate the realistic work potential of different subsystems; it also provides a significant guidance for the improvement of engine performance, reduction of fuel consumption and optimization of engine combustion. (Noori et al. 2015) made use of four objective functions (F_s, TSFC, η_{th} and η_p) for the optimization of an ideal turbojet engine with afterburner. (Nasab and Ehyaei 2019) conducted an exergy analysis for the J85-GE-21 turbojet engine with afterburner where the highest exergy efficiency was demonstrated by the diffuser and the lowest belonged to the compressor. (Liu et al. 2023) performed a cycle optimization of a turboramjet to determine the optimal switch point in terms of both altitude and Mach number between the turbojet and ramjet. (Rajashankar et al. 2024) performed a switch point analysis for an engine component optimization of the turbojet for a set mass flow such that the desired thrust at the handover point to the ramjet is achieved. (Xi et al. 2023) investigated a thrust augmentation control schedule during mode transition of a turboramjet engine based on the air inlet, available airflow and the engine demand airflow. In latest developments, (Lockheed Martin 2024) is designing the successor of the TBCC wrap around type configuration SR-71 (maximum Mach 3.3) as an intelligence, surveillance and reconnaissance (ISR) hypersonic aircraft with an under over type configuration utilizing a turbine engine at low speeds and a scramjet engine at high speeds (maximum Mach 6); the succesor aircraft is called the SR-72 and also denoted as the "Son of Blackird" or "Darkstar".

It is clear that the use of exergy as an analysis tool provides an advantage in the evaluation and optimization of aircraft gas turbine propulsion systems. Identification of the level of exergy destruction can be made on a component level and subsequently exploit optimization functions for the improvement of TSFC, ST, η_{th} and η_p thus reducing the ecological impact of aircraft based engines on the environment.

This paper presents two case studies for various gas turbine engine configurations where the performance analysis and comparison takes a shift towards the more constraining parameters which are primarily Mach number and altitude. Case I begins with the performance evaluation on a maximum power basis between a turbojet with and without an AB, in addition to utilizing the PLOS and EPLOS optimization functions as previously defined by (Fawal and Kodal 2019, 2021). Moreover, the size variation of individual engine components amongst both engine configurations was evaluated. Subsequently, Case II examines the performance of the TBCC turboramjet wraparound configuration was also evaluated on a maximum power basis for dual mode operation. In dual mode operation assessments were made for variations of altitude and inlet air mass flow; the split of air mass flow between the turbojet and ramjet. Note that in dual mode operation the turbojet engine AB are considered to be ON.

THEORETICAL REPRESENTATION

The basis of the turboramjet powerplant with an afterburner (AB) depends on the irreversible Brayton configuration and its T-s diagram are illustrated in Figure 1. The fundamental precept of this Brayton configuration has all the same processes as the turbojet with and without an AB and the ramjet. As previously stated the turboramjet engine with an AB operates amongst a heat source at high temperature, T_H, and a heat sink at low temperature, T_L. In the AB configuration there are two ($\dot{Q}_{H1}$) rates of heat transferred from the heat source to the turbojet engine; in the ramjet mode only one ($\dot{Q}_{H2}$) rate of heat is transferred from the high temperature source; however, there is still only one ($\dot{Q}_L$) rate of heat is dissipated to the heat sink from the turboramjet powerplant with an AB. Figure 1b also depicts the various engine thermodynamic cycle configurations: turbojet without an AB (**orang**); turbojet with an AB (**black**) and ramjet (**green**).

Similar to the turbojet with an AB and ramjet engines the performance analysis and comparison for the turboramjet engine also takes a transformation towards Mach number and altitude. Moreover, the **dual** mode operation was considered and assessed as variations of altitude and inlet air mass flow; the split of air mass flow between the turbojet and ramjet. Note that in dual mode operation the turbojet engine AB are considered to be ON. In addition, the performance evaluations have also been assessed under a maximum power regime for the turboramjet.

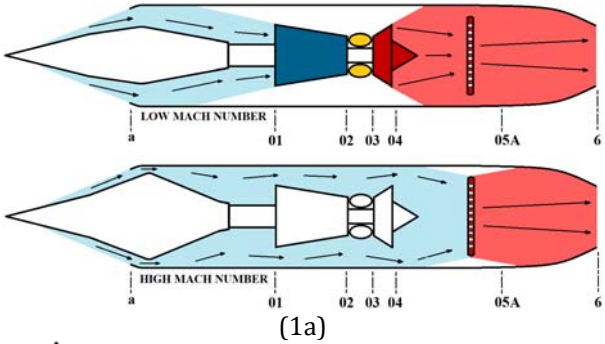

(1a)

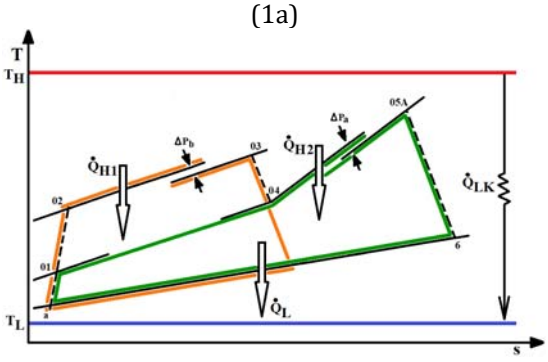

(1b)

Figure 1. Engine arrangement (a) and T-s schematic representation of a turboramjet cycle (b) with an afterburner

Table 1 represents the combination of values taken for the turbojet with and without an AB as well as the values for the ramjet condition (the inlet area of the ramjet is now considered as 0.5m^2); departures from these quantities are represented within the necessary figures. The essential propulsion equations for the powerplant state point computations may be obtained from (El-Sayed 2016).

Table 1. Delegated variable inputs for Turboramjet condition.

T_L = 200 K	η_j = 0.95	γ_g = 1.333
T_H = 2200 K	η_m = 0.99	R = 287 J/kg K
T_a = 223.3 K	η_b = 0.98	Di = 0.8 m
P_a = 26.5 kPa	C_{pa} = 1.005 kJ/kg K	Q_R = 43000 kJ/kg
ξ = 0.01	C_{pg} = 1. 148 kJ/kg K	η_c = 0.87
η_i = 0.93	γ_a = 1.4	η_t = 0.9
M = 0.5	ΔP_b = 0.96	T_{03} = 1200 K
η_{ab} = 0.9	ΔP_{ab} = 0.97	T_{05} = 2000 K
δ = 12	A_i = 0.5 m^2	ALT = 10000 m

Case I: Turbojet with and without AB

The power generated by the turbojet powerplant configuration with an AB is defined as:

$$\dot{\boldsymbol{W}} = \dot{\boldsymbol{Q}}_{\boldsymbol{HT}} - \dot{\boldsymbol{Q}}_{\boldsymbol{LT}} = \dot{\boldsymbol{Q}}_{\boldsymbol{H}} - \dot{\boldsymbol{Q}}_{\boldsymbol{L}} \quad (1)$$

The total heat dissipation rates from the high temperature reservoirs to the combustion chamber and the AB are given as:

$$\dot{\boldsymbol{Q}}_{\boldsymbol{HT}} = \dot{\boldsymbol{Q}}_{\boldsymbol{H}} + \dot{\boldsymbol{Q}}_{\boldsymbol{LK}} = \dot{\boldsymbol{m}}_{\boldsymbol{fb}}\boldsymbol{Q}_{\boldsymbol{R}}\boldsymbol{\eta}_{\boldsymbol{b}} + \dot{\boldsymbol{m}}_{\boldsymbol{fab}}\boldsymbol{Q}_{\boldsymbol{R}}\boldsymbol{\eta}_{\boldsymbol{ab}} + \dot{\boldsymbol{m}}_{\boldsymbol{a}}\boldsymbol{\xi}\boldsymbol{C}_{\boldsymbol{pa}}(\boldsymbol{T}_{\boldsymbol{H}} - \boldsymbol{T}_{\boldsymbol{L}}) \quad (2)$$

Where $\dot{Q}_H = \dot{Q}_{H1} + \dot{Q}_{H2}$ which are the heat transfer rates from the combustion chamber and afterburner respectively.

Exergy destruction is defined as the reversible power, less the actual power of a cycle; where the reversible work is the power generated by the Carnot cycle and the actual power is given as the kinetic energy of the cycle and their formulation is given below:

$$\dot{X}_{DES} = \dot{W}_{rev} - \dot{W}$$

$$\dot{W}_{rev} = \dot{m}_f Q_R \eta_{Carnot}$$

$$\dot{W} = 0.5(1+f)C_6^2 - C_a^2$$

Where η_{Carnot} is the Carnot efficiency

In addition, two supplementary cycle optimization functions are prescribed as power loss (PLOS) and effective power loss (EPLOS). Where PLOS is defined as the quotient between destroyed exergy and reversible power:

$$PLOS = \frac{\dot{X}_{DES}}{\dot{W}_{rev}} \quad (3)$$

EPLOS is designated as the ratio of ideal minus actual power of the Brayton cycle to the reversible power.

$$EPLOS = \frac{\dot{W}_{Bray} - \dot{W}}{\dot{W}_{rev}} \quad (4)$$

Where $\dot{W}_{Bray} = Q_{HT}\left[1 - {}^{1}/_{\theta_c}\right]$

As (Fawal and Kodal 2019) prescribed, PLOS and EPLOS provide a better assessment of the performance and power losses throughout the operation of the engine cycle. The evaluation of the turbojet with and without an AB using PLOS and EPLOS can be seen from Figure 5 for variations of compressor efficiency and Figure 6 for variations of Mach number.

The fuel used for the combustion chamber is assumed to be the same as for the AB, therefore, Q_R is still the fuel heat liberated per unit mass for both the combustion chamber and the AB, $\dot{m}_{fb}$ is the fuel mass flow rate and η_b is the efficiency for the combustion chamber, $\dot{m}_{fAB}$ is the fuel mass flow rate and η_{ab} is the efficiency for the AB.

Compression ratio parameter, θ_c is still given as before and taken to be: $\theta_c = (P_{02}/P_{01})^{(\gamma-1)/\gamma}$.

By applying an energy balance across the burner (combustion chamber) and the after burner the total fuel to air ratio, f_{TJ} is determined as:

$$f_{TJ} = f_b + f_{ab} = \frac{C_{pt}T_{03} - C_{pa}T_{02}}{Q_R\eta_b - C_{pt}T_{03}} + \frac{(1+f_b)C_{pt}(T_{05}-T_{04})}{\eta_{ab}Q_R - C_{pt}T_{05}} \quad (5)$$

The thermal efficiency of the turbojet cycle with an AB becomes:

$$\eta_{th} = \frac{\dot{W}}{\dot{Q}_{HT}} = \frac{\dot{W}}{\dot{m}_{fb}Q_R\eta_b + \dot{m}_{fab}Q_R\eta_{ab}} \quad (6)$$

The thrust equation is reobtained by applying integral momentum equation through the appropriate selection of the new control volume across the engine.

$$F_{TJ} = \dot{m}_{aTJ}[(1 + f_b + f_{ab})C_6 - C_a] + A_6(p_6 - p_a) \quad (7)$$

where C_6 is now the new exit velocity at the exhaust nozzle after the AB, C_a is the flight speed, A_6 is the exhaust nozzle exit cross section area and f_b *and* f_{ab} are the fuel to air mass flow rate ratio of the combustion chamber and AB respectively.

As before, by presuming perfect expansion and taking into account a per unit mass basis, the specific thrust is rewritten as:

$$F_{STJ} = (1 + f_b + f_{ab})C_6 - C_a \quad (8)$$

In addition to the numerical optimization procedures, the Mass Flow, Gas Generator Speed, Shaft Force, Altitude models and propulsion equations are still applicable to the turbojet with an AB.

Case II: Turboramjet in Dual Mode Operation

Equations (1) to (6) of the turbojet with an AB are still applicable when considering the turboramjet engine configuration. However, for the ramjet portion distinct considerations must be accounted for and provided in the formulations below.

The diffuser stagnation pressure ratio (ram recovery) for the ramjet is based on the (MIL-E-5007D 1973) specification and valid for Mach numbers between 1-5:

$$r_d = 1 \quad For\ Mach\ Number < 1 \quad (9)$$

$$r_d = 1 - 0.075(M_\infty - 1)^{1.35} \quad From\ Mach\ 1\ to\ 5 \quad (10)$$

$$r_d = 800/(M^4 + 938) \quad For\ Mach\ Number > 5 \quad (11)$$

The Mach number entering the afterburners is assumed not to exceed 0.25, thus ensuring subsonic burning conditions.

Implementing an energy balance at the inlet and exit of the afterburners and Rayleigh flow solutions based on tables and formulations of gas dynamics obtained from (Keith and John 2006) the fuel to air ratio, f_R for the ramjet is derived as:

$$f_R = \frac{C_{pa}(T_{04} - T_{0a})}{Q_R \eta_{ab} - C_{pa} T_{04}} \quad (12)$$

The mass flow for the ramjet engine is now defined from free stream conditions as:

$$\dot{m}_{aR} = \rho_a A_1 C_a \quad (13)$$

The total thrust generated by the turboramjet is considered as:

$$F = F_{TJ} + F_R = \dot{m}_{aTJ}[(1 + f_b + f_{ab})C_6 - C_a] + \dot{m}_{aR}[(1 + f_R)C_6 - C_a] \quad (14)$$

The specific thrust is also given as a total for the turboramjet as:

$$F_S = \left(F_{TJ} + F_R\right)/\left(\dot{m}_{aTJ} + \dot{m}_{aR}\right) \quad (15)$$

RESULTS AND DISCUSSION

The application of a turboramjet engine is to extract performance advantage from both Brayton configuration types: turbojet with AB and Ramjet utilizing an AB. As (Fawal and Kodal 2019, 2021) have exhaustively evaluated the turbojet without an AB, here, the provision of Case I was deemed necessary before progressing onwards to Case II. The disclosed Brayton cycle configurations in Case I and Case II are intended to highlight the advantages and limitations of the performance parameters and optimization functions of the respective powerplants.

Case I focuses on a maximum power assessment for variations of altitude and Mach number. Moreover, a component based comparison at maximum power for variations of Mach number at a given altitude is provided. In addition PLOS and EPLOS optimization functions for variations of compressor ratio parameter (θ_c) were evaluated.

Case II also evaluates the turboramjet on a maximum power basis for variations of Mach number, altitude and inlet air mass flow split.

Case I: Turbojet with and without AB

Figure 2 expresses the variations of thermal η_{th} (a), overall η_o (b) and propulsive η_p (c) efficiency for changes in altitude as a function of flight Mach number, M_∞. For Mach numbers higher than unity the thermal efficiency of the turbojet with an AB becomes more advantageous at all altitudes; this is due to the much higher work / thrust output of the turbojet with an AB in comparison to the turbojet without an AB (see Figure 4). In addition, the thermal efficiency for a turbojet with an AB show an increase with increasing Mach number, whereas the turbojet without an AB show a slight decrease with increasing Mach number. On the other hand, the propulsive efficiency for a turbojet without an AB are about 20% higher for flight Mach numbers above 0.8 and at all altitudes than the turbojet with an AB; for Mach numbers below 0.8 the propulsive efficiency for a turbojet without an AB become about 10% higher than that of the turbojet with an AB, below Mach number of 0.4 the difference between the two configurations becomes increasingly smaller. The overall efficiency for a turbojet without an AB still show greater advantage up to a Mach number of ~ 1.6; above this value the turbojet with an AB show a comparable advantage where the difference between the two engine configurations is around 5%. Figure 3 clearly shows that for a turbojet with an AB both the fuel to air ratio and TSFC are higher than that of a turbojet without an AB; this is an unavoidable consequence for the trade-off in increased thrust.

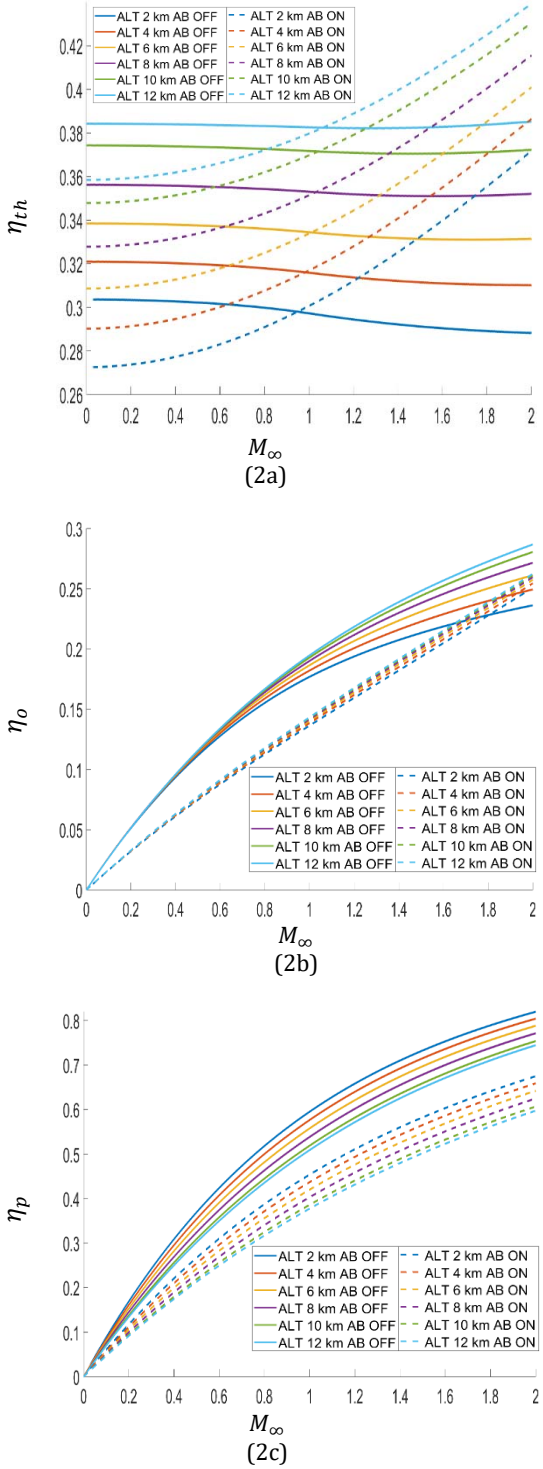

Figure 2. η_{th}, η_o and η_p efficiency for variations of altitude as a function of flight Mach number, M_∞.

Figure 3 clearly shows that for a turbojet with an AB both the fuel to air ratio and TSFC are higher than that of a turbojet without an AB; this is an unavoidable consequence for the trade-off in increased thrust.

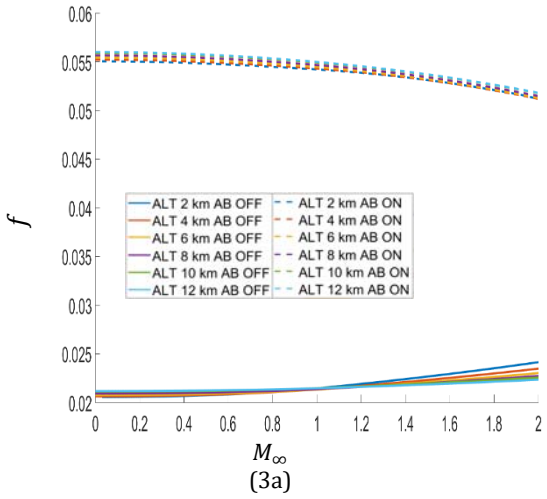

(3a)

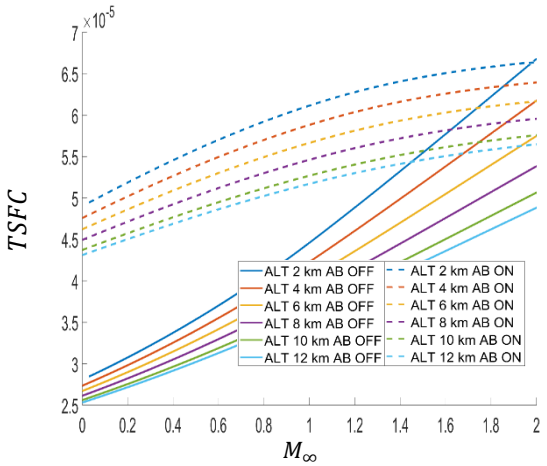

(3b)

Figure 3. f and $TSFC$ efficiency for distinct quantities of altitude for variaitons M_∞.

It is important to keep in mind that the purpose of using a turbojet with an AB is the significant increase in thrust, power and impulse of the system at all altitudes and flight Mach numbers (Figure 4). However, this comes at the expenditure for higher fuel consumption and heavier weight due to the increase in exhaust nozzle specific volume (Figure 4d). For altitudes higher than 6 km the thrust and power of both engine configurations intersect at a point. For example at an altitude of 12 km the red dot on Figure 4b corresponds to the two red dots on Figure 4a; what is seen is that the turbojet with an AB can achieve the same thrust and power as the turbojet without an AB at a much lower Mach number (0.6 vs. 1.6 respectively).

As previously mentioned, the main objective of the turbojet with an AB is the higher power output of the system, this can be seen again from Figure 5 and Figure 6. From both figures it can be seen that the difference in effective power loss parameter (EPLOS) between both engine configurations is quite small ~5% at maximum power for both turbojets with and without an AB; in addition, as the Mach number is increased from 0.8 to 1 the difference in EPLOS decreases. Thus the compressor efficiency η_c has a greater influence on EPLOS than the Mach number; this can also be seen from the figures presented by (Fawal et al. 2019). Therefore, from an EPLOS perspective (ignoring the margin of power gain) there is no significant advantage as to which engine configuration is used.

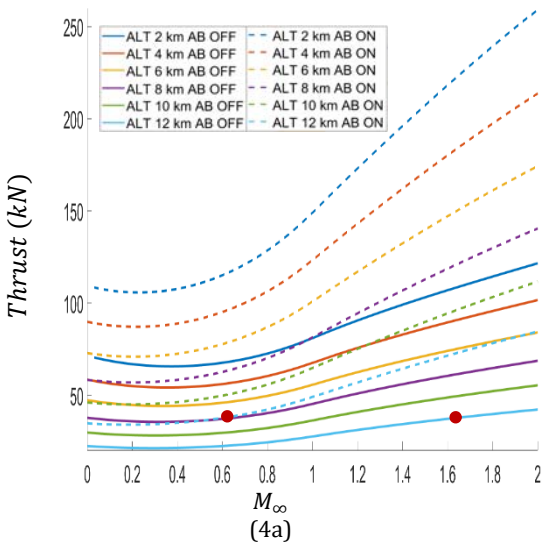

(4a)

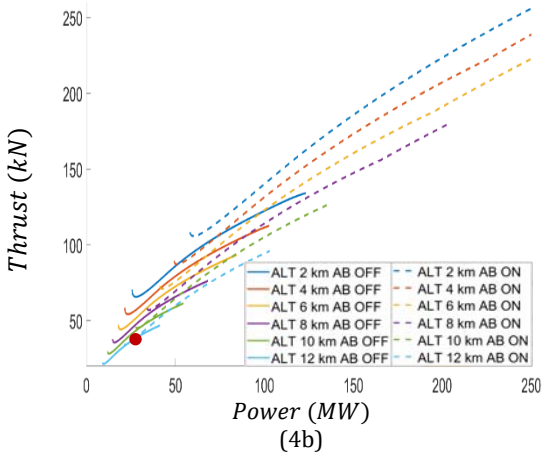

(4b)

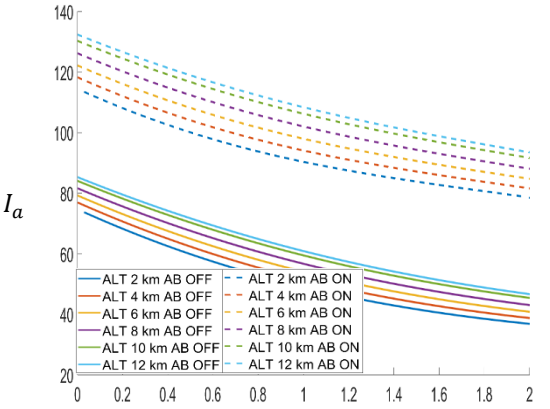

(4c)

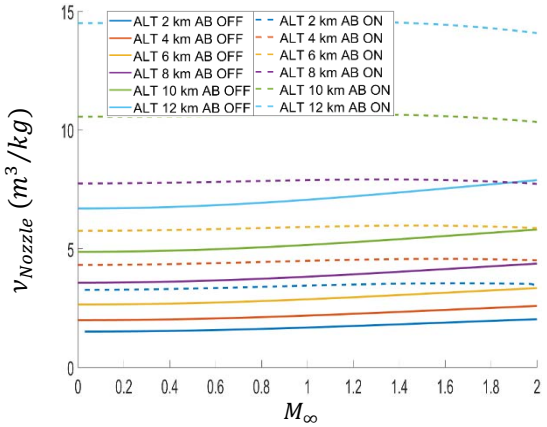

(4d)

Figure 4. $Thrust$ (a), I_a (c) and v_{Nozzle} (d) for variations of altitude as a function of M_∞ and $Thrust$ (b) as a function of $Power$.

On the other hand, from PLOS point of view the, the exergy destruction of the turbojet with an AB is overall higher than a turbojet without an AB; at minimum PLOS 65% vs. 55% respectively. In addition, the difference at minimum PLOS between both engine configurations is about 10%. Moreover, for variations of compressor efficiency (Figure 5), at minimum PLOS for the turbojet with an AB occurs at the maximum power output ~34 MW and lower compressor ratio parameter θ_c ~2.62, whereas the minimum PLOS for the turbojet without an AB is slightly shifted towards the right at lower power ~12 MW output and higher compressor ratio parameter θ_c ~2.88, which means an increase in compressor size and inevitably weight.

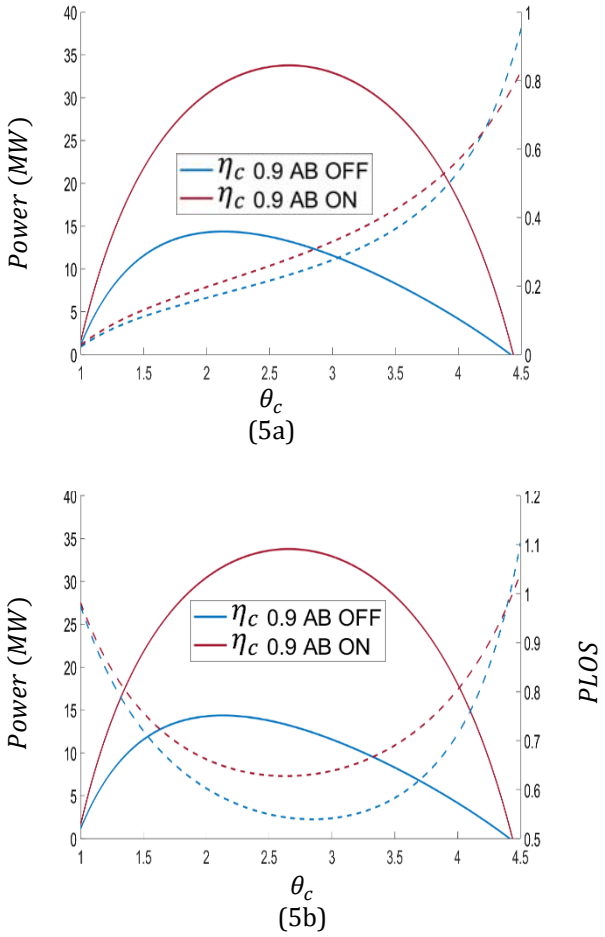

Figure 5. *Power*, *EPLOS* and *PLOS* for distinct quantitis of η_c for variations of θ_c.

Furthermore, for variations of Mach number (Figure 6), at minimum PLOS the turbojet with an AB has a higher power output as Mach number increases at lower compressor pressure ratio: Mach 0.8, ~42 MW and θ_c ~2.47 vs. Mach 1, ~52 MW and θ_c ~2.39; whereas the turbojet without an AB, Mach 0.8, ~15 MW and θ_c ~2.65 vs. Mach 1, ~18 MW and θ_c ~2.52. Therefore, the turbojet with an AB displays an advantage of: lower θ_c and compressor weight and higher power output at the expense of higher exergy destruction. However, the turbojet with an AB having a lower θ_c and lower compressor weight needs to be compared to the increase in weight gain due to the AB components and exhaust nozzle.

From Figure 7, for a constant altitude of 10 km and changes in Mach number and as previously stated, that the overall dimension of the powerplant does not change while the respective powerplant constituents undergo size metamorphosis. For both engine configurations, at higher Mach numbers dimensions for diffuser increases, therefore, the selection of diffuser (ram recovery) develops as a crucial role than at reduced Mach numbers. In addition, the exhaust nozzle for the turbojet with an AB is on average ~85% larger than that of the turbojet without an AB, which inevitably corresponds to an increase in engine weight. Therefore, a comparative and trade-off study of the decrease in θ_c and thus compressor weight, the ~85% increase in exhaust nozzle specific volume and the AB fuel components need to be examined.

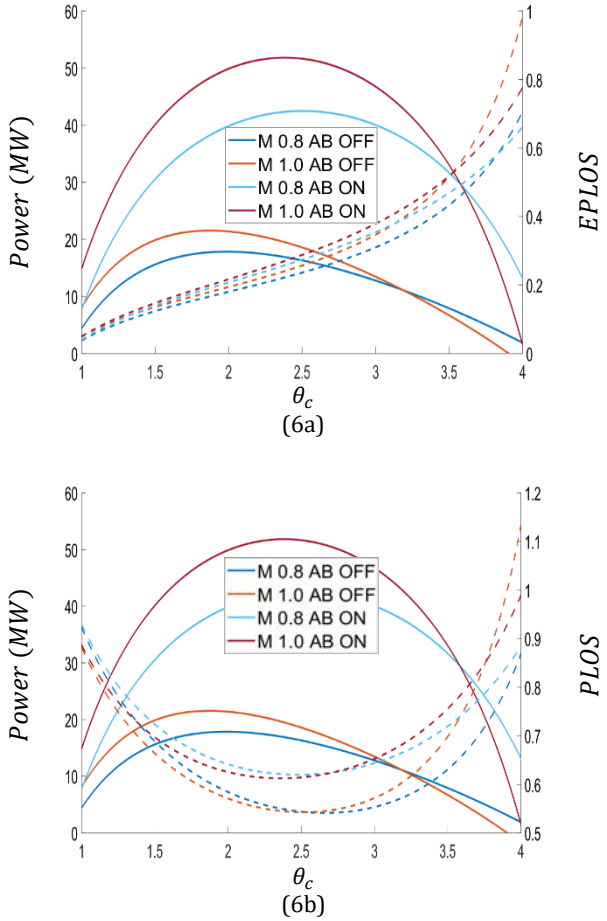

Figure 6. *Power*, *EPLOS* and *PLOS* for distinct quantities of M_∞ as a function of θ_c.

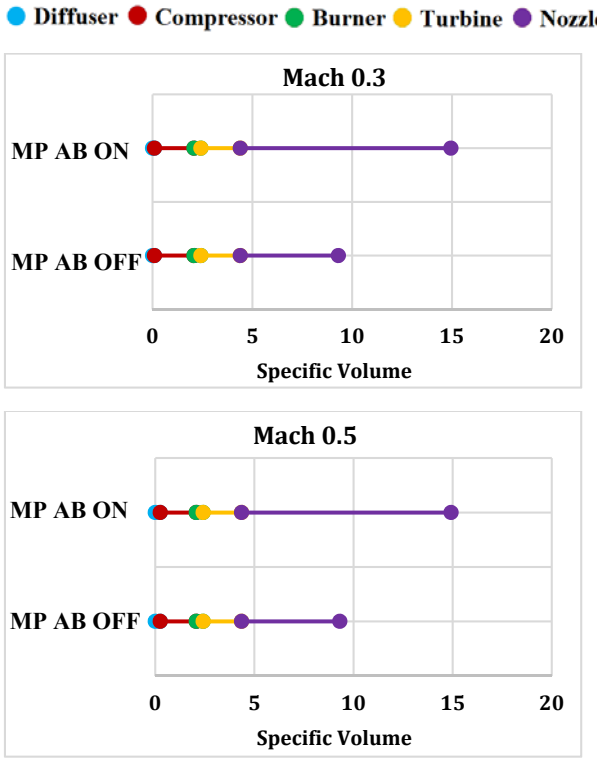

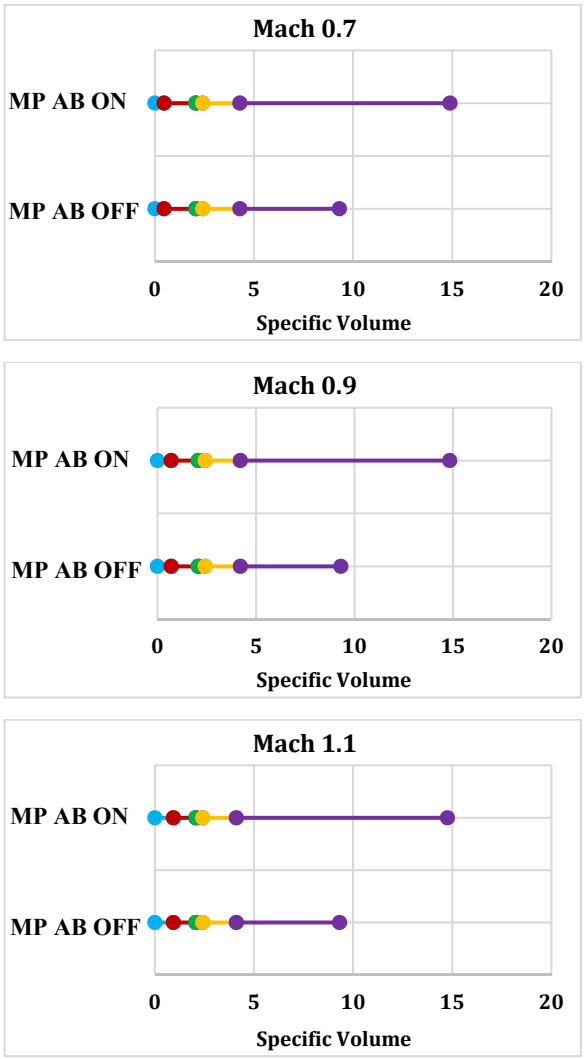

Figure 7. Dimensional metamorphoses of respective engine modules at maximum MP for variations M_∞.

Case II: Turboramjet in Dual Mode Operation

Figure 8 to Figure 10 is an altitude assessment of the turboramjet in dual mode operation at maximum power for variations of Mach number for a 25% to 75% inlet air mass flow split between the turbojet and ramjet respectively. The performance parameters of: thermal, propulsive and overall efficiency; fuel to air ratio, TSFC, impulse, thrust, power and specific volume were evaluated.

Figure 8 distinctly shows the limitation of turbojet operation as a function of altitude and Mach number. The maximum feasible operating range in terms of Mach number at an altitude of 2 km, 4 km, 6 km, 8 km, 10 km and 12 km to 20 km are 1.97, 2.08, 2.19, 2.31, 2.44 and 2.51 respectively, after which a divergence in the propulsion solutions are encountered. The propulsive efficiency of the turbojet still outweighs the use of the ramjet up to a Mach number of 2.5. However, falls short in terms of thermal and overall efficiency in the overlapping region of Mach 1.97 and 2.51. In terms of overall efficiency, the ramjet indicates highest performance at 3.36, 3.55, 3.74, 3.94, 4.15, 4.34, 4.47, 4.63, 4.73 and 4.89 Mach with 0.52, 0.54, 0.56, 0.58, 0.60, 0.63, 0.65, 0.68, 0.70 and 0.73 overall efficiencies for each altitude from 2 km to 20 km respectively. Whereas the turbojet reaches its maximum performance capability at 1.97, 2.08, 2.19, 2.31, 2.44 and 2.51 Mach with 0.25, 0.26, 0.28, 0.30, 0.31 and 0.32 overall efficiencies respectively for each altitude from 2 km to 12 km; note that beyond 12 km the overall efficiency and Mach number remains the same. The thermal efficiency of the ramjet depicts a gradual decrease and takes a sharp decline beyond a Mach number of 4; thus, at 4.09, 4.24, 4.41, 4.6, 4.76, 4.9, 5.03, 5.16, 5.26, and 5.38 Mach with 0.48, 0.51, 0.54, 0.56, 0.60, 0.62, 0.64, 0.66, 0.68 and 0.70 thermal efficiencies are achieved. Whereas the turbojet reaches its maximum performance capability at 1.97, 2.08, 2.19, 2.31, 2.44 and 2.51 Mach with 0.37, 0.39, 0.42, 0.44, 0.46 and 0.48 thermal efficiencies respectively for each altitude from 2 km to 12 km; similarly, beyond 12 km the thermal efficiency and Mach number remains the same. The propulsive efficiency of the ramjet is nearly linear and illustrates an upper saturation limit for 2 km and 20 km at Mach numbers of 4.27, 4.45, 4.65, 4.85, 5.07, 5.22, 5.3, 5.37, 5.44 and 5.5 respectively; in addition, at a Mach number of 2 the propulsive efficiency decreases from 0.59 to 0.50 as the altitude increases from 2 km to 20 km. Whereas the turbojet reaches its maximum performance capability at 1.97, 2.08, 2.19, 2.31, 2.44 and 2.51 Mach with 0.67 propulsive efficiency respectively for each altitude from 2 km to 20 km; also the Mach number and propulsive efficiency does not change beyond 12 km.

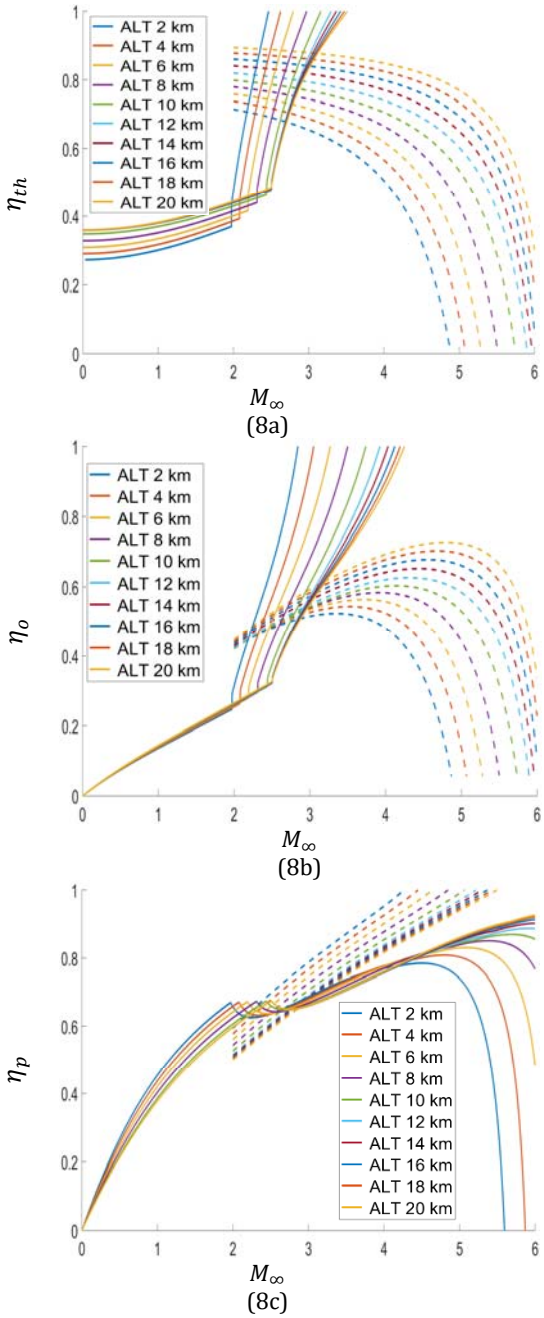

Figure 8. η_{th}, η_0 and η_p for variations of altitude for turboramjet engine as a function of M_∞.

Figure 9 shows the f, $TSFC$ (kg/N-s) and I_a (s) of the dual mode operating system. For all altitudes the ramjet indicates lower f and $TSFC$ and higher I_a than the turbojet. The minimum attainable f for the turbojet ranges from 0.05137, 0.0508, 0.05033, 0.04993 and 0.04861 for the previously specified Mach numbers and altitudes; in addition to showing a decrease if f for increasing altitude. On the other hand, the ramjet experiences an increase in f as the altitude increases. Nevertheless, at a Mach number of 2 the f increases from 0.04122 to 0.0441 which is still much lower than the f of the turbojet. Evidently this is due to the turbojet fuel contribution stemming from both the combustion chamber and afterburner, whereas the ramjet only utilizes the afterburner fuel for thrust generation. In addition, the ramjet exhibits a much greater advantage of attaining higher Mach numbers for even lower values of fuel to air ratio; i.e. as the Mach number increases the f also decreases. The turbojet reaches a maximum TSFC capability at 1.97, 2.08, 2.19, 2.31, 2.44 and 2.51 Mach with 6.637e-05, 6.415 e-05, 6.215 e-05, 6.032 e-05, 5.865 e-05 and 5.694 e-05 TSFC respectively for each altitude from 2 km to 12 km; in addition to a decrease in TSFC with increasing altitude notwithstanding that the Mach number and TSFC do not changing beyond 12 km. For a TSFC of 5.694 e-05, the operating range for the ramjet in term of Mach numbers are: 3.46, 3.67, 3.9, 4.14, 4.4, 4.62, 4.79, 4.96, 5.11 and 5.26 for altitudes from 2 km to 20 km respectively; where beyond a TSFC of 5.694 e-05 operation becomes unrealistic.

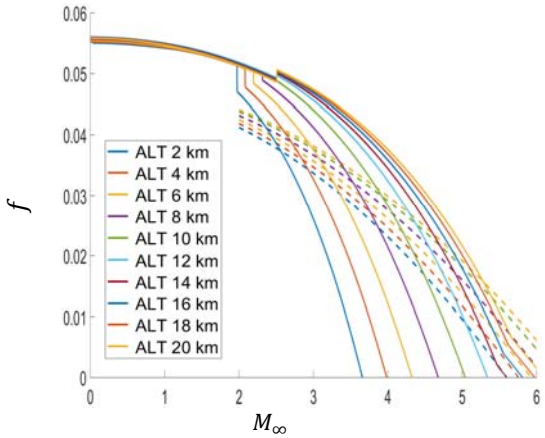

(9a)

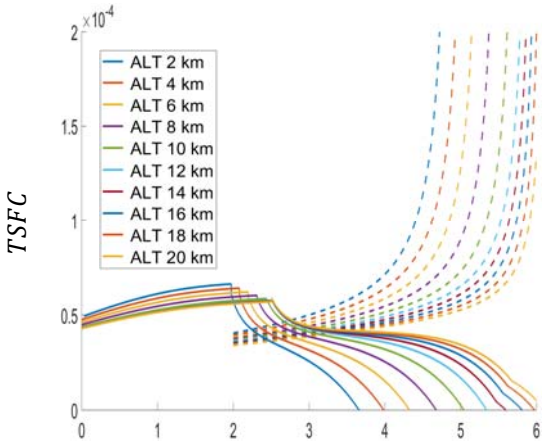

(9b)

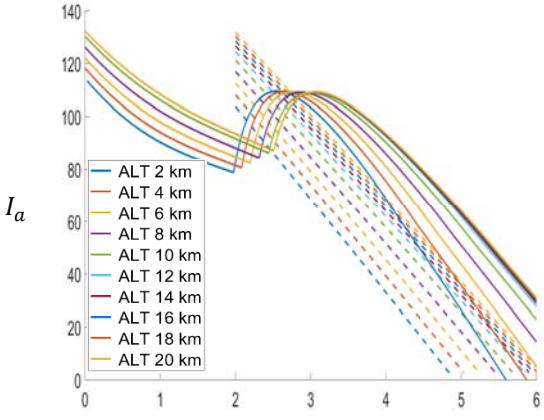

(9c)

Figure 9. f, $TSFC$ and I_a for variations of altitude for turboramjet engine as a function of M_∞.

Figure 10 depicts the thrust (kN) for variations of Mach number and power and the exit nozzle specific volume (m^3/kg) for variations of Mach number. In terms of thrust the turbojet is capable of achieving 64, 55, 47, 39, 32, 25, 18, 13, 10 and 7 kN of thrust at Mach numbers of 1.97, 2.08, 2.19, 2.31, 2.44, and 2.51 respectively for each altitude from 2 km to 20 km. Whereas the ramjet can produce 257, 213, 174, 140, 111, 85, 63, 47, 34 and 25 kN of thrust at a Mach number of 2 for each altitude from 2 km to 20 km. As expected, the thrust and power of the dual system decreases with altitude. Nonetheless, the ramjet is still capable of producing 7 kN of thrust at a Mach number of 5.73. When examining the specific volume, the ramjet has a lower exit nozzle specific volume than the turbojet at all altitudes. For the turbojet, specific volumes of 3.5, 4.5, 5.8, 7.5, 9.9, 13.3, 18.3, 25, 34.3 and 46.9 are achieved at Mach numbers of 1.97, 2.08, 2.19, 2.31, 2.44, and 2.51 respectively for each altitude from 2 km to 20 km. Whereas the ramjet experiences limitations in specific volumes of 2.4, 2.9, 3.6, 4.5, 5.7, 7.3, 9.4, 12.0, 15.4 and 19.8 for operable Mach number maximums of 4.87, 5.07, 5.28, 5.5, 5.73, 5.89, 5.95 and 6 as the altitude increases from 2 km to 20 km. Moreover, as the altitude increases the specific volume of the turbojet becomes far too large for efficient operation and therefore too heavy. Altitudes at and above 10 km show approximately twice the increase in specific volume for the turbojet than the ramjet. Therefore, the turbojet can be used up to an altitude of 8 km and then completely switch to ramjet operation for altitudes of 10 km and beyond. Where at 20 km the specific volume of the ramjet is ~20 (which is obtained at 14 km for the turbojet) and ~47 for the turbojet respectively.

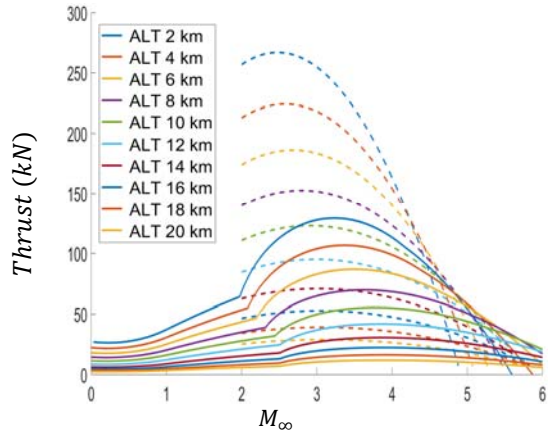

(10a)

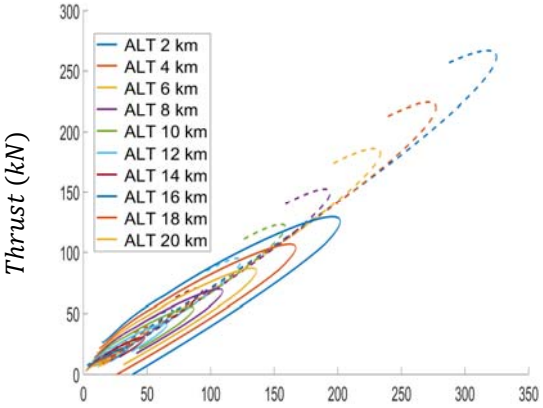

(10b)

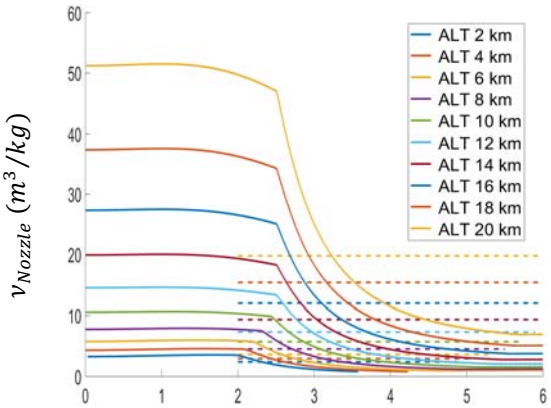

(10c)

Figure 10. Thrust (a) and v_{Nozzle} (c) as a function of M_∞ and Thrust vs. Power for variations in altitude.

Figure 11 to Figure 19 is an assessment of variations of inlet air mass flow split between the turbojet and ramjet as a function of Mach number at 10 km and 20 km (all figures on the right and left respectively). The legend in these figures indicates the percentage of air mass flow being diverted to the ramjet (-- **dashed lines**) and the remaining percentage being directed to the turbojet (**— solid lines**). It is also to note that curves of the same colour are complementary to each other; for example, the blue curves imply a 25% to 75% inlet air mass flow split between the ramjet and turbojet respectively. However, the exception to the previous statement are the **purple** curves, where 100% inlet air mass flow to the ramjet means 0% to the turbojet and vice versa. In addition, this part of the analysis has restricted the operation of the turbojet up to a Mach number of 2.5; as has previously mentioned the limitation of the turbojet application reaches a maximum operable Mach number of 2.4 for both altitudes of 10 km and 20 km respectively. Whereas, the constraint for the discussion of the ramjet analysis will be kept to a maximum Mach number of 4.4 and 5.26 for the altitudes of 10 km and 20 km respectively; this is due to the feasibility in terms of *TSFC* as stated previously. Also to note, the pressure and temperature at 10 km vs. 20 km are: 26.43 kPa and 223.15 K vs. 5.47 kPa and 216.65 K respectively.

Figure 11 and Figure 12 show that at 25% inlet air mass flow the turbojet is economically more effective in terms of both thermal and overall efficiency respectively at Mach 2. As the split of mass flow to the ramjet is increased (50% to 100%) it becomes quite distinct that the ramjet is much more beneficial. Also, in general, as the inlet mass flow of either system increases, so do the thermal and overall efficiencies. For the altitudes of 10 km and 20 km the maximum attainable thermal efficiencies are: 0.23, 0.34, 0.41 and 0.46 versus 0.24, 0.36, 0.43 and 0.47 respectively. Whereas the ramjet thermal efficiencies are: 0.19, 0.35, 0.5 and 0.66 versus 0.21, 0.38, 0.56 and 0.73 at 10 km and 20 km respectively. In terms of overall efficiency, the turbojet achieves 0.16, 0.23, 0.27 and 0.3 versus 0.16, 0.24, 0.28 and 0.31 at 10 km and 20 km respectively. Whereas the ramjet overall efficiencies are: 0.19, 0.33, 0.46 and 0.6 versus 0.23, 0.39, 0.55 and 0.7 at 10 km and 20 km respectively. Note however, that the maximum overall efficiency (same as previous values) for the ramjet at 10 km are achievable at slightly lower Mach numbers: 4.35, 4.26, 4.2 and 4.17 for increases of inlet air mass flow split. Similarly, at 20 km the maximum overall efficiency for the ramjet are attained at: 5.07, 4.95, 4.88 and 4.82 Mach numbers for increasing mass flow split; in addition, for 50% to 75% air flow split the overall efficiency increases by 1% and at a 100% air flow split the overall efficiency increases by 3%.

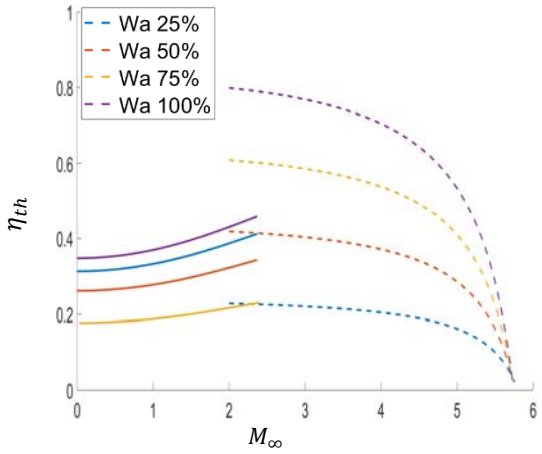

(11a)

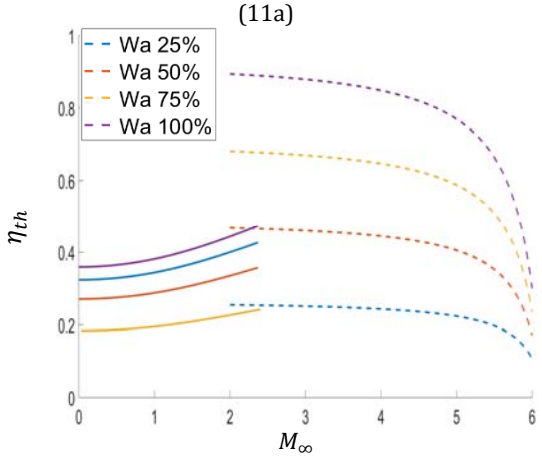

(11b)

Figure 11. η_{th} for variations of inlet air mass flow at 10 km (a) and 20 km (b) for turboramjet engine as a function of M_∞.

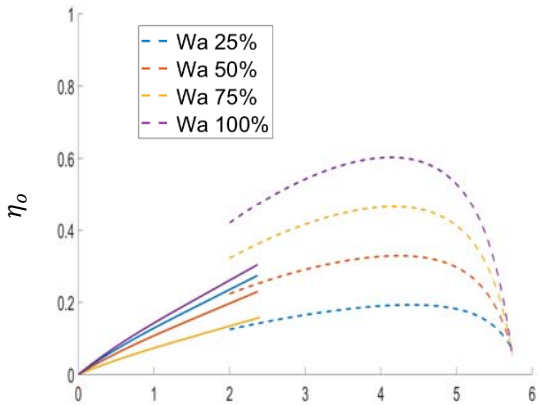

(12a)

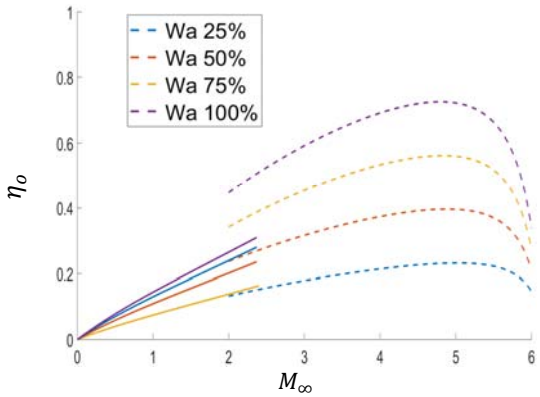

(12b)

Figure 12. η_0 for variations of inlet air mass flow at 10 km (a) and 20 km (b) for turboramjet engine as a function of M_∞.

On the other hand Figure 13 indicates a better propulsive efficiency for the turbojet over the ramjet at all inlet air mass flow splits up to Mach 2. Beyond a Mach number of 2 the ramjet takes over and has a dominating effect on system performance. However, unlike the thermal and propulsive efficiency, the propulsive efficiency decreases as the inlet air mass flow to either system increases. This is due to the kinetic energy added to the air mass flow through the engine being higher than the propulsive power generated by the fully expanded exhaust jet. For the turbojet, the attainable propulsive efficiencies are: 0.69, 0.67, 0.67 and 0.66 versus 0.68, 0.66, 0.66 and 0.65 7 at 10 km and 20 km respectively. Whereas the ramjet propulsive efficiencies are: 1, 0.94, 0.92 and 0.91 versus 1, 1, 0.99 and 0.97 at 10 km and 20 km respectively; however, at 20 km and for 25% and 50% inlet air mass flow split the maximum propulsive efficiency is reached at 4.77 and 5.18 Mach respectively.

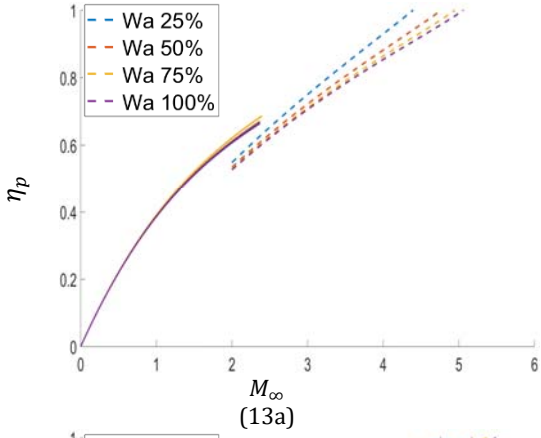

(13a)

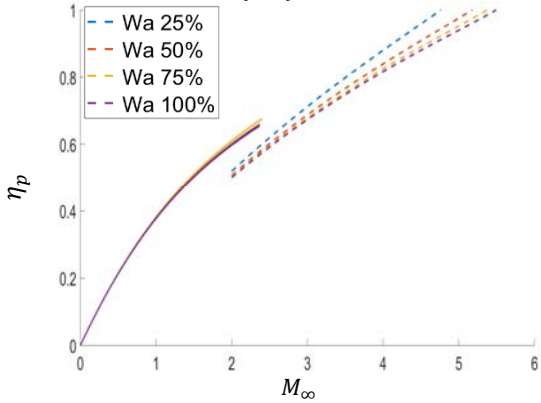

(13b)

Figure 13. η_p for variations of inlet air mass at 10 km (a) and 20 km (b) flow for turboramjet engine as a function of M_∞.

What is also interesting to note from Figure 11 to Figure 13 is that the variations on thermal overall and propulsive efficiency for the turbojet show slight variations from 10 km to 20 km, whereas for the ramjet the changes are more pronounced. This effect is a direct result of the much higher attainable Mach numbers for the ramjet vs. the turbojet.

From Figure 14 and Figure 15 it is seen that the both the *f* and TSFC of either system decreases as the inlet air mass flow is increased. For a constant input of fuel this is an expected result. However, what is interesting to see is that the ramjet is not competitive enough with the turbojet until 75% inlet air mass flow is reached; below 75% (25% and 50%) the turbojet experiences lower *f* and *TSFC*. In addition, notwithstanding the changes of inlet air mass flow, the small change in temperature from 10 km 223 K to 20 km 216K has very little impact on the variation of *f*, which is completely independent of the free stream pressure and strongly dependent on the maximum temperature of the cycle; this effect is also observed on *TSFC*. For the turbojet the attainable *f* are: 0.103, 0.067, 0.056 and 0.05 versus 0.01, 0.066, 0.055 and 0.049 at 10 km and 20 km respectively. Whereas the ramjet *f* are: 0.1, 0.05, 0.033 and 0.025 versus 0.064, 0.032, 0.021 and 0.016 at 10 km and 20 km respectively. Here, we also see that the difference in altitude for the turbojet has very little impact on the *f*, whereas the ramjet experiences a significant decrease on *f* for an increase in altitude from 10 km to 20 km. When examining TSFC, the turbojet attains values of: 1.11e-04, 7.64e-05, 6.45e-05 and 5.85e-05 versus 1.06e-04, 7.34e-05, 6.23e-05 and 5.67e-05 at altitudes of 10 km and 20 km respectively. Whereas the ramjet TSFC values are:1.76e-04, 1.04e-04, 7.36e-05 and 5.70e-05 versus 1.74e-04, 1.03e-04, 7.33e-05 and 5.69e-05 at 10 km and 20 km respectively. Interestingly, it is observed that for the turbojet the TSFC slightly decreases for an increase in altitude from 10 km to 20 km and therefore more fuel efficient, however, the ramjet values of TSFC are extremely close to each other. Therefore, with just an increase in altitude the ramjet remains static in terms of fuel efficiency to thrust output however has an advantage of a higher Mach number.

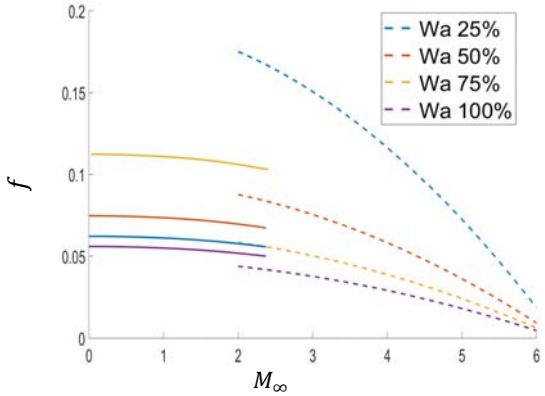

(14a)

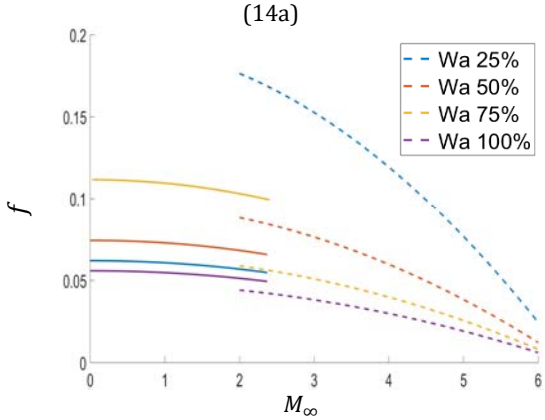

(14b)

Figure 14. *f* for variations of inlet air mass flow at 10 km (a) and 20 km (b) for turboramjet engine as a function of M_∞.

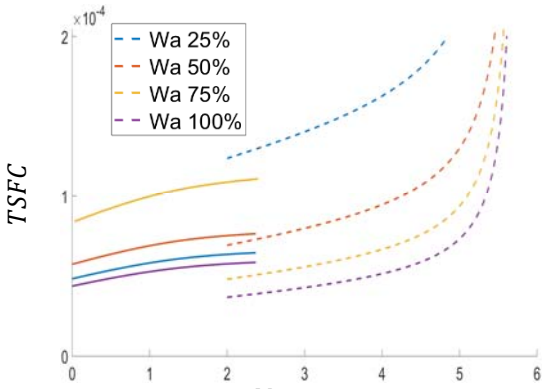

(15a)

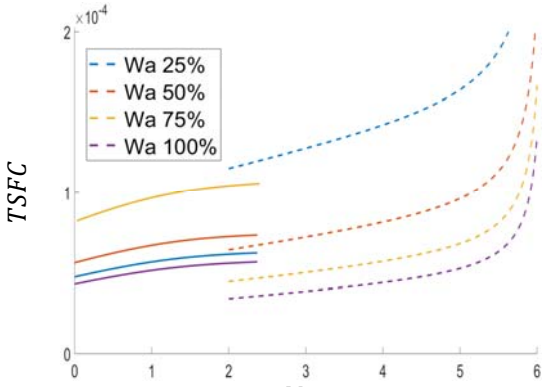

(15b)

Figure 15. *TSFC* for variations of inlet air mass flow at 10 km (a) and 20 km (b) for turboramjet engine as a function of M_∞.

Figure 16 also shows that as the inlet air mass flow to either system is increased the I_a (s) decreases. This occurs as a consequence of the specific thrust; whereas the air mass flow increases the specific thrust decreases and therefore, so does the I_a. In general, the ramjet indicates higher attainable I_a at Mach 2 than the turbojet. In addition, the variations of I_a for the turbojet are modest between 10 km and 20 km, whereas the ramjet variations are slightly more pronounced. The turbojet attains specific impulse values of: 95, 90, 88 and 87 versus 96, 91, 90 and 89 at altitudes of 10 km and 20 km respectively. Whereas the ramjet specific impulse values are: 58, 49, 46 and 45 versus 38, 32, 30 and 29 at 10 km and 20 km respectively. However, for a value of 45s and at an altitude of 20 km the ramjet achieves Mach numbers of: 5.07, 4.87, 4.79 and 4.75. Therefore, for the same value of specific impulse, the ramjet is able to reach higher Mach numbers as the altitude increases.

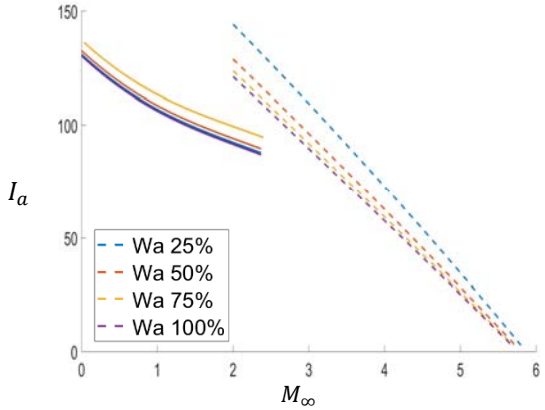

(16a)

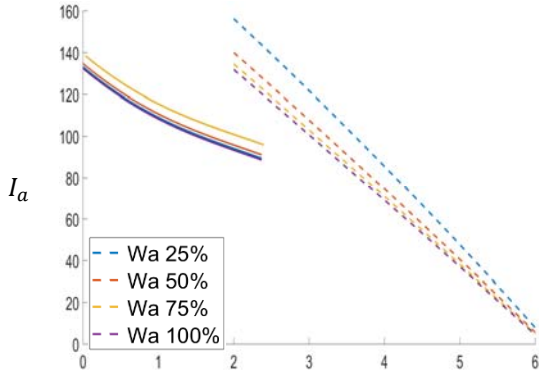

(16b)

Figure 16. I_a for variations of inlet air mass flow at 10 km (a) and 20 km (b) for turboramjet engine as a function of M_∞.

In general, Figure 17 and Figure 18 illustrate that as the inlet air mass flow is increased to either system, the thrust and power also increases. At a Mach number of 2 the ramjet indicates improved thrust over the turbojet for an inlet mass flow above 25%. However, it is also clearly seen that as the altitude increases from 10 km to 20 km the thrust output decreases from both systems. The turbojet achieves maximum thrust values of: 35, 65, 95 and 126 versus 7, 14, 20 and 27 kN at 10 km and 20 km respectively; a decrease of approximately 4 to 5 fold for an increase in altitude. Whereas the ramjet attains thrust values of: 39, 66, 93 and 120 versus 6, 11, 15 and 19 kN at 10 km and 20 km respectively; a decrease of approximately 6 fold for an increase of altitude. However, the maximum attainable thrust for the ramjet at 10 km are: 50, 88, 126 and 165 at Mach numbers of 3.05, 2.96, 2.99 and 2.92 respectively. Whereas at 20 km the maximum thrust values for the ramjet are: 12, 21, 30 and 39 for Mach number of 3.29, 3.18, 3.16 and 3.12 respectively.

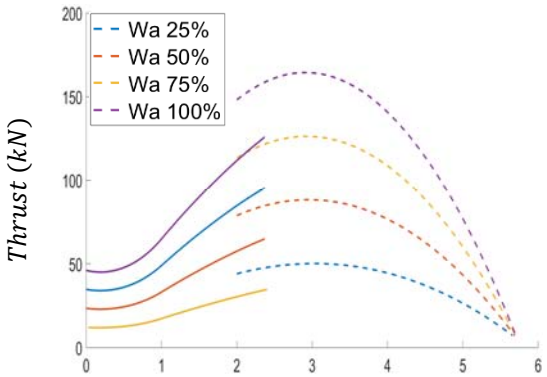

(17a)

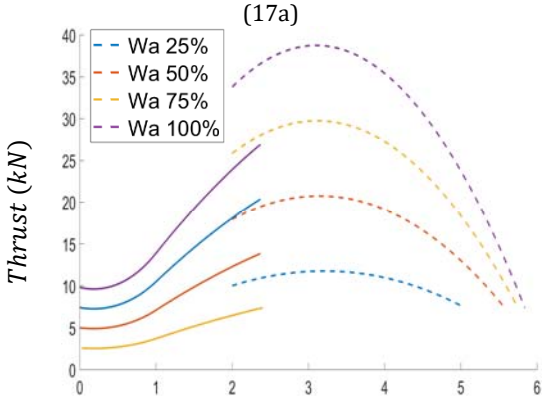

(17b)

Figure 17. *Thrust* for variations of inlet air mass flow at 10 km (a) and 20 km (b) for turboramjet engine as a function of M_∞.

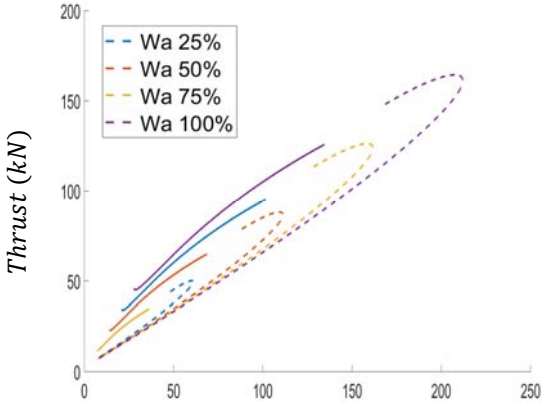

(18a)

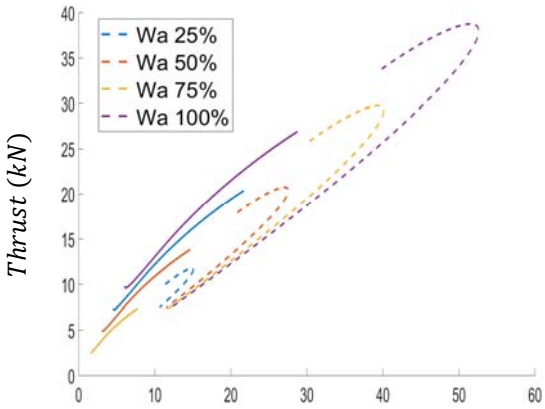

(18b)

Figure 18. *Thrust* for variations of inlet air mass flow at 10 km (a) and 20 km (b) for turboramjet engine as a function of *Power*.

From Figure 19 it can clearly be seen that at all Mach numbers the ramjet is far more advantageous than the turbojet and especially at 20 km. The specific volume of the turbojet at 10 km and 20 km is 10.63 and 51.25 (m^3/kg) respectively; whereas the ramjet values at 10 km and 20 km are 6 and 20 (m^3/kg) respectively. Therefore, the specific volume is 1.7 and 2.4 times larger than that of the ramjet at each altitude respectively; therefore, the trade off in weight is unequivocal. In addition, due to a weak dependency, the variation of inlet air mass flow has very little impact on the specific volume of the exhaust nozzle for both the turbojet and ramjet.

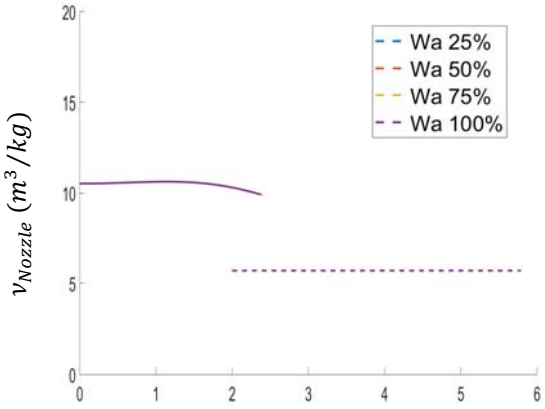

(19a)

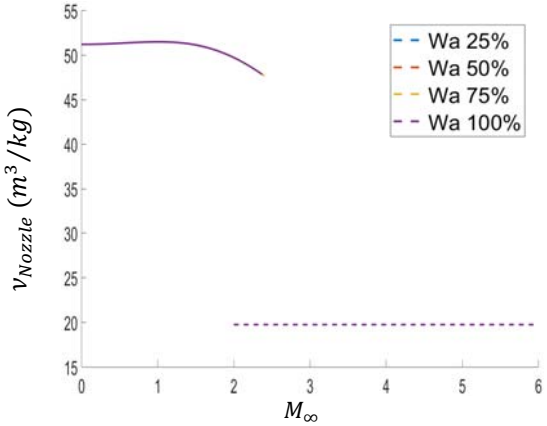

(19b)

Figure 19. v_{Nozzle} for variations of inlet air mass flow at 10 km (a) and 20 km (b) for turboramjet engine as a function of M_∞.

CONCLUSION

This investigation presented two case studies: Case I was a comparison between the Turbojet with and without an AB considering PLOS, EPLOS and maximum power; Case II was an evaluation of a Turboramjet in Dual Mode Operation under maximum power optimization function.

When evaluating Case I, the primary purpose of a turbojet with an AB is to increase thrust, power, specific impulse at the expense of higher fuel consumption, exergy destruction and overall weight of the engine configuration. When evaluating the turbojet with and without and AB from an EPLOS, the variations in Mach number have a very small effect and as the Mach number increase the difference in EPLOS between both engine configuration decreases. PLOS values for both engine configurations indicate a higher exergy destruction for the turbojet with an AB. Nonetheless, at minimum PLOS values the turbojet with an AB can operate at lower θ_c and generate more power that the turbojet without an AB; therefore a decrease in weight is attained as an advantage for the turbojet with an AB. However, a concessional study of a decrease in θ_c and thus compressor weight versus the ~85% increase in exhaust nozzle specific volume and AB fuel components must be conducted. Under maximum power evaluations, the turbojet with an AB has a significant advantage of increase in thrust at all altitudes and Mach numbers, it is only beyond a Mach number of unity does the thermal efficiency of the engine configuration portray higher relevance. On the other hand, it was also seen that for a given altitude, the turbojet with an AB was able to attain the same power and thrust output as the turbojet without an AB at a much lower Mach number. Therefore, when considering lower Mach numbers, the turbojet with AB has a higher advantage in attaining shorter Take-Off distances, especially for military aircrafts on aircraft carriers (i.e. warships). In addition, at higher Mach numbers, the turbojet with an AB has a significantly higher amount of thrust which becomes critical for military type aircrafts in combat mode.

Case II considered the performance evaluation of the turboramjet engine under a maximum power objective function in dual mode operation for variation of altitude and inlet air mass flow split as a function of Mach number. Under dual mode operation the turbojet engine AB were taken to be in the operative state. The results show that the

turbojet operation exhibits a Mach number limitation of 2.51 beyond an altitude of 12 km, whereas the ramjet limitation is in terms of TSFC where beyond a value of 5.694 e-05 at a Mach number of 5.26 and altitude of 20 km operation becomes unrealistic. Moreover, as the split of inlet air mass flow to the ramjet was increased beyond 50% the advantage in terms of η_{th}, η_o, f, TSFC, I_a, thrust and v_{NOZZLE} far supersede that of the turbojet with an AB. The ramjet experiences a significant decrease on f for an increase in altitude from 10 km to 20 km and becomes more fuel efficient than the turbojet with an AB at inlet air mass flow splits above 75%. Furthermore, the ramjet is more economical at 20 km than at 10 km operation where for the same value of TSFC a higher Mach number can be attained 5.26 vs. 4.4 however at the expense of lower than maximum thrust. Where maximum thrust for the ramjet occurs at lower Mach number values: 165 kN at 2.92 Mach vs. 39 kN at 3.12 Mach at 10 km and 20 km respectively. Likewise, for the same value of specific impulse (45 s), the ramjet is able to reach higher Mach numbers (4.4 vs. 4.75 at 100% inlet air mass flow split) as the altitude increases, whereas for the turbojet the I_a exhibits minimal change. In addition, the specific volume of the turbojet with an AB is 1.7 and 2.4 times larger than that of the ramjet for an increase in altitude from 10 km to 20 km; therefore, the trade off in weight is indisputable. Moreover, it is seen that the ramjet can commence operation at a Mach number of 2 and begin diverting the inlet mass flow rate from the turbojet with an AB to the ramjet while still remaining competitive with the turbojet with an AB.

REFERENCES

Şöhret Y., Ekici S. and Karakoç T. H. (2017). Using Exergy for Performance Evaluation of a conceptual Ramjet Engine Burning Hydrogen Fuel, International Journal of Hydrogen Energy, XXX I-6.
https://doi.org/10.1016/j.ijhydene.2017.12.060

Latypov A. F. (2009). Exergy Analysis of Ramjet, Thermophysics and Aeromechanics, Vol. 16, No. 2.
https://doi.org/10.1134/S0869864309020152

Latypov A. F. (2013). Exergy Method for Estimating the Ramjet Specific Impulse, Thermophysics and Aeromechanics, 2013, Vol. 20, No. 5.
https://doi.org/10.1134/S0869864313050023

Ayaz S. K. and Altuntaş Ö. (2017). Assessment of Ramjet Engine for Different Mach Numbers, International Journal of Sustainable Aviation, Vol. 3, No. 4.
https://doi.org/10.1504/IJSA.2017.090299

Moorhouse D. J. (2003). Proposed System-Level Multidisciplinary Analysis Technique Based on Exergy Methods, Journal of Aircraft, Vol. 40, No. 1, January – February.
https://doi.org/10.2514/2.3088

Moorhouse D. J. and Suchomel C. F. (2001). Exergy Method Applied to the Hypersonic Vehicle Challenge, AIAA paper # 2001 – 3063.

Moorhouse D. J., Hoke C. M. and Prendergast J. P. (2002). Thermal Analysis of Hypersonic Inlet Flow with Exergy-Based Design Methods, International Journal of Thermodynamics, vol. 5 (No. 4), pp. 161-168, December.

Marley C. D. and Riggins D. W. (2011). The Thermodynamics of Exergy Losses and Thrust Production in Gas Turbine Engines, AIAA, 2011-6130.

Ispir A. C., Gonçalves P., Kurban E. And Saraçoğlu B. H. (2020). Thermodynamic Efficiency Analysis and Investigation of Exergic Efficiencies of STRATOFLY MR3 Aircraft Propulsion Plant, AIAA SciTech Forum, 6-10 January.

Ehyaei M. A., Anjiridezfuli A. And Rosen M. A. (2013). Exergic Analysis of an Aircraft Turbojet Engine with an Afterburner, Thermal Science, Vol. 17, No. 4, pp 1181-1194.
https://doi.org/10.2298/TSCI110911043E

Roth B. and Marvis D. (2000). A Method for Propulsion Technology Impact Evaluation via Thermodynamic Work Potential, AIAA 2000-4854.

Camberos J. A. And Moorhouse D. J. (2011). Exergy Analysis and Design Optimization for Aerospace Vehicles and Systems, AIAA, Vol. 238, Progress in Astronautics and Aeronautics.

Hayes D., Lone M. and Whidborne J. F., Camberos J. and Coetzee E. (2017). Adopting exergy analysis for use in aerospace, Progress in Aerospace Sciences xxx 1–22.
https://doi.org/10.1016/j.paerosci.2017.07.004

Riggins D. W. and Taylor T. (2006). Methodology for Performance Analysis of Aerospace Vehicles Using the Laws of Thermodynamics, JOURNAL OF AIRCRAFT, Vol. 43, No. 4, July–August.
https://doi.org/10.2514/1.16426

Balli Ö. (2017). Advanced exergy analyses to evaluate the performance of a military aircraft turbojet engine (TJE) with afterburner system: Splitting exergy destruction into unavoidable/avoidable and endogenous/exogenous, Applied Thermal Engineering 111 152–169.
https://doi.org/10.1515/tjj-2016-0074

Balli Ö. (2017). Exergetic, Exergoeconomic, Sustainability and Environmental Damage Cost Analyses of J85 Turbojet Engine with Afterburner, International Journal of Turbo & Jet Engines.
https://doi.org/10.1515/tjj-2017-0019

Balli Ö. (2014). Afterburning effect on the energetic and exergetic performance of an experimental turbojet engine (TJE), International Journal of Exergy, January.
https://doi.org/10.1504/IJEX.2014.060278

Akkaya A.V., Şahin B. and Erdem H.H. (2007). Exergetic performance coefficient analysis of a simple fuel cell system, International Journal of Hydrogen Energy 32 4600 – 4609.
https://doi.org/10.1016/j.ijhydene.2007.03.038

Yüksel B., Balli Ö., Günerhan H. and Hepbaslı A. (2020). Comparative Performance Metric Assessment of a Military Turbojet Engine Utilizing Hydrogen and Kerosene Fuels Through Advanced Exergy Analysis Method, Energies, 13, 1205.
https://doi.org/10.3390/en13051205

Balli Ö., Adak İ. and Güneş S. (2017). Afterburner Effect on the Energetic and Exergetic Performance of J79-GE-17 Engine with Afterburner System used on F-4 Phantom II Aircrafts, International Symposium on Sustainable Aviation (ISSA-2017), Kiev, Ukraine, 10 – 13 September.

Akkaya A.V., Şahin B. and Erdem H.H. (2008). An analysis of SOFC/GT CHP system based on exergetic performance criteria, International Journal of Hydrogen Energy 33 2566 – 2577. https://doi.org/10.1016/j.ijhydene.2008.03.013

Bastani M., Jafari R. and Ghasemi H. (2015). Exergy Analysis of an Aircraft Turbojet Engine, International Journal of Engineering Sciences & Research Technology, ISSN: 2277-9655, April.

Yüksel B., Günerhan H. and Hepbaslı A. (2020). Assessing Exergy-Based Economic and Sustainability Analyses of a Military Gas Turbine Engine Fueled with Various Fuels, Energies, 13, 3823. https://doi.org/10.3390/en13153823

Niknamian S. (2020). The optimization of a jet turbojet engine by PSO and searching algorithms, Social Science Research Network, https://ssrn.com/abstract=3503740, January. https://doi.org/10.35877/454RI.asci3195

Sürer M.G. and Arat H.T. (2018). A Critical Review of Exergy Studies on Jet Engines, 16th International Conference on Clean Energy (ICCE-2018), May.

Dong Z., Li D., Wang Z. and Sun M. (2018). A Review on Exergy Analysis of Aerospace Power Systems, Acta Astronautica, AA 7090, S0094-5765(18)31012-9, September. https://doi.org/10.1016/j.actaastro.2018.09.003

Noori F., Gorji M., Kazemi A. and Nemati H. (2015). Thermodynamic optimization of ideal turbojet with afterburner engines using non-dominated sorting genetic algorithm II, Journal of. Aerospace Engineering, Proc. IMechE Vol. 224 Part G, February. https://doi.org/10.1243/09544100JAERO771

Nasab M.R.A. and Ehyaei M.A. (2019). Optimization of turbojet engine cycle with dual-purpose PSO algorithm, Mechanics & Industry 20, 604, March. https://doi.org/10.1051/meca/2019029

Liu, Y., Mo, D. and Wu, Y. (2023). Design of Hypersonic Variable Cycle Turboramjet Engine Based on Hydrogen Fuel Aiming at 2060 Carbon Neutralization. The Proceedings of the 2021 Asia-Pacific International Symposium on Aerospace Technology (APISAT 2021), Volume 2. APISAT 2021. Lecture Notes in Electrical Engineering, vol 913. Springer, Singapore. https://doi.org/10.1007/978-981-19-2635-8_85

Rajashankar S., Ananthkrishnan N., Sharma A., Lee J. and Namkoung H.J. (2024). Turbojet Module Sizing for Integration with Turbine-Based Combined Cycle Engine, Cornell University, Physics, Fluid Dynamics, arXiv:2406.19472v1 [physics.flu-dyn] 27 Jun 2024. https://doi.org/10.48550/arXiv.2406.19472

Xi Z., Zhang H., Chen M., Cai C. and Wang J. (2023). Design of thrust augmentation control schedule during mode transition for turbo-ramjet engine, Aerospace Science and Technology Volume 138, July 2023, 108352 https://doi.org/10.1016/j.ast.2023.108352

Lockheed Martin SR-72, "Son of Blackbird" (2024). https://en.m.wikipedia.org/wiki/Lockheed_Martin_SR-72 https://www.youtube.com/watch?v=vFMIQOMaUXI

Fawal S. and Kodal A. (2019). Comparative performance analysis of various optimization functions for an irreversible Brayton cycle applicable to turbojet engines, Energy Conversion and Management, 199 111976. https://doi.org/10.1016/j.enconman.2019.111976

Fawal S. and Kodal A. (2021). Overall and Component Basis Performance Evaluations for Turbojet Engines Under Various Optimal Operating Conditions, Aerospace Science and Technology 117 106943. https://doi.org/10.1016/j.ast.2021.106943

MIL-E-5007D (1973). General Specification for Engines, Aircraft, Turbojet and Turbofan, Military Specification, Department of the Air Force, Wright-Paterson AFB, OH, September.

Keith T.G. and John J.E. (2006). Gas Dynamics, Third Edition, Pearson, Prentice Hall, Upper Saddle River, NJ.

El-Sayed A.F. (2016). Fundamentals of Aircraft and Rocket propulsion, Department of Mechanical Engineering, Zagazig University, Zagazig, Egypt, Springer-Verlag London.

Mattingly J. D. (1996). Elements of Gas Turbine Propulsion, TATA McGraw-Hill Edition.

Farokhi S. (2014). Aircraft Propulsion, 2nd Edition, Wiley.

Journal Homepage: https://dergipark.org.tr/tr/pub/isibted

Isı Bilimi ve Tekniği Dergisi

Archive: https://tibtd.org.tr/dergi

Assessing Risks of Electric Vehicles in Underground Parking Facilities: Strategies for Enhancing Urban Sustainability

Orhan TOPAL [1,2]

[1] *Aselsan Inc., Yenimahalle, 06200, Ankara, Türkiye*
[2] *OSTİM Technical University, Department of Electrical and Electronics Engineering, Ankara, Türkiye*

A R T I C L E I N F O

2025, vol. 45, no.1, pp. 84-96

doi: 10.47480/isibted.1541539

Review Article
Received: 31 August 2024
Accepted: 04 December 2024

* *Corresponding Author*
e-mail: otopal@aselsan.com.tr
orhan.topal@ostimteknik.edu.tr

Keywords:
electric vehicle fire, indoor car park, charging station integration, emergency response

ORCID Numbers in author order:
0000-0003-3857-5689

A B S T R A C T

As cities confront the dual challenges of global warming and urban environmental degradation, adopting sustainable mobility strategies has become essential for future resilience and sustainability. The use of electric vehicles, which have minimal emissions and are constructed in an energy-efficient manner, represents a viable solution to this issue. Conversely, the secure and effective implementation of electric vehicles in car parks presents a multitude of technical and infrastructural challenges. Despite the anticipated substantial rise in the use of electric vehicles in the near future, there are proposals for them to be subject to a range of restrictions due to fire safety concerns. It has been established that charging processes represent the primary cause of fires in electric vehicles. The utilisation of charging stations in enclosed and particularly subterranean garages situated within edifices that serve a multiplicity of purposes, including commercial, residential and retail, is on the rise. As a result, it poses a greater risk in a potential fire scenario than a charging station located in the open air. The pressure on charging times, especially for electric vehicles, requires the use of chargers with a higher power rating, which may increase the risk. It is noted that although electric vehicle fires and combustion engine vehicle fires have similar characteristics, there are differences in the fire behaviour of electric vehicles. This paper aims to provide a strategic guide to achieving urban sustainability goals by looking at innovative approaches to the deployment of electric vehicles in car parks and solutions to potential risks. The use of car parks is crucial to strengthening the role of electric vehicles in future urban mobility systems. It aims to facilitate the harmonisation of electric vehicles and charging stations, contributing to a more sustainable future by reducing the environmental impact of cities.

Yeraltı Otoparklarında Elektrikli Araç Risklerinin Değerlendirilmesi ve Kentsel Sürdürülebilirlik Stratejileri

M A K A L E B İ L G İ S İ

Anahtar Kelimeler:
elektrikli araç yangını, kapalı otopark, şarj istasyonu entegrasyonu, acil müdahale

Ö Z E T

Şehirler, küresel ısınma ve çevresel bozulma gibi iki önemli zorlukla karşı karşıya kalırken, sürdürülebilir ulaşım stratejilerinin benimsenmesi, sürdürülebilir bir gelecek için zorunluluk haline gelmiştir. Elektrikli araçların, minimum emisyon ve yüksek enerji verimliliği sağlamak üzere tasarlanması, bu sorunlara yönelik etkili bir çözüm sunmaktadır. Ancak, elektrikli araçların otoparklarda güvenli ve etkili bir şekilde kullanılabilmesi, beraberinde çeşitli teknik ve altyapısal zorlukları da gündeme getirmektedir. Yakın gelecekte elektrikli araç kullanımında beklenen önemli artışa rağmen, yangın güvenliği endişeleri nedeniyle bu araçların çeşitli kısıtlamalara tabi tutulmasını öneren yaklaşımlar giderek daha fazla tartışılmaktadır. Araştırmalar, elektrikli araçlarda meydana gelen yangınların birincil nedeninin şarj işlemleri olduğunu ortaya koymuştur. Ticari, konut ve perakende gibi çeşitli amaçlara hizmet eden yapılardaki kapalı, özellikle yer altı garajlarında şarj istasyonlarının kullanımı giderek artmaktadır. Sonuç olarak, olası bir yangın senaryosunda, kapalı alanlardaki şarj istasyonları, açık havada bulunan şarj istasyonlarına kıyasla daha büyük bir risk teşkil etmektedir. Özellikle elektrikli araçlar için şarj sürelerini azaltma baskısı, riski artırabilecek daha yüksek güç kapasitesine sahip şarj cihazlarının kullanımını zorunlu kılmaktadır. Elektrikli araç yangınlarının, içten yanmalı motorlu araç yangınlarıyla benzer özellikler taşımasına rağmen, yangın davranışlarında belirgin farklılıklar gösterdiği vurgulanmaktadır. Bu çalışmada, otoparklarda konuşlandırılan elektrikli araç yönelik olası riskler ele alınmıştır. Söz konusu duruma yönelik çözümler incelenerek, kentsel sürdürülebilirlik hedeflerine ulaşmak için stratejik bir rehber sunulması amaçlanmaktadır. Otoparkların kullanımı, elektrikli araçların gelecekteki kentsel hareketlilik sistemlerindeki rolünü güçlendirmek açısından büyük bir öneme sahiptir. Elektrikli araçlar ve şarj istasyonlarının uyumlaştırılmasını kolaylaştırarak, şehirlerin çevresel etkisini azaltmayı ve daha sürdürülebilir bir geleceğe katkıda bulunmayı amaçlamaktadır.

NOMENCLATURE

m	combustion rate (kg/s)	m″	combustion flux (kg/m^2/s)
ΔHe	heat of combustion (MJ/kg)	ŋ	combustion flux
Af	base or surface area of the fuel or fire	ΔHc	state of charge

INTRODUCTION

The growing prevalence of electric vehicles and the imperative for environmental sustainability necessitate a corresponding evolution in the infrastructure of car parks, with the requisite adaptations to accommodate these technologies. In this context, it is of paramount importance to ensure the safe and efficient use of electric vehicles, particularly in indoor car parks, in order to facilitate modern urbanism and transport planning. The integration of electric vehicle charging infrastructure, fire safety, energy management and user accessibility represent key issues that must be addressed in the redesign of car parks. The installation of electric vehicle charging points in car parks offers dual benefits; it provides convenience for car owners and plays an important role in meeting cities' energy management and sustainability goals. The strategic placement of charging stations is of critical importance for the efficient distribution of energy and the sustainable satisfaction of users' charging needs. Nevertheless, adherence to the established fire safety protocols and regulations is indispensable for the safe and effective operation of charging stations. It is imperative to consider the potential fire risk associated with electric vehicle batteries, particularly in enclosed parking facilities.

The rise in the number of fires caused by electric vehicles in recent years has prompted concerns about the safety of this new technology. The high energy density of electric vehicle propulsion batteries and the potential for battery cells to ignite due to the risk of thermal runaway necessitate the implementation of safe storage and charging practices, particularly in enclosed settings. In this context, it is of paramount importance to develop effective fire-suppression systems and emergency protocols for the mitigation of electric vehicle fires, particularly in indoor car parks. Furthermore, it is of paramount importance for both electric vehicle users and car park operators to engage in regular maintenance and safety inspections, with the objective of reducing the risk of fire. The objective of this study is to provide an overview of recent studies addressing different aspects of the deployment of electric vehicles in car parks. A comprehensive examination of the technical and safety aspects of the deployment of electric vehicles in car parks will be conducted. It is of paramount importance to integrate electric vehicles in a safe, efficient and sustainable manner if modern urbanism and transport planning are to progress. The objective of this approach is to present novel approaches and solutions to relevant audiences for the deployment of electric vehicles in indoor car parks, based on an analysis of existing literature and technology.

Electric Vehicle Safety and Risks in Underground Parking: A Literature Review

The proliferation of electric vehicles has precipitated substantial shifts in the realms of sustainable transportation and environmentally conscious urbanism. In this context, a number of academic studies and technical reports have been published in recent years examining the deployment of electric vehicles in car parks and the integration of charging infrastructure.

The influence of energy management strategies pertaining to the utilisation of electric vehicles in indoor car parks and the impact of charging stations on energy demand has been subjected to investigation. The research addressed the integration of renewable energy sources, energy storage solutions and the sustainability of the charging infrastructure of electric vehicles (Wang et al., 2023).

Smith and Brown undertook a review of the extant regulations and standards pertaining to the deployment of electric vehicles in car parks, identifying deficiencies in this domain. The study recommended that safety and performance standards should be updated and that a regulatory framework should be developed to adapt to new technologies (Wang et al., 2023).

The potential fire risk associated with electric vehicle batteries and the optimal strategies for mitigating this risk in parking facilities have been subjected to rigorous examination. The study presents a series of innovative fire safety protocols designed to prevent thermal runaway events in drive coils. Additionally, it offers a range of approaches aimed at enhancing the efficacy of fire suppression systems in car parks (Bai et al., 2022).

Liu et al. examined the accessibility of electric vehicle users to charging stations in parking garages, as well as the challenges they face in this regard. The study highlighted the necessity for the ergonomic design of the charging infrastructure and the creation of user-friendly applications with the objective of enhancing the user experience (Liu et al., 2022).

The calculations were conducted using the Fire Dynamics Simulator (FDS) program to analyse the potential outcomes of an electric vehicle fire in an underground car park. The scenario involved 10 vehicles and was designed to represent a realistic setting for such an incident. The present study employs numerical analysis to elucidate the dispersion and temperature distribution of hydrogen fluoride in the aftermath of the fire. It has been established that a fire involving a small-capacity lithium-ion battery releases hydrogen fluoride in quantities that are dangerous even for individuals exposed to the fire (Krol & Krol, 2022).

In the study conducted by Hao et al. on the requisite charging infrastructure for electric vehicles and its integration in indoor car parks, efficiency analyses pertaining to the optimal positioning of charging stations were conducted. The objective is to enhance energy efficiency by employing sophisticated algorithms to identify the optimal location for charging stations (Hao et al., 2021).

In a study examining the environmental impact of electric vehicle fire extinguishing systems, it was found that the water used for extinguishing and cooling purposes in the event of an electric vehicle fire was significantly contaminated. It was therefore stated that the residual liquid in question, due to the concentrations of heavy metals such as lithium, cobalt, nickel and manganese, exceeds the current limit values for discharge into the sewerage system. It was further recommended that appropriate pre-treatment should be applied in practice (Mellert et al.,2020).

The question of whether the charging of electric vehicles in car parks poses a fire risk, and what measures are necessary to ensure that the risk remains at an acceptable level, has been addressed by Mellert et al. The study comprised a comprehensive assessment of the fire risk associated with electric vehicles during the charging process. This encompassed an evaluation of the fire risk posed by the electrical installation in the car park during charging, the vehicle layout in the car park and the active fire extinguishing systems. It has been argued that the findings derived from the statistical analysis and literature review are not sufficiently robust to indicate that the charging of electric vehicles in closed car parks will increase the probability of fire (Mellert et al.,2020).

It has been asserted that the extant regulatory framework pertaining to the installation of charging points for electric vehicles is adequate to ensure that the fire risk associated with the charging of electric vehicles in enclosed car parks is maintained at an acceptable level. It is stated that the commissioning of these charging stations should be carried out in accordance with the relevant legislation and in compliance with the recommendations of the vehicle and charging station manufacturers regarding the application. It is inadvisable to utilise electrical sockets and extension cables that have not been specifically designed for the purpose of charging vehicles. In indoor car parks where electric vehicles can be charged, the necessity for fixed water-based fire extinguishing systems is no greater than in other car parks (Brandt & Clansberg, 2020).

The present study investigates emergency response methods for fire incidents occurring in electric (battery) construction equipment operating in underground conditions, such as those found in mines in Finland. It is stated that thermal runaway in the drive batteries is the most common fire scenario. It is therefore generally recommended that water or water-based extinguishing materials be used for the purpose of extinguishing fires caused by electric vehicle drive batteries. In the event of a drive battery fire occurring underground, it is imperative that underground operations are immediately ceased. Attempting to allow the battery pack to burn and self-extinguish is not a viable option, given the potential deterioration of rock integrity due to the high heat generated and the inevitable production losses that will occur. Instead, high-voltage resistant personal protective equipment specific to electric vehicles should be utilised, rather than conventional personal protective equipment typically employed for risks associated with the extinguishing of the battery pack with water (Välisalo, 2019).

The objective of this study is to examine the conditions under which underground car parks in Spain are used by electric vehicles. In addition, the study will review relevant literature, assess compliance with standards and requirements, and identify potential hazards. Furthermore, the study will investigate the necessity for near-future solutions to establish testable performance guidelines for qualified emergency response personnel. In particular, it was recommended that information and discussions aimed at influencing consumer perceptions in a way that is not grounded in evidence be avoided. This is to prevent the creation of an agenda that is not based on facts (Blanco-Muruzábal et al.,2022).

In Türkiye, the Istanbul Metropolitan Municipality and Fire Department conducted a training exercise to extinguish a 75.2 kWh propulsion battery used in electric buses. The objective of the exercise is to ascertain the potential hazards associated with electric vehicle drive battery fires and to evaluate the measures that can be taken to mitigate these risks. Additionally, the exercise aims to assess the effectiveness of various fire extinguishing techniques in such scenarios. It was indicated that 11 distinct extinguishing agents were employed in the aforementioned exercise, and the effects produced were quantified and assessed with the aid of a thermal camera (İstanbul Metropolitan Municipality Fire Department, 2024).

A review of the occurrence of battery fires in electric vehicles, related safety issues and fire protection strategies, as presented by Brzezinska and Bryant. It has been posited that as the market share of electric vehicles continues to expand, the incidence of fires resulting from accidents involving such vehicles has concomitantly increased. It was asserted that pragmatic engineering methodologies for mitigating the risk of fire in electric vehicles are constrained. In this context, it was posited that the generally accepted heat release rate (HRR) for fire engineering design in car parks is approximately 7 MW. It has been demonstrated that the rate of growth of fires in propulsion batteries in electric vehicles is significantly faster than in vehicles powered by conventional fuels. The findings of the study, which employed fire dynamic simulation (CFD) to anticipate the dispersion of smoke and temperature during an electric vehicle fire, are presented herein. This demonstrates that as the fire intensifies, the temperature within the garage rises and visibility declines. This indicates that the circumstances under which people may be safely removed from the garage are becoming increasingly unfavourable. It is indicated that the estimated evacuation time for individuals may vary according to the intended purpose of the garage. The objective of the fire dynamic simulations (CFD) conducted in this context is to ascertain whether an electric vehicle fire in a garage presents a risk to individuals who may be trapped inside and whether there is sufficient time to evacuate before the critical boundary conditions of the fire occur (Brzezinska ve Bryant, 2022).

Dorsz and Lewandowski conducted a comparative analysis of the characteristics of fires in electric and internal combustion engine cars. The utilisation of fire dynamic simulations (CFD) facilitated the attainment of results pertaining to the impact of fire on life and property safety in enclosed structures. It is therefore imperative that fire prevention and extinguishing systems are correctly designed in existing building and tunnel structures to cater for the potential occurrence of battery electric vehicle fires in underground garages or tunnels. In the event of a fire, ventilation or sprinkler system are provided to indicate the horizontal escape routes of individuals in danger and to facilitate favourable conditions for evacuation. It is observed that the available data for these systems, which form the basis of rescue and firefighting operations, is inadequate (Dorsz & Lewandowski,2022).

The primary distinction between the origin, progression, and extinguishing of fires in electric vehicles and those in conventional vehicles lies in the utilisation of lithium-ion (Li-ion), nickel metal hydride (Ni-MH), and other similar components in the drive battery for energy storage (Iclodean et al., 2017). In contrast to conventional liquid or gas fuel tanks (petrol, diesel, LPG, CNG), the principal distinctions between these alternative energy sources lie in the electric

traction motor, on-board charger, charging port, DC/DC converter and other power electronics components, as well as the thermal systems employed to regulate them (Larminie & Lowry,2003). The batteries used in electric vehicles are considered to be the main source of hazard, as they are susceptible to a number of influences, including mechanical, thermal and electrical, which can lead to the initiation and/or growth of fire. Similarly, in the case of traction batteries, the higher the temperature of the chemistry, the more exothermic the reaction chain, especially when it comes to the dangerous heating curve. The thermal effects of the reaction cause a significant increase in heat released. As a result, there may be a fire or explosion hazard (Hou et al., 2020). In this context, it is asserted that a multitude of factors exert an influence on the drive battery. Such incidents may include instances of overcharging, short circuits, mechanical impact (such as the penetration of the cell by a nail or other object), and thermal impact (exposure to extreme temperatures) (Bisschop et al., 2020). The analysis also encompasses other factors, including the state of charge (SoC), the state of health (SoH), the capacity and energy density of the battery, and the ambient temperature (Essl et al.,2020).

The occurrence of fires in electric vehicles in enclosed spaces, such as road tunnels and car parks, has given rise to concerns among the general public. This situation gives rise to measures such as the prohibition of the parking of electric vehicles, particularly in enclosed car parks. It is an inevitable consequence of the success of electromobility that electric vehicles will become widespread, thereby reducing the use of fossil fuels and increasing the use of renewable energy. It was highlighted that technical solutions should be implemented to address the fire risks and potential consequences associated with electric vehicles. The study concluded that a comprehensive risk assessment and systematic hazard identification are necessary for electric vehicle fires. A workshop was convened with representatives from three distinct fire and rescue organisations in Sweden. The efficacy of emergency rescue forms/response manuals was evaluated, and the results are presented below. It is therefore recommended that improvements be made to the statistics on electric vehicle fires, as the data currently available lacks information on the main causes of such fires. Such a course of action could result in the introduction of new regulatory measures that lack a robust and evidence-based foundation. The data analysed by Hynynen et al. indicates that fires in electric vehicles are no more common than in vehicles with internal combustion engines. It has been argued that the most effective risk mitigation measure to limit the spread of EV fires is the implementation of appropriate infrastructural arrangements. The implementation of fire detection and extinguishing systems, in addition to the creation of a safe distance between parked vehicles, are regarded as fundamental strategies (Hynynen et al.,2023). In a study on safety approaches to electric vehicle fires that may occur in underground car parks, it is stated that, in comparison to conventional internal combustion vehicles with high sales values and high prevalence, electric vehicles give rise to concerns regarding fire safety.

Boehmer et al. and Bisschop et al. conducted a study on the safety approaches to electric vehicle fires that may occur in underground car parks. It has been asserted that electric vehicles give rise to concerns regarding fire safety when compared to conventional internal combustion vehicles, which are currently in high demand and widely prevalent. Furthermore, it was posited that these concerns have been exacerbated by the occurrence of electric vehicle fires in previous years. It has been established that the majority of fires in electric vehicles are caused by thermal leakage from the drive batteries. Furthermore, it has been demonstrated that the phenomenon in question is caused by external fires that occur as a result of thermal runaway, which manifests spontaneously in parking lots or while driving, and sometimes following traffic accidents (Wang et al., 2012).

It has been posited that the most significant aspect of drive battery fire dynamics in electric vehicles is the battery material and chemistry (Ouyang et al.,2019). The safety of lithium-based battery packs is a topic of concern, particularly in relation to their scale of use and energy density (Ouyang et al.,2019). The deformation of electric vehicle drive batteries can result in the generation of sparks, flammable gases and the release of toxic chemicals as a consequence of combustion (Tobishime et al.,1999). The aforementioned issues have the potential to result in the ignition of a fire, which may subsequently evolve into a combustion process and/or a gas explosion. While a typical electric vehicle drive battery system is unlikely to ignite in normal conditions, external influences, including thermal, mechanical, and electrical factors, may lead to such an outcome when the battery is subjected to unfavourable operating conditions or collision accidents (Liu et al., 2021).

The presence of low ceilings, particularly in enclosed parking facilities, serves to facilitate the propagation of fire and may impede the implementation of rescue operations. The rise in the overall number of electric vehicles is also driving the installation of electric vehicle charging stations in public car parks, which represents a novel risk factor for car park fires. In light of these considerations, Sun et al. propose the prohibition of electric vehicle charging in parking facilities or the imposition of restrictions on the number and density of parked vehicles (Sun et al.,2020).

In the context of fire assessments involving electric vehicles, the drive battery is frequently identified as the primary causal factor. However, that electric vehicle battery fires can be caused by a number of factors, including charging system failures, overloading of high-voltage power cables or external interventions (such as arson) UK Road Vehicle Fires Dataset,2019) (Huang & Nakamura, 2020). A study conducted by the Swedish Research Institute has revealed that the failure of an electric vehicle drive battery can result in a range of potential consequences, including ventilation, fire and an internal explosion of the battery cells. Furthermore, it is indicated that in the event of the accumulation of gas from the batteries within a confined space of the vehicle body, an external explosion may occur beyond the boundaries of the battery pack. However, such external explosions are not included in the assessment of the drive batteries during the validation tests (Bisschop et al.,2019).

The occurrence of fires in electric vehicles can be attributed to one or more of the following potential causal factors (Sun et al., 2020).

The ignition of a fire in an electric vehicle may be caused by a number of factors, including exposure to extreme weather conditions (such as low or high temperatures and high humidity) or damage caused by saltwater. Internal cell failure may also be a contributing factor.

A fire may be ignited during the charging of an electric vehicle. This may be caused by overcharging, the presence of faulty or unsafe charging stations, or installation-related faults.

In the event of an electric vehicle being involved in a collision or other form of damage, or if the road surface is uneven, the fire will continue to burn.

In instances where fires have been observed in electric vehicle batteries, it has been noted that the fire may rekindle due to thermal leakage, which may occur even after the initial fire has been extinguished.

It has been posited that thermal leakage, resulting from a markedly elevated battery temperature, represents the primary causal factor in the aforementioned incidents of electric vehicle fires (Babrauskas,2003). The occurrence of thermal runaways in batteries is frequently accompanied by the emission of smoke, sparks and flames. Furthermore, the release of gas in a confined space may result in an explosive reaction if the accumulated gas is in contact with the surrounding oxygen. Conversely, when the ambient temperature is low, the temperature gradient experienced by the cells within the drive battery packs results in a reduction in performance. In this regard, there is a notable elevation in the internal resistance value. In such circumstances, an additional thermal effect may be generated, thereby increasing the probability of fire. It is therefore recommended that electric vehicles be stored in a closed garage, particularly when not in use, in order to protect them from exposure to extreme temperatures, both hot and cold, which may be experienced outdoors. Conversely, electric vehicles are anticipated to be recharged with minimal delay and to offer high driving dynamics. In particular, the intensive charging and discharging of the drive battery cells, in conjunction with other drive components that generate external heat, can result in a Joule effect within the drive battery structure. Furthermore, this situation has the potential to elicit unintentional chemical reactions, which could result in an internal short circuit. The utilisation of rapid charging techniques, particularly those conducted in parking facilities, is regarded as one of the most hazardous concerns within this domain. It can be reasonably deduced that the following factors contribute to an elevated risk of fire: the lack of competence of the service provided for electric vehicles; the absence of technical standards for the charging station and its sub-components; and the BMS functions that do not possess sufficient safety parameters (Larsson & Mellander, 2017)

In the event of thermal runaway, which can be triggered by mechanical, thermal and electrical damage occurring in batteries, a reduction in voltage level is observed as a consequence of damage to the electrodes in the battery cells. The pressure within the battery pack rises as a consequence of the chemical reaction between the active materials, the evaporation of the organic electrolyte, and the formation of a flammable gas. This results in the accumulation of gas within the battery pack (Kong et al., 2018). In this context, it is stated that the primary parameters to be measured during the testing of propulsion batteries are voltage, current, and temperature (IEC Standart Part 2 Reliability and Abuse Testing). Furthermore, it is postulated that the ramifications of electric vehicle fires that may transpire in indoor parking lots will be considerably more grave than those in outdoor settings.

The Heat Release Rate (HRR) value serves as the foundation for evaluating potential fire hazards. This parameter, which corresponds to the total heat release value caused by the fire, provides a standardised measurement approach for the size of the fire that occurs. It serves as a point of reference for the design of security systems intended to mitigate the risk of fire in parking lots, particularly in the context of electric vehicles. The heat release rate (HRR) is calculated in accordance with the Equation (1.1) and Equation (1.2) below.

$$HRR = m\,\Delta \mathrm{He} \tag{1.1}$$

$$HRR = Af\, m''\, \eta\, \Delta \mathrm{H\,c} \tag{1.2}$$

In this context,

- m is the combustion rate, determined by the mass loss rate obtained from the test and expressed in kilograms per second (kg/s).
- ΔHe is the heat of combustion, expressed in megajoules per kilogram (MJ/kg).
- Af is the base or surface area of the fuel or fire, which serves as the basis for the electric vehicle.
- m″ is the combustion flux, expressed in kilograms per square metre per second (kg/m^2/s).
- ŋ, is the combustion efficiency, dependent upon the source of oxygen. The heat of combustion value for electric vehicle propulsion batteries,
- ΔHc, is contingent upon the specific type of propulsion battery employed and the battery charge rate (state of charge, SoC).

There are a number of different approaches that can be taken with regard to the fire size caused by the electric vehicle drive battery. It is notable that the 2250 kg Tesla Model S is equipped with a propulsion battery comprising a total of 18,650 individual cells, with each cell weighing 45 g. It is therefore evident that the heat release rate (HRR) value can vary considerably, from a few kW for a battery cell to several hundred kW for a single EV battery module and up to MW for a full capacity electric vehicle propulsion battery pack (Sun et al., 2020) (Liu et al., 2016). The fundamental premise is contingent upon the point of origin of the fire reaction, which may manifest as a cell, module, or package.

Furthermore, the energy released in the event of an electric vehicle fire can be quantified through the calculation of the average heat flux (q″) of the battery pack and its surface area. In order to facilitate the calculations, it would be appropriate to assume that the battery charge rate (state of charge, SOC) is 100%, which represents the most adverse fire scenario. To illustrate the functionality of an electric vehicle powered by a propulsion battery with Lithium Titanate (LTO) chemistry, it can be observed that the average heat flux (q″) is approximately 2.3 MW/m^2 when the battery capacity is 100%. Assuming a traction battery area of approximately 3 m^2 (Af), the average heat release rate (HRR) of an electric vehicle fire can be calculated using Equation (1.3).

$$HRR = Af\, q'' = 3\,m2 \times 2.3\,MW/m2 \approx 7\,MW \tag{1.3}$$

The calculated heat release rate (HRR) value is also employed in the determination of the quantity of water or alternative fire-extinguishing agents that are necessary in the event of an electric vehicle fire (US Department of Transportation 2014).

Strategies for Reducing Fire Severity and Enhancing Fire Suppression

The extinguishing of battery fires in electric vehicles is a challenging endeavour, necessitating the use of significant quantities of extinguishing agents. It has been observed that, on occasion, the potential for re-ignition to occur following the extinguishing process may manifest randomly. Extinguishing electric vehicle battery fires in full-scale tests has demonstrated that the quantity of water necessary to extinguish such fires can range from 2,500 to 6,000 litres, which exceeds the water capacity of a standard fire truck. Furthermore, it has been documented that the recommended liquid flow rate for quenching and cooling purposes is relatively high, with a rate of approximately 200 litres per minute (VDA, 2017) (Zhang et al., 2022).

It is generally accepted that in the event of an electric vehicle fire caused by a drive battery, the most appropriate course of action is to cool the source. It is often challenging to gain access to the fire area due to the fact that the battery pack is frequently situated in locations that are difficult to reach. Conversely, the efficacy of cooling and suppressing agents other than water is frequently called into question. The utilisation of chemical substances represents one of the principal methods of fire control. Whilst such substances are effective in extinguishing flames, the potential for explosion is heightened with the accumulation of flammable gases. It has been demonstrated that in instances where only carbon dioxide or other chemical agents are employed to extinguish a battery fire, the fire can be successfully contained; however, the battery pack remains uncooled and unreignited. Consequently, in the context of cooling and controlling electric vehicle drive battery fires, despite the potential negative effects, such as short circuits or toxic discharge, water is currently regarded as the most effective intervention method for cooling electric vehicle fires, despite the inherent risks (Schiemann et al., 2016) (Bisschop et al., 2019).

Large-scale fire tests utilising water mist systems have been conducted by Colella. The findings indicated that water mist can be an effective method for regulating fire temperatures (Colella, 2016).

In light of the rising number of electric vehicle (EV) charging stations, the National Fire Protection Association (NFPA) of America has developed a set of standards aimed at enhancing safety. These standards recommend that EVs with damaged or depleted drive batteries be stored or parked at a minimum distance of 15 metres from charging stations, flammable materials, and other vehicles. Furthermore, the recommendation is that the charging process be conducted for interventions and/or approaches (detections), with monitoring of the operations conducted via a thermal camera (NFPA, 2024)

Conversely, in contrast to the NFPA, the SAE J2293 and J1772 standards stipulate that electric vehicles should be stored in areas with fireproof walls on three sides and a minimum of 15 metres of open space on the fourth side until the requisite inspections have been completed in accordance with the procedures set out in SAE J2990. It is recommended that ventilation be provided to facilitate the circulation of potentially hazardous gases and that the vehicle be protected from precipitation in the event of an opening (or potential damage or fragmentation) in the drive battery shell (SAE International, 2024).

In addition, the EDUCAM information and training platform on the use of electric vehicles stipulates that, in the event of a fire in an electric vehicle, the relevant emergency response guide must be followed (Educam, 2024):

- It is therefore imperative that the auxiliary battery employed for low-voltage systems be disconnected,

- In order to safeguard the item from all surrounding elements, a safety distance of 10 metres must be maintained for a minimum of 48 hours, with a further 2 metres of safety distance to be observed after this period,

- Furthermore, the manufacturer's instructions indicate that the product should not be deployed inside buildings and that, in the event of leakage, the area should be isolated using an appropriate collection device.

Fire Safety Standards and Simulation Techniques in Parking Facilities

In the event of a fire in a confined space, it is imperative that the relevant safety measures are put in place to ensure the protection of individuals. In this context, it is stated that simulations (CFD) should be conducted to ensure the safety of individuals in the event of an electric vehicle fire in a closed garage. In light of the CFD simulation results, which demonstrate the feasibility of meeting the specified evacuation time requirements in the event of a fire, it can be stated that as the fire progresses, the temperature within the garage will increase and visibility will diminish. Although this situation has a negative impact on the ability to evacuate from the garage, it is important to note that the fire brigade teams that will respond should commence extinguishing operations at the scene of the incident. Additionally, the fire flames should not exceed a height of 1.8 metres above the ground, and the ambient temperature should not exceed 60 °C (British Standards Institution, PD 7974-6:2004, 2019).

In accordance with the parking regulations currently in force in Türkiye, all newly constructed parking lots with a capacity of more than 20 vehicles are required to allocate at least 10% of their total number of spaces to electric vehicles. Furthermore, the installation of charging stations in these parking lots is also mandatory. It is recommended that at least one charging station be installed for every ten electric vehicle parking spaces. Furthermore, the charging stations should be situated in the closest possible proximity to the electric vehicle parking spaces, and their technical specifications must comply with the conditions specified in the relevant regulations. Furthermore, the regulation stipulates a transition period for existing parking lots. Consequently, it is obligatory to reserve 10% of electric vehicle parking spaces and install charging stations in these parking lots by 2026 ([Otopark Yönetmeliği]). Conversely, the Electric Vehicle Charging Stations Regulation in Türkiye encompasses the requisite permits and licenses for the establishment of charging stations, the technical specifications of charging stations, and the operation and inspection of charging stations (EPDK, 2017) (TC Ministry of Environment and Urbanization,2018).

In addition, the selection of the agent employed in fire-fighting operations merits consideration in the context of electric vehicles. In this context, the most commonly recommended extinguishing agents by manufacturers of Li-ion batteries are

water, chemical/dry powder, CO2 and dry-foam. It is important to consider the potential drawbacks of water, as it can release lithium and facilitate its reaction with hydrogen, which could result in further adverse outcomes (Ghiji et al., 2020) (Park, 2013). Despite the cooling effect of water, which has a detrimental impact on short circuits and the flow/exit of toxic liquids and gases, it is currently regarded as the most effective and accurate extinguishing method. In this context, it is asserted that the practice of throwing a burning vehicle into a water-filled container has commenced in numerous countries across the globe (Rosenbauer America 2022).

The risk of fire in a parking lot caused by an electric vehicle is a significant concern, particularly in relation to the potential impact on emergency response teams. In this instance, it is imperative that the fire be contained. In the context of underground parking facilities, it is of paramount importance to ensure that physical access to the fire scene is conducted in a safe and secure manner, with the objective of reaching the burning vehicle. It is essential to ensure adequate ventilation of the environment and the prompt evacuation of smoke. In some instances, camera systems deployed at the scene of a fire may be able to identify the point of origin. Nevertheless, in the absence of any other identifying features, it becomes exceedingly challenging for emergency response teams to ascertain the vehicle that initiated the fire. In this context, it is necessary to ascertain whether the vehicle in question is an electric vehicle, once it has been physically reached. It may prove challenging to discern the brand, model, writing, emblem, and other identifying elements among the dense smoke. Nevertheless, in the event that the device is connected to a power source, it is crucial to ascertain the specific charging cable that is linked to the charger, as this can serve as a crucial identifier. It is established that inhaling the smoke produced during fire-fighting operations is a significant health hazard. It has been asserted that this phenomenon, which is not solely attributable to the battery, is significantly prevalent due to the combustion of the carbon fibre structural components employed for the purpose of reducing the weight of electric vehicles (Coldcut Systems, 2024).

The diverse chemical compositions of electric vehicle propulsion batteries may exhibit disparate behaviours in the event of potential thermal runaway. To illustrate, the maximum resistance temperature in cells utilising lithium iron phosphate (LFP) chemistry is approximately 600 °C, whereas this value rises to over 1000 °C in cells employing nickel manganese cobalt oxide (NMC) chemistry. Conversely, it has been demonstrated that in the event of thermal runaway in cells utilising LFP chemistry, the particle ejection is less pronounced than in cells employing NMC chemistry. This can result in disparate consequences for the surrounding environment, particularly in terms of dispersion. Conversely, cells utilising LFP and low-nickel content NMC chemistries exhibit reduced energy density. Consequently, even in the event of a cell catching fire, the probability of the fire spreading to neighbouring cells is deemed to be low. Furthermore, the diverse cells within the drive batteries utilized in electric vehicles are distinguished by their morphology and dimensions. To illustrate, cylindrical and prismatic cells are equipped with natural ventilation capabilities as a consequence of their intrinsic design. Furthermore, given that cells with diminished energy capacity are capable of storing less energy, the potential for thermal runaway is also less pronounced in comparison to larger cells.

Battery management systems that are capable of meeting the requisite safety standards are designed to ensure that each cell of the drive battery operates within safe limits, while simultaneously managing the energy and thermal effects within the battery at the pack level. This is of critical importance to the safe and efficient operation of the battery. In this context, the thermal management provided by the battery management system ensures effective and sustainable conditions are maintained to avoid high thermal stresses caused by excessive heat, following periods of power-intensive driving or fast charging. In this context, following the conclusion of a period of intensive driving or fast charging, the battery management system enables the thermal management system to operate in an effective manner. This guarantees the implementation of effective and sustainable measures to prevent the occurrence of elevated thermal stresses resulting from the presence of excessive heat. Furthermore, the utilisation of thermal insulation between modules and cells in battery packs serves to mitigate the risk of thermal runaway scenarios. The insulation of intercellular spaces can be achieved through the use of foams, sheets, or resins, which effectively prevent the transfer of heat between cells by providing a thermal barrier. Nevertheless, the cooling of a thermally isolated cell is also challenging due to the limited cooling capacity resulting from the system isolation. This limitation is particularly evident. This approach has the indirect effect of reducing the amount of heat that can be removed from the cells, while simultaneously limiting the speed at which the cells can be charged and the high performance requirements. In addition to the density of the cells and/or modules in the battery packs and the insulation between them, the material from which the outer shell of the battery is made is also a significant factor. In the unlikely event of a fire, the use of electro-coated steel with a melting point above 1500 °C will prove to be a more effective form of protection than aluminium and some polymer composites. Additionally, the selection of appropriate interface materials is crucial. Adhesives with high thermal conductivity are essential to facilitate efficient heat transfer to heat sink surfaces or cooling plates at the cell level. Conversely, the utilisation of thermal insulation and flame retardant materials positioned between the cells serves to effectively impede the transfer of unwanted heat. It is imperative that such materials are of a structure that does not produce toxic fumes. It is considered that this constitutes an important design input, providing additional time for passenger evacuation in the event of an electric vehicle fire.
Consequently, an array of studies is currently underway, with the objective of integrating machine learning and artificial intelligence models – two of the most prevalent approaches in the field today – into battery management systems. The application of artificial intelligence (AI) to the design and testing processes for propulsion batteries is a promising avenue of research, particularly with regard to the enhancement of safety and the mitigation of thermal runaway. Notwithstanding the difficulties inherent in simulating propulsion batteries through on-board testing, the prevailing approach to validation is to conduct physical testing to ascertain that different cell chemistries meet performance requirements and that safety standards are met under varying conditions. The training of artificial intelligence applications used in battery management systems in propulsion batteries is primarily based on three types of data: typical measurement data from batteries, live data from electric vehicle fleets, and offline data from battery packs. The

algorithms in question employ a combination of signal processing techniques to extract insights from measurement data, which are then subjected to machine learning models in order to extract diagnostic and thermal runaway-related risk information from these insights. This innovative approach has the potential to significantly reduce thermal risks to drive batteries and is regarded as an effective method for integrating battery expertise and modern machine learning (Thermal Hazard Technology,2024).

Analysis and Case Studies of Electric Vehicle Fire Incidents

In October 2013, on a highway in Washington State, an incident occurred that was to become known as the first mass-produced electric car fire in the world. A piece of metal came into direct contact with the modules in the battery pack, resulting in the vehicle being completely burned. It is confirmed that no fatalities or injuries were sustained by any of those involved in this incident. The inaugural fatality resulting from an electric vehicle fire occurred in May 2018. It has been documented that this fire occurred subsequent to an incident in Florida, wherein an electric vehicle that was exceeding the speed limit veered off the roadway (NTSB, 2020).

As reported by the International Energy Agency, approximately 14 million new electric vehicles were registered globally in 2023, resulting in a total of 40 million electric vehicles on the road. A total of 511 confirmed, officially recorded electric vehicle fires have occurred worldwide between 2010 and 2024 (as of June 2024), according to data from Australian government fire agencies. In consequence, 117 fires were documented in underground or enclosed garages, 173 fires occurred in outdoor settings with vehicles parked, and 155 fires occurred while individuals were operating motor vehicles. Furthermore, no documentation was available for 67 fires. Furthermore, the report indicates that 489 fires were initiated by sparks or jet-like directional flames, while 22 fires commenced with the presence of dense smoke, followed by an explosion and subsequently by intense flames. The available records indicate that 80 fires occurred during the charging process of electric vehicles, while 10 fires occurred at the maximum of 60 minutes after the end of the charging process (Austalia Defence Department, 2024).

This study also considers electric buses, with a particular focus on those with high battery capacity and used in public transportation systems. By 2022, the number of electric buses in use in public transportation systems worldwide had exceeded 800,000, representing more than 3% of the total number of buses. In 2022, approximately 66,000 electric buses were sold worldwide, with China accounting for 54,000 of these, representing approximately 4.5% of all bus sales. It is projected that the number of electric buses in operation will reach 1.4 million in 2025 and 2.7 million in 2030, with one in ten buses expected to be electric (BloombergNEF, 2023).

Accordingly, a review of official records from around the globe revealed that at least 27 high-voltage drive battery fires occurred in electric buses utilized in public transportation systems between 2010 and 2024 (June 30). As evidenced in the aforementioned records, one fire originated in the maintenance and repair workshop, while 12 fires occurred in garages during the act of parking. Similarly, it is stated that 7 fires occurred during the charging process (while the plug was connected), and a further 7 fires occurred by spillover from other fires that were affecting each other. (Austalia Defence Department, 2024).

From the perspective of emergency response to fire situations on electric buses, this significant challenge also pertains to the location of the batteries. The drive batteries of low-floor buses, particularly those designed for disabled access, are often mounted on the roof rather than inside the chassis, as is the case with electric vehicles of the M1 class. This design approach allows for the integration of roof-mounted batteries into conversion projects involving existing diesel buses, while also reducing the need for cooling due to natural air circulation while driving. In the event of thermal runaway in the drive batteries of electric buses, there are no issues with delivering water for cooling, as is the case with chassis-integrated drive batteries in electric vehicles.

It is not possible to obtain specific official records on electric vehicle fires in Türkiye. However, according to the information reflected in the visual and written media, the most prominent cases of electric vehicle fires in Türkiye over the past year have been those occurring during charging in Gaziantep, while the vehicle was being towed by a tow truck on the highway in Adana, and in Istanbul, where a total of six electric vehicles were burned on a truck trailer. In addition, there was one death in the city of Kayseri.

Some of the details of the electric bus fires that were mentioned above are included in this section.

As shown in Figure 1, in accordance with the aforementioned, a fire occurred in the area where electric buses are stationed for charging in Shenzhen, China, where the use of electric buses is the most prevalent. It has been stated that the charging process did not take place. The incident in question is understood to have occurred in a warehouse parking lot that is enclosed on three sides.

Figure 1 Electric bus fire in Shenzhen, China (EVfiresafe,2024)

It has been reported that in Düsseldorf, Germany, in 2021, in the garage where a total of 40 electric and diesel buses were deployed, all of the buses were burned and extensive damage occurred in the fire. Figure 2 illustrates the visual representation of the incident as it was presented in the press. The cause of the fire is currently unknown.

Figure 2 Electric bus fire in Düsseldorf, Germany (EVfiresafe, 2024)

In a further incident that occurred in Hannover, Germany in 2021, it is documented that five electric buses, two hybrid electric buses and one diesel bus caught fire in the garage where the buses were located. Figure 3 indicates the manner in which the incident was represented in the press following the fire. Also there is no data available to indicate whether the buses were undergoing charging at the time.

Figure 3 Electric bus fire in Hannover, Germany (Sustainable Bus Magazine, 2023)

In the incident that resulted in the burning of 25 electric buses (Mercedes eCitaro) in Stuttgart, Germany in 2021, it was stated that the charging centre and garage were completely burned along with the buses in the fire that broke out due to a technical malfunction during the charging process. In Figure 4, the visual presented in the aftermath of the fire event.

Figure 4 Electric bus fire in Stuttgart, Germany (Sustainable Bus Magazine, 2021)

It has been reported that 149 electric buses of the same make and model operating in Paris have been taken out of service for safety reasons due to the successive fires in 2021 in two electric buses (Bolloré Bluebus) operated by RATP in Paris, France and used since 2016. The image of the bus engulfed in flames during the trip is shown in Figure 5. In consequence of these incidents, the entire fleet has been withdrawn from service.

Figure 5 Electric bus fire in Paris, France (Ile-de-France, 2023)

In Türkiye, electric buses, which have been supplied by different local governments in various specifications since 2016, are currently being utilised in the public transportation system. In accordance with the aforementioned, in Türkiye, contracts have been concluded for a total of 241 electric buses, with a length ranging from 6 metres to 25 metres. The fires that occurred in 3 electric buses at disparate times were recorded. Two of the fires were reported to have occurred in garages. The fires occurred in electric buses operated by ESHOT in Izmir. In total, there were five electric buses involved in the incidents. Figure 6 illustrates the use of The combustion of electric buses in public transportation in Izmir, as reported in the local press.

Figure 6 Electric bus fire in İzmir, Türkiye (Yeniasır, 2021)

In Guangxi, China, in 2021, it was reported that four buses had been completely burned down due to an unidentified fire in one of the electric buses that had been parked in an entirely open area. Figure 7 presents a visual representation of the incident.

Figure 7 Electric bus fire in Guangxi, China (South China Morning Post, 2021)

In the City of London, England, it was reported that a total of six electric buses were damaged in a fire that broke out in electric buses operated by Transport for London (TfL) in 2022. In the City of London, England, it was reported that a total of 6 electric buses were damaged in a fire that broke out in electric buses operated by Transport for London (TfL) in 2022. It was reported that as a result of the investigation into the causes of the fire at Potters Garage, operated by Metroline, a decision was taken to withdraw 90 electric buses from operation as a precautionary measure. Also It was reported that, following a fire on a double-decker electric bus operated by Transport for London (TfL) in London, electric buses on the affected route were removed from service as a precaution in January 2024. The visual representations of both events are presented in Figure 8.

Figure 8 Electric bus fires in London, England (BBC News 2022,2024)

Assessment and Conclusions: Key Insights and Implications

The findings of the statistical analysis and literature review indicate that there is no clear indication that the charging of electric vehicles in parking garages will increase the probability of fire. In consideration of the extant regulations pertaining to electric vehicle charging points, it is determined that the fire risk associated with the charging of electric vehicles in parking garages is within an acceptable range. A series of tests conducted by NFPA in 2023 revealed that electric and internal combustion engine vehicles exhibit comparable combustion temperatures (Brandt & Glansberg, 2020). It is additionally observed that fires in electric vehicles do not result in a considerable enhancement in heat dissipation when compared to conventional vehicles, which utilise diesel or gasoline engines. It is thus concluded that the necessity for fixed water-based fire extinguishing systems in parking garages will be adequate for those where electric vehicles can be charged. However, the potential for fires caused by electric vehicle drive batteries in parking garages should be taken into consideration. Such fires are likely to spread more rapidly. It is thus concluded that the necessity for fixed water-based fire extinguishing systems in parking garages will be adequate for those where electric vehicles can be charged. It is important to note that fires occurring in parking garages tend to spread at a faster rate than fires caused by electric vehicle drive batteries.

In this context, it is important to distinguish electric vehicle fires from fires in electric vehicle traction batteries. As electric vehicle fires have similar characteristics to fires in conventional motor vehicles, the extinguishing and intervention methods for such fires are also similar. If a fire in an electric vehicle starts at a location other than the traction battery, taking into account the time it takes for the fire to reach the temperature to cause thermal runaway in the battery, technical intervention methods such as fire extinguishing works or automatic extinguishing systems should be applied in the same way as for conventional vehicle fires. On the other hand, the fire-fighting measures are different if the fire starts directly in the battery pack or if the battery is exposed to high temperatures for long enough for the fire to spread to the battery pack. In M1 class vehicles, the battery packs are generally located inside the vehicle and under the chassis to provide effective isolation from the external environment. This makes it difficult to access the batteries from the outside and prevents water from entering the pack due to the insulation provided in accordance with the battery standards, which makes it difficult to intervene directly in the fire. It is very difficult to stop the chemical reactions that cause thermal runaway in the cells inside the pack without physically opening the pack. It may be possible to achieve adequate cooling of the cells in question using methods of intervention that require the use of large quantities of water. In this context, if the temperature inside the battery is not reduced sufficiently, it may lead to a re-ignition, even if the fire appears to have been extinguished.

It is recommended to monitor the battery pack with a thermal imager to check the temperature of the traction battery in electric vehicles. However, thermal cameras are only able to detect the temperature of the surface of the battery. Therefore, in order to check that the surface temperature has not risen again, the cooling process should be interrupted, a certain period of time should be allowed to elapse, and then the intervention process should be continued with the following check.

The most appropriate fire-fighting scenario for electric vehicles, even in cases where the traction battery temperature is high, is to ensure the safety of the surroundings before moving the vehicle, to intervene where the vehicle is located and, if possible, to extinguish the fire. In the next stage, it may be preferable to allow the vehicle to burn out or to continue cooling the battery pack until the temperature of the battery pack has reached a sufficiently low level in a position where the safety conditions of the vehicle are met. In the case of fires in enclosed car parks, this will depend on the layout of the car park (e.g. multi-storey or multi-pillar structures), the location of the vehicle in the car park, the availability of the necessary equipment to remove it and the availability of competent emergency response personnel to carry out this activity. The most important case is to start work as soon as possible and to prevent the spread of fire from the fire engine to other vehicles.

In the case of uninterrupted water flow in electric vehicle fires, the research reports state that the risk of electric shock from electric vehicle high-voltage batteries is very low and there are no global case records for emergency services. However, given that electric vehicles may always be live during the operations to be carried out, maximum care must be taken to ensure that appropriate personal protective equipment is used and that the body of the vehicle does not come into contact with high-voltage cables and other basic high-voltage components, which are coloured orange according to the standards.

In addition, the rotation of the wheels, particularly when transporting an electric vehicle with a partially burnt-out traction battery after an accident, can cause the regenerative braking system to be activated and power to be supplied to the traction battery. This situation should be considered as an important issue that represents a risk of battery re-ignition. Tow-truck operators, especially for electric vehicles, should be specially trained in emergency procedures and, if possible, the vehicle should be transported on a vehicle (e.g. a flatbed) rather than towed.

As a result, the existing regulations for electric vehicle charging points are considered sufficient to keep the fire risk that may arise from charging electric vehicles in car parks at an acceptable level. In this context, the need for fixed water-based fire extinguishing systems in indoor car parks where electric vehicles can be charged is assessed at a similar level to other car parks. In addition, it is essential that charging stations and their installations comply with applicable legislation and that the use recommendations of vehicle and charging station manufacturers are followed. For this reason, it should be noted that wall sockets and, in particular, extension cords that are not designed for vehicle charging should be avoided.

REFERENCES

After a fire in the bus depot – probably not an e-bus as the cause (12 Jan 2024) EVfiresafe. Retrieved from: https://www.evfiresafe.com/post/why-do-e-buses-catch-fire

Babrauskas, V. (2003). Fire Science Publishers/Society of Fire Protection Engineers; Ignition Handbook.

Bai, S., Zhu, Y., Li, T., Zhang, Y., Wu, L., Geng, D., & Li, B. (2022, July). Overview of electric vehicle charging standards. In 2022 IEEE/IAS Industrial and Commercial Power System Asia (I&CPS Asia) (pp. 700-705). IEEE. https://doi.org/10.1109/ICPSAsia55496.2022.9949844

Bisschop, R.; Willstrand, O.; Amon, F.; Rosengren, M. Fire Safety of Lithium-Ion Batteries in Road Vehicles; Safety & Transport Fire Research; RISE Report 2019/50; Research Institutes of Sweden: Borås, Sweden, 2019. https://doi.org/10.13140/RG.2.2.18738.15049

Bisschop, R., Willstrand, O., & Rosengren, M. (2020). Handling lithium-ion batteries in electric vehicles: preventing and recovering from hazardous events. *Fire technology*, 56, 2671-2694. https://doi.org/10.1007/s10694-020-01038-1

Blanco-Muruzábal, M., Martín-Gómez, C., Zuazua-Ros, A., Echarri, T. T., de las Heras, J. V., & Mambrilla-Herrero, N. (2022). From Combustion Vehicle to Electric Vehicle Parking, Through a Review of Legislation and Publications. Archit Res, 12(1), 1-11. https://doi.org/10.5923/j.arch.20221201.01

BloombergNEF. Electric Vehicle Outlook 2023. Retrieved from: https://assets.bbhub.io/professional/sites/24/2431510_BNEFElectricVehicleOutlook2023_ExecSummary.pdf (accessed on 19 March 2025).

Boehmer, H., Klassen, M., & Olenick, S. (2020). Modern vehicle hazards in parking structures and vehicle carriers. Fire Protection Research Foundation. Retrieved from: https://www.nfpa.org/education-and-research/research/fire-protection-research-foundation/projects-and-reports/modern-vehicle-hazards-in-parking-garages-vehicle-carriers (accessed on 19 March 2025)

Brandt, A. W., & Glansberg, K. (2020). Charging of electric cars in parking garages.

Brzezińska, D. (2019). LPG cars in a car park environment—How to make it safe. International journal of environmental research and public health, 16(6), 1062.. https://doi.org/10.3390/ijerph16061062

Brzezińska, D. (2018). Ventilation system influence on hydrogen explosion hazards in industrial lead-acid battery rooms. Energies, 11(8), 2086. https://doi.org/10.3390/en11082086

Brzezinska, D., & Bryant, P. (2022). Performance-based analysis in evaluation of safety in car parks under electric vehicle fire conditions. Energies, 15(2), 649. https://doi.org/10.3390/en15020649

Brzezinska, D., & Markowski, A. S. (2017). Experimental investigation and CFD modelling of the internal car park environment in case of accidental LPG release. Process Safety and Environmental Protection, 110, 5-14. https://doi.org/10.1016/j.psep.2016.12.001

Bluebus électriques: Jean Castex attend "toutes les garanties" de sécurité pour une remise en circulation (11 May 2023) Paris Île-de-France. Retrieved from: https://www.bfmtv.com/paris/bluebus-electriques-jean-castex-attend-toutes-les-garanties-de-securite-pour-une-remise-en-circulation_AN-202305100969.html (accessed on 19 March 2025)

Colella, F., Understanding Electric Vehicle Fires, 8th Annual Fire Protection and Safety in Tunnels, 2016, 06-08 September 2016, Stavanger, Norway.

Defence, Science & Technology Group Australian Government, Department of Defence, EV FireSafe, Global Passenger EV LIB Fire Incidents Retrieved from: https://static.wixstatic.com/media/8b9ad1_7e072de415f141ada9a4b2054ffc838d~mv2.png (accessed on 19 March 2025)

Defence, Science & Technology Group Australian Government, Department of Defence, EV FireSafe, How many electric bus battery fire have there been globally Retrieved from: https://www.evfiresafe.com/_files/ugd/8b9ad1_1e058681d2e447fdbe00fce9c46d4ec8.pdf (accessed on 19 March 2025)

Dorsz, A.; Lewandowski, M. Analysis of Fire Hazards Associated with the Operation of Electric Vehicles in Enclosed Structures. Energies 2022, 15, 11. https://doi.org/10.3390/en15010011

EDUCAM. Sectorale Norm EDU 100 V3.0: Veilig Werken aan HEV (Hybrid & Electric Vehicles). Available online: https://www.educam.be/sites/default/files/inline-files/EDU100V4.0%20NL_activiteitendomein_garage.pdf (accessed on 20 February 2025).

Ekatpure, R. (2024). Optimizing Battery Lifespan and Performance in Electric Vehicles through Intelligent Battery Management Systems. Journal of Sustainable Urban Futures, 14(5), 11-28. Available online: https://neuralslate.com/index.php/Journal-of-Sustainable-Urban-Fut/article/view/131/99 (accessed on 10 February 2025).

Electric bus bursts into flames, sets nearby vehicles on fire in China (June 4, 2021) South China Morning Post. Retrieved from:https://www.scmp.com/video/china/3136069/electric-bus-bursts-flames-sets-nearby-vehicles-fire-china (accessed on 10 December 2024).

Resmî Gazete. (2022, 2 Nisan). [Şarj Hizmeti Yönetmeliği] (Sayı: 31797).https://www.resmigazete.gov.tr/eskiler/2022/04/20220402-2. (accessed on 28 June 2024)

Essl, C., Golubkov, A. W., & Fuchs, A. (2020). Comparing different thermal runaway triggers for two automotive lithium-ion battery cell types. Journal of the Electrochemical Society, 167(13), 130542. https://doi.org/10.1149/1945-7111/abbe5a

Fire in SBB Stuttgart's depot «could have been caused by e-bus charging». MVG Munich takes 8 e-buses out of service (11 October 2021) Sustainable Bus Magazine. Retrieved from: https://www.sustainable-bus.com/electric-bus/sbb-stuttgart-fire-electric-bus-depot/ (accessed on 28 Jan. 2025)

Ghiji, M., Novozhilov, V., Moinuddin, K., Joseph, P., Burch, I., Suendermann, B., & Gamble, G. (2020). A Review of Lithium-Ion Battery Fire Suppression. Energies, 13(19), 5117. https://doi.org/10.3390/en13195117

Gough, N. Sony Warns Some New Laptop Batteries May Catch Fire. The New York Times, 12 April 2014. Available online: https://www.nytimes.com/2014/04/12/technology/sony-warns-some-new-laptop-batteries-may-catch-fire.html (accessed on 20 September 2024).

Hao, X., Yuan, Y., Wang, H., & Ouyang, M. (2021). Plug-in hybrid electric vehicle utility factor in China cities: Influencing factors, empirical research, and energy and environmental application. Etransportation, 10, 100138. https://doi.org/10.1016/j.etran.2021.100138

He, X., Restuccia, F., Zhang, Y. et al. (2020) Experimental Study of Self-heating Ignition of Lithium-Ion Batteries During Storage: Effect of the Number of Cells. Fire Technol 56, 2649–2669. https://doi.org/10.1007/s10694-020-01011-y

Hou, J., Lu, L., Wang, L. et al. Thermal runaway of Lithium-ion batteries employing LiN(SO2F)2-based concentrated electrolytes. Nat Commun 11, 5100 (2020). https://doi.org/10.1038/s41467-020-18868-w

Huang, X., Nakamura, Y. A Review of Fundamental Combustion Phenomena in Wire Fires. Fire Technol 56, 315–360 (2020). https://doi.org/10.1007/s10694-019-00918-5

Hynynen, J., Quant, M., Pramanik, R., Olofsson, A., Li, Y. Z., Arvidson, M., & Andersson, P. (2023). Electric vehicle fire safety in enclosed spaces. Available online: https://trid.trb.org/View/2344751 (accessed on 20 October 2024).

Iclodean, C.; Varga, B.; Burnete, N.; Cimerdean, D.; Jurchiş, B. Comparison of Different Battery Types for Electric Vehicles. IOP Conf. Ser. Mater. Sci. Eng. 2017, 252, 012058 https://iopscience.iop.org/article/10.1088/1757-899X/252/1/012058/pdf

İzmir'de elektrikli otobüs alev alev yandı! Yolcular dakikalarla kurtuldu. (2022, 28 Nisan). YeniAsır Available online: https://www.yeniasir.com.tr/izmir/2021/06/28/izmirde-elektrikli-otobus-alev-alev-yandi-yolcular-dakikalarla-kurtuldu (accessed on 20 May 2024).

IEC 62660-2. Secondary Lithium-Ion Cells for the Propulsion of Electric Road Vehicles—Part 2: Reliability and Abuse Testing; International Electrotechnical Commission: Geneva, Switzerland, 2010. https://webstore.iec.ch/en/publication/27387

Kong, L., Li, C., Jiang, J., & Pecht, M. G. (2018). Li-Ion Battery Fire Hazards and Safety Strategies. Energies, 11(9), 2191. https://doi.org/10.3390/en11092191

Krol, M., Krol, A. (2022). The Threats Related to Parking Electric Vehicle in Underground Car Parks. In: Sierpiński, G. (eds) Intelligent Solutions for Cities and Mobility of the Future. TSTP 2021. Lecture Notes in Networks and Systems, vol 352. Springer, Cham. https://doi.org/10.1007/978-3-030-91156-0_6

Larminie, J., & Lowry, J. (2012).Electric vehicle technology explained* (2nd ed.). Wiley.

Larsson, C. F. (2017). Lithium-ion battery safety - Assessment by abuse testing, fluoride gas emissions and fire propagation (Doctoral dissertation). Chalmers University of Technology Available online: https://publications.lib.chalmers.se/records/fulltext/251352/251352.pdf

Larsson, F., & Mellander, B. (2017). Lithium-ion Batteries used in Electrified Vehicles – General Risk Assessment and Construction Guidelines from a Fire and Gas Release Perspective.

Lecocq, A.; Eshetu, G.G.; Grugeon, S.; Martin, N.; Laruelle, S.; Marlair, G. (2016) Scenario-based prediction of Li-ion batteries fire-induced toxicity. J. Power Sources 2016, 316, 197–206 https://doi.org/10.1016/j.jpowsour.2016.02.090

Liu, X.; Wu, Z.; Stoliarov, S.I.; Denlinger, M.; Masias, A.; Snyder, K. Heat release during thermally-induced failure of a lithium ion battery: Impact of cathode composition. Fire Saf. J. 2016, 85, 10–22. https://doi.org/10.1016/j.firesaf.2016.08.001

Liu, Y., Zhang, Y., Yu, H., Nie, Z., Liu, Y., & Chen, Z. (2022). A novel data-driven controller for plug-in hybrid electric vehicles with improved adaptabilities to driving environment. Journal of Cleaner Production, 334, 130250. https://doi.org/10.1016/j.jclepro.2021.130250

Liu, Y.; Sun, P.; Niu, H.; Huang, X.; Rein, G. (2021) Propensity to self-heating ignition of open-circuit pouch Lithium-ion battery pile on a hot boundary. Fire Saf. J. , 120, 103081. https://doi.org/10.1016/j.firesaf.2020.103081

Mechanical stress and physical damage as causes for battery fire (4 October 2023), Sustainable Bus Magazine Retrieved from: https://www.sustainable-bus.com/news/electric-bus-battery-fire-reasons-solutions/ (accessed on 20 October 2024).

Mellert, L. D., Welte, U., Tuchschmid, M., Held, M., Hermann, M., Kompatscher, M., ... & Nachef, L. (2020). Risk minimisation of electric vehicle fires in underground traffic infrastructures. Schweizer Verband der Strassen-und Verkehrsfachleute (VSS), 1678(1), 1-102. Available online: https://amstein-walthert.ch/media/files/2021/01/AGT_2018_006_EMob_RiskMin_Undergr_Infrastr_Final_Report_V1.0.pdf (accessed on 20 October 2024).

Gastelu, G. (2018, June 26). NTSB: Tesla was going 116 mph at time of fatal Florida accident; battery pack reignited twice afterwards. Fox News. Available online: https://www.foxnews.com/auto/ntsb-tesla-was-going-116-mph-at-time-of-fatal-florida-accident-battery-pack-reignited-twice-afterwards (accessed on 25 December 2024).

Ouyang, D., Chen, M., Huang, Q., Weng, J., Wang, Z., & Wang, J. (2019). A review on the thermal hazards of the lithium-ion battery and the corresponding countermeasures. Applied Sciences, 9(12), 2483.

Park, O. B. (2013). Best practices for emergency response to incidents involving electric vehicles battery hazards: A report on full-scale testing results. The Fire Protection Research Foundation, Quincy, MA, Report, (1205174.000), F0F0. Available online: http://tkolb.net/FireReports/2014/EV%20BatteriesPart1.pdf

PD 7974-6:2004; Application of Fire Safety Engineering Principles to the Design of Buildings. Part 6: Human Factors: Life Safety Strategies—Occupant Evacuation, Behaviour and Condition (Sub-System 6). British Standards Institution: London, UK, 2019.

BBC News. (2022, May 22). Potters Bar: Buses catch fire at town centre transport depot. BBC News Retrieved from: https://www.bbc.com/news/uk-england-beds-bucks-herts-61543634 (accessed on 30 December 2024).

Rosenbauer America. (n.d.). Rosenbauer introduces the battery extinguishing system technology (BEST). Rosenbauer America. https://rosenbaueramerica.com/rosenbauer-battery-extinguishing-system-technology/

SAE International. (2024). Surface vehicle recommended practice J2990: Hybrid and EV first and second responder recommended practice. Society of Automotive Engineers. https://www.sae.org/standards/content/j2990_201907/

Schiemann, M., Bergthorson, J., Fischer, P., Scherer, V., Taroata, D., & Schmid, G. (2016). A review on lithium combustion. Applied energy, 162, 948-965.

Sun, P., Bisschop, R., Niu, H., & Huang, X. (2020). A review of battery fires in electric vehicles. Fire technology, 56(4), 1361-1410. https://doi.org/10.1007/s10694-020-00958-2

T.C. Çevre ve Şehircilik Bakanlığı. Otopark Yönetmeliği. Available online: https://www.mevzuat.gov.tr/mevzuat?MevzuatNo=24408&MevzuatTur=7&MevzuatTertip=5 (accessed on 20 November 2024).

Cold Cut Systems AB. (t.y.). A proven solution for EV fires. Cold Cut Systems AB. Available online https://www.coldcutsystems.com/news/a-proven-solution-for-ev-fires/ (accessed on 20 November 2024).

Bunkley, N. (2013, October 2). Highway fire of Tesla Model S included its lithium battery. The New York Times. https://archive.nytimes.com/wheels.blogs.nytimes.com/2013/10/02/highway-fire-of-tesla-model-s-included-its-lithium-battery/(accessed on 21 May 2024).

The Home Office, Road Vehicle Fires Dataset, UK, August 2019. Available online: https://www.gov.uk/government/statistics/fire-statistics-incident-level-datasets (accessed on 20 March 2024).

Tobishima, S. I., & Yamaki, J. I. (1999). A consideration of lithium cell safety. Journal of Power Sources, 81, 882-886. https://doi.org/10.1016/S0378-7753(98)00240-7

U.S. Department of Transportation. (2014). Interim guidance for electric and hybrid electric vehicles equipped with high-voltage batteries. U.S. Department of Transportation. Available online: https://www.nhtsa.gov/sites/nhtsa.gov/files/interimguide_electrichybridvehicles_012012_v3.pdf

U.S. National Highway Traffic Safety Administration. (2012). Interim guidance for electric and hybrid-electric vehicles equipped with high voltage batteries (Law Enforcement/Emergency Medical Services/Fire Department). Available online: U.S. Department of Transportation. https://www.nhtsa.gov/document/interim-guidance-electric-and-hybrid-electric-vehicles-equipped-high-voltage-batteries-law

Välisalo, T. (2019). *Firefighting in case of Li-Ion battery fire in underground conditions: Literature study*. VTT Technical Research Centre of Finland. VTT Research Report No. VTT-R-00066-19

Verband der Automobilindustrie (VDA). (2017). Accident assistance and recovery of vehicles with high-voltage systems (pp. 1–30). Verband der Automobilindustrie e.V. Available online: https://www.vda.de/dam/jcr:09ed3246-75c6-4ab6-9b70-c6495c703312/Accident_Assistance_Recovery_FAQ_en_082020.pdf

Brandt, A. W., & Glansberg, K. (2020). Charging of electric cars in parking garages. RISE Report, (2020: 30). https://trid.trb.org/View/1875962

Wang, F., Zhang, S., Zhao, Y., Ma, Y., Zhang, Y., Hove, A., & Wu, Y. (2023). Multisectoral drivers of decarbonizing battery electric vehicles in China. PNAS nexus, 2(5), pgad123. https://doi.org/10.1093/pnasnexus/pgad123

Wang, H., Meng, Q., & Xiao, L. (2024). Electric-vehicle charging facility deployment models for dense-city residential carparks considering demand uncertainty and grid dynamics. Transportation Research Part C: Emerging Technologies, 168, 104579. https://doi.org/10.1016/j.trc.2024.104579

Wang, Q., Ping, P., Zhao, X., Chu, G., Sun, J., & Chen, C. (2012). Thermal runaway caused fire and explosion of lithium ion battery. Journal of power sources, 208, 210-224. https://doi.org/10.1016/j.jpowsour.2012.02.038

BBC News. (2023, July 9). Wimbledon: Electric buses withdrawn in south London after fire. BBC News. Available online https://www.bbc.com/news/uk-england-london-67967421

Why do e-buses catch fire? (12 Jan 2024) EVfiresafe. Retrieved from: https://www.evfiresafe.com/post/why-do-e-buses-catch-fire

Zhang, B., Bewley, R. L., Tanim, T. R., & Walker, L. K. (2022). Electric vehicle post-crash Recovery—Stranded energy issues and mitigation strategy. Journal of Power Sources, 552, 232239. https://doi.org/10.1016/j.jpowsour.2022.232239

Journal Homepage: https://dergipark.org.tr/tr/pub/isibted

Isı Bilimi ve Tekniği Dergisi

Archive: https://tibtd.org.tr/dergi

Investigation Of Increasing Process Gas Cooling Performance By Improving Ammonia Oxidation Reactor Heat Exchangers

Fadime Menekşe İKBAL [1], Oğuzhan ERBAŞ [1,*]

[1] *Kütahya Dumlupınar Üniversitesi, Mühendislik Fakültesi, Makine Mühendisliği Bölümü, 43100, Kütahya, Türkiye*

A R T I C L E I N F O

2025, vol. 45, no.1, pp. 97-110

doi: 10.47480/isibted.1566904

Research Article
Received: 14 October 2024
Accepted: 16 December 2024

* *Corresponding Author*
e-mail: oguzhan.erbas@dpu.edu.tr

Keywords:
Process Gas Cooling
Oxidation Reactor
Heat Exchanger
CFD Analysis

ORCID Numbers in author order:
0000-0002-5665-7306
0000-0001-9424-4273

A B S T R A C T

This study aims to increase the cooling performance of NO_x gas by improving the heat exchangers of an industrial-type ammonia oxidation reactor with a diameter of 3.8 m and a height of 6.5 m in a nitric acid production plant with a capacity of 610 tons/day. The reactor produces 100% HNO_3, 56% diluted nitric acid, and 33 tons/hour of superheated steam. To this end, the parametric analysis study, in which the horizontal and vertical distance between the exchanger tubes, the pipe diameters, and the distance between the exchanger packages (pre-evaporator, superheater, evaporator, economizer) were used separately, was carried out with the help of Ansys Fluent program and the flow properties and performance values were examined. The best cooling performance (for the inner part of the ammonia oxidation reactor) resulted from different parametric studies; there was a study in which the process gas temperature was obtained at 270.51^{0}C with a 56 mm horizontal distance between the heat exchanger tubes (a). Thus, a 9.1% decrease in the actual gas outlet temperature of the operating reactor was achieved. In other parametric studies, the lowest process gas temperatures are; it was found to be 323.20^{0}C for the distance between heat exchanger packages (L), 318.42 ^{0}C for the vertical distance between heat exchanger tubes (b), and 296.67 ^{0}C for the heat exchanger tube diameter (D). In addition, when the CFD simulation results, which provide the best cooling performance, are compared with actual operating data (SCADA online data), In the ammonia oxidation reactor, the fluid outlet temperature increased by 8.2% in the economizer, 9.7% in the evaporator and 4.3% in the superheater.

Amonyak Oksidasyon Reaktörü Isı Değiştiricilerinin İyileştirilerek Proses Gaz Soğutma Performansının Artırılmasının Araştırılması

M A K A L E B İ L G İ S İ

Anahtar Kelimeler:
Proses Gaz Soğutma
Oksidasyon Reaktörü
Isı Değiştirici
CFD Analizi

Ö Z E T

Bu çalışmada, 610 ton/gün kapasiteli bir nitrik asit üretim tesisindeki 3,8 m çapında ve 6,5 m yüksekliğindeki endüstriyel tip amonyak oksidasyon reaktörünün ısı değiştiricilerini iyileştirerek, NO_x gazının soğutma performansının artırılması amaçlanmıştır. Reaktör, % 100 HNO_3, %56 seyreltilmiş nitrik asit ve 33 ton/saat aşırı ısıtılmış buhar üretmektedir. Bu amaçla, eşanjör boruları arasındaki yatay ve düşey mesafe, boru çapları ve eşanjör paketleri (ön buharlaştırıcı, aşırı ısıtıcı, buharlaştırıcı, ekonomizer) arasındaki mesafenin ayrı ayrı kullanıldığı parametrik analiz çalışması, Ansys Fluent programı yardımıyla yapılmış ve akış özellikleri ile performans değerleri incelenmiştir. En iyi soğutma performansı farklı parametrik çalışmalar sonucunda; ısı değiştirici boruları arasında yatay olarak 56 mm mesafede proses gazı sıcaklığının 270,5 ^{0}C elde edildiği çalışma ile sağlanmıştır. Böylece, reaktörün gaz çıkış sıcaklığında % 9,1'lik bir azalma sağlanmıştır. Diğer parametrik çalışmalarda ise en düşük proses gazı sıcaklıkları; ısı değiştirici paketleri arasındaki mesafe (L) için 323,2 ^{0}C, ısı değiştirici boruları arasındaki dikey mesafe (b) için 318,4 ^{0}C ve ısı değiştirici boru çapı (D) için 296,6 ^{0}C olarak bulunmuştur. Ayrıca, en iyi soğutma performansını sağlayan CFD simülasyon sonuçları, gerçek işletme verileriyle (SCADA verileri ile) karşılaştırıldığında; amonyak oksidasyon reaktöründe soğutucu akışkan çıkış sıcaklığı ekonomizerde %8,2, buharlaştırıcıda %9,7 ve süperheater'da %4,3 artmıştır.

NOMENCLATURE

SCADA	Supervisory control and data acquisition
CFD	Computational fluid dynamics
Pt-Rh	Platinum radium
LMN	La Mont nozzles
ρ	Gas phase density (kg/m^3)
C_p	Gas phase heat capacity (J/mol.k)
K_h	Heat transfer coefficient (W/m^2.K)
AOR	Ammonia oxidation reactor
PGC	Process gas cooler
HEP	Heat Exchanger Packages
D	Heat exchanger tube diameter
L	Distance between heat exchanger packages
b_t	Vertical distance between heat exchanger tubes
TNT	Trinitrotoluene

INTRODUCTION

Energy efficiency has an essential place in the policies of most developed countries. The importance of energy efficiency as a policy goal depends on its benefits for trade, industrial competitiveness, and energy security. "Nitric acid production," one of the essential inorganic acids, also includes a series of energy conversion processes. It neutralizes nitric acid with ammonia, making ammonium nitrate the most critical component of worldwide mineral fertilizers. It provides plants and ornamental plants with the nitrogen they need to grow in high, easily digestible doses (Heck et al., 1982; Juangsa et al., 2019). Additionally, HNO_3 can be used for soil acidification in horticulture. In the chemical industry, nitric acid is primarily a precursor to organic nitrogen compounds such as nitrobenzenes. Combined with aromatic compounds, it gives substances used to make explosives, such as TNT and nitroglycerin. Another critical application is rocket fuel. For this purpose, a mixture of HNO_3, dinitrogen tetroxide, and hydrogen peroxide, also known as red-fuming nitric acid, is prepared (Hernández et al., 2021). Its use in the space industry depends on efficiently storing raw materials. The potential of nitric acid for plastic production is also notable. The oxidation it initiates produces adipic acid, also used to make synthetic fibers such as nylon (Neumann et al., 2024; Sadykov et al., 2020). In the production of nitric acid, first ammonia is oxidized to obtain nitric oxide (nitrogen monoxide, NO); then NO is further oxidized to NO_2 (nitrogen dioxide). In the last stage, NO_2 gas is absorbed with water to obtain Nitric Acid (HNO_3). This process is called the "Ostwald Process". The ammonia oxidation reactor is the most crucial step in this process flow diagram. The filtered air is heated after being pressurized. After evaporation with heated air, the filtered NH_3 is mixed and fed to the reactor containing a platinum/rhodium alloy catalyst. A reversible and exothermic reaction occurs between NH_3 and oxygen in the reactor, releasing nitrogen oxides (NO_x) (Dong et al., 2023; Chatterjee et al., 2008). This heat released from the oxidation reaction can be recovered using heat exchangers, and the system's energy efficiency can be increased. Heat is usually used in other processes to save energy. In addition, the temperature of the NO_x gases affects the reaction's progress and the catalyst's efficiency. If the reactor temperature is too high, unwanted side reactions and by-products can occur. In addition, very high temperatures can lead to catalyst deterioration or inefficient operation. Therefore, controlled cooling of the temperature of the NO_x gases is essential for the efficiency of the reaction. NO_x gases can become more stable at very high temperatures, making subsequent purification and reaction stages difficult. Cooling helps to keep the NO_x in a more stable and processable form. In addition, in some cases, NO_x gases, after cooling, can be more easily processed or separated by other reactions. As a result, controlled cooling of the temperature of the NO_x gases is a critical step in reaction efficiency, energy management, and chemical processing (Abbasfard et al., 2014; Mewada et al., 2015).

When temperatures are low or the catalyst is not working, the chemical reaction can slow down or partially slow down (Salam et al., 2016). The entrance region of the reactor is a critical point where the chemical reaction begins. Optimizing this region's temperature, pressure, and flow rate is necessary to initiate and continue the reaction (Amirsadat et al., 2024). Burner head geometry and design directly affect the mixing and distribution of gases. If a homogeneous gas distribution is not achieved, temperature and reactant distribution irregularities may occur on the catalyst, reducing efficiency (Nascimento et al., 2024; Holma et al., 1979). When literature studies on ammonia oxidation reactors examine production and process efficiency, they generally focus on the reactor inlet region and burner head geometry design, flow pattern and catalyst structure, and gauze platinum losses. Moszowski et al. (2019) analyzed the gas velocity distribution in an ammonia oxidation reactor. Three different design arrangements of the burner head (reactor header - inlet section) were examined to verify the effects of the liquid flow rate entering the catalysts. This paper analyzes how different burner head designs, such as screens made of perforated plates, cone diffusers, and guide vanes, affect the uniformity of the gas flow through the catalyst gauze in a nitric acid plant reactor. It was found that the accurately selected perforated plate and the conical diffuser solved the problem of ensuring the proper flow of gas on ammonia oxidation catalysts and catalysts for nitrous oxide decomposition (Kraehnert et al., 2008). Using CFD analysis, Abbasfard et al. (2012) simulated the flow inside the industrial ammonia oxidation reactor. The simulation results clearly showed the poor flow distribution inside the reactor. The direct effect of such a failure can be seen in the uneven (non-homogeneous) temperature distribution around the reactor shell. Thermography experiments were also conducted to support this claim and revealed the fact that the left side of the reactor experienced higher temperatures. The contour plots also showed some stagnant and swirling regions before or after the distribution of the reactor due to the poor flow distribution. Wiser examined a modeling approach in which a mechanistic model of ammonia oxidation on platinum (catalyst site), previously published by Kraehnert and Baerns, was implemented in a CFD simulation using a rate-matching approach. The effect of geometry on the process performance of the catalytic gauze was improved by using the knowledge gained through CFD simulations in which detailed kinetics were included(Wiser et al., 2020). Chatterjee et al. (2008) attempted to understand the rate-controlling step for the ammonia oxidation process, mass transfer and chemical reaction rates for nitrogen oxide absorption, and the combined effects of various equilibria in optimizing heat recovery from a product stream in the ammonia oxidation reactor. Also, the impact of geometrical parameters, excess air, degree of absorption, product acid concentration, temperature, and pressure for the absorption column were analyzed to optimize the nitric acid plant. They found that the optimum operating pressure increases as the restriction on the NO_x outlet

concentration increases. Grande et al. (2018) aimed to convert the homogeneous noncatalytic nitric oxide oxidation into a faster catalytic step. With this conversion, the energy recovery of nitric acid production is expected to increase by up to 10%. For this purpose, a platinum-catalyzed process on alumina was investigated. They found that since the reaction also proceeds in the gas phase, it is essential to limit the contact time of NO and O_2 before the catalyst and, for the same reason, the outlet flow length between the reactor and the analyzer should be reduced as much as possible (to limit the interaction of unconverted NO and O_2) (Grande et al., 2018). Elsayed et al. (2023) present a model for an industrial catalytic ammonia oxidation reactor using a Pt/Rh catalyst gauze for nitric oxide production in a nitric acid plant. They utilized two fundamental models to perform mass and energy balance analyses integrated with MATLAB 2017. The first model focused on mass balance, predicting the variations in concentrations of nitrogen (N), nitric oxide (NO), and oxygen (O) along the catalyst bed of the reactor, which has a diameter of 4.8 meters and a height of 1 meter. The second model addressed energy balance, predicting temperature variations within the same catalyst bed. In the mass balance model, the deviation for nitric oxide concentration did not exceed 6.2%. For the energy balance model, the deviation was only 0.4%. These mathematical models accurately predicted operational values with minimal deviation(Elsayed et al., 2023; Kayapinar et al., 2024). Scheuer et al. (2011) modeled a high-efficiency single-channel monolith reactor for ammonia oxidation. A mechanistic model was used to oxidize ammonia on platinum, and all internal and external mass transfer effects were included. Model efficiencies were derived from using previously calculated solutions of the mass balance equations (Scheuer et al., 2011; Ardy et al., 2021).

In high-capacity chemical processes such as nitric acid production, the gas flow dynamics, temperature profiles, and heat transfer mechanisms of these reactors directly affect the overall performance and sustainability of the system. The main objective of this study is to investigate the thermal performance of an ammonia oxidation reactor used in a nitric acid production facility with a capacity of 610 tons/day. The study aims to optimize the heat transfer between the reactor and the cooling exchangers. In particular, the effects of geometric parameters such as horizontal and vertical distance between the pipes on the temperature profile of the process gas are analyzed. The reactors in the nitric acid production facility consist of two parts: the catalyst, where catalytic combustion occurs, and the waste heat boiler (where the heat exchanger packages are located), where heat transfer occurs. It is seen that the studies in the literature mainly focus on the inlet part of the ammonia oxidation reactor (air + NH_3) gas mixing reaction (gas flow properties) and the geometry of this region. This study focuses on determining energy-intensive processes in the nitric acid production plant, significantly improving the NOx gas cooling performance by enhancing the ammonia oxidation reactor heat exchangers. A parametric analysis was performed to achieve this goal, and flow characteristics and performance values were examined using the Ansys Fluent program. Especially in such critical processes, heat exchangers are essential in increasing energy efficiency and optimizing system performance. Therefore, it was decided to examine the following factors.

- Fluid Inlet-Outlet Points and Temperature Distribution: The temperature distribution at the inlet and outlet points directly affects the heat transfer efficiency. Optimizing the temperature differences increases the efficiency of heat exchangers.
- Distance Between Tubes: The horizontal and vertical distance between the tubes affects the interaction of the fluids with each other and heat transfer. Optimizing this distance can increase the cooling performance of the gas and thus increase the system's overall efficiency.
- Tube Diameter: The tube diameter affects the flow rate and heat transfer surface. Choosing the correct diameter allows the fluid to be cooled more effectively and minimizes energy losses. Examining these elements regarding system efficiency is necessary to reduce energy consumption, lower operating costs, and minimize environmental impacts. In addition, simulation techniques such as CFD (Computational Fluid Dynamics) allow detailed analysis of these parameters to obtain more effective designs. In line with these hypotheses, the effects of critical parameters of the reactor system design on thermal performance were simulated by the computational fluid dynamics (CFD) method in the study, and the results were compared with actual operating data (SCADA). The study aims to develop design recommendations that can optimize the system performance and evaluate these findings regarding economic and environmental sustainability.

STRUCTURE AND PROPERTIES OF THE ANALYZED AMMONIA OXIDATION REACTOR

The oxidation reactor and heat exchanger pipes within the nitric acid production facility, which were analyzed to increase efficiency, are shown (Figure 1).

Figure 1. Analyzed Industrial Ammonia Oxidation Reactor and Heat Exchanger Pipes (Process Gas Coolers Oper. and Maint. Man., 2024)

This reactor is a cylindrical body with a diameter of 3.8 m and a length of 6.5 m. It contains a catalyst layer made of platinum-rhodium. Ammonia is gasified with water in the ammonia gasifier and comes to the combustion unit. The air required for the combustion of ammonia is cleaned in the oil filter and sucked from the atmosphere through the turbo compressor and comes to the combustion unit reactor. Then, ammonia and air at the same temperature are mixed in the mixer section. A chemical reaction in the platinum-radium catalyst burns this mixture of ammonia and air. Filter tubes made of porous ceramic material are placed at the bottom. The gas mixture is cleaned by passing through porous tubes. Then, by passing through the catalyst layer, ammonia turns into NO. An exothermic reaction occurs between ammonia and oxygen in the gas phase. The NO_x gases released from this catalyst come to the waste heat boiler and leave the reactor, leaving their heat in the coils. Regarding the system's overall

efficiency, it aims to cool NO_x gases as much as possible in this part of the process (Hannevold et al., 2005; Hung et al., 2008). This ammonia oxidation reactor consists of two main parts. The first is the combustion unit part (chemical reaction), and the second is the waste heat boiler part, which produces steam. Combustion unit: The roof part, where the catalyst is located, is where the chemical reaction occurs. The ammonia-air mixture is burned to form nitrogen monoxide and water vapor. This part is also called the incinerator. This is the first part of the facility. Reactors that contain a gauze catalyst are used in the production of HCN from CH_4, NH_3, and O_2 (known as the Russow process), as well as in the creation of nitrogen oxides during the production of nitric acid (known as the Ostwald process). The Ostwald process occurs here at the catalyst (Fajardo et al., 2018; Elsayed et al., 2023). Chemical reaction on catalysts occurs at high temperatures (860 ~ 900°C). Approximately 11 % ammonia reacts with 89 % air in the chemical reaction. Figure 2. shows the main steps of the Ostwald process.

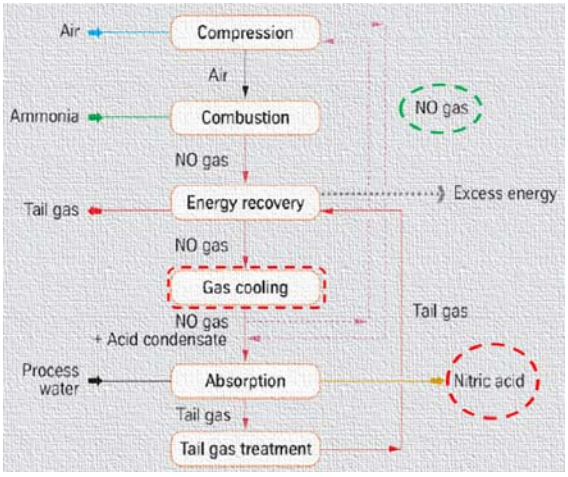

Figure 2. Block diagram of the Ostwald process (Grande et al., 2018)

The only catalyst used industrially in the process is the platinum-radium catalyst, which contains 5 % to 10 % radium and is called platinum. This catalyst, that is, platinum radium (Pt-Rh) catalyst, contains 95 % platinum and 5 % radium. It is in the form of a fine mesh. The reaction occurs in a very short time. Conversion efficiency varies between 90-96% depending on reaction conditions. Oxygen atoms are absorbed on the platinum surface. The reaction takes place between oxygen atoms and ammonia molecules on the surface. Then, the ammonia molecule turns into NO. The system uses two 320 m^3/h capacity circulation pumps. The pumps have an inlet pressure of 44 bar and an outlet pressure of 47.9 bar. The cooling water circulating in the system is also a suitable, non-aggressive fluid that is not prone to deposit formation and does not contain suspended particles. The acceptable hardness value for this fluid in the system is 1.4 mmol/l, and the pH value is approximately between 7.5 and 9. Thanks to the nozzles inside the reactor, water is directed equally to the evaporator and cooling tubes, contributing to increased cooling performance. This prevents thermal stresses and equipment damage that may arise from temperature differences. The location and types of nozzles and their diameter characteristics are given in Table 1. The holes of different diameters used in La Mont nozzles (LMN) are optimized according to these different thermal loads. Larger holes provide higher water flow, while smaller holes provide lower flow. This ensures that each system section is cooled according to its requirements.

Table 1. Locations, Types, and Features of La Mont Nozzles (LMN) in Cooling Zones

Locations	Tube [mm]	pcs.	Ø [mm]	Locations	Tube [mm]	pcs.	Ø [mm]
Pre-evap. Layer 1, 2	42.4 x 4	13	9	Evap. Layer 4, 6	42.4 x 4	6	8
Pre-evap. Layer 3	42.4 x 4	3 1	9,5 10	Evap. Layer 7,8	42.4 x 4	4	7.5
Evap. Layer 1, 2	2.4 x 4	6	8	Evap. Layer 9,10	42.4 x 4	3 1	7 10
Evap. Layer 3	42.4 x 4	2	8,5	Evap. Layer11,12	42.4 x 4	2	8

Kinetic Mechanism of Ammonia Oxidation

Figure 3. shows the oxidation reaction mechanism with Pt-Rh catalyzed raschig rings (Il'chenko et al., 1975).

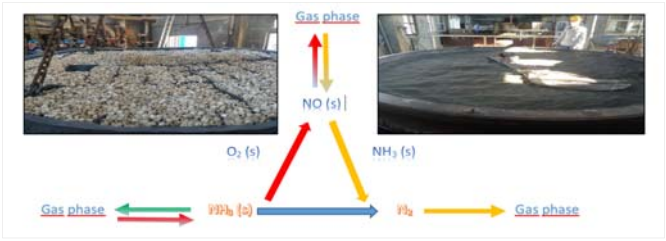

Figure 3. Mechanism of Oxidation Reaction with Pt-Rh Catalyzed Raschig Rings.

The kinetic mechanism of ammonia oxidation provides fundamental information for reactor design and chemical engineering in general. For these reasons, the kinetic mechanism of ammonia oxidation is essential for research and applications (Fila et al., 1994; Il'chenko et al., 1975). The reaction rate is controlled by the transfer of ammonia from the bulk gas to the platinum surface, depending on contact time and reaction mixture composition. Previous theories regarding ammonia oxidation on platinum presumed that transient compounds are formed. However, experiments indicate that the reactions of components on the catalyst surface involve no transient compounds. Pignet and Schmidt conducted a study on the selectivity of the oxidation of NH on Pt and the kinetics of oxidation on Pt-Rh and Pd. They conducted experiments in a low-pressure reactor connected to a mass spectrometer and suggested a simple series-parallel mechanism based on the concept by Fogel and Coworkers. Zhan et al. (2024) developed a kinetic model applicable to ammonia oxidation under high-pressure conditions. They validated it against the performance of other recently published kinetic models concerning various parameters related to ammonia oxidation and NO_x emission under high-pressure situations. The developed model was also validated with published experimental data collected under high-pressure conditions (Zhan et al., 2024; Chernyshev et al., 2001). The kinetic parameters in equations (1,2,3) and (4,5,6) were obtained from experimental data measured at low pressures, not exceeding 15 Pa. While the kinetic equations can be applied to calculate reactors operating at atmospheric or elevated pressures, it is essential to note that outer diffusion has a strong effect on the total reaction rates, leading to a substantial decrease in the concentrations of reactants on the catalyst surface. In industrial applications of the Pt-Rh catalyst under conventional conditions, the ratio of ammonia partial pressure in the gas phase to that at the catalyst surface is approximately 10-4 (Il'chenko et al., 1975). The following relations give the formation rates for NO and N_2 (Fila et al., 1994).

$$F_{NO} = \frac{2.209.10^{-11} exp\left(\frac{90\,791.6}{RT_S}\right) P_{NH_3} Po_2^{1/2}}{(£_{NOa} + £_{NOb})} \quad (1)$$

$$£_{NOa} = \left(1 + 6.928.10^{-3} \exp\left(\frac{1\,840.93}{RT_S}\right) Po_2^{\frac{1}{2}}\right) \quad (2)$$

$$£_{NOb} = \left(\left(1 + 1.2.10^{-5} exp\left(\frac{106.690.5}{RT_S}\right) Po_2^{1/2}\right) P_{NH_3}\right) \quad (3)$$

$$F_{N_2} = £_{N_{2a}} + £_{N_{2b}} \quad (4)$$

$$£_{N_{2a}} \frac{2.36.10^{-15} exp\left(\frac{108\,782.5}{RT_S}\right) P_{NH_3} P_{NO}}{\left(1+4.05.10^{-4} exp\left(\frac{45\,605}{RT_S}\right) PO_2 + 3.38.10^{-8} exp\left(\frac{87\,444}{RT_S}\right) P_{NH_3}\right)^2} \quad (5)$$

$$£_{N_{2b}} \frac{1.65.10^{-8} exp\left(\frac{-2.385}{RT_S}\right) P_{NH_3}}{\left(1+4.05.10^{-4} exp\left(\frac{45\,605}{RT_S}\right) PO_2 + 3.38.10^{-8} exp\left(\frac{87\,444}{RT_S}\right) P_{NH_3}\right)} \quad (6)$$

In industrial converters, total pressure hurts the NO yield due to the reaction between NH and NO in the gas phase. Wisc and Frech have examined the kinetics of this reaction. They derived an equation based on experiments where they monitored the total gas pressure in the apparatus over time due to reaction (Equations 7 and 8).

$$\frac{dP}{d_t} = k\, P_{NH_3} Po_{NO}^{-1/2} \quad (7)$$

k= 9.527 .109 exp (-229 018 / RT) (Pa ½ s-1) (8)

Equations (7-8) are mathematical equations representing the kinetics of NH oxidation on Pt gauzes in the temperature range from 600 to 1200 K. Consequently; these equations are used in industrial reactor modeling for the oxidation of NH_3 (Il'chenko et al., 1975).

Energy Balance Equation for an Industrial Ammonia Oxidation Reactor

In oxide studies, catalysts' activity is typically estimated by measuring their performance about the selectivity towards NO under industrial conditions. The lower the reaction ignition temperature, the higher the maximum NO selectivity and the lower the adequate activation energy and reaction order. This means that external diffusion limitations are more severe. Therefore, the selectivity towards NO is an essential measure of catalyst activity. This approach has been widely used in evaluating catalysts in practice (Kirova-Yordanova et al., 2011; Srinivasan et al., 1997). The catalytic ammonia oxidation process was simulated using a typical monolithic reactor model (Fila et al., 1994; Belghaieb et al., 2010), represented by the equation:

$$\rho C_P \frac{dT}{dt} = -v\, \rho C_P \frac{dT}{dz} - K_h(z) \frac{\alpha}{\varepsilon} (T - T^*) \quad (9)$$

The following variables are used in the equation: gas phase density (ρ) in kg/m^3 and gas phase heat capacity (C_p) in J/mol.k, gas phase temperature (T) in K, time (t) in s, linear velocity (v) in m/s, axial coordinate (z) in m, heat transfer coefficient (K_h) in W/m^2.K, specific surface area (a) in m^{-1}, void fraction (ε), and solid phase temperature (T^*) in K. The equation assumes one-dimensional steady-state conditions, constant solid phase temperature, and heat transfer coefficient (K_h). Therefore, the equation becomes as follows:

$$\frac{dT}{dt} = \frac{-K_h \alpha}{\varepsilon v \rho C_p} (T - T^*) \quad (10)$$

The value of ρ is calculated (Eq. 11) as the average density of the gas mixture at the inlet and outlet conditions of the catalyst bed.

$$\rho = \frac{PM_{mix}}{RT} \quad (11)$$

It is assumed that the C_p value is the average value between the C_p values of the gas mixture at the inlet and outlet conditions of the catalyst. This is based on previous research. The value of the heat transfer coefficient, K_h, is taken from the literature (Fila et al., 1994).

STUDY TO IMPROVE THE PROCESS GAS COOLING PERFORMANCE OF OXIDATION REACTOR HEAT EXCHANGERS

In the nitric acid production facility, the central heart of the process is the oxidation reactor. The main parameters affecting the system efficiency in the oxidation reactor are the NH_3 burning rate, platinum bottom temperature, and NO gas exit temperature. Reactor malfunction, maintenance, etc., and cut-out and stop times also affect system efficiency (Figure 4).

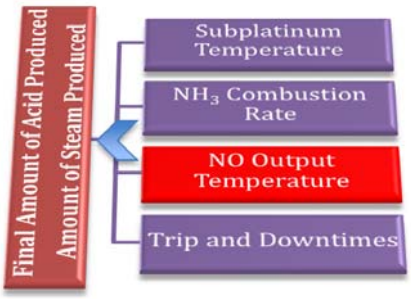

Figure 4. Main parameters affecting process efficiency

The effect of these parameters determines the final amounts of acid produced by the steam produced in the facility. The best option to increase system efficiency by improving these parameters is to reduce the NO gas outlet temperature as much as possible (Pfefferle et al., 1987; Moszowski et al., 2019). In the ammonia oxidation reactor, a mixture of approximately 11% ammonia + 89 % air is burned at approximately 870 °C on platinum-rhodium-palladium catalysts under 2.5–3.5 atu (kg/cm^2) pressure to obtain nitrogen oxide gas (NO). This gas obtained is the superheater, evaporator, pre-evaporator, and economizer, which also provide steam by transferring their heat to the circulating water. The more heat (cooling efficiency) extracted from NO gases in this process region increases, the more system efficiency will increase(Kraehnert et al., 2008; Schumacher et al., 2019). Exothermic reactions occurring within the reactor require thermal management. Heat exchangers help maintain process gases at appropriate temperatures (Bagheri et al., 2024; Juangsa et al., 2019). Controlling the temperature of process gases increases the efficiency of the reactor and prevents overheating of the reactor materials (Song et al., 2016; García-Ruiz et al., 2023). The reactor temperature must be constantly monitored and controlled. Automatic control systems ensure the temperature is kept within the desired range (Stagni et al., 2020). For this reason, the functions of gas cooling in the ammonia oxidation reactor are as follows: a design modeling study was carried out with CFD analysis for the pre-evaporator, superheater, evaporator, and economizer region. The numerical model used in the study is an exact scale model of the coils in the ammonia oxidation reactor.

The numerical model was drawn using the Solidworks program. The drawn model was transferred to the Ansys Workbench Space Claim program. It is known that an important parameter affecting the accuracy of the numerical solution is mesh independence (Colak, A. B. et al., 2024; Enger et al., 2018). For this reason, before moving on to numerical analysis, the drawn model was divided into different numbers of finite volumes for mesh independence studies. Figure 5. shows the created CAD/CAM model of the reactor. Mesh structures created with the Ansys Workbench Mesh program were also transferred to the Ansys Fluent program. Additionally, a mesh structure that does not affect the outcome of the solution for steady-state was determined.

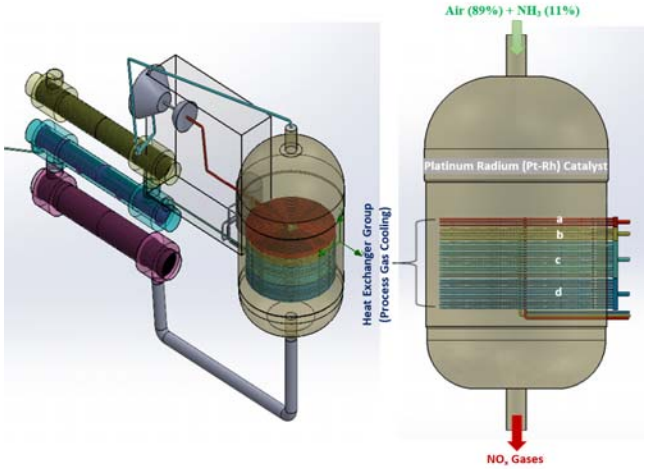

a: Pre-Evaporator b: Superheater c: Evaporator d: Economizer
Figure 5. Ammonia Oxidation Reactor (AOR) CAD/CAM Model

The mesh was created with the help of the Ansys Watertight geometry mesh program, as shown in Figure 6. Polyhedral elements were used in the border regions, and hex elements were used in the other areas. This study determined the most suitable mesh structure, turbulence model, and wall function for the problem studied. The number of meshes is closely related to the computer's RAM being studied. The maximum number of grids and elements was created according to the RAM capacity of the workstation where the calculations will be made.

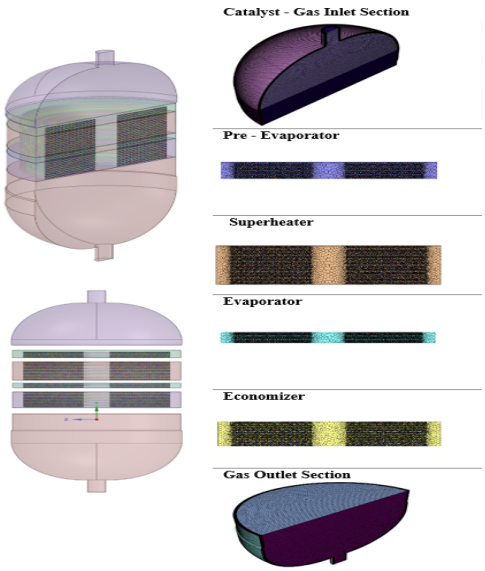

Figure 6. Model Mesh Structure of Ammonia Oxidation Reactor (AOR) Sections

The study used an Ansys Watertight Geometry mesh module to generate a mesh in the reactor inlet and catalyst section. Infiltration was defined on the system walls, and the total number of elements was determined to be 1755000. In the mesh thrown into section 1. (catalyst - gas inlet section), orthogonal quality was 0.20. Since the value obtained in orthogonal quality is desired to be close to 1, a result between 0.15-0.20 is acceptable. The skewness value was found to be 0.799. Since this value is chosen to be close to 0, a value between 0.5-0.8 is a good result. The total number of elements for the 2nd section (pre - evaporator) is 4355000, the total number of elements for the 3rd section (superheater) is 7872000, the total number of elements for the 4th section (evaporator) is 4355000, the total number of elements for the 5th section (economizer region) is 6600000, and the total number of elements for the 6th section outlet region is 2120000. The mesh independence graph obtained against the number of elements and created based on temperature and pressure values is also shown in Figure 7.

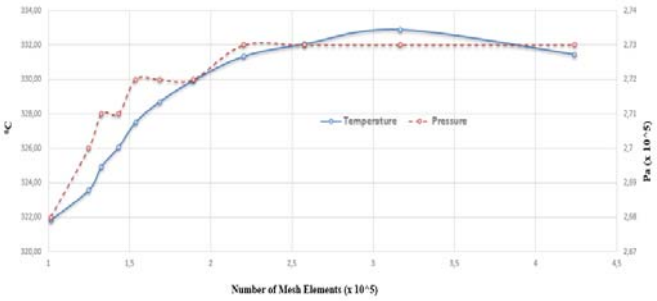

Figure 7. Grid Independence

The solver type in ANSYS Fluent is determined to be pressure-based and in a steady state (Kishan et al., 2020). Realizable SST k-omega is selected as the turbulent flow model. In addition, the effects of pressure gradient and buoyancy forces are also taken into account. The convergence criterion is 1E-06 for continuity and 1E-04 for other parameters. For analyses with Ansys Fluent, simulations were performed using the settings and conservation equations in Table 2.

Table 2. Settings and conservation equations used for CFD Simulations

Energy	On
Species Model	Species Transport Model-Mixture Material
Viscous Model	K-omega (2 equations)
K-omega Model	SST
Options	-Low-Re Correction
	-Viscous Heating
	-Curvature Correction
	-Production Limiter
	-Buoyancy Effect (Full)
General	-Steady State
	-Gravity (on)
Metarial	H_2O 16,35 %
	N_2 68,25 %
	NO 9,8 %
	O_2 5,6 %

In ANSYS Fluent, the upper reactor inlet is defined as a "velocity inlet." The lower reactor outlet is defined as a "pressure outlet." The serpentines in the waste heat boiler section of the ammonia oxidation reactor are spiral-shaped. They are wrapped from the inside out as a sleeve pie. The serpentines are arranged in a way that they are 29 layers on top of each other and connected. Since the NO_x gas flowing through the reactor's main body and the water flow passing through the coils are turbulent, the Realizable k-ω turbulence model was chosen as the turbulence model

to get closer results. With a parametric study, the flow and hydrodynamic structure (velocity, temperature, and pressure distributions) of NO_x gas coming from the regions where the economizer, evaporator, superheater, and pre-evaporator coils are located were examined with the help of CFD analysis. The boundary conditions, gas properties, and material properties used for Ansys Fluent Analysis are also shown in Table 3.

Table 3. Input Gas Operating Values (Boundary Conditions) and Material Properties of the Reactor

Operating Values of Inlet Gas		Material Properties of the Reactor	
Inlet Pressure	342.000 Pa	Superheater	13 CrMo4-5
Input Velocity	29 m/s	Vaporizer	P235GH
Input Flow Rate	51.525 Nm^3/h	Pre-Evaporator	P235GH
Inlet Temperature	870 °C	Economizer	SA213

The plant SCADA gas pressure values comparison with CFD model values (with error percentages) is shown in Figure 8, and the plant SCADA gas velocity values comparison with CFD model values (with error percentages) is also shown in Figure 9. This online SCADA data from the plant (such as gas pressure and velocity values) provides us with real-time measurements of plant operations. Since the CFD model data is compatible with this data, the model is proven to be accurate and reliable. A validated model also more reliably predicts how design improvements will work.

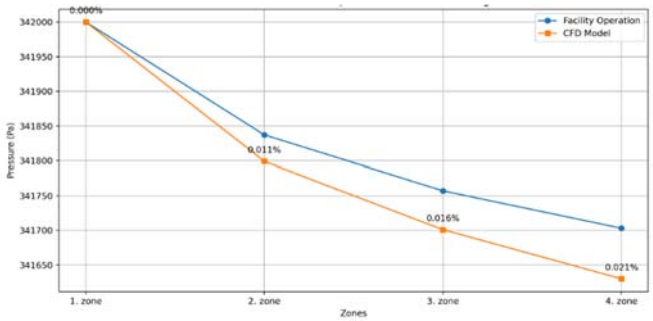

Figure 8. Comparison of Facility SCADA Gas Pressure Values with CFD Model Values (with error percentages)

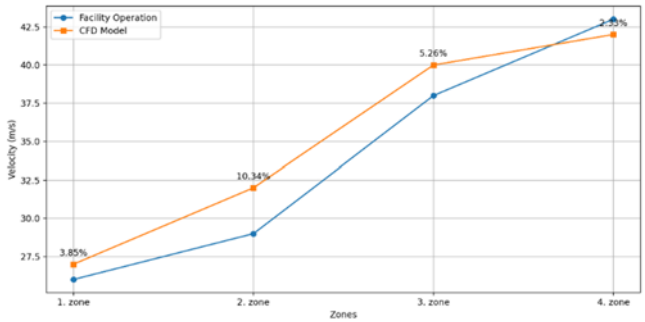

Figure 9. Comparison of Facility SCADA Gas Velocity Values with CFD Model Values (with error percentages)

Table 4. gives the numerical values used for the parametric study in the reactor analysis with the CFD model. In this study, for parametric study with CFD analysis, four parameter values were examined separately; these models:

1. Analysis model: The horizontal distance value (a) between the heat exchanger pipes was studied. In the current operation, the horizontal distance value between the heat exchanger pipes of the reactor is (a) = 48 mm. Parameter values of 44 mm, 46 mm, 52 mm, and 54 mm were created to find the optimum level for the horizontal distance between heat exchanger pipes.

Table 4. Numerical Values Used for Parametric Study in the Analysis of the Reactor with CFD Model

Between Pipes Horizontal Distance (a)	Between Pipes Vertical Distance (b)	Between Heat Exchanger Packages Distance (L)	Pipe Diameter (D)
Current Reactor (48mm)	Current Reactor (63mm)	Current Reactor (0mm)	Current Reactor (42mm)
44 mm	57 mm	100 mm	38 mm
46 mm	60 mm	150 mm	40 mm
52 mm	66 mm	250 mm	44 mm
56 mm	69 mm	300 mm	46 mm

2. Analysis model: The vertical distance value (b) between the heat exchanger pipes was studied. In the current operation, the perpendicular distance between the heat exchanger pipes of the reactor is (b) = 63 mm. Parameter values of 57 mm, 60 mm, 66 mm, and 69 mm were created to find the optimum level for the vertical distance between heat exchanger pipes.

3. Analysis model: The distance (L) between heat exchanger packages (pre-evaporator, superheater, evaporator, and economizer) was studied. In the current operation, the distance between the heat exchangers in the reactor is (L) = 0 mm. So it is all on top of each other. To find the optimum exchanger arrangement, parameters of 100 mm, 150 mm, 250 mm, and 350 mm were created.

4. Analysis model: The heat exchangers' pipe diameter (D) was studied. Currently, the reactor's heat exchanger group pipe diameters are (D) = 42 mm. Parameter values of 38 mm, 40 mm, 44 mm, and 46 mm were created to find the optimum heat exchanger pipe diameter. While creating these parameters, the most efficient values were tried to be seen by comparing the values above and below them based on the existing operating data.

RESULTS AND DISCUSSION

The NH_3 boiler produces nitrous gases and recovers the heat produced during the reaction. Ammonia enriched with O_2 undergoes catalytic combustion (oxidation) at the Pt-Rh gauze in each reactor. Before starting the catalytic reaction, the platinum gauze in the catalyst basket is heated by a stationary H_2 ignitor. The process begins with the ignition of H_2, which initiates the oxidation of ammonia (NH_3) with compressed air, leading to catalytic combustion (Pottbacker et al., 2022; Kayapinar et al., 2024). The reaction is exothermic, and the combustion temperature can be controlled by adjusting the ratio of ammonia and air.

The nitrous gases are cooled downstream of the catalyst gauze using heating surfaces. Heat is transferred to water in the pre-evaporator, superheater, evaporator, and economizer to cool the NO_x process gas formed in the

catalyst due to oxidation in the system. An instant SCADA image of the ammonia oxidation reactor during operation is shown in Figure 10. The feed water is heated in the economizer located in the process gas cooler. This heated water then flows into the steam drum, compensating for the water partly evaporated in the evaporator heating surfaces in the PGC. Circulation pumps provide the boiler water circulation. The steam drum separates the water-steam mixture, and the saturated steam is superheated in the superheater. An attemperator is located in the water volume of the steam drum, where a part of the superheated steam flow is cooled down to control the required superheated steam temperature.

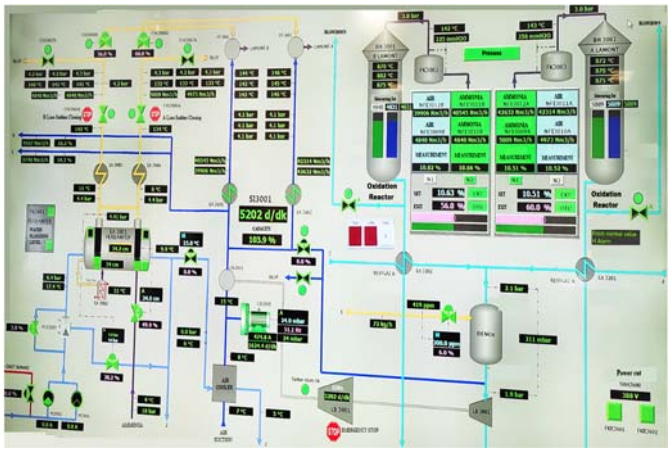

Figure 10. Instant SCADA View of Oxidation Reactors

Steam and water side of the process operating data and gas analysis values in the catalyst basket Table 5. is also given.

Table 5. Analysis Content of The Gas in The Catalyst Basket and Operating Values of the Steam-Water Side

Operating Data For Steam and Water Side		Gas Analysis at Catalyst Basket	
Parameter	**Value**	**Parameter**	**Vol %**
Steam generation (at 100% state)	36500 kg/h	H_2O	16,35
Blowdown (maximum)	1-2 %	N_2	68,25
Steam temperature	430 ^{0}C	NO	9,8
Steam pressure	41 barg	O_2	5,6
Feed water temperature	150 °C	Design pressure, gas side 4,5 barg	

The primary function of cooling devices in an ammonia oxidation reactor is to manage the temperature of the gases leaving the reactor. Figure 11. shows the process of gas entry-exit points to the pre-evaporator tube packages, symmetrical plane details, and the temperature distribution of the fluid in the heat exchanger tubes.

By cooling these hot process gases and promoting the evaporation of water flowing through the system, these devices effectively dissipate excess heat and prevent overheating within the reactor system. Effectively cooling hot process gases and promoting water evaporation, this application zone plays a critical role in maintaining desired temperature conditions in the ammonia oxidation reactor. This helps ensure efficient and safe reactor operation while minimizing the risk of thermal problems or equipment damage.

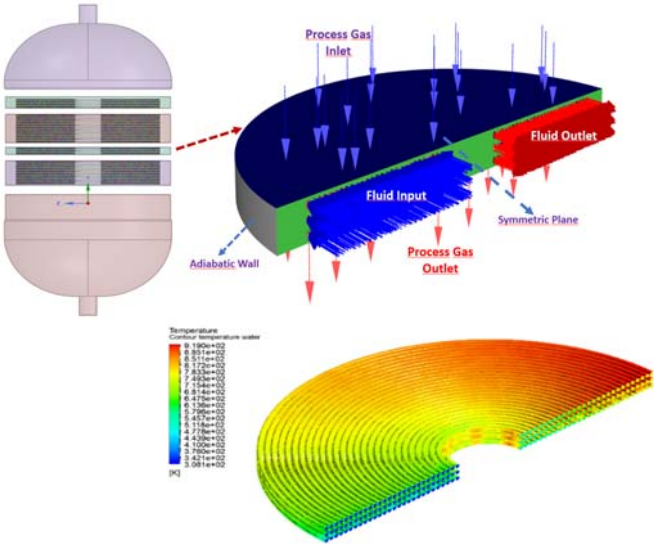

Figure 11. Temperature Distribution for Fluid Input-Outlet Points and Water Side of Pre-Evaporator Tube Packages Analyzed with CFD

The temperature distribution contours formed on the inlet and outlet for the gas side of the pre-evaporator in the ammonia oxidation reactor are shown below (Figure 12).

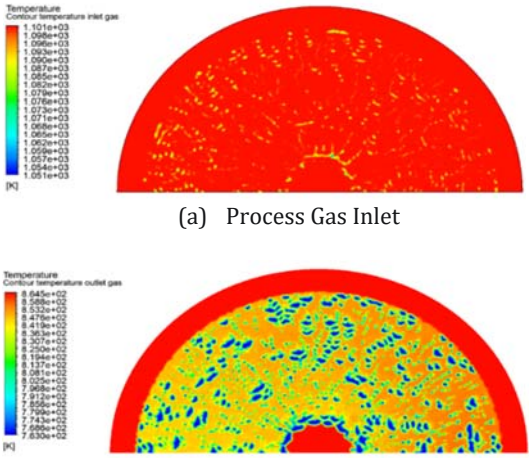

(a) Process Gas Inlet

(b) Process Gas Outlet

Figure 12. Temperature Distribution Contours of the Process Gas Inlet (a) and Outlet (b) in the Pre-evaporator

Effect of Distance Between Heat Exchanger Packages on Gas Cooling

The heating surfaces consist of tube coils, parallel arranged in a spiral. One spiral is one layer located among each other and vertically oriented to the gas flow in the vessel. The spiral heating surfaces are surrounded by wall cooling coils, protecting the vessel shell. The feed water is heated in the economizer before entering the steam drum. The economizer heating surface consists of 10 layers. The ten layers are fed by 20 inlets and routed in a 2-way cross-flow.

The distributor and collector are arranged externally on the vessel. The saturated steam is superheated in the superheater. The superheater surface is made of parallel arranged tube banks horizontally in layers. There are always two layers connected. Figure 13. shows the CFD model results of the oxidation reactor analyzed with 100, 150, 250, and 300 mm gaps between the heat exchanger packages. The temperature values at the system outlet were measured as 329.73, 327.12, 326.685, and 323.205°C, respectively.

The minimal differences between the outlet temperatures indicate that the distance between the exchangers minimizes thermal performance. It is also seen that the velocity and pressure values at the system outlet are pretty close to each other. The results obtained show that the effects depending on the distance are limited. If the distance does not create an impact that will change the temperature or velocity profiles of the fluid, its effect on thermal performance is also minimal.

In the reactor currently in operation, the heat exchanger tube packages (pre-evaporator, superheater, evaporator, and economizer) used to cool the process gas were designed without leaving any space between them. The CFD study compared and analyzed the models created with 100, 150, 250, and 300 mm distances between these heat exchanger packages.

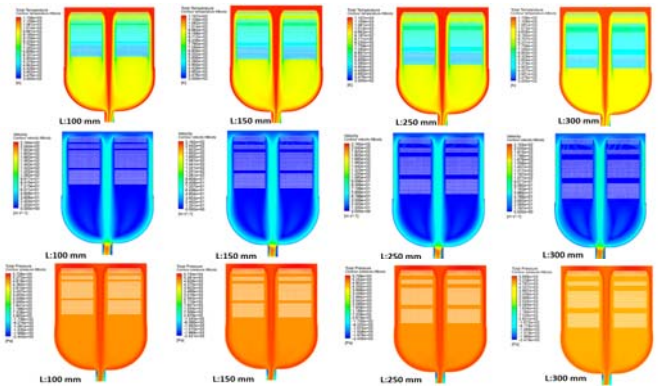

Figure 13. Effect of Distance Between Heat Exchanger Packages on Temperature, Speed, and Pressure (CFD Model Results)

Proper spacing and routing help maintain an even temperature throughout the gas flow, preventing hot spots or areas of inadequate cooling. Increasing the performance in heat exchanger tube packages will also mean increasing performance in the gas cooling process.

The optimum distance between tube packages will increase the heat transfer rate. It is necessary to have the proper amount and quality of feed water, heating steam, and cooling water. It should be done slowly when hot water fills to avoid thermal stress or shock on the pumps.

In Figure 14, the effect of the distance between heat exchanger packages on the temperature and pressure of the cooling process gas is shown by comparing all models. Sufficient optimum space between packages makes inspection, cleaning, and repair activities easier. Conversely, tight intervals can create difficulties for maintenance personnel and increase downtime during service.

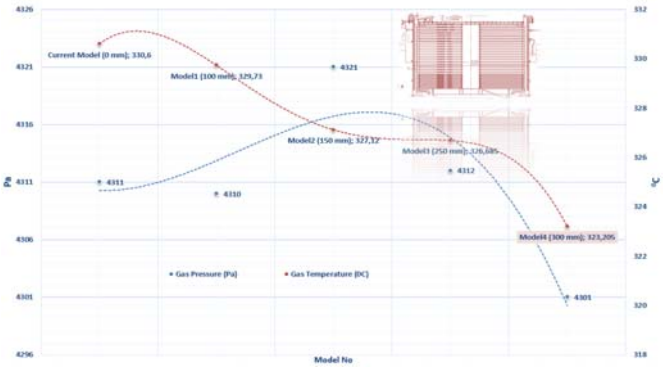

Figure 14. Effect of Distance Between Heat Exchanger Packages (HEP) Cooling Process Gas on Temperature and Pressure

Effect of Horizontal and Vertical Distance Between Heat Exchanger Tubes on Gas Cooling

The distance between heat exchanger tubes is critical in gas cooling systems, affecting heat transfer efficiency, temperature distribution, pressure drop, system optimization, maintenance, and overall economy. For a given number of pipes, the smaller the pipe spacing, the smaller the body diameter and, therefore, the lower the cost. As a result, designers tend to bundle together as many pipes as mechanically possible. However, in the case of heat transfer (thermal-hydraulic or thermo-hydraulic), the optimum pipe spacing and pipe diameter ratio must be determined to convert pressure into heat transfer. Closer spacing will result in insufficient fluid permeability by the body-side fluid and difficulty in mechanically cleaning the outer surfaces of the tubes.

The gap between the heat exchanger tubes can affect the temperature distribution of the gas as it passes through the cooling system. Proper spacing ensures even cooling throughout the gas flow, preventing hot spots or undercooled areas. A smaller distance may lead to less pressure drop and increase the risk of flow instability. Widening the horizontal distance between heat exchanger pipes ensures homogeneous fluid distribution (Noorollahi et al., 2018). This provides a more equal heat transfer and a more homogeneous temperature distribution. The narrowing of the horizontal distance between pipes causes the flow to accelerate and local flow velocities to increase. In this case, the temperature profile is irregular, and heat transfer is less in certain regions.

Figure 15. shows the effect of the horizontal distance between the heat exchanger tubes on temperature, speed, and pressure (CFD model results). The outlet temperature was measured as 334.95 °C when the horizontal distance between the tubes was 44 mm, 327.12 °C when the distance between the tubes was 46 mm, 286.23 °C when the distance between the tubes was 52 mm, and 270.51°C when the distance between the tubes was 56 mm. When the distance between the tubes was increased, the resistance to flow decreased, and the thermal efficiency increased because, especially by improving the horizontal distance between the tubes and reducing the cross-sectional area of the fluid passing through the middle of the system, a homogeneous pipe distribution was obtained in the system. Increasing the distance between the tubes ensures that the fluid encounters fewer obstacles throughout the exchanger. This reduces the flow resistance and optimizes turbulence at the same time.

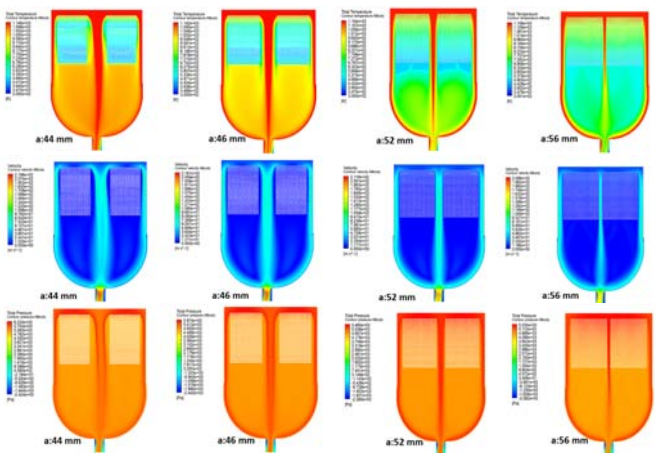

Figure 15. Effect of Horizontal Distance Between Heat Exchanger Pipes on Temperature, Speed, and Pressure (CFD Model Results)

Figure 16. shows the effect of the horizontal distance between the heat exchanger pipes on the temperature and pressure of the cooling process gas. Regarding facility and system efficiency, the lowest temperature of the process gas (270.51^{0}C) was obtained in the model with a horizontal distance of 56 mm. This was the best cooling performance model obtained among all parametric study models.

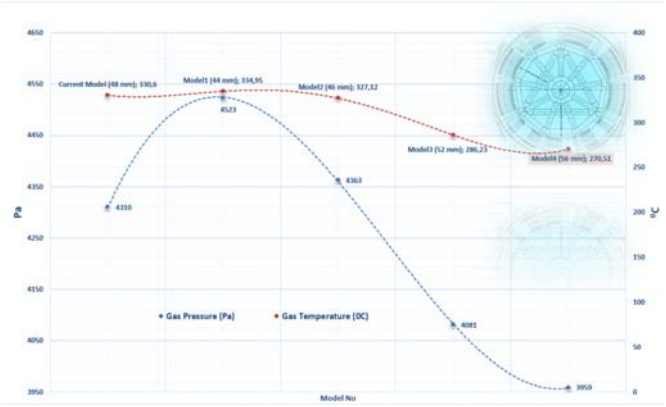

Figure 16. Effect of Horizontal Distance Between Heat Exchanger Pipes on Temperature and Pressure of Cooling Process Gas

The vertical distance between the heat exchanger pipes in the gas cooling zone of the existing oxidation reactor is 63 mm. Figure 17. the CFD model results of the oxidation reactor were analyzed with a vertical distance of 57, 60, 66, and 69 mm between the heat exchanger pipes. As a result of the studies, when the perpendicular distance between the pipes is 57 mm, the system outlet temperature is measured as 318.42 °C; for 60 mm, it is 319.29 °C; for 66 mm, it is 320.59 °C, and for 69 mm, it is 321.9 °C. As seen in Figure 9, where the effect of the distance between the exchangers on the system efficiency is examined, it has been determined that its impact is low. In addition, it has been observed that thermal efficiency decreases when the distance between the pipes increases vertically.

In this case, it has been determined that the most efficient model has a vertical distance of 57 mm. Increasing the vertical distance reduces the pipe density in the exchanger.
A less dense pipe arrangement causes the gas fluid to pass more efficiently throughout the system without losing energy. However, this also causes the fluid to leave the system without cooling sufficiently, which increases the outlet temperature. It also causes the thermal interaction areas around each pipe to decrease.

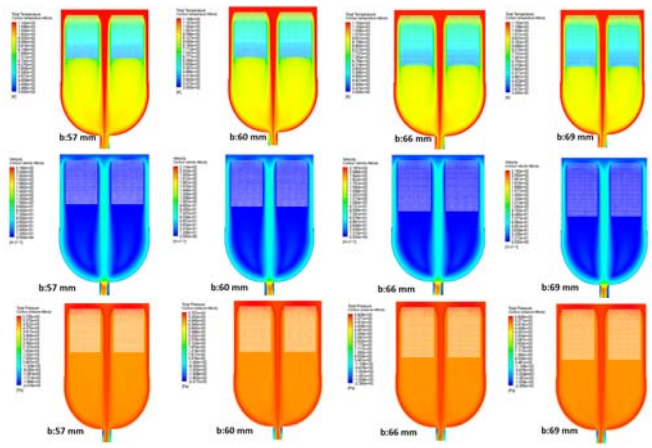

Figure 17. Effect of Vertical Distance Between Heat Exchanger Pipes on Temperature, Speed, and Pressure (CFD Model Results)

This results in the "heat transfer effect" created by the pipes on the fluid becoming isolated from each other. Thus, the synergistic heat transfer between the pipes is reduced. Since the fluid spends less time between the pipes, the heat exchange with the pipes is also restricted. This causes the gas to leave the system at a higher temperature. Figure 18. shows the effect of the vertical distance between the heat exchanger pipes on the temperature and pressure of the cooling process gas. Regarding facility and system efficiency, the lowest temperature of the process gas (318 ^{0}C) was obtained in the model with a vertical distance of 57 mm.

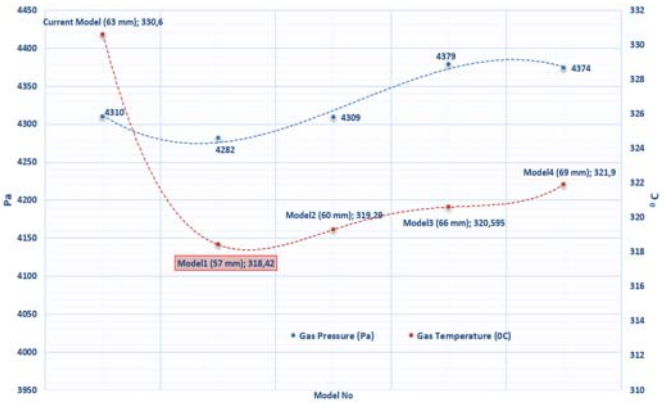

Figure 18. Effect of Vertical Distance Between Heat Exchanger Pipes on Temperature and Pressure of Cooling Process Gas

Effect of Heat Exchanger Tube Diameter on Gas Cooling

The heat exchanger pipe diameters in the existing oxidation reactor gas cooling zone are 42 mm. Figure 19. the CFD model results of the oxidation reactor were analyzed with heat exchanger pipe diameters of 38, 40, 44, and 46 mm. When the temperature contour graphs are examined, the system outlet temperature for the diameter of 38 mm is measured as 296.67 °C, for 40 mm as 310.15°C, for 44 mm as 325.38 mm, and for the diameter of 46 mm as 334.51°C. It has been determined that the change in diameter significantly affects the system efficiency and that the most efficient model is a diameter of 38 mm. Since this diameter value offers a higher surface area-to-volume ratio compared to the others, the heat transfer efficiency increases. As the diameter increases, the gas cooling performance decreases. It can be said that small-diameter pipes increase the total heat transfer surface by fitting more pipes in the same area.

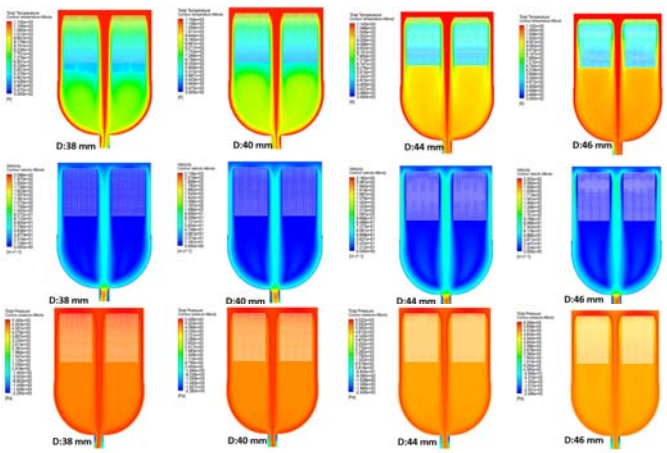

Figure 19. Effect of Heat Exchanger Pipe Diameter on Temperature, Speed, and Pressure (CFD Model Results)

The effect of heat exchanger pipe diameter on cooling process gas temperature and pressure is shown in Figure 20. Many parameters are effective in the optimization and design of heat exchangers. The manufacturing method of the heat exchanger, the heat transfer mechanism, and the flow states of the fluids are effective in the design and efficient use of heat exchangers. Regarding facility and system efficiency, the lowest temperature of the process gas (296.67 ^{0}C) was obtained in the model with a pipe diameter of 38 mm. In the process of cooling the process gas, the hot gas fluid that comes into contact with the surface area of the heat exchanger tube packages at low speeds provides a better performance with smaller diameter heat exchanger pipes (with water circulating in them).

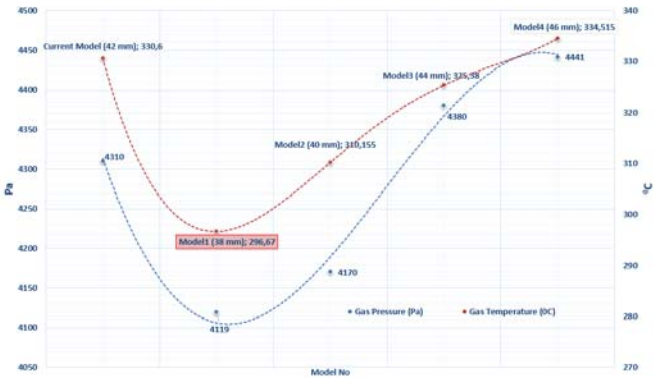

Figure 20. Effect of Heat Exchanger Pipe Diameter on Cooling Process Gas Temperature and Pressure

Because it ensures that the fluid (water) remains in the pipes for longer, providing more heat transfer. Additionally, smaller diameter pipes offer a more compact design. Thus, providing a better flow distribution and a more homogeneous temperature profile increases efficiency by delivering more heat transfer surfaces. An important point to consider while cooling the process gas is this: during regular operation, the circulation water is circulated by electrically driven pumps. Flow measurements are taken and monitored for accurate control. Additionally, a second electrically-driven pump is available as a standby in case of any issues. Low water-steam mixture velocities can cause water-steam separation in the horizontally designed evaporator heating surfaces. This can decrease the cooling efficiency of the upper part of the tubes, leading to overheating and severe damage. Using smaller diameter pipes in the liquid passing parts on the cold side has been observed to affect several factors that increase heat transfer. When the pipe diameter decreases for the same flow rate, the flow rate increases, which makes the flow more dynamic. Increasing velocity causes the liquid to interact more with the pipe wall, increasing heat transfer. In smaller-diameter pipes, the possibility of the flow becoming turbulent increases. Turbulent flow increases heat transfer coefficients because the movement of the fluid provides better mixing and temperature distribution. These factors explain why the pipes through which the liquid on the cold side passes are smaller in diameter, increasing heat transfer and, therefore, cooling performance. However, these advantages may vary depending on the overall design of the system and operating conditions.

Table 6. gives the hourly SCADA data (process gas temperature and flow rate values) taken online at operating conditions for the ammonia oxidation reactor of the relevant nitric acid production facility. Additionally, Table 7 compares this study's design values with those obtained in studies in the literature. When the actual operating SCADA values of the ammonia oxidation reactor modeled with CFD analysis are examined, it is seen that the gas outlet temperature is around 297 ^{0}C on average. Considering this average temperature value, a decrease in gas temperature of approximately 9% was achieved with this study.

Table 6. Hourly SCADA Data for Process Gas Temperature and Flow Rate in Ammonia Oxidation Reactor

Time	Process gas inlet (^{o}C)	Process gas outlet (^{o}C)	Process gas flow (Nm^3/h)
02:00	870	297	51700
04:00	874	296	52100
06:00	874	298	52374
08:00	879	297	51680
10:00	870	297	51630
12:00	877	299	51706
14:00	871	296	51620
16:00	874	298	51600
18:00	875	299	51843
20:00	881	293	52495
22:00	866	292	52444
00:00	871	296	52470

When the absolute operating SCADA values of the ammonia oxidation reactor modeled with CFD analysis are examined, it is seen that the gas outlet temperature is around 297 ^{0}C on average. Considering this average temperature value, a decrease of approximately 9% in gas temperature has been achieved with this study.

Table 7. Comparison of Values for Different Models in the Ammonium Oxidation Reactor

Model	Reactor Zone	System Conditions
This study	Heat exchangers	Average gas flow: 51971 Nm^3/h Reactor Height: 6500 mm Gas side pressure:4.5 barg
Abbasfard et al., (2012)	Reactor inlet and distributor	Gas inlet speed: 13.77 m/s Outlet pressure: 5.33 bar Nominal flow: 32543 m^3 / h
Grande et al. (2018).	Platinum catalyst	Activation energy: 114 kJ/mol Pressure value: 4.7 bar Flow rate value: 1.698 SLPM
Amirsadat et al. (2024)	Inlet feed pipeline	Pressure value: 12.65 bar Nominal flow: 6466 m^3 / h Reactor Height: 9082 mm
Nascimento et al. (2024).	Absorption column	Pressure value: 456.62 kPa Air molar flow: 310.74 kmol/h Cooling coils area: 8.47 m^2

This decrease in the percentage of cooling of these hot NOx gases formed due to chemical reactions in the ammonia oxidation reactor catalyst is significant for the following criteria and system reactions. Because as the temperature value decreases,

- NOx gases (especially NO and NO_2) have high energy and tend to enter side reactions.
- The chemical stability of NO_x gases increases; this prevents undesirable reactions.
- This gas leaving the reactor is then sent to the absorption towers. As the gas temperature decreases, the reaction kinetics accelerates due to the low solubility of the gases. The conversion rate of NO_x to nitric acid and product efficiency also increases.

The distribution of maximum temperature values for steam is necessary to manage major critical factors such as equipment life, energy exchange, chemical change, system stability, and observed protection. High temperatures can cause metal surfaces to melt, oxidize, or expand, leading to equipment failure. These temperature limitations help the system to be efficient, safe, and long-lasting.

Extreme temperatures can create extreme stresses on valves, pipelines, and other components in the system. Based on the design of the heat exchanger packages of the ammonia oxidation reactor of the relevant facility, the maximum fluid (water) temperature was limited to 266 ^{0}C in the economizer and evaporator and 470^{0}C in the superheater. With CFD simulation analysis, the model results in which the lowest process gas temperature was obtained with a 56 mm horizontal distance between the heat exchanger pipes were compared with the actual operating values obtained from the facility's online SCADA data system.

Accordingly, there was an increase of 8.2% in the fluid outlet temperature obtained in the economizer, 9.7 % in the evaporator, and 4.3 % in the superheater. These changes received as a result of the simulation are consistent with the temperature values that are the basis for the design and the limited ones. Table 8. shows the temperature change values of the fluid circulating in the heat exchanger packages.

Table 8. Temperature change values of the fluid in the heat exchanger packages

Component	a	b	c
Facility SCADA Data System Fluid Temperature (^{0}C)	430	301	202
CFD Simulation Data Fluid Temperature (^{0}C)	448,4	330.1	218,5
Rate of Increase in Temperature Value (%)	4.3	9.7	8.2

a: Superheater b: Evaporator c: Economizer

Other problems affecting the gas cooling process and solution suggestions

After a shutdown or emergency stop of the process gas cooler, the entire system must be vented after an ammonia trip to remove corrosive flue gas. If the gas cooler is disconnected from the steam network, the start-up valve must be activated to release the steam and cool the superheater. During this process, monitoring the outlet temperature at the superheater is crucial. Monitoring the overall circulation volume and current consumption during operation is essential to avoid overloading the circulation pump. As the heat-up process progresses, the circulation volume should be reduced at the discharge slide gate valve. The heat-up process commences by opening the steam injection valve to the steam drum. To control the heat-up process, the steam quantity and heat supplied and the steam discharge via the start-up valve should be adjusted. Ensuring a continuous steam flow to the drum is crucial to prevent hammering. During the heating-up process, it is essential to maintain the drum water level above the "low" level. The water level will increase due to thermal expansion and condensed heating steam. After the heating-up process commences, the water level should not decrease. Boiling out is a commonly used method for cleaning the water and water/steam system, involving fast temperature changes instead of chemicals. This method effectively dissolves iron oxide layers, dust, and sand while forming a protective magnetite layer (only above 200°C). Flushing is often done before boiling out. There are two methods for boiling out the Process gas cooler system: constant pressure and fluctuating pressure (respiratory method). The respiratory method is preferred as it accelerates flaking. Boiling out is most effective for new plants, while pickling is more efficient for existing plants where deposits have already formed in the pipes. The temperature can be monitored and controlled if there is a measurement in the water circulation system. When the drum pressure is 0.2 MPag, the valve should be closed. Once the steam pressure reaches around 0.2-0.3 MPag, the bypass valve of the steam traps can be closed, and the steam traps can be put into operation. During the heat-up phase and after the start of the reaction, the superheater and the superheated steam line must be drained repeatedly via the bypass valves. It is important to gradually increase the temperature of superheated steam, particularly during the initial heat-up phase, after ignition, and the start of catalytic combustion (when the attemperator is fully open). While heating up and after the reaction has started, it is necessary to repeatedly drain the superheated steam line and the superheaters via the bypass valves. The facility is heated up using external steam from the "20 atu net", which is nozzle-fed into the steam drum via a bleed pipe. To avoid water hammer, the steam valves must be opened slowly and carefully. During the heat-up, the water level of the drum must be within the visible range. It is not allowed to operate the system with a water level below "low."The manual regulating valve on the heating line adjusts the jet-fed external steam quantity. Steam hammering is to be avoided.

CONCLUSION

Proper gas flow and distribution within ammonia oxidation reactors are essential for a homogeneous reaction environment. A well-designed reactor system can achieve the desired conversion efficiency and ensure the process is economically and environmentally sustainable. One of the most critical parameters here is the NO outlet temperature. This NO gas formed in the catalyst reaches high temperatures until it enters the cooling exchangers. The system efficiency value decreases at every ^{o}C level where the NO outlet temperature exceeds the design value. The same model of the ammonia oxidation reactor of the 610 ton/day nitric acid production plant considered in this study was analyzed in CFD simulation. Regarding plant and system efficiency, the lowest temperature of the process gas (270.51°C) was obtained in the model where the horizontal distance between the heat exchanger tubes was 56 mm. The increased horizontal distance between the tubes allowed each tube to contribute equally to heat transfer and reduced the "dead zones" (where temperature changes are minimal). This model has shown the most effective cooling performance among all parametric study models. In response to the cooling performance of this hot gas, there has also been an increase in the current temperature values of the refrigerant circulating in the exchanger packages. When the CFD simulation results are compared with the actual operating data (SCADA online data), the fluid outlet temperature in the ammonia oxidation reactor has increased by 8.2% in the economizer, 9.7% in the evaporator, and 4.3% in the superheater. In other simulations, it has been observed that the distance between the exchanger packages has a minimal effect on the thermal performance (the speed and pressure values at the system outlet are pretty close to each other) and that the thermal efficiency decreases when the distance between the tubes is increased vertically and the tube diameter increases. Increasing the vertical distance between the tubes reduces the contact time to the heat transfer surface and the thermal interaction zones between the tubes. This results in lower thermal efficiency and higher outlet temperatures for hot gas cooling. The approximate temperature change for a vertical distance change of 12 mm is 3.48 °C. Therefore, vertical distance changes appear to have less impact on system efficiency. The following study aims to investigate the effect of different design types of La Mont nozzles, which are located at the inlet of each evaporator and wall cooling pipe, on the system efficiency (by CFD simulation

analysis), ensuring that the required water flow reaches separate regions and that all sections are sufficiently cooled.

REFERENCES

Abbasfard, H., Ghanbari, M., Ghasemi, A., Ghader, S., Rafsanjani, H. H., & Moradi, A. (2012). Failure analysis and modeling of superheater tubes of a waste heat boiler thermally coupled in an ammonia oxidation reactor. *Engineering Failure Analysis*, *26*, 285-292. https://doi.org/10.1016/j.engfailanal.2012.06.012

Abbasfard, H., Ghanbari, M., Ghasemi, A., Ghahraman, G., Jokar, S. M., & Rahimpour, M. R. (2014). CFD modeling of flow mal-distribution in an industrial ammonia oxidation reactor: A case study. *Applied thermal engineering*, *67*(1-2), 223-229. https://doi.org/10.1016/j.applthermaleng.2014.03.035

Amirsadat, S. M., Azari, A., Nazari, M., & Akrami, M. (2024). Conversion augmentation of an industrial NH3 oxidation reactor by geometry modification to improve the flow and temperature pattern uniformity using CFD modeling. *Chemical Engineering Journal Advances*, *19*, 100629. https://doi.org/10.1016/j.ceja.2024.100629

Ardy, H., Putra, Y. P., Anggoro, A. D., & Wibowo, A. (2021). Failure analysis of primary waste heat boiler tube in ammonia plant. Heliyon, 7(2). https://doi.org/10.1016/j.heliyon.2021.e06151

Bagheri, H., Bagheri, S., Hashemipour, H., & Rahimpour, M. R. (2024). Modeling and optimization of ammonia reactor. In *Progresses in Ammonia: Science, Technology and Membranes* (pp. 173-204). Elsevier. https://doi.org/10.1016/B978-0-323-88516-4.00001-9

Belghaieb, J., Dkhil, O., Elhajbelgacem, A., Hajji, N., & Labidi, J. (2010). Energy optimization of a network of exchangers-reactors in a nitric acid production plant. Chemical Engineering, 21. https://doi.org/10.3303/CET1021046

Chatterjee, I. B., & Joshi, J. B. (2008). Modeling, simulation, and optimization: Mono pressure nitric acid process. Chemical Engineering Journal, 138(1-3), 556-577. https://doi.org/10.1016/j.cej.2007.07.064

Chernyshev, V. I., & Zjuzin, S. V. (2001). Improved start-up for the ammonia oxidation reaction. Platinum Metals Review, 45(1), 22-30.

Colak, A. B., & Arslan, O. (2024). Numerical analysis-based performance assessment of the small-scale organic Rankine cycle turbine design for residential applications. *Thermal Science and Engineering Progress*, *51*, 102626. https://doi.org/10.1016/j.tsep.2024.102626

Dong, Y., Zhang, D., Li, D., Jia, H., & Qin, W. (2023). Control of Ostwald ripening. *Science China Materials*, *66*(3), 1249-1255. https://doi.org/10.1007/s40843-022-2233-3

Elsayed, S., & Farag, H. A. (2023). Modelling of an Industrial Reactor for Ammonia Oxidation. *ERJ. Engineering Research Journal*, *46*(4), 451-456. https://doi.org/10.21608/erjm.2023.142966.1177

Enger, B. C., Auvray, X., Lødeng, R., Menon, M., Waller, D., & Rønning, M. (2018). Catalytic oxidation of NO to NO_2 for nitric acid production over a Pt/Al2O3 catalyst. *Applied Catalysis A: General*, *564*, 142-146. https://doi.org/10.1016/j.apcata.2018.07.019

Fajardo, J., Valle, H., & Buelvas, A. (2018). Avoidable and Unavoidable Exergetic Destruction Analysis of a Nitric Acid Production Plant. In ASME International Mechanical Engineering Congress and Exposition (Vol. 52088, p. V06BT08A009). American Society of Mechanical Engineers. https://doi.org/10.2298/TSCI120503181V

Fíla, V., & Bernauer, B. (1994). A mathematical model of a gauze reactor for the ammonia oxidation. *Collection of Czechoslovak chemical communications*, *59*(4), 855-874. https://doi.org/10.1135/cccc19940855

García-Ruiz, P., Uruén, M., Abián, M., & Alzueta, M. U. (2023). High pressure ammonia oxidation in a flow reactor. *Fuel*, *348*, 128302. https://doi.org/10.1016/j.fuel.2023.128302

Grande, C. A., Andreassen, K. A., Cavka, J. H., Waller, D., Lorentsen, O. A., Øien, H., ... & Modeshia, D. (2018). Process intensification in nitric acid plants by catalytic oxidation of nitric oxide. *Industrial & Engineering Chemistry Research*, *57*(31), 10180-10186. https://doi.org/10.1021/acs.iecr.8b01483

Hannevold, L., Nilsen, O., Kjekshus, A., & Fjellvåg, H. (2005). Reconstruction of platinum–rhodium catalysts during oxidation of ammonia. *Applied Catalysis A: General*, *284*(1-2), 163-176. https://doi.org/10.1016/j.apcata.2005.01.033

Heck, R. M., Bonacci, J. C., Hatfield, W. R., & Hsiung, T. H. (1982). A new research pilot plant unit for ammonia oxidation processes and some gauze data comparisons for nitric acid process. *Industrial & Engineering Chemistry Process Design and Development*, *21*(1), 73-79. https://doi.org/10.1021/i200016a014

Hernández, A. B., Fajardo, J. G., Barreto, D., Caballero, G. E. C., Escorcia, Y. C., Tovar, C. R. V., & Hernández, Y. G. (2021). Conventional and advanced exergoeconomic indicators of a nitric acid production plant concerning the cooling temperature in compression Train's intermediate stages—case *Studies in Thermal Engineering*, *27*, 101214. https://doi.org/10.1016/j.csite.2021.101214

Holma, H., & Sohlo, J. (1979). A mathematical model of an absorption tower of nitrogen oxides in nitric acid production. *Computers & Chemical Engineering*, *3*(1-4), 135-141. https://doi.org/10.1016/0098-1354(79)80024-1

Hung, C. M. (2008). Catalytic wet oxidation of ammonia solution with platinum-palladium-rhodium composite oxide catalyst. *J. Environ. Eng. Manage*, *18*(2), 85-91.

Il'chenko, N. I., & Golodets, G. I. (1975). Catalytic oxidation of ammonia: II. Relationship between catalytic properties of substances and surface oxygen bond energy. General regularities in catalytic oxidation of ammonia and organic substances. Journal of Catalysis, 39(1), 73-86. https://doi.org/10.1016/0021-9517(75)90283-3

Juangsa, F. B., & Aziz, M. (2019). Integrated system of thermochemical cycle of ammonia, nitrogen production, and power generation. *International Journal of Hydrogen Energy*, *44*(33), 17525-17534. https://doi.org/10.1016/j.ijhydene.2019.05.110

Kayapinar, O., Arslan, A. E., Arslan, O., & Genc, M. S. (2024). Multi-criteria analysis on the simulation-based optimal design of a new stack-type natural ventilation system for industrial buildings. *Thermal Science and Engineering Progress*, *51*, 102657. https://doi.org/10.1016/j.tsep.2024.102657

Kirova-Yordanova, Z. (2011). Application of the exergy method to the environmental impact estimation: The nitric acid production as a case study. Energy, 36(6), 3733-3744. https://doi.org/10.1016/j.energy.2010.12.039

Kishan, R., Singh, D., & Sharma, A. K. (2020). CFD Analysis of heat exchanger models designs using Ansys fluent—International *Journal of Mechanical Engineering and Technology*, *11*(2). https://www.doi.org/10.34218/IJMET.11.2.2020.001

Kraehnert, R., & Baerns, M. (2008). Kinetics of ammonia oxidation over Pt foil studied in a micro-structured quartz-reactor. Chemical engineering journal, 137(2), 361-375. https://doi.org/10.1016/j.cej.2007.05.005

Lim, J., Fernández, C. A., Lee, S. W., & Hatzell, M. C. (2021). Ammonia and nitric acid demand for fertilizer use in 2050. *ACS Energy Letters*, *6*(10), 3676-3685. https://doi.org/10.1021/acsenergylett.1c01614

Mewada, R. K., & Nimkar, S. C. (2015). Minimization of exergy losses in mono high-pressure nitric acid process. International Journal of Exergy, 17(2), 192-218. https://doi.org/10.1504/IJEX.2015.069990

Moszowski, B., Wajman, T., Sobczak, K., Inger, M., & Wilk, M. (2019). The analysis of distribution of the reaction mixture in ammonia oxidation reactor. Polish Journal of Chemical Technology, 21(1), 9-12. https://doi.org/10.2478/pjct-2019-0002

Nascimento, G. R., & Dangelo, J. V. (2024). Operating parameters analysis of a nitric acid plant to increase production and reduce NOx gases emission. *Chemical Engineering and Processing-Process Intensification*, *196*, 109662. https://doi.org/10.1016/j.cep.2024.109662

Neumann, N. C., Baumstark, D., Martínez, P. L., Monnerie, N., & Roeb, M. (2024). Exploiting synergies between sustainable ammonia and nitric acid production: A techno-economic assessment. *Journal of Cleaner Production*, *438*, 140740. https://doi.org/10.1016/j.jclepro.2024.140740

Noorollahi, Y., Saeidi, R., Mohammadi, M., Amiri, A., & Hosseinzadeh, M. (2018). The effects of ground heat exchanger parameters changes on geothermal heat pump performance–A review. *Applied Thermal Engineering*, *129*, 1645-1658. https://doi.org/10.1016/j.applthermaleng.2017.10.111

Pfefferle, L. D., & Pfefferle, W. C. (1987). Catalysis in combustion. *Catalysis Reviews Science and Engineering*, *29*(2-3), 219-267. https://doi.org/10.1080/01614948708078071

Pottbacker, J., Jakobtorweihen, S., Behnecke, A. S., Abdullah, A., Özdemir, M., Warner, M., ... & Horn, R. (2022). Resolving gradients in an ammonia oxidation reactor under industrial conditions: A combined experimental and simulation study. *Chemical engineering journal*, *439*, 135350. https://doi.org/10.1016/j.cej.2022.135350

Process Gas Coolers Operation and Maintenance Manual (2024). Istanbul Fertilizer Industry Inc. Kutahya Production Facilities.

Rajeshkumar, M., Logesh, K., Thangaraj, M., & Govindan, S. (2021). Heat transfer study on finned tube heat exchanger using CFD. *International Journal of Ambient Energy*, *42*(3), 239-243 https://doi.org/10.1080/01430750.2018.1542621

Sadykov, V. A., Isupova, L. A., Zolotarskii, I. A., Bobrova, L. N., Noskov, A. S., Parmon, V. N., ... & Lunin, V. V. (2000). Oxide catalysts for ammonia oxidation in nitric acid production: properties and perspectives. *Applied Catalysis A: General*, *204*(1), 59-87. https://doi.org/10.1016/S0926-860X(00)00506-8

Salam, M. A., Nassef, E., Elkheriany, E., & El Tawel, Y. (2016). Modeling and Simulation of Gauze Reactor of Ammonia Oxidation. *American Journal of Chemical Engineering*, *4*(1), 16-22. https://doi.org/10.11648/j.ajche.20160401.13

Scheuer, A., Hirsch, O., Hayes, R., Vogel, H., & Votsmeier, M. (2011). Efficient simulation of an ammonia oxidation reactor using a solution mapping approach. *Catalysis Today*, *175*(1), 141-146. https://doi.org/10.1016/j.cattod.2011.03.036

Schumacher, K., Engelbrecht, N., Everson, R. C., Friedl, M., & Bessarabov, D. G. (2019). Steady-state and transient modelling of a microchannel reactor for coupled ammonia decomposition and oxidation. *International Journal of Hydrogen Energy*, *44*(13), 6415-6426. https://doi.org/10.1016/j.ijhydene.2019.01.132

Song, Y., Hashemi, H., Christensen, J. M., Zou, C., Marshall, P., & Glarborg, P. (2016). Ammonia oxidation at high pressure and intermediate temperatures. *Fuel*, *181*, 358-365. https://doi.org/10.1016/j.fuel.2016.04.100

Srinivasan, R., Hsing, I. M., Berger, P. E., Jensen, K. F., Firebaugh, S. L., Schmidt, M. A., ... & Ryley, J. F. (1997). Micromachined reactors for catalytic partial oxidation reactions. *AIChE Journal*, *43*(11), 3059-3069. https://doi.org/10.1016/j.ces.2007.09.021

Stagni, A., Cavallotti, C., Arunthanayothin, S., Song, Y., Herbinet, O., Battin-Leclerc, F., & Faravelli, T. (2020). An experimental, theoretical and kinetic-modeling study of the gas-phase oxidation of ammonia. *Reaction Chemistry & Engineering*, *5*(4), 696-711. https://doi.org/10.1039/C9RE00429G

Wiser, Artur M. (2020), Investigation of the Industrial NH3 Oxidation by CFD Simulations Including Detailed Surface Kinetics (Ph.D. thesis), Technische Universität Darmstadt. https://doi.org/10.25534/tuprints-00017208

Zhan, H., Li, S., Yin, G., Hu, E., & Huang, Z. (2024). Experimental and kinetic study of ammonia oxidation and NOx emissions at elevated pressures. *Combustion and Flame*, *263*, 113129. https://doi.org/10.1016/j.ijhydene.2024.12.214

Journal Homepage: https://dergipark.org.tr/tr/pub/isibted

Isı Bilimi ve Tekniği Dergisi

Archive: https://tibtd.org.tr/dergi

Enhancing Thermal Efficiency in Fluidized Bed Cooling Towers: An Experimental Approach to Bed Design

Mukilarasan Nedunchezhiyan [1], Ravikumar Jayabal [2,*], Sathiyamoorthy Ramalingam [3], Senthil Sambath [4]

[1] *Department of Mechanical Engineering, Academy of Maritime Education and Training, Kanathur, Tamil Nadu, India.*
[2] *Department of Mechanical Engineering, Saveetha School of Engineering, Saveetha Institute of Medical and Technical Sciences (SIMATS), Chennai, Tamil Nadu, India.*
[3] *Department of Mechanical Engineering, Chennai Institute of Technology, Chennai, Tamil Nadu, India.*
[4*] *Department of Mechanical Engineering, Panimalar Engineering College, Chennai, Tamil Nadu, India.*

A R T I C L E I N F O

2025, vol. 45, no.1, pp. 111-118

doi: 10.47480/isibted.1567713

Research Article
Received: 15 October 2024
Accepted: 06 January 2025

* *Corresponding Author*
e-mail:
ravikumarj.sse@saveetha.com

Keywords:
fluidized bed cooling tower
bed height
heat transfer
velocity
efficiency
cooling

ORCID Numbers in author order:
0000-0002-0662-3589
0000-0001-7877-9913
0000-0002-5428-3996
0000-0002-8504-6790

A B S T R A C T

The study aimed to investigate the thermal performance of a fluidized bed cooling tower (FBCT) by examining the effects of varying bed heights and circular tempestuous spheres on cooling efficiency. An experimental setup was designed to evaluate the FBCT's performance under different conditions, including variable water flow rates, bed heights ranging from 200 to 300 mm, and spherical balls with diameters of 25 mm and 50 mm. Critical parameters such as the range and approach of temperature and the liquid-to-gas (L/G) ratio were analyzed to understand their influence on the cooling tower's efficiency. The findings indicated that more petite turbulence balls significantly enhanced air mixing efficiency, improving thermal performance. It was observed that an increase in the ratio of water mass flux to air mass flux resulted in decreased cooling tower effectiveness. The static bed height was also identified as a critical factor affecting performance, with the entry water temperature impacting the static bed height. The study concluded that optimizing bed height and utilizing more petite (25mm) spherical balls can enhance the thermal efficiency (92.83%) of fluidized bed cooling towers. The relationship between water and air mass flow rates is crucial for achieving effective cooling performance, highlighting the importance of these parameters in the design and operation of FBCTs in industrial applications.

Akışkan Yataklı Soğutma Kulelerinde Isıl Verimliliğin Artırılması: Yatak Tasarımına Deneysel Bir Yaklaşım

M A K A L E B İ L G İ S İ

***Anahtar Kelimeler**:*
akışkan yataklı soğutma kulesi
yatak yüksekliği
ısı transferi
hız
verim
soğutma

Ö Z E T

Bu çalışma, değişen yatak yüksekliklerinin ve dairesel fırtınalı kürelerin soğutma verimliliği üzerindeki etkilerini inceleyerek akışkan yataklı bir soğutma kulesinin (FBCT) termal performansını araştırmayı amaçlamıştır. FBCT'nin performansını, değişken su akış hızları, 200 ila 300 mm arasında değişen yatak yükseklikleri ve 25 mm ve 50 mm çapında küresel toplar dahil olmak üzere farklı koşullar altında değerlendirmek için bir deney düzeneği tasarlandı. Sıcaklığın aralığı ve yaklaşımı ile sıvı-gaz (L/G) oranı gibi kritik parametreler, soğutma kulesinin verimliliği üzerindeki etkilerini anlamak için analiz edildi. Bulgular, daha küçük türbülans toplarının hava karıştırma verimliliğini önemli ölçüde arttırdığını ve termal performansı iyileştirdiğini gösterdi. Su kütle akısının hava kütle akısına oranındaki artışın soğutma kulesi etkinliğinin azalmasına neden olduğu gözlendi. Statik yatak yüksekliğinin de performansı etkileyen kritik bir faktör olduğu ve giriş suyu sıcaklığının statik yatak yüksekliğini etkilediği belirlendi. Çalışma, yatak yüksekliğini optimize etmenin ve daha küçük (25 mm) küresel bilyalar kullanmanın, akışkan yataklı soğutma kulelerinin termal verimliliğini (%92,83) artırabileceği sonucuna varmıştır. Su ve hava kütle akış hızları arasındaki ilişki, etkili soğutma performansı elde etmek için çok önemlidir ve bu parametrelerin endüstriyel uygulamalarda FBCT'lerin tasarımı ve çalıştırılmasındaki önemini vurgulamaktadır.

INTRODUCTION

Since the beginning of the twenty-first century, there has been a significant rise in the number of people around the world who are experiencing water scarcity. There are a number of causes that are posing an increasing threat to the availability of freshwater resources. These include drought, contamination of water reserves, and changes in the patterns of rainfall. All of these concerns have been made worse by human activities and the consequences of climate change (Distefano and Kelly, 2017). Businesses that deal in oil and gas in the Middle Eastern region, which has a limited supply of water, are always looking for alternative sources of groundwater. An industry may face risks associated with water that can be classified as physical, regulation, or reputational (Moglia et al., 2024). At the ideal concentration, municipally recovered water exhibited reduced inorganic scale formation and did not deposit any scale on the surfaces of the cooling system. Based on the findings of the biohazard assessment that was carried out on the operations of cooling towers, it was determined that the deployment of a comprehensive water treatment system that included disinfection, in conjunction with stringent operating procedures, successfully reduced the potential for adverse health effects (Badruzzaman et al., 2022). Desalination is an innovative method employed to address worldwide water limitations. Desalination is the process of converting seawater and saltwater into freshwater (Ayaz et al., 2022). The feasibility of zero-liquid discharge cooling tower technique was evaluated in several parts of the Mediterranean basin, considering environmental concerns. Based on the findings of this investigation, the induced draft cooling tower has the capacity to evaporate 177 litres per hour of brine liquid fraction at a temperature of 23 °C (deNicolas et al., 2023).

Both the economic and social growth of a region are significantly impacted when there is a shortage of water. Having access to clean water is critical for several different industries as well as for human well-being; nevertheless, a lack of this resource can have a detrimental effect on agricultural and livestock production, which can result in higher food prices and insecurity (Dolan et al., 2021). Desalination plants have been developed in the region in recent years to treat water that contains substantial levels of salt and nitrate. This is done to ensure that people continue to have access to water that is free of contamination from this contaminated aquifer. This strategy, on the other hand, does have a few significant limitations, such as the significant expenditures that are associated with the treatment method and the discharge of brine that has been rejected into the ecosystem that is located nearby (Shalaby et al., 2022). Sedimentation and corrosion not only hinder the functioning of cooling tower pipes and equipment, but also impede heat transfer and result in higher energy consumption (Safari et al., 2013; Turetgen, 2014; Wang et al., 2019). Ultraviolet C/ Vacuum Ultraviolet (UVC/VUV) treatment performance is improved in acidic conditions due to increased light absorbance. On the other hand, alkaline environments enhance the performance of Photochemical Degradation (PCD) treatment. The influence of pH on other therapies is minimal (Saha et al., 2021).

Usually, freshwater sources are utilised to provide the water, and additional substances like acids, anticalins, corrosion inhibitors, and microbiological inhibition are included. Water concentration increases by evaporation, a process in which heat is transformed into latent heat. When the cooling tower discharges water (CTBD), the water gets released in order to keep the water's quality consistent throughout the entire processing system. As a consequence of this, the discharge from the cooling tower, which is known as cooling tower blow down (CTBD), is anticipated to have high levels of salt and to contain varying quantities of humic substances (HS) in addition to other organic compounds (OCs) (Yu et al., 2013). The thermal and diffusion properties of a wet cooling tower that employs a counter flow configuration and packs foam made from ceramics were investigated in a study that was carried out. According to the findings of the study, applying of foam-type ceramic material for packing led to a superior cooling performance for the tower in contrast to the deployment of alternative packing materials Huang et al (Chaibi et al., 2013). The temperature ratio improved the efficiency of the tower by increasing the rate of airflow and decreasing the temperature of the water at the output. This was done in order to evaluate the efficacy of employing plastic balls as packaging in FBCT (Ren, 2008). A higher temperature ratio has led to greater NTU values with various L/G ratios. Increased airflow resulted in a greater reduction in pressure. The findings indicated that this approach exhibited a 50% quicker cooling rate compared to alternative methods. Lower liquid-to-gas (L/G) ratios resulted in higher cooling rates (El-Dessouky, 1993).

The primary parameters that have a considerable impact on the tower's performance are the spray characteristics and the precise location of the manifold. The results that were acquired indicate that the configuration with the taller manifold is the most advantageous solution for all of the mass flow ratios that occurs when the tower operates. It obtains a performance that is 25% higher than that of the intermediate manifold and a performance that is 37% higher than that of the lower manifold respectively (Muscio et al., 2023). The design and operation of a wet cooling tower's fill, water supply system, and drift eliminator are the factors that affect the thermal efficiency of the tower. For the purpose of determining the impact that the filling have on the thermal performance of the cooling tower, a comprehensive analysis has been carried out (Navarro et al., 2023; Mohiuddin and Kant, 1996). For the purpose of determining the thermodynamic effectiveness of a mechanical system, an investigation was carried out. The cooling tower makes use of a number of different drift eliminators and distribution of water strategies during operation. With reference to the drift eliminators, the researchers arrived at a conclusion. As a result of the fact that the existence of an eliminator is unlikely to inevitably decrease the effectiveness of a cooling tower, this is an essential aspect to take into consideration. It is logical to infer that there is an effect, as there is a further reduction in air pressure throughout the airflow (MirabdolahLavasani et al., 2014). The presence of biohazards in high-temperature conditions poses challenges to the utilisation of municipal reclaimed water. Microbiological growth can occur in cooling towers within the temperature range of 20 to 50 °C (68 to 122 °F).

In order for the implementation to be successful, it is vital to have effective regulation of the replication of both bacteria and viruses. The levels of bacteria and viruses that are present in wastewater that has not been treated might vary

substantially. Both the primary and secondary treatment techniques have the potential to lower viral concentrations, despite the fact that they were not specifically developed for this objective specifically. As a consequence of this, tertiary treatments, which incorporate filtration, are commonly incorporated in order to construct numerous barriers. It has been determined that cooling towers are the source of every single outbreak of Legionnaire's disease that has ever occurred (Lucas et al., 2013; Tsao et al., 2019). It is possible for the efficiency of a cooling tower to be affected by a number of factors, including the temperature of the air around them, the humidity, and the temperature of the wet bulb. This study proposes a new cooling tower structure that contains an innovative control system that is capable of making optimal use of energy based on the weather conditions that are currently in effect. By implementing this concept, the overall efficiency of the cooling system is going to be improved (Crook et al., 2020). A comparison of the novel packing to the conventional straight-wave packing revealed that the novel packing exhibited a 14.4% gain in cooling efficiency. This phenomenon has a significant impact and presents a novel approach to improving heat transport in cooling towers, that can be employed in engineering procedures thanks to its unique nature. After examining the present operational characteristics of the tower, it has been concluded that raising the height of the packaging enhances the cooling process. Furthermore, by decreasing the ratio of gas to liquid and air volume needs, substantial air volume reductions of up to 30% can be achieved (Salins et al., 2023).

Novelty and objective of the research

The novelty of this study on fluidized bed cooling towers (FBCT) lies in its comprehensive examination of the combined effects of varying bed heights (200 mm and 300 mm) and different sizes of spherical turbulence balls (25 mm and 50 mm) on thermal performance have not been extensively explored in prior research. By analyzing air-water interactions and providing detailed metrics on air-side pressure drops and fluidization velocities, the study aims to evaluate how these parameters influence cooling efficiency, explicitly focusing on enhancing air mixing efficiency through more petite spherical balls. Additionally, the research seeks to understand the relationship between water flow rates, air flow rates, and inlet temperatures on the thermal performance of FBCTs, ultimately contributing to improved design and operational strategies for enhanced energy efficiency and reduced costs in industrial cooling applications.

HEAT TRANSFER BEHAVIOUR IN FLUIDIZED BED COOLING SYSTEMS

This highly specialist type of heat exchanger, known as fluidized bed cooling towers, has been utilised in a wide variety of industrial applications for the purpose of chilling hot water. In order to determine the thermal parameters of a fluidized bed cooling tower, it is necessary to conduct comprehensive investigation of heat transfer, fluid flow, and thermodynamics throughout the entire system. Heat transfer mechanisms, fluidization, and temperature gradients are some of the important aspects that can be used to characterise the thermal characteristics of fluidized bed cooling towers. Shape factors to be considered include the height of the bed, the size of the particles, and the shape of the heat exchange surface.

EXPERIMENTAL ARRANGEMENT AND METHODOLOGY

Figure 1 depicts a comprehensive experimental setup as well as the components that were utilised to ascertain the heat and mass transport properties of a fluidized bed cooling tower. The dimensions of the duct's cross-sectional area are 20 cm x 20 cm, as shown in Table 1. The height of the duct is 100 cm. There is a thickness of 0.15 cm in the conduit. One of the components that supplied the cooling water was a rotameter, which had a discharge capacity of 2-18 lpm. The water was consistently dispersed throughout the cooling tower in a uniform manner. After careful consideration, it was decided to deliberately set up a water reservoir in close proximity to the lowest of the tower in order to collect the cold water that was expelled from the tower. An aquatic pump was employed in order to transport water from the storage tank to the highest point of the tower column. To determine the pressure difference that existed between the airflow channels, a manometer with a U-tube was utilised. For the goal of measuring a wide range of temperatures, the RTD sensors were use. An inductive water heater with a power output of three thousand watts was utilised to supply thermal energy. For supplying fluidized air, the tower was fitted with a centrifugal air blower that had a capacity of 650 watts. When it came to adjusting the rate of airflow to the column, a valve that had controls was utilised. In addition, a bypass connection was installed prior to the throttle valve in order to safeguard the air blower against any potential damage. This action was taken in order to avoid any potential destruction. An electric air heater was employed in order to achieve the desired effect of adjusting the temperature of the air that was being circulated. The experimental setup is depicted in a schematic form in Figure 1, which features an illustration. Experiments were conducted for the following parameters.

1. Variable air velocity
2. Variable water flow rate
3. Bed height (200-300 mm)
4. Fluidized Ball diameter (25mm and 50mm spherical balls).

Table 1. Cooling Tower Specifications

Parameter	***Measurement***
Tower magnitudes	100 cm height and 20x20 cm cross-section (square)
Width	0.15cm
Air Blower	650 Watts
Rotameter	2-18 lpm
Induction Heating System	3000 Watts

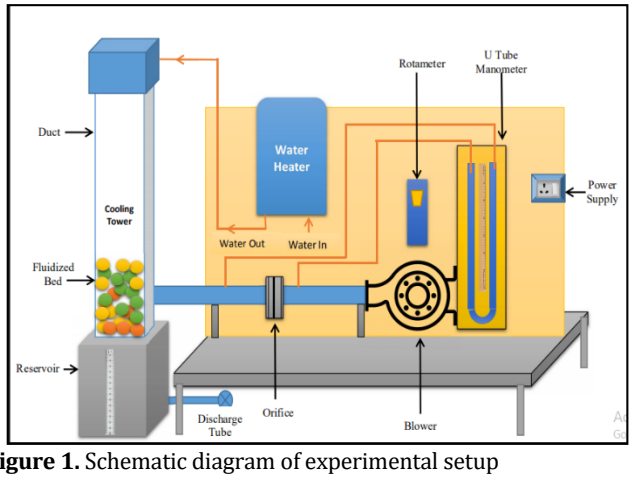

Figure 1. Schematic diagram of experimental setup

RESULTS AND DISCUSSION

Both the range, which corresponds to the difference in temperature between the cold water that enters and leaves the tower, and the approach, that is the difference in temperature among the cold water and the temperature of the wet bulb, are the key parameters that govern the features of a cooling tower. The range is the difference in temperature between the cold water and the wet bulb. The range and the approach are the terms that are used to refer to both of these distinctions, respectively. Additionally, the ratio of the flow rate of liquid to the flow rate of gas, usually commonly referred to as the L/G ratio, is also an important factor in the process. This ratio plays a significant role in the process. It was established that the two significant zones in the cooling tower were identified as a result of the interaction between the air and the water in the cooling tower. In situations where the water flow rates are quite low, the first zone that takes place is referred to as the pellicular regime (PR), and it is the zone that takes place. The bubble and dispersion phase, sometimes abbreviated as Bubble and dispersion phase (BDR), is a distinct regime that occurs at greater flow rates. It is commonly referred to as the bubble and dispersion phase.

Air velocity vs. Cooling tower efficiency

The variation in cooling tower effectiveness that occurs at various air velocities is seen in Figure 2. In compared to the other cases, the cooling tower efficiency of the BH300 mm with BD50 mm configuration was found to be significantly greater. The Wet Bulb Temperature (WBT) of the surrounding air is the point at which the water that has been cooled reaches its lowest temperature. The efficiency of the cooling tower was calculated for a BH (height of the cooling tower) of 300 mm and a BD (diameter of the cooling tower) of 25 mm, with a water flow rate of 2 litres per minute. The efficiency values achieved were 78.94%, 86.36%, 91.85%, 90.14%, and 92.83% when the air flow rates were 4.1 m/s, 6.3 m/s, 7.0 m/s, 8.2 m/s, and 8.5 m/s, correspondingly. Conventional cooling towers are unable to reach water cooling temperatures that are like the Wet Bulb Temperature (WBT). This is due to the minimal interaction between water and fresh air as the water flows over the fill surface [23].

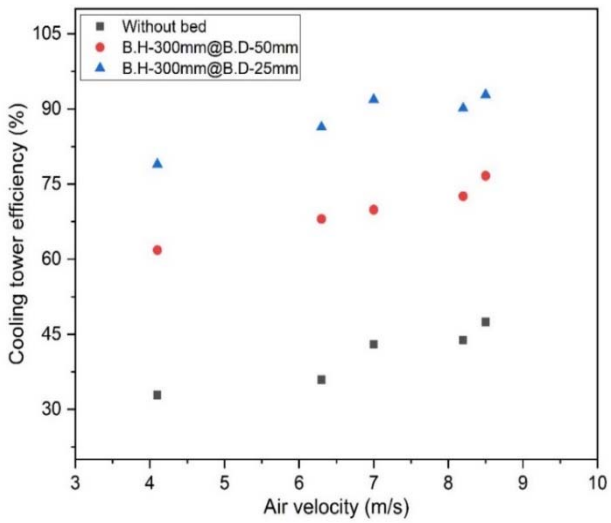

Figure 2. Air velocity vs. cooling tower efficiency

Air velocity vs. Evaporative loss

Figure 3 depicts the relationship between air velocities and the variance of evaporative loss. The evaporation rate is more significant for a BH of 300 mm and BD of 50 mm compared to other scenarios. While natural convection drives the airflow in cooling tower packing, gravitational forces primarily influence the water flow. It is feasible for water to evaporate into the air in a cooling tower, which results in the loss of heat. This phenomenon is known as evaporative loss.

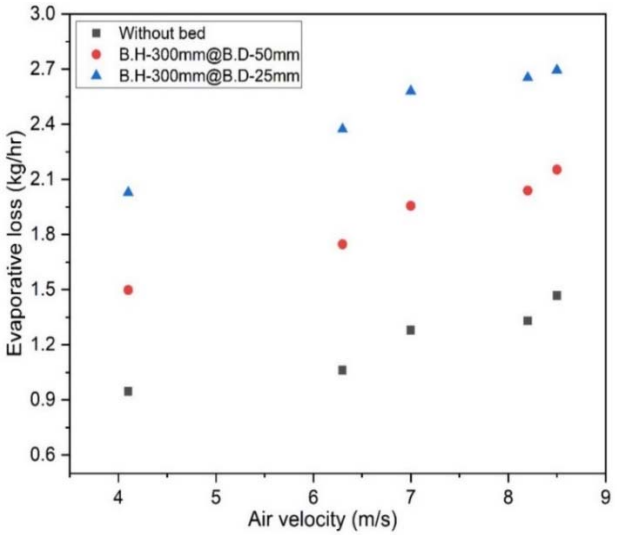

Figure 3. Air velocity vs Evaporative loss

It is good because this result has the effect of increasing the cooling impact, which is why it is desirable. In order to determine the amount of water that is lost through evaporation, there are a number of factors that play a role. These factors include the temperature difference between the water and the air, the relative humidity of the air, and the surface area that is accessible for evaporation. When the velocity of the air that is being transported rises, the potential for evaporative loss also increases. This is because improved water-to-air contact and higher evaporation both contribute to this potential increased loss (Agarwal et al., 2022). The results demonstrate that although elevated air velocity augments evaporative loss through enhanced water-to-air interaction, this increase is not limitless. The findings indicate a notable increase in evaporative loss with elevated air velocities; nevertheless, practical factors, like environmental humidity and system limitations, may restrict the maximum attainable benefit (Amir et al., 2023). The augmentation of air velocity is substantial in improving evaporative loss, especially for the configuration including a bed height (BH) of 300 mm and a ball diameter (BD) of 50 mm. However, at a certain threshold, efficiency improvements may stabilize or decline due to possible air over-saturation or constraints in water distribution efficacy (Agarwal et al., 2022). Mass loss (evaporation) directly influences the effectiveness of the cooling tower by enhancing heat removal via latent heat. Augmented evaporative loss amplifies the cooling effect, hence enhancing thermal performance. Excessive mass loss without corresponding cooling advantages may result in water wastage and operational inefficiencies (Salins et al., 2023).

Air velocity vs. L/G

Figure 4 shows the graphical representation of the fluctuation in the liquid-to-gas (L/G) ratio across different air velocities. The maximum length-to-girth ratio was observed for the tree with a B.D of 50 mm and BH of 300 mm. Based on the graphical representation, the L/G ratio exhibited a rapid increase followed by a subsequent decrease. Eventually, the curve reached a point of stability where it maintained a constant value. The primary factors that exert influence are temperature and enthalpy. At elevated temperatures, the liquid-to-gas ratio exhibits a near-constant behaviour. However, if the L/G ratio is excessively high, which indicates that there is an abundance of water in comparison to the air, this might lead to an increase in the amount of water that is carried over.

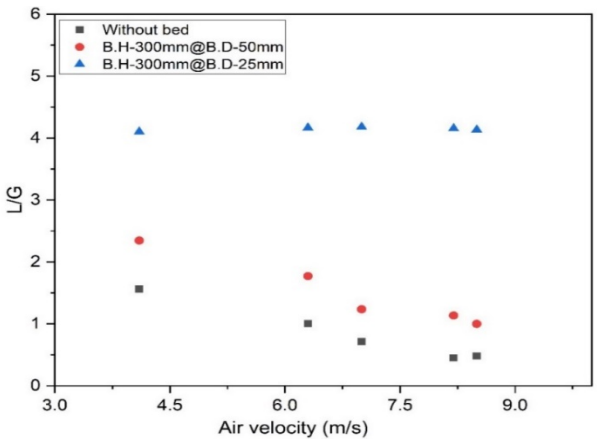

Figure 4. Air velocity vs L/G ratio

Extremely high L/G ratios have the potential to cause water droplets to be carried out of the tower along with the exhaust air, which can have adverse effects on both the environment and the operations of the tower. When it comes to maximizing the performance of cooling towers, it is essential to strike the appropriate balance between the L/G ratio and the air velocity. The use of suitable fill media, effective water distribution systems, and suitable tower designs can maintain the required L/G ratio and increase heat transfer efficiency (Xi et al., 2023).

Air velocity vs. NTU

Figure 5 depicts the correlation between NTU (Number of Transfer Units) and different air velocities. The BH 300 mm with BD 25 mm demonstrates the most minimal NTU in comparison to other variations. The relationship between air velocity and NTU in a cooling tower is complex and dependent on various factors, including the design, water flow rate, and ambient conditions. Increasing the speed of the airflow can result in a decrease in the NTU value. As the velocity of the air increases, the amount of time that the air and water are in touch with one another reduces. This leads to a reduction in the amount of heat that is transferred. This can be counteracted by modifying alternative design characteristics or tweaking operational circumstances to maintain or improve the overall efficiency of the cooling tower. The relationship between air velocity and NTU is a vital component of the thorough optimisation process for cooling tower design. Scientists consider several factors, including water distribution, material for packing, air distribution, and operating circumstances in order to achieve the necessary heat transfer efficiency (Salins et al., 2023).

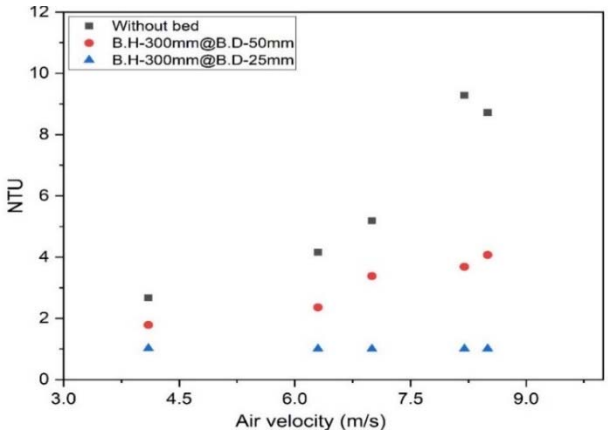

Figure 5. Air velocity vs. NTU

Water flow rate vs. cooling tower efficiency

It is common practice to measure the efficiency of a cooling tower based on its heat transfer performance. This performance is what defines the quantity of evaporative cooling that may be achieved. Figure 6 provides a visual representation of the connection that exists between the effectiveness of a cooling tower and the rate at which water enters and exits the tower. The ratio of the actual decrease in water temperature to the highest decrease that was conceivable was determined in order to evaluate the effectiveness of the heat transfer system. This ratio represented the ratio between the real decline and the maximum decrease. The capacity of the cooling tower was increased as a result of increasing the total quantity of water that was running through it simultaneously. A bed height of 300 mm and a ball diameter of 50mm allowed the cooling tower to achieve its maximum effectiveness. Utilising the height of the bed allowed for this to be accomplished. A number of different air flow rates were tested, and it was found that the cooling tower had an efficiency of 31.4%, 36.5%, 43%, 43.4%, and 47.4% when the bed material was not there. When determining the effectiveness of the cooling tower, a fluidized bed with a height of 300 millimetres, a water flow rate of two litres per minute, and a ball diameter of fifty millimetres was utilised in the calculation. According to the findings, the tower exhibited an efficiency of 61.81%, 68.01%, 69.88%, 72.59%, and 76.99% for the various air rates that were tested during the experiment. There is a potential for a substantial disparity in enthalpy to occur between the hot water which is being introduced into the tower and the water which is being cooled at the point of intake (Shublaq and Sleiti, 2020). A possible explanation for the tower's superior efficiency is that this differential is accountable for it.

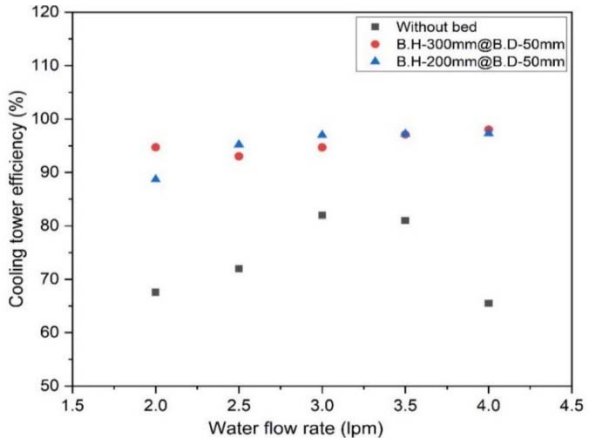

Figure 6. Water flow rate vs. cooling tower efficiency

Water flow rate vs. evaporative loss

Figure 7 depicts the fluctuation in evaporative loss that occurs as a result of switching between different water flow rates. It is possible to draw the conclusion from the figure that the rate of evaporation was lower for BH 200 mm in comparison to BD 50 mm on the other hand. The measures of BH 300 mm and BD 50 mm were the ones that experienced the highest level of evaporation.

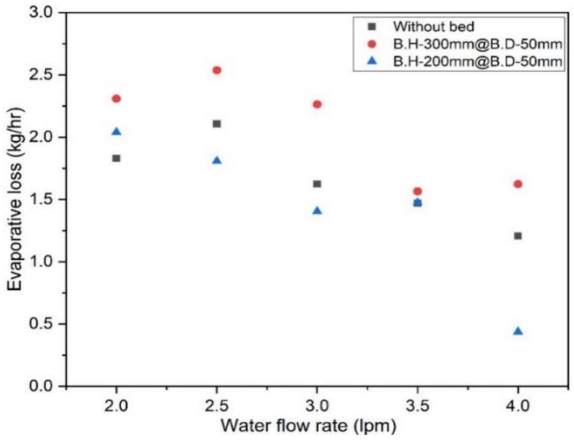

Figure 7. Water flow rate vs. evaporative loss

Water flow rate vs L/G

The variation in the L/G ratio that occurs in respect to the various water flow rates is seen in Figure 8. When compared to the situation in which a bed was present, the L/G ratio displayed a greater magnitude when there was no bed present. It is possible to establish a connection between the increased cooling capacity of the tower and a decrease in the water flow rate, which ultimately leads to a diminished cooling potential at higher water flow rates. With an air flow velocity of 8.47 metres per second, the L/G ratio was measured to be 0.5, 0.75, 1, 1.25, and 1.5 for water flow rates of 2 lpm, 2.5 lpm, 3 lpm, 3.5 lpm, and 4 lpm, respectively. This was done without the presence of the fluidized bed. It has been noted that the rate at which water flows has a crucial impact on the ratio of liquid to gas (L/G), which in turn has a substantial influence on the performance and features of a system. Enhancing the liquid flow rate in comparison to the gas flow rate facilitates the transfer of mass between the liquid and gas regimes. Increasing the flow velocity of the liquid can lead to higher reductions in pressure inside the system. This can have a significant impact on the overall efficiency and sustainability of a process, especially in instances where restrictions on pressure are crucial. The practical execution of perpetual cooling is not achievable (Xi et al., 2023).

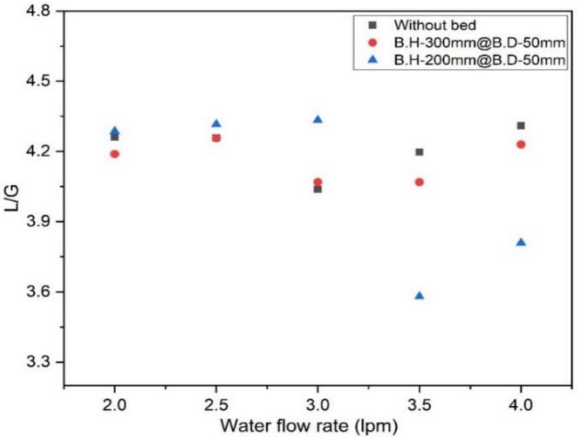

Figure 8. Water flow rate vs L/G ratio

Water flow rate vs NTU

Figure 9 illustrates the variation in the number of transfer units (NTU) that occurs when the water flow rate is changed. This variation can be observed in the figure. It was discovered that the NTU value was at its highest when the bed height was precisely 200 millimetres and the ball diameter was precisely fifty millimetres. As the ratio of L to G is raised, there is a corresponding reduction in the mass flux that takes place. The decrease in the rate of heat and mass transfer that occurred as a result of the interfacial activity level led to an increase in the temperature of the cold water. This was the result of the interfacial activity happening. When the velocity of the water with the lowest fluidization hits a critical point, the fluidized bed begins to exhibit instability. A decrease in the water flow rate is implemented in order to establish a fluidized bed that is stable. This leads to a decrease in the temperatures at the exit. In a cooling tower, the link between the mean thermal unit (NTU) and the water flow rate in the cooling tower is influenced by both the design of the cooling tower and the operational parameters of the cooling tower. Several aspects are taken into consideration while calculating the NTU. These aspects include the surface area of the heat exchanger, the heat transfer coefficient, and the rate of flow of both the hot and cold fluids flowing through the heat exchanger. It is of the utmost importance to take into consideration the fact that the influence of flow velocity on NTU and the efficiency of the cooling tower may be dramatically different depending on the architecture and characteristics of the cooling tower (Ren, 2008).

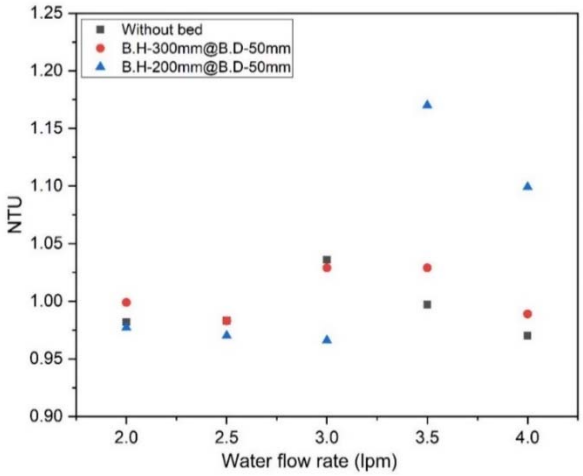

Figure 9. Water flow rate vs NTU

CONCLUSION

In conclusion, this study demonstrates that varying bed heights and the use of different sizes of spherical turbulence balls significantly impact the thermal performance of FBCT.

- Increasing the bed height from 200 mm to 300 mm significantly enhances the cooling tower's thermal efficiency.
- Compared to larger balls (50 mm), smaller spherical turbulence balls (25 mm) improve air mixing efficiency, leading to better thermal performance.
- The study reports cooling tower efficiency values reaching up to 92.83% under optimal conditions, highlighting the effectiveness of the FBCT design.
- The FBCT research achieved a maximum efficiency of 92.83%, which is competitive with, and in certain instances surpasses,

the efficiencies of traditional cooling tower designs. This indicates that fluidized bed cooling towers may provide substantial benefits in thermal performance, especially in scenarios where optimizing cooling efficiency is essential.
- The cooling tower's interaction between air and water is critical in determining heat transfer capabilities. The study identifies two distinct regimes (pellicular and bubble dispersion) crucial in this interaction.
- The research emphasizes the importance of water flow rates and air flow rates in determining the cooling tower's overall thermal performance.
- The findings provide insights for improving the design and operation of FBCTs, contributing to enhanced energy efficiency and reduced operational costs in industrial settings.

AUTHORS STATEMENTS

Sathiyamoorthi Ramalingam: Investigation, supervision, Project administration, Resource Mukilarasan Nedunchezhiyan, Ravikumar Jayabal: Methodology, Interpretation, Conducted the experiments, Writing manuscript.

REFERENCES

Agarwal, N. K., Biswas, P., & Shirke, A. (2022). Novel model predictive control by hypothetical stages to improve energy efficiency of industrial cooling tower. *Applied Thermal Engineering, 215*, 118899. https://doi.org/10.1016/j.applthermaleng.2022.118899

Amir, F. M., Yusoff, M. Z., & Hassan, S. H. A. (2023). Cooling tower performance and the ambiguity of the L/G ratio scheme in optimization: A single cell control volume approach. *International Communications in Heat and Mass Transfer, 142*, 106653. https://doi.org/10.1016/j.icheatmasstransfer.2023.106653

Ayaz, M., Namazi, M., ud Din, M. A., Ershath, M. M., Mansour, A., & Aggounee, M. (2022). Sustainable seawater desalination: Current status, environmental implications, and future expectations. *Desalination, 540*, 116022. https://doi.org/10.1016/j.desal.2022.116022

Badruzzaman, M., et al. (2022). Municipal reclaimed water as makeup water for cooling systems: Water efficiency, biohazards, and reliability. *Water Resources and Industry, 28*, 100188. https://doi.org/10.1016/j.wri.2022.100188

Chaibi, M. T., Bourouni, K., & Bassem, M. M. (2013). Experimental analysis of the performance of a mechanical geothermal water cooling tower in South Tunisia. *American Journal of Energy Research, 1*, 1–6. https://doi.org/10.12691/ajer-1-1-1

Crook, B., Willerton, L., Smith, D., Wilson, L., Poran, V., Helps, J., & McDermott, P. (2020). Legionella risk in evaporative cooling systems and underlying causes of associated breaches in health and safety compliance. *International Journal of Hygiene and Environmental Health, 224*, 113425. https://doi.org/10.1016/j.ijheh.2019.113425

deNicolás, A. P., Molina-García, A., & Vera-García, F. (2023). Performance evaluation and feasibility study of a cooling tower model for zero liquid discharge-desalination processes. *Energy Conversion and Management, 297*, 117673. https://doi.org/10.1016/J.ENCONMAN.2023.117673

Distefano, T., & Kelly, S. (2017). Are we in deep water? Water scarcity and its limits to economic growth. *Ecological Economics, 142*, 130-147. https://doi.org/10.1016/j.ecolecon.2017.06.019

Dolan, F., Lamontagne, J., Link, R., Hejazi, M., Reed, P., & Edmonds, J. (2021). Evaluating the economic impact of water scarcity in a changing world. *Nature Communications, 12*(1), 1915. https://doi.org/10.1038/s41467-021-22194-0

El-Dessouky, H. (1993). Thermal and hydraulic performance of a three-phase fluidized bed cooling tower. *Experimental Thermal and Fluid Science, 3*, 417–426. https://doi.org/10.1016/0894-1777(93)90018-E

Lucas, M., Ruiz, J., Martínez, P. J., Kaiser, A. S., Viedma, A., & Zamora, B. (2013). Experimental study on the performance of a mechanical cooling tower fitted with different types of water distribution systems and drift eliminators. *Applied Thermal Engineering, 50*(1), 282–292. https://doi.org/10.1016/j.applthermaleng.2012.06.030

MirabdolahLavasani, A., NamdarBaboli, Z., Zamanizadeh, M., & Zareh, M. (2014). Experimental study on the thermal performance of mechanical cooling tower with rotational splash type packing. *Energy Conversion and Management, 87*, 530–538. https://doi.org/10.1016/j.enconman.2014.07.036

Moglia, A., Bracco, L., Chiolo, M., & Buffagni, M. (2024). *E&P Operations in Water Stressed Areas: An Approach to the Identification, Selection and Implementation of Initiatives for a Sustainable Water Management, Withdrawal Reduction and Water Valorization*. https://doi.org/10.2118/220301-ms

Mohiuddin, A., & Kant, K. (1996). Knowledge base for the systematic design of wet cooling towers. Part II: Fill and other design parameters. *International Journal of Refrigeration, 19*(1), 52–60. https://doi.org/10.1016/0140-7007(95)00060-7

Muscio, A., et al. (2023). A modified ε-NTU analytical model for the investigation of counter-flow Maisotsenko-based cooling systems. *Applied Thermal Engineering, 120944*. https://doi.org/10.1016/j.applthermaleng.2023.120944

Navarro, P., et al. (2023). Effect of fill length and distribution on the thermal performance of an inverted cooling tower. *Applied Thermal Engineering, 120876*. https://doi.org/10.1016/j.applthermaleng.2023.120876

Ren, C.-Q. (2008). Corrections to the simple effectiveness-NTU method for counterflow cooling towers and packed bed liquid desiccant–air contact systems. *International Journal of Heat and Mass Transfer, 51*(1–2), 237–245. https://doi.org/10.1016/j.ijheatmasstransfer.2007.04.028

Safari, I., Walker, M. E., Hsieh, M.-K., Dzombak, D. A., Liu, W., Vidic, R. D., Miller, D. C., & Abbasian, J. (2013). Utilization of municipal wastewater for cooling in thermoelectric power plants. *Fuel, 111*, 103–113. https://doi.org/10.1016/j.fuel.2013.03.062

Saha, P., et al. (2021). Advanced oxidation processes for removal of organics from cooling tower blowdown:

Efficiencies and evaluation of chlorinated species. *Separation and Purification Technology, 278*, 119537. https://doi.org/10.1016/j.seppur.2021.119537

Salins, S. S., et al. (2023). Influence of packing configuration and flow rate on the performance of a forced draft wet cooling tower. *Journal of Building Engineering, 72*, 106615. https://doi.org/10.1016/j.jobe.2023.106615

Shalaby, S., Sharshir, S. W., Kabeel, A., Kandeal, A., Abosheiasha, H., & Abdelgaied, M., et al. (2022). Reverse osmosis desalination systems powered by solar energy: Preheating techniques and brine disposal challenges–A detailed review. *Energy Conversion and Management, 251*, 114971. https://doi.org/10.1016/j.enconman.2021.114971

Shublaq, M., & Sleiti, A. K. (2020). Experimental analysis of water evaporation losses in cooling towers using filters. *Applied Thermal Engineering, 175*, 115418. https://doi.org/10.1016/j.applthermaleng.2020.115418

Tsao, H. F., Scheikl, U., Herbold, C., Indra, A., Walochnik, J., & Horn, M. (2019). The cooling tower water microbiota: Seasonal dynamics and co-occurrence of bacterial and protist phylotypes. *Water Research, 159*, 464–479. https://doi.org/10.1016/j.watres.2019.04

Turetgen, I. (2004). Comparison of the efficacy of free residual chlorine and monochloramine against biofilms in model and full-scale cooling towers. *Biofouling, 20*, 81–85. https://doi.org/10.1080/08927010410001710027

Wang, Y., Shen, C., Tang, Z., Yao, Y., Wang, X., & Park, B. (2019). Interaction between particulate fouling and precipitation fouling: Sticking probability and deposit bond strength. *International Journal of Heat and Mass Transfer, 144*, 118700. https://doi.org/10.1016/j.ijheatmasstransfer.2019.118700

Xi, Y., et al. (2023). Research on heat and mass transfer characteristics of a counterflow wet cooling tower using a new type of straight wave packing. *International Journal of Thermal Sciences, 193*, 108540. https://doi.org/10.1016/j.ijthermalsci.2023.108540

Yu, X., Yang, H., Lei, H., & Shapiro, A. (2013). Experimental evaluation on concentrating cooling tower blowdown water by direct contact membrane distillation. *Desalination, 323*, 134–141. https://doi.org/10.1016/j.desal.2013.01.029

TÜRK ISI BİLİMİ VE TEKNİĞİ DERNEĞİ

TURKISH SOCIETY FOR THERMAL SCIENCE AND TECHNOLOGY

TIBTD